SIMULATION OF FILTRATION FOR SUSPENSION TRANSPORT IN POROUS MEDIA

by

Yun Sung Kim

M.S., Department of Civil and Environmental Engineering
Korea Advanced Institute of Science and Technology, 1998

B.S., Department of Civil and Environmental Engineering
Korea Advanced Institute of Science and Technology, 1996

Submitted to the Department of Civil and Environmental Engineering in Partial Fulfillment of the Requirements for the Degree of

Doctor of Philosophy in Geotechnical and Geoenvironmental Engineering at the Massachusetts Institute of Technology

February 2005

Signature of Author: .....
Department of Civil and Environmental Engineering
November 1, 2004

Certified by: .....
Andrew J. Whittle
Professor of Civil and Environmental Engineering
Thesis Supervisor

Accepted by: .....
Andrew J. Whittle
Chairman, Committee for Graduate Students

Simulation of Filtration for Suspension Transport in Porous Media

by

Yun Sung Kim

Submitted to the Department of Civil and Environmental Engineering
on November 1, 2004 in partial fulfillment of the requirements for the
Degree of Doctor of Philosophy in
Geotechnical and Geoenvironmental Engineering

ABSTRACT

This thesis describes the development and application of a novel method for analyzing the filtration of particles transported through a granular porous medium. The proposed analysis considers the deposition of particles through discrete simulations of particle-laden flow in a cylindrical model pore. The pore model assumes that particles collect, mound up and ultimately clog the pore under the action of hydrodynamic and gravitational forces. By simulating particle deposition processes at the pore scale, the current analyses provide a more realistic physical framework for interpreting filtration experiments than conventional continuum models that implicitly assume length scales much larger than the pores.

A detailed parametric study has established relationships between the collection efficiency, mound height and deposit depth as functions of the model pore dimensions, orientation (relative to the gravitational field) and particle settling velocity for injection at constant flow rate. The results showed that the maximum mound height and deposit depth can be correlated with the pressure difference necessary to maintain flow through the model pore.

A quasi one-dimensional network 'bubble' model (Datta and Redner, 1998) was developed to simulate 1-D suspension transport problems. The bubble model comprises a serial linkage of bundles of cylindrical bonds with shared nodes at each end. Bubble model simulations include distribution functions for the pore dimensions. Filtration in an individual bond is characterized by correlations from the model pore simulations.

The bubble model has been applied to interpret filtration data from two sets of column experiments: acrylic particle transport through glass beads by Yoon et al. (2004), and microfine cement suspension through a sand bed by Bouchelaghem and Vulliet (2001). It was found that the collection efficiency obtained from model pore simulations overestimates the measured filtration rates due to detachment process that are not considered in the parametric study. Two empirical parameters, attachment probability and detachment rate were employed to partition the deposited particles between those firmly attached and those detachable, and its rate of re-entrainment. With these parameters, the bubble model produced successful predictions of measured temporal and spatial filtration extent in column tests that have proved difficult to simulate with continuum models.

Thesis Supervisor: Andrew J. Whittle
Title: Professor of Civil and Environmental Engineering

ACKNOWLEDGEMENTS

I would like to acknowledge and thank people to whom I am deeply indebted for the completion of this thesis:

To my thesis advisor, Professor Andrew Whittle for his insights and knowledge that rescued me from the deep sea of confusion multiple times. I am also very grateful of his careful review of this thesis;

To members of my thesis committee, Professor Patricia Culligan, Professor Charles Harvey, and Professor Franz-Josef Ulm for providing many valuable comments and constructive suggestions;

To Professor Herbert Einstein, Doctor John Germaine, and Professor Charles Ladd who taught me all I know about soils and rocks through their wonderful (and sometimes very demanding) courses;

To Yo-Ming (now, Professor Hsieh) and Professor Ruaidhri O'Connor for their help on numerical computing, and to Joon Sik Yoon for providing laboratory data, which were essential to this thesis;

To Professor Seung-Rae Lee at KAIST, Korea, who is responsible for initiating my interest in soils that has brought me this far;

To all of Building 1 people I have met over the years, including Christoph Haas, Alice Kalemkiarian, Sung-June Kim, Attasit 'Pong' Korchaiyapruk, Sangyoon Min, Maria Nikolinakou, Sanjay Pahuja, Moonseo Park, Jianyong Pei, Federico Pinto, Anamika Prasad, and Kartal Toker with whom I shared lots of fun, and, in many aspects, wonderfully educational moments in classrooms, offices, and sometimes outside MIT;

To my dearest 'sisters': Jaeyeon Jung, Eun Soo Lee, Eun-Jin Lee, Young-Su Lee, Jeong-Hwa Pae, Hesson Park, Jiehyun Seong, and Ji Hyun Yang with whose ever-patient ears I am greatly blessed;

Finally, I owe my deepest gratitude to my family: Umma (Mom), Appa (Dad), Unni (Sister), Taksu (Brother), Niki (the Dog), and Dulia (the Cat) who have never stopped giving me unquestioned love and support. I dedicate this thesis to them with love and respect.

"I'll never be able to be here again. As the minutes slide by, I move on. The flow of time is something I cannot stop. I haven't a choice. I go.

One caravan has stopped, another starts up. There are people I have yet to meet, others I'll never see again. People who are gone before you know it, people who are just passing through. Even as we exchange hellos, they seem to grow transparent. I must keep living with the flowing river before my eyes.

I earnestly pray that a trace of myself will always be with you.

For waving good-bye. I thank you. For your hand keeping waving and waving, thank you."

From *Moonlight Shadow* by Banana Yoshimoto

CONTENTS

LIST OF FIGURES

LIST OF TABLES

CHAPTER 1. INTRODUCTION

1.0 FILTRATION

Filtration is a term used to describe the deposition and attachment of solid particles from the transport of a fluid suspension through a porous medium. Filtration is encountered widely in natural and industrial systems. Examples of natural system include subsurface transport of colloidal pollutant (see review by Ryan and Elimelech, 1996), and migration of fines (see review by Sahimi et al., 1990). In the chemical and biological engineering fields, deep-beds of granular material are designed as filters (see review by Tien, 1989). Filtration can also occur as an undesirable characteristic of ground improvement processes such as permeation grouting. In this technique, low viscosity fluid grout in injected to water filled voids with minimal displacement of the soil skeleton (Landry et al., 2000; Arenzana et al., 1989; Schwarz and Krizek, 1994; Santagata and Collepardi, 1998; De Paoli et al., 1992; Perret et al., 2000). Filtration can cause blockage of the pores and inhibit or constrict effective permeation of the soil mass.

The dynamics of filtration are determined by the structure of the filters, the particle size distribution, hydrodynamic conditions, and surface forces of both the transported particles and host medium. When a porous medium works as a filter, the suspended particles become trapped when they are either larger than the pores or pore throats (straining) or when they separate from the transporting fluid and adhere to the grain surface (infiltration) (Hwang and Redner, 2001). Filtered particles by either of these mechanisms will affect the subsequent flow and filtration process. Therefore, the prediction of particle collection rate and assessment of the effect of filtered particles on subsequent flow are essential components in the study of particle transport through porous media.

1.1 EXAMPLES OF FILTRATION IN GRANULAR POROUS MEDIUM

Filtration observed in 1-D laboratory column injection tests, where measurements of effluent concentration (referred to as 'breakthrough curves'), provide indirect evidence of filtration. For example, Figure 1.1a shows the effluent concentration, C, normalized by the input concentration, C_0, from injection tests with a colloidal protozoan parasite (*C. parvum*) through a 10cm long sand column (Harter et al., 2000). The parasite oocysts have a diameter of 4.5-5.5μm, while the coarse sand particles range in diameter from 1.4 to 2.4mm. The tests were performed at a constant seepage velocity (1.94 m/day) for a time period corresponding to 2.5 pore volumes (pV), the column was then flushed with 5 pV of de-aired water. The same sequence was repeated using a reference chloride solution. The breakthrough curves for both oocysts and chloride clearly show an increase in the effluent concentration as the injection progresses. It is interesting to notice that initial arrival of oocysts occurs earlier than $1pV$, showing the effects of hydrodynamic dispersion, while that of chloride solution happens after almost exactly $1pV$ of injection. The breakthrough concentration of oocysts reaches a maximum value corresponding to 10% of the initial concentration, soon after initial breakthrough and remains within the range 8-13% during the solution injection phase. This result shows that approximately 90% of the injected oocysts were filtered by the sand grains. This behavior can be contrasted with the breakthrough curve of the chloride solution which reaches almost 100% of the injected concentration at $1pV$ and remains constant during injection. The concentration of the filtered oocysts was measured by sampling the sand column after completion of the test as shown in Figure 1.1b. It is noticeable from this figure that the concentration decreases with distance from input. This can be explained by a decrease in oocyst concentration due to filtration, and suggests that filtration occurs at a rate proportional to the concentration. The fact that the breakthrough concentration of the oocysts stays almost consistently at 10% implies that filtration occurs at a constant rate.

Figure 1.2 shows breakthrough curves obtained from another experimental study by Liu (1994) using colloidal aluminum oxide (Al_2O_3) particles of diameter 0.12μm, injected through a packed column of quartz sand (average diameter, 0.21mm). The

column height was 14.2cm, and the pore velocity was 0.1cm/sec. In this case, the breakthrough concentration ultimately reaches the initial concentration after more than $20pV$-$80pV$ (depending on the input concentration). This fact is indicative of a decreasing filtration rate. This can occur when deposited alumina particles repel other positively charged particles in solution inhibiting further filtration.

When there is sufficient accumulation of filtered material, the pressure required for injection at a constant flow rate must increase. For example, Reddi et al. (2000) performed long duration (up to $1{,}100pV$) injection tests of a kaolinite suspension (particle size, 1.9-12 μm) into a sand column (64mm long, and 76mm diameter) at a constant flow rate. The sand particle diameter is distributed from 0.1mm to 7mm (with D_{50} = 1mm). As a result, a significant increase in the pressure change was measured across the sand column. The measured pressures were then interpreted as measures of the permeability assuming Darcy's law. Figure 1.3 shows the corresponding decreases in apparent permeability in the sand column for two different tests with input concentration of kaolinite C_0 = 0.5g/L and 1.0g/L. Permeability initially decreases at rapid rates in both cases as the injection progresses. They slow down and stabilize at around 400 pV's. The extent of decrease is higher for the high initial concentration case (C_0 = 1.0g/L), again suggesting the dependency of filtration rate on the suspension concentration. The fact that the stabilized permeability values are above zero implies complete clogging was not reached. This must be due to increased flow velocity (the tests were done in constant flow rate and hence, seepage velocity must increase in order to compensate for the reduction in permeability) that worked to reduce filtration by shortening the duration of residency of particles in the sample. Another possible effect of increase in flow velocity, increased rate of re-entrainment process will be discussed in Chapter 6 in detail.

1.2 ANALYSIS OF SUSPENSION TRANSPORT THROUGH POROUS MEDIA

Continuum models, which are based on the solutions of mass/momentum conservation equations, are often used in analyses of suspension transport. These have the

advantage of simplicity and can easily be adapted (as shown in Chapter 2). Continuum mechanics is based on the assumption that the scale of the problem is much larger than the pore scale, such that pore-level phenomena need not be considered. However, the transport, of suspended particles is strongly affected by the structural features of pores and characteristics of their connections. For example, the shape and orientation of a pore are significant factors which can determine whether a particle will settle under the effect of gravity. Once the particle settles on the pore wall, the particle may be attached if the attraction force is larger than repelling force. These forces are also dependent on local characteristics in pores. More specifically, they depend on the conditions such as surface roughness, balance of electrical forces, and flow velocity (Tien, 1989). These conditions, in turn, will be affected by the pre-existence of other collected particles and the changed conditions will determine the fate of particles later moving into the pore.

An alternative to the continuum approach is to use network models. A network model is a regular or a random lattice of pores and pore throats with simplified geometry and topology. The simplified model pores and pore throats are statistically connected to have similar characteristics with the medium of interest (Sahimi, 1998). Therefore, a network model can deal with pore-scale behavior by providing a pore representation into which the microscopic modeling results can be incorporated. Network models are often used in filtration problems as well as two-phase transport problems such as oil extraction, wetting/drying of soil etc. (see review by Berkowitz, 1998).

Microscopic modeling of suspension particle flow problems is extensively done in chemical engineering and physics fields (Höfler and Schwarzer, 2000). To the author's knowledge, there have been no previous applications of particle flow simulation to characterize the filtration rate, which is to be used in network model simulation of suspension transport. Instead, semi-empirical analytical solutions are often used in network models for filtration problems (Bai and Tien, 2000). They assume that the pore walls are clean and hence, obtain the initial deposition rate of particles and use empirical approaches to account for the effect of collected particles on subsequent flow (i.e. the collected particles complicate the boundaries of the flow filed making the pore-scale simulation difficult).

This thesis introduces a multiple-particle flow simulator to provide correlations of the deposition rate and its effects on the flow field due to particle accumulation network model representations of porous granular media.

1.3 ORGANIZATION OF CHAPTERS

Chapter 2 summarizes the use of continuum models for filtration of particle laden flows in porous media. The chapter gives an overview on a number of rate laws for filtration and various empirical and theoretical approaches using these rate laws. Among these approaches, a method using trajectory analysis with a simplified model of filter (a Unit Bed Element, UBE) is reviewed in detail.

Chapter 3 reviews the concept of network models for porous media. A one-dimensional network model referred to as a "bubble model", is described in detail including the principles and assumptions of the model, and an algorithm for its implementation.

Chapter 4 presents a new method of simulating particle flow through a cylindrical model pore. Principles of the developed simulator that utilized a fine grid to detect complex geometry of particles collected inside a cylindrical pore as well as to discretize the governing flow equations are explained. The key features of the simulator are explained including the evaluation of hydrodynamic drag (exchanged between particles and fluid) and the search algorithm for particle contacts.

Chapter 5 presents results from a parametric study using the particle simulator from Chapter 4. Changes in collection efficiency and pressure drop are studied with varying particle radius, settling velocity, attachment probability of deposited particles and pore length/orientation. The results are summarized using a series of correlation equations that can be used in network model simulations.

Chapter 6 presents the first application case using a bubble model mounted with correlations obtained through the parametric study. A series of experiments of acrylic particles passing through glass bead column by Yoon et al. (2004) is simulated and the results are compared with measurements.

Chapter 7 describes a second application introducing filtration of a microfine cement particles in a sand column. The simulation results are compared with the results with a continuum model, as well as measured values by Bouchelaghem and Vulliet (2001).

Finally, Chapter 8 presents a summary, conclusions of the thesis, and recommendations for further research.

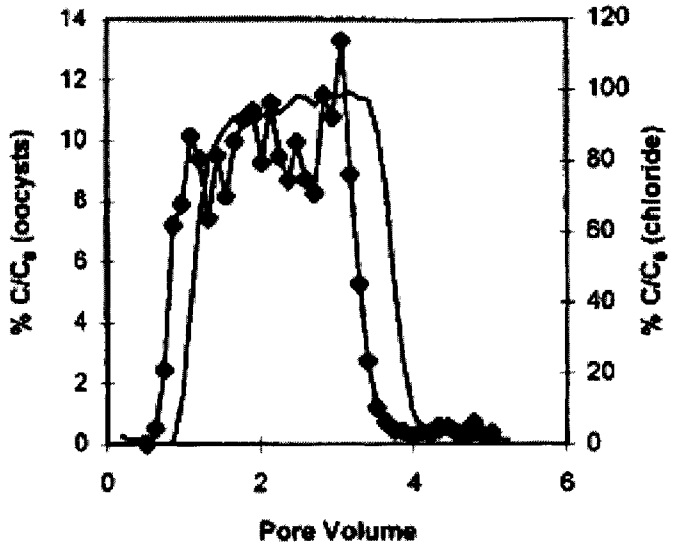

(a) Measured *C. parvum* (diamonds) and chloride (line) breakthrough curves

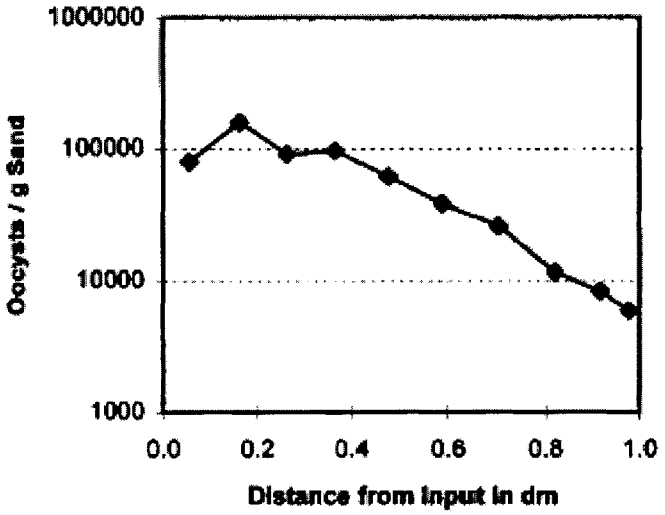

(b) Column profile of *C. parvum* after the completion of the experiment

Figure 1.1 Results of a column injection test with C. parvum solution after Harter et al. (2000)

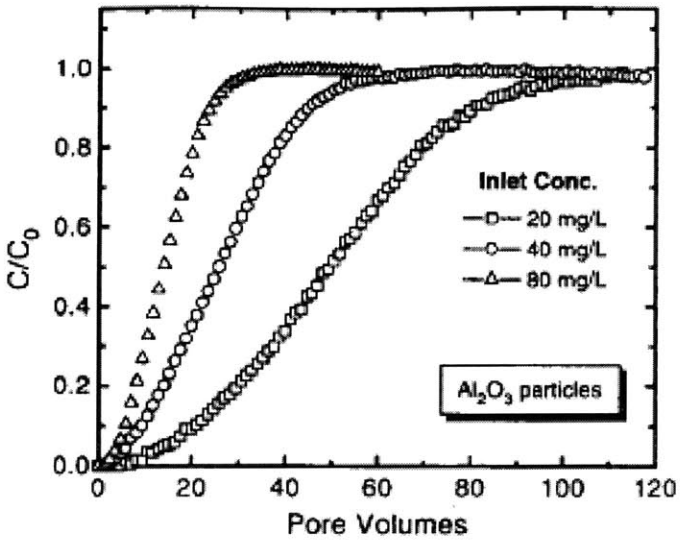

Figure 1.2 Particle breakthrough curves for colloidal alumina depositing onto quartz sand grains after Liu (1994)

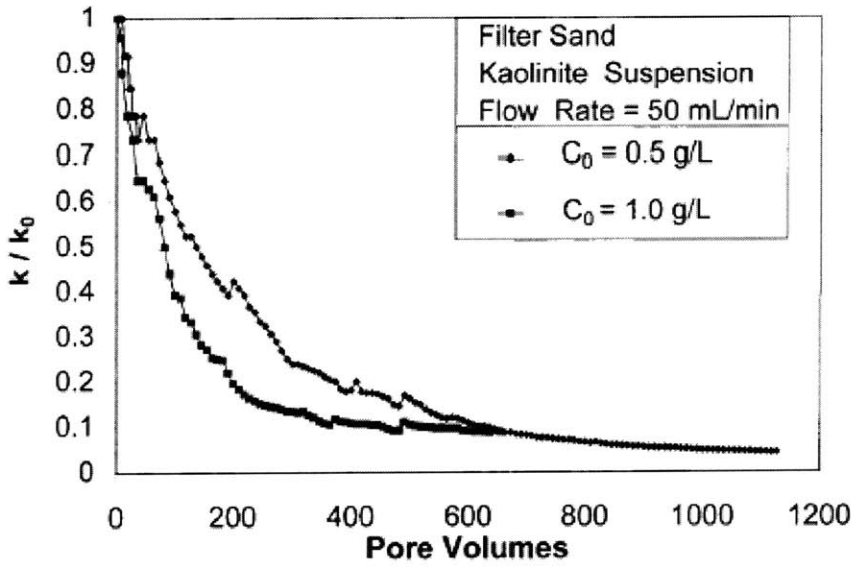

Figure 1.3 Effect of kaolinite filtration on permeability reduction of filter sand after Reddi et al. (2000)

CHAPTER 2. CONTINUUM MODELS FOR PARTICLE TRANSPORT AND FILTRATION

2.0 INTRODUCTION

This chapter reviews continuum models commonly used to describe filtration processes in porous media. The main focus is on transport of suspension in porous granular media where seepage velocities are sufficiently slow that the flow can be modeled without considering the inertia of the fluid, as is the case for most natural and industrial filtration processes through granular filters.

The analysis of suspended particle transport through a porous medium can be represented macroscopically as a problem of solute transport through a homogeneous medium. The governing equation of this classic problem is given by the convection-diffusion equation:

$$\frac{\partial(nC)}{\partial t} + \mathbf{v}\cdot\nabla(nC) - \nabla\cdot(n\mathbf{D}\nabla C) = 0 \qquad (2.1)$$

where n is the porosity ($n = V_v/V$, when V_v is the void volume, and V that of the porous medium), C the concentration of the solute (mass per unit volume), $\mathbf{v}$ the fluid velocity and $\mathbf{D}$ the hydrodynamic dispersion tensor of dimension $[\mathbf{D}] = L^2/T$. This continuum approximation is often used to solve transport of miscible solutes in soils (see for example, Bear and Bachmat 1991). When mass transfer occurs between the medium and the solute, a rate term can be added to equation 2.1:

$$\frac{\partial(nC)}{\partial t} + \mathbf{v}\cdot\nabla(nC) - \nabla\cdot(n\mathbf{D}\nabla C) = -\frac{\partial\sigma}{\partial t} \tag{2.2}$$

where σ is the specific deposit, which is defined as the mass of filtered particles per unit porous medium volume (i.e. $\sigma = M_D / V$ when M_D is the mass of deposit, and V the volume of the medium).

In order to implement this governing equation, a kinetics equation of mass transfer is required. Most continuum models of this type can be found in studies on 'deep-bed-filtration' (see for example, Tien, 1989 for review), which is a term used to describe filtration process through deep filters made of granular material. This chapter summarizes the range of rate laws that have been developed and reviews key results from these analyses.

2.1 FILTRATION RATE KINETICS

2.1.1 First-order law

The most commonly applied kinetics for filtration rate is the first-order law (Iwasaki, 1937):

$$\frac{\partial\sigma}{\partial t} = \lambda C \tag{2.3}$$

where λ is a coefficient often referred to as the filtration rate that has the dimension of reciprocal time, [1/T].

There exist many variations of equation 2.3 depending on the variable used to measure the amount of filtered material. A common choice other than the specific deposit, σ, is the concentration of the deposit, S, defined as the mass of filtered material divided by the pore volume (for example, see Reddi and Bonala, 1997; Gruesbeck and Collins, 1982; Saltelli et al., 1984). The concentration and specific deposits are related as follows:

$$S = \frac{M_D}{V_v} = \frac{M_D}{nV} = \frac{\sigma}{n} \tag{2.4}$$

Many references in the colloid literature (for example, Harvey and Garabedian, 1991; Corapcioglu and Choi, 1996; Bolster et al. 1999; Schijven and Hassanizadeh, 2000) prefer to use the dimensionless solid phase concentration, s, which is the mass of the matter collected per unit mass of the medium (including pore liquid):

$$s = \frac{\sigma}{\rho_b} \tag{2.5}$$

where ρ_b [1]is the bulk density of the porous medium.

Frequently, the first-order law is written as a function of the fluid velocity, v, as below:

$$\frac{\partial \sigma}{\partial t} = v\lambda^* C \tag{2.6}$$

In this case, the filtration rate, λ^* has the dimension of reciprocal length, [1/L]. Therefore, this rate constant represents the filtration per unit length since the dependence on injection rate is isolated by the pore velocity, v.

2.1.2 Second-order laws and effect of deposits

A first-order law that uses a constant filtration rate throughout the process implicitly assumes a clean filter. However, it is clear that the attachment rate should change when deposits cover an extensive area of the porous medium in the advanced stages of filtration. A second-order kinetics law limits the attachment ratio by the solid-phase concentration (Tien, 1989). Second-order laws can be generally expressed as:

[1] $\rho_b/\rho_w = G_s(1-n) + n$ when ρ_w is the density of water and G_s is the specific gravity of the soil

$$\frac{\partial \sigma}{\partial t} = \lambda_0 F(\sigma) C \tag{2.7}$$

where λ_0 denotes the clean-filter filtration rate, and $F(\sigma)$ is the deposition rate function.

There are many phenomenological models for the deposition rate function, $F(\sigma)$ containing empirical parameters as illustrated in Table 2.1. For example, Soo and Radke (1986) suggested a three-parameter equation for the deposition rate function for modeling oil-in-water emulsions transporting through quartz sand packs:

$$F(\sigma) = 1 - a\frac{\sigma}{n_0} \tag{2.8}$$

where a is an average flow redistribution parameter, a constant ranges from zero to one, which parameterizes the effects of deposits on flow.

Bai and Tien (2000) suggested an optimization algorithm to find a polynomial function for $F(\sigma)$ with objective values of experimentally measured effluent concentrations.

$$F(\sigma) = 1 + k_1\sigma + k_2\sigma^2 + k_3\sigma^3 + \ldots \tag{2.9}$$

Johnson and Elimelech (1995) present a second order model where deposited particles inhibit further deposition. They particularly consider charged particles having high repulsive electrostatic forces between each other while being attracted to oppositely charged filter grains. In this case, particle deposition is restricted to monolayer coverage. This type of deposition can be described by a Random Sequential Adsorption (RSA) mechanism (Widom, 1966). The RSA mechanism assumes particles are randomly deposited irreversibly onto stationary surfaces. According to the constraints of the RSA theory, (i.e. no particle contacts, surface diffusion or detachment), the only mechanism that interferes in this random process is the blocking by deposited particles. A function referred to as 'dynamic blocking function' was proposed to incorporate blocking in RSA mechanism. The rate equation for surface coverage in the RSA mechanism is then:

$$\frac{\partial \varphi}{\partial t} = \frac{\eta U}{4} \pi r_p^2 N_p B(\varphi) \tag{2.10a}$$

φ denotes fractional surface coverage (i.e. relative amount of collector surface area where covered by deposited particles); N_p is the particle concentration given as number of particles per unit pore volume; r_p the particle radius; U the pore fluid velocity; and η the unit collector efficiency, which is the filtration rate for an elementary model filter whose detailed explanation will be followed in next section.

Surface coverage can be converted to specific deposit, σ, if the values of specific surface (i.e. surface per volume of granular material) for the pore medium, S_{PM} and that of deposits, S_D:

$$\sigma = \varphi \frac{S_{PM}}{S_D} \tag{2.10b}$$

Then, equation 2.10a can be directly applied to equation 2.2 as a rate law. The function, $B(\varphi)$ in equation 2.10a describes the dynamic blocking that characterizes the transient nature of the filtration rate. Therefore the value of $B(\varphi)$ is initially unity when the collector is clean. It then decreases as the blocked area increases with filtration until the maximum coverage, i.e. $\varphi = \varphi_{max}$ is reached at $B(\varphi) = 0$.

Theoretically, the maximum coverage that can be attained for monolayer of close-packed hard spheres is 90.7% (Graton and Fraser, 1935). In the RSA mechanism, because deposition restricts surface coverage, the theoretical maximum reduces to 54.6% (Feder and Giaever, 1980). Actual values of φ_{max} can differ from this theoretical maximum, φ_∞= 54.6% depending on given particle geometry and physicochemical conditions (Johnson and Elimelech, 1995).

Two different mathematical expressions have been suggested for $B(\varphi)$ depending on the extent of coverage. For moderate coverage, the one by Schaaf and Talbot (1989) was used as given:

$$B(\varphi) = 1 - 4\varphi + \frac{6\sqrt{3}}{\pi}\varphi^2 + \left(\frac{40}{\sqrt{3}\pi} - \frac{176}{3\pi^2}\right)\varphi^3, \quad \varphi \le 0.8\varphi_\infty \tag{2.11a}$$

while an equation by Pomeau (1980) for severe coverage:

$$B(\varphi) = \frac{(\varphi_{\max} - \varphi)^3}{2j^2} \tag{2.11b}$$

where j is the 'jamming limit slope', which is determined in plots of surface coverage, φ, versus square root of a dimensionless time variable time, $t_d^{-1/2}$. The parameter t_d is referred to as the porous medium deposition time and defined as the total area of collected particles divided by maximum coverage, $\varphi_{\max}$:

$$t_d = \frac{\eta U}{4}\frac{\pi r_p^2}{\varphi_{\max}}\int_0^t N_p dt \tag{2.11c}$$

These functions were applied with the kinetics in equation 2.10a to simulate experimental breakthrough curves of column tests with positively charged latex colloids (diameter 0.48μm) through negatively charged glass beads (diameter 0.46mm). Figure 2.1a shows the resulting breakthrough curves for the suspension concentration number, N_p, normalized by its initial value, N_0. Breakthrough curves show reduction with increasing ionic strength, which is resulted from reduction in ζ- potential [2] that consequently lowers repulsive force between particles. The fractional surface coverage, φ, can be calculated from the measured effluent concentrations:

$$\varphi = \frac{\pi r_p^2 v a_g \int_0^t (N_0 - N_p)dt}{3H(1-n_0)} \tag{2.12}$$

[2] The electrical potential that exists across the interface of all solids and liquids. Also known as electrokinetic potential.

where H is the length of the column, a_g the representative radius of the filter grain. Then related parameters, φ_{max} and j were obtained from these curves, which, in turn, were used in continuum model simulations for determining the fractional surface area. The simulated breakthrough curves showed good match with the experimental values. Results with two different ionic strengths values, 10^{-5}M and 10^{-1}M are given in Figure 2.1b. The relative poor fit with 10^{-1}M of ionic strength, the largest value among used values, was suspected to be related to multi-layering in the deposit structure that violates the basic assumption of RSA mechanics. The simulated curves were compared with results when the Langmuirian blocking functions were used replacing RSA functions in equation 2.11a and 2.11b. Langmuirian blocking function is the linear blocking function that was introduced in Langmuir's molecular adsorption model (Langmuir, 1918):

$$B(\varphi) = \frac{(\varphi_{max} - \varphi)^3}{2j^2} \tag{2.13}$$

Since Langmuirian function was addressed to model surface exclusion of point-size molecules, it naturally underestimates blocking effect of larger colloidal particles (Schaaf and Talbot, 1989) is illustrated in Figure 2.1b.

Ko and Elimelech (2000) investigated the dependence of hydrodynamic forces and particle size on the maximum surface coverage, φ_{max} using latex particles of three different sizes (0133, 288 and 899 nm) and quartz sand (mean diameter 0.32mm), as illustrated in Figure 2.2. This figure shows that the maximum surface coverage decreases with increasing flow velocity and is higher with smaller particle radius at the same flow velocity.

The second order model based on the RSA mechanics seem to effectively identify the role of deposited particles on filtration mechanism but depends on empirical expressions for the dynamic blocking function, $B(\varphi)$. However, the model is intrinsically limited in use because of the assumption of monolayer coverage, and only applicable when repulsive force between particles prevails. In addition, maximum surface coverage φ_{max}, the key parameter that determines the limit of monolayer coverage must be

carefully obtained for given conditions of particle radius, flow velocity and ionic strength for successful use of the model.

2.1.3 Modeling of re-entrainment

Some deposited particles can detach and become re-transported (equivalent to re-entrainment in the fluid). This reversible process is commonly modeled by introducing a new term in the kinetics equation, equation 2.3 (e.g. Saiers et al., 1994):

$$\text{Filtration \& re-entrainment: } \frac{\partial \sigma}{\partial t} = \lambda C - k_r \sigma \tag{2.14}$$

where k_r is the detachment rate that models the rate of re-entrainment from the deposit. More details of detachment process and its implication on overall filtration will be discussed in Chapter 6.

Most studies on the theoretical prediction of filtration processes focus on finding expressions for the filtration rate, λ, and comparatively little research have been done to study the re-entrainment. As a result, the value of detachment rate is usually empirically determined without any theoretical considerations. Meinders and Busscher (1995) measured the influence of flow on the detachment ratio using a parallel plate flow chamber of glass beads as a filter for polystyrene particles. They concluded that the detachment rate increased linearly with the concentration of suspension particles due to higher numbers of collisions per unit time, and also that the higher pore flow velocity resulted in higher rate of detachment. Bai and Tien (1997) also investigated the particle detachment mechanism experimentally. Polydispersed suspensions of PVC powders (0.5-14 μm in diameter) were injected into a column filled with glass ballotini of two different sizes (0.6-0.71 mm, and 0.42-0.5 mm diameter). The results show that larger particles were more likely to become detached and detachment rates were more significant at higher pressure gradients.

2.2 THEORIES FOR PREDICTING FILTRATION RATE PARAMETERS

The fundamental goal of filtration theories is to develop models that can predict realistically the performance of filters. In order to achieve this goal, it is imperative that the filtration rate, λ, for a given suspension under known physical and chemical conditions, is defined in terms of input parameters that can be obtained from well-defined tests. The following paragraphs describe existing methods for estimating filtration rate parameters.

2.2.1 Phenomenological methods

Most early studies (using continuum models) evaluate the initial filtration rate by matching the experimentally measured effluent concentration, C_{out} (for example, see Iwasaki, 1937, Ives, 1960, and Herzig et al., 1970). For example, Mackie and Zhao (1998) have used a second-order kinetics model calibrated with one set of lab-scale filtration tests and then propose a method of adjusting the parameters to enable predictions for other filtration tests. Their proposed kinetics law models include filtration rates (ripening) that increase up to a maximum value, and subsequently, decrease to zero at the final deposit condition. The calculations show good predictions using the methodology for tests by Mackie and Bai (1992) with the PVC microspheres (diameter, $2r_p$ = 0.63μm to 10.08μm) filtering through ballotini glass beads ($2r_p$ = 420-710μm). However, the microscopic mechanism of filtration that determined such characteristics of filtration rate was not discussed in detail in conjunction with hydrodynamic and physicochemical forces.

Saiers et al. (1994) used curve fitting to duplicate column tests in their study of migration of colloidal particles of silica and boehmite [AlO(OH)] through sand in order to compare the first- and a second-order kinetics approaches. Sorensen et al. (1999a and b) have applied a continuum filtration model to simulate platelet deposition onto biomaterials such as prosthetic heart valves, synthetic vascular grafts and ventricular-assist devices during blood flow. They have used separate rate parameters for each of five

different species of platelets and thrombin in blood subjected to deposition, which were empirically obtained. The model was applied to simulate lab tests of platelet deposition onto collagen plates separated at 200 μm. Although this configuration is different from granular filters that are the main focus of this thesis, the study presents an example of applying a phenomenological approach. Their simulations include tests of three different constant injection rates (with shear rates of 100 sec^{-1}, 500 sec^{-1} and 1500 sec^{-1}) and their average flow velocities (U_{flav} = 0.67cm/sec, 3.33cm/sec and 10cm/sec). In addition, a benchmark case was tested and used for calibration of filtration rates. Predicted results showed good agreement except for cases at the highest flow rate (U_{flav} = 10cm/sec). This was attributed to reduced adhesion due to a change in the hydrodynamics (not considered in the model).

Although phenomenological models of filtration rate do have some apparent predictive power (as demonstrated in these studies) they are intrinsically limited because they do not consider mechanisms affecting filtration due to interactions between the suspended particles and the porous medium and other filtered particles. It is often impossible to amend a phenomenological model to reflect the influence of changes in the filtration state. Therefore, advanced models that consider microscopic filtration mechanisms is required for fundamental studies of filtration process.

2.2.2 Single collector efficiency, η

In order to study microscopic filtration mechanisms, individual filters need to be modeled. The simplest way of modeling is to have one filter to represent the complete filtering medium. This is clearly a gross approximation as most filters are heterogeneous in their structure. The efficiency of the model filter can be scaled up to give filtration rate of the whole filter bed, λ. The idea of representing elemental filtering medium with a model filter of well-defined geometry referred to as a "Unit Collector" or "Unit Bed Element" (UBE), was first proposed by Payatakes et al. (1973a,b). The filter bed is assumed to comprise a number of UBE's connected in series. The thickness of each UBE, L, can be calculated from the known porosity, n_0:

$$L = \left[\frac{4\pi}{3(1-n_0)}\right]^{1/3} a_g \tag{2.15}$$

where a_g is the average filter-grain radius.

Figure 2.3 shows a schematic representation of granular filter bed with UBE's quoted by Tien (1989). It shows the three most popular types of unit collectors: capillary tubes, spheres and constricted tubes. The single collector efficiency, η can be defined as difference between the influent and effluent concentration of the i^{th} UBE:

$$\eta_i = \left|\frac{C_{in} - C_{eff}}{C_{in}}\right|_i \tag{2.16}$$

Yao et al. (1971) proposed a very simple UBE assuming an isolated sphere could represent an elementary volume space of the filter grains and the surrounding pore space. In this case, the single collector efficiency can be defined as the rate at which particles strike a single grain of the porous media divided by the rate at which particles move toward the grain. Assuming Stokes flow (i.e. ignoring inertial in the fluid) and well-defined boundary conditions, this type of UBE can be solved analytically. For example, the stream function for flow around an isolated sphere, ψ_{IS} is given as below by Lamb (1895):

$$\psi_{IS} = \frac{1}{2} v a_g^2 \sin^2\theta \left(\frac{1}{2r'} - \frac{3r'}{2} + r'^2\right) \tag{2.17}$$

where $r' = \frac{r}{a_g}$, (r,θ) is the spherical coordinate system used, and v is the far-field flow velocity.

The trajectory of a particle (i.e. the path a particle follows in the flow field) can be calculated if the forces acting on the particle are known. Yao et al. (1971) considered two sets of forces: Brownian diffusion and gravity. Figure 2.4 shows the conceptual sketch of an isolated sphere with three particle trajectories that will generate particle deposition: A)

interception B) sedimentation and C) diffusion (Brownian motion). The Brownian diffusion force, because of its stochastic nature, was not included in the particle trajectory calculation. Instead, the efficiency of particle collection via Brownian diffusion, η_D, was independently evaluated from mass transfer theory (Smoluchowski-Levich approximation, Levich, 1962):

$$\eta_D = 4\left[\frac{D_{BM}}{a_g v}\right]^{2/3} \tag{2.18}$$

where D_{BM} is the particle diffusion coefficient, a_g is the grain radius. The current study is focused on filtration where Brownian diffusion is not significant. Effects of gravitation, on the other hand, can be directly added to the fluid stream function, ψ_{IS}:

$$\psi = \psi_{IS}(r,\theta) + \frac{1}{2} v a_g^2 N_G r'^2 \sin^2\theta \tag{2.19a}$$

$$N_G = \frac{2(\rho_s - \rho) g r_p^2}{9\mu v} \tag{2.19b}$$

where N_G is a non-dimensional factor for the gravitational force; ρ_s and ρ are the mass densities of the mass particles and fluid, respectively; μ the fluid viscosity; and r_p the particle radius.

Collection by interception is defined by the trajectory that grazes the boundary of the grain, which is often referred to as the limit trajectory. The limit trajectory partitions the suspension into two parts: those whose trajectories will come within one particle radius of the collector surface (and are therefore collectable), and those particles that flow past the collector (with no possibility of collection). Particles inside the limit trajectory will end up settling out on the grain. The collector efficiency can then be determined from the limiting trajectory, ψ_L:

$$\eta(r_p) = \frac{2\pi\psi_L}{\pi v a_g^{\ 2}} \tag{2.20}$$

The limiting trajectory can be obtained from equation 2.19, as the particle trajectory passing through the point ($r = a_g + r_p$, $\theta = \pi/2$). Then the final version of the single collector efficiency, η, is given by adding that by diffusion, η_D, given in equation 2.18:

$$\eta = \eta_D + 1.5N_R^2 + N_G \tag{2.21}$$

where N_R is a dimensionless particle radius ratio to the grain radius, i.e. $N_R = r_p/a_g$. Tufenkji and Elimelech (2004) have developed a more complete version of this model by including effects of van der Waals attraction forces.

The single collector efficiency can be easily scaled up to give the filtration rate, λ based on the UBE representation concept. The mass flux of suspension particles of concentration, C that pass through a spherical collector of radius a_g per unit time can be written:

$$\dot{M} = n\pi a_g^3 vC \tag{2.22}$$

where v is the velocity of the suspension approaching the collector.

Hence $\eta\dot{M}$ describes the mass flux flowing out of the collector, and the rate of specific deposit is then found from equation 2.22:

$$\frac{\partial\sigma}{\partial t} = \lambda C = \frac{\eta\dot{M}C}{V_s} = \frac{1-n}{3\pi/4\, a_g^3}\left[n\pi a_g^2 v\right] C\eta \tag{2.23}$$

where V_s denotes the volume of collector. The filtration rate, λ (equation 2.3) can then be related directly to the collector efficiency for the UBE model.

$$\lambda = \frac{3(1-n)}{4a_g} n\eta v \tag{2.24}$$

2.2.3 Other methods based on trajectory analysis

More recent models of granular filters represent the pore space as well as the grain geometry and can be categorized into: internal flow and external flow models. External flow models focus on the filter grain geometry while internal models deal with pore geometry. Rajagopalan and Tien (1976) propose a model that consists of a solid sphere of radius, a_g, surrounded by a fluid envelope of radius, b, for which the stream functions are given by Happel (1958), and is accordingly referred to as Happel's model. Through trajectory analysis considering diffusion, gravitational, and van der Waals forces, they provide a correlation for the single collector efficiency:

$$\eta = \eta_D A_s^{1/3} + A_s N_{vdW}^{1/8} N_R^{15/8} + 3.38\times10^{-3} A_s N_G^{1.2} N_R^{-0.4} \tag{2.25}$$

where A_s is a dimensionless parameter depending on porosity:

$$A_s = \frac{2(1-d^5)}{w} \tag{2.26a}$$

$$d = (1\text{-}n_0)^{1/3} \tag{2.26b}$$

$$w = 2\text{-}3d\text{+}3d^5\text{-}2d^6 \tag{2.26c}$$

N_{vdW} is a parameter related to van der Waals force and the related Hamaker constant, A_H[3]:

$$N_{vdW} = \frac{4A_H}{9\pi\mu r_p^2 v} \tag{2.27}$$

[3] Hamaker 'constant' is a physical property that defines the van der Waals interaction energy between two bodies.

Further details of trajectory analysis in Happel's model and one kind of internal model (constricted tube model) are given in Chapter 4. A review of the trajectory analysis and its application on deep bed filtration process can be found in Tien (1989).

Trajectory analysis does not consider subsequent changes in geometry of the collector, i.e. the radius of the grain in a unit collector, a_g is kept constant. Therefore, these models only provide measures of efficiency for clean filter beds or situations where there is limited deposition of particles. There are some studies that amend the single collector efficiency equations (such equations 2.21 and 2.25) to account for previously deposited particles. For example, Choo and Tien (1995) suggested a relationship between the current efficiency and the clean bed efficiency, η/η_0 by solving flow through a cylinder with a deposited layer of porosity n_d and permeability k_d:

$$\frac{\eta}{\eta_0} = Y\left[1+9.61(1-n_0)^{2/3}\left(\frac{\sigma}{1-n_d}\right)\right] + (1-Y)\left[1+\frac{0.6794}{1-n_0}\left(\frac{1}{N_R}-0.921\right)\left(\frac{\sigma}{1-n_d}\right) + \frac{0.1731}{(1-n_0)^2}\left(\frac{1}{N_R^2}+\frac{3}{N_R}-1.171\times10^2\right)\left(\frac{\sigma}{1-n_d}\right)^2\right] \quad (2.28a)$$

In this equation, Y is a weighting function for the deposit permeability, k_d:

$$Y = \frac{f\,k_d^m}{1+f\,k_d^m} \quad (2.28b)$$

m is a constant; f is a function of initial filter porosity, n_0, specific deposit, σ, deposit porosity, n_d, and the ratio of particle radius to the grain radius, N_R:

$$f = 0.578(1-n_0)^{-2}\left(1+\frac{0.0128}{N_R}\right)\left\{\frac{\sigma}{5(1-n_d)}\right\}^{1.63+5.5\times10^{-4}/N_R} \quad (2.28c)$$

Ryan and Elimelech (1996) presented a thorough review on theoretical and experimental studies of colloid transport in groundwater, including applications of continuum filtration models. There also exist many studies using phenomenological approaches applied in organic colloidal transport such as bacteria, whose review can be found in Lawrence and Hendry (1996) and also Schijven and Hassanizadeh (2000).

2.3 ADHESION (ATTACHMENT) MODELS

2.3.1 Collision coefficient, α

It is generally agreed that theoretically evaluated collection efficiencies overestimate the experimental measurements of filtration when repulsive double layer interactions predominate (Ryan and Elimelech, 1996). As a result, the initial collection efficiency is often modified to include an empirical factor, α:

$$\eta = \alpha \eta_{full} \tag{2.29}$$

where η_{full} is the calculated single collector efficiency and α, defined as the empirical collision efficiency that describes the fraction of collisions with filter grains that actually result in attachment.

Collision efficiency can be thought as a parameter quantifying the surface interactions between particles, and between particle and the collector wall. These effects are very difficult to model analytically. Elimelech and O'Melia (1990) carried out an experimental investigation on the effect of ionic strength on the values of α. Experiments were done with polystyrene latex particles of three different sizes (0.046,0.0378, and 0.753 μm in diameter) transported through a 20cm-deep spherical glass beads (0.2 to 0.4 mm in diameter) column, where KCl and $CaCl_2$ solutions were used as destabilizing electrolytes. The experiments clearly showed increase in attachment efficiency as the electrolytes concentration increases (i.e. there is a reduction in the energy barrier between glass beads and the particles), as illustrated in Figure 2.5 where breakthrough concentrations decrease with increasing KCl concentration.

There are many applications using equation 2.29. For example, Harvey and Garabedian (1991) applied the expression by Yao et al. (1971) given in equation 2.21 in their study of bacteria transport to evaluate η_{full}, and then found the collision efficiency empirically through separate injection tests. The resulting single collector efficiency, η was converted to the filtration rate, λ using equation 2.24 derived from the UBE representation concept, and applied to simulate bacterial transport in ground water, with the first order attachment-detachment kinetics (equation 2.14).

Harter et al. (2000) used a similar approach to model column tests of bacterial transport through sandy soil. They used equation 2.25 (Rajagopalan and Tien, 1976) to evaluate η_{full}, while the collision efficiency and the detachment coefficient (a, k_r, respectively) were obtained by calibrating the breakthrough curve for each test. Bradford et al. (2002) also used equation 2.25 to model experiments on latex colloid transport through a sand column. The values of the detachment coefficient and the collision efficiency were obtained by calibrating the breakthrough curves. Calibrated collision efficiency values were two orders of magnitude higher than the theoretical maximum value (i.e. unity). The data were also highly scattered for tests done with soil of similar characteristics, implying inadequacy of the analytical single collector efficiency equation. In addition, the simulated profile of accumulated colloid mass did not match very closely the measured spatial distribution, which showed a concentrated accumulation near the injection point.

2.3.2 Effect of surface roughness

Apart from surface chemistry, the surface roughness must also be an important parameter affecting the attachment process. Varidyanathan and Tien (1988) proposed a theory that considers surface roughness as the main source of adhesion. The basic principle is that a particle in contact with a plane boundary will stay in place if there is sufficient frictional resistance between the two bodies. In order to model the surface roughness, grain surfaces are assumed to have protrusions of known dimensions. The degree of roughness can be represented by the density of protrusions and their height. If a particle settles on to a smooth pore surface, it will roll along until it encounters a

protrusion. The adhesion model determines whether a particle remains attached or not from calculations of angular momentum conservation. If the moment exerted by the attractive force is greater than that exerted by the fluid, the particle will become attached to the grain surface. The configuration of a particle encountering a protrusion is shown in Figure 2.6. The drag force, F_D, and moment, M_D, acting on a spherical particle of radius, r_p, due to a Newtonian fluid flow under no-slip condition on the grain surface were calculated by Goldman et al. (1967):

$$F_D = 10.205\pi r_p^2 \tau_w \tag{2.30a}$$

$$M_D = 3.776\pi r_p^3 \tau_w \tag{2.30b}$$

where τ_w is the shear stress on the wall by the fluid.

The adhesion condition when the attractive moment is larger than the drag moment in this configuration is:

$$F_A(2r_p h - h^2)^{1/2} \geq F_D(r_p - h) + M_D \tag{2.31}$$

where F_A is the net attractive force to the grain surface. Goldman's solution is strictly applicable for infinite space bounded only by the wall, and is not appropriate to represent pore space. It is also very difficult to select the wall shear stress, τ_w, parameter for a pore wall.

Varidyanathan and Tien (1988) completed calculations for situations where van der Waals force is the dominant adhesive force:

$$F_{vdW} = \frac{A_H r_p}{6\delta^2} \tag{2.32}$$

where $A_H = 10^{-13}$ erg (10^{-20} J) is the Hamaker constant, and δ is the separation distance between the surface and the particle.

Imdakm and Sahimi (1991) used the formula given by Herzig et al. (1970) to estimate the minimum separation distance δ:

$$\delta^2 = \frac{2A_H}{2\pi r_p^2 g(\rho_s - \rho)} \tag{2.33}$$

where ρ_s, ρ are the density of the particle and water, and g is the acceleration of gravity. If equation 2.33 is substituted in equation 2.32, the resulting van der Waals force is $F_{vdW} = \frac{F_G}{8}$, where $F_G = \frac{4}{3}\pi r_p^3 g(\rho_s - \rho)$ is the gravitational force.

Although the theory appropriately recognizes the crucial role of surface roughness in filtration process and distinguishes related forces, it has limited applicability for porous filters because it does not account for the effects of the pore walls. It also does not account for effects of previously collected particles on hydrodynamic forces. The influence of pore wall on flow and its effect on filtration process are discussed in Chapter 4.

2.4 METHOD BASED ON CAPILLARY MODEL OF POROUS MEDIA

Reddi and Bonala (1997) developed a method for evaluating the filtration rate, λ using a capillary tube model for porous media, as shown in Figure 2.7. The porous medium is represented as a bundle of capillary tubes of various radii sharing a common length. This model can be thought as a primitive network model, i.e. a lattice representation of pores and pore throats. (Network models are discussed in detail in Chapter 3). If the initial pore space is modeled by a bundle of circular tubes (capillary model) with known probability density function, $f(R)$, and the probability of capture for a particle inside a circular tube of radius R, $p(R)$, is also known, the deposition rate can be expressed as

$$\frac{\partial S(z,t)}{\partial t} = C(z,t)N_t \int_0^\infty p(R)q(R)f(R)dR \tag{2.34}$$

where S is the deposit concentration, N_t the total number of pore tubes in unit pore volume and $q(R)$ is the flow rate, which is given according to the Poiseuille equation:

$$q(R) = \frac{\pi\rho g}{8\mu} iR^4 \tag{2.35}$$

when i is the hydraulic gradient, i.e. $i = \nabla p/\rho g$.

A correlation originally suggested by Stein (1941) was used for the probability of capture for a spherical particle of radius, r_p, inside a circular tube of radius, R:

$$p(R) = 4[(\phi r_p / R)^2 - (\phi r_p / R)^3] + (\phi r_p / R)^4 \tag{2.36a}$$

where ϕ is a parameter that takes into account the effect on deposition of several inter-particle forces such as gravitational, inertial, hydrodynamic, electric double layer, and van der Waals forces.

The deposition coefficient can be found by selecting the pore size distribution, the representative number of pores, N_t, the parameter, ϕ, and the representative particle size, a. The principle uncertainty lies in the selection of the pore size distribution and the parameter, ϕ. Rege and Fogler (1988) suggested an exponential function of flow velocity for ϕ:

$$\phi = 3\exp[-v/v_{cr}] \tag{2.36b}$$

where v is the pore fluid velocity and v_{cr} a critical pore velocity beyond which no particle capture is allowed (i.e. $\phi = 0$).

This equation is based on the experimental observations of Gruesbeck and Collins (1982) of decreasing filtration rate with increasing pore velocity, which ultimately was reduced to zero when a critical velocity was reached.

Reddi et al. (2000) applied this method to simulate the filtration of kaolinite in a sand column, whose experimental measurements were already presented in Figure 1.3. Figure 2.8 compares the simulated values and measured values of apparent permeability. For the simulations, the probability density function $f(R)$ of the sand as well as the corresponding number of pores, N_t, were evaluated from the measured soil-water characteristic curve with critical velocity of $v_{cr} = 0.1\text{cm/sec}$[4]. The figure clearly shows the simulation results with lower input concentration, C = 0.5g/L, underestimating the measured permeability values. This indicates that the model overestimates the extent of filtration. Although the reason for this overestimation was not well discussed in Reddi et al. (2000), it should be noted that it implies filtration rate increasing as deposit volume increases, which is not included in the presented model.

2.5 PRESSURE GRADIENT-FLOW RATE RELATIONSHIP

Darcy's equation is generally used as a constitutive equation in continuum models of flow in porous media:

$$i = \frac{\mu}{k\rho g} V \tag{2.37}$$

where k is the permeability [L^2], and V is the superficial flow velocity.

There are not many studies that exist on the effects of deposition/filtration on pressure changes occurring within the porous medium (at constant flow rate). In continuum transport models, the effect is most often measured by changes in permeability of the filter bed utilizing the Kozeny-Carman equation. The Kozeny-

[4] Not explicitly stated by the Authors, but necessary to match the permeability evolution for input concentration, C = 1.0g/L

Carman equation gives the hydraulic gradient, i, when an incompressible fluid flows through a granular medium of spheres of uniform size (a_g, the radius).

$$i = K_C \frac{\mu V}{4a_g^2} \frac{(1-n)^2}{n^3} \tag{2.38}$$

where K_C is an parameter depending on the porous media structure. Using this equation, the ratio between the hydraulic gradient, i, to the initial gradient, i_0, can be computed if the filter grain radius a_g reduces from its initial value, a_{g0}, due to an accumulation of filtered material:

$$G = \frac{i}{i_0} = \left(\frac{a_{g0}}{a_g}\right)^2 \frac{n_0^3(1-n)^2}{n^3(1-n_0)^2} \tag{2.39}$$

This equation works under the assumption that the filtered material forms a smooth surface on the collector such that its effect can be represented by change in filter radius and does not affect the interstitial velocity, v or viscosity, μ. Then, the filter grain radius can be expressed with porosity:

$$\frac{a_g}{a_{g0}} = \left(\frac{1-n}{1-n_0}\right)^{1/3} \tag{2.40}$$

Porosity has the following relationship with the specific deposit, σ:

$$n = n_0 - \frac{\sigma}{1-n_d} \tag{2.41}$$

where n_d is the deposit porosity that depends on the morphology of the deposit formed. Substituting the above two equations to equation 2.39:

$$G = \left(\frac{1-n_0}{1-n}\right)^{2/3}\left(\frac{n_0}{n}\right)^{3}\left(\frac{1-n}{1-n_0}\right)^{2} = \left[1-\frac{\sigma}{n_0(1-n_d)}\right]^{-3}\left[1+\frac{\sigma}{(1-n_0)(1-n_d)}\right]^{4/3} \tag{2.42}$$

Table 2.2 summarizes other the existing phenomenological models for the flow gradient enhancement function, G.

Hunt et al. (1993) suggested a new function based on the finding made during a series of experiments of kaolin powder transport through a sand column that the normalized increase in hydraulic gradient, $(i-i_0)/i_0$ can be directly linked to the specific deposit through a power law function, $i \sim \sigma^{2/3}$.

Boller and Kavanaugh (1995) used the relationship by Ives (1969) in Table 2.2 to study the influence of particle size on the change increase with related parameters (d = 35, m_1 = 1.5 and m_2 = -1). Constant flow rate injection test results with suspensions of spherical latex particles with diameter 6.5μm, 2.1μm and 0.63μm through 9cm column with glass bead of 0.55mm diameter were used for the study. Using Ives's equation to calibrate the experimental measurements of pressure changes, the deposit density was back calculated. The calculation showed that deposit density decreases with increasing radius, indicating that smaller particles make looser deposits, and, consequently explain the observed results showing faster headloss using smaller particles. No measurement, however, was made to validate the calibrated density values.

Choo and Tien (1995) have proposed equations to explain the change in pressure gradient for a cylindrical tube collector due to deposition of mono-sized particles, which later can be incorporated in the UBE filter model. They have defined three stages of particle deposition depending on the number of particles (Figure 2.9):

Stage 1: Monolayer deposition,

Stage 2: Moderate deposition,

Stage 3: Severe accumulation of deposits to cause the deposited particles on top and bottom meet to make a bridge at a point across the tube.

From the first stage, the pressure drop is based on the analytic solution by Happel and Brenner (1973) (single particle collection) scaled by the number of deposited

particles (i.e. assuming no change in flow field due to previously deposited particles). However, the assumption is flawed as explained in Chapter 4 when a full particle flow simulation method developed. For stage 2 and 3, a smooth layer of deposited matter of porosity n_d was assumed to solve the flow.

Stephan and Chase (2000) suggested a novel method to find a correlation for permeability loss within a deep-bed filter. Their research models the changes in effective surface area due to filtered particles with a constitutive equation in terms of porosity, particle diameter, and sphericity (Bird et al. 1960). This equation was then incorporated in continuum model equations through volume averaging. They also suggested an optimization scheme to find associated parameters with experimental results and applied it for the flooding test results As noted by the authors, the size distribution of particles is an important factor omitted in the research that can have an important influence on the change in surface area.

2.6 CONCLUSIONS

Continuum models that use simple continuity equations as governing equations are easy to implement and hence, have been used in many studies of transport of fine particles through porous media. Filtration processes are incorporated in these models through kinetics equations that require a number of material parameters. It is often a challenge to select these parameters in practical applications. Various methods have been proposed for predicting filtration based on theoretical and empirical methods. Theoretical calculations of filtration rate are possible, through trajectory analyses, but are confined to initial conditions (clean bed conditions). Phenomenological and empirical models are generally needed to handle effects of prior particle deposition. Hence, continuum models are inevitably based on empirical parameters back-calculated or calibrating to measured breakthrough curves. As a result, the continuum models of filtration are generally not very robust. In addition, an up-scaling process is required to retrieve the rate parameters in kinetics equations from the single collector efficiency values (i.e. trajectory analysis). Unit bed element representation method, in which a serial connection of collectors of simple geometry (unit bed elements) models entire filter bed, is often adopted in

continuum approach as a simple up-scaling technique. The UBE representation, however, is often found inadequate to model the complicated topology of pore spaces for real granular filtering media.

Theoretical studies on the pressure drop change due to deposition are rare despite their importance in advanced stages of filtration where there is a significant build-up of deposits.

These limitations of continuum models generate a need for new comprehensive methods that address local scale deposition phenomena. These are described in subsequent chapters.

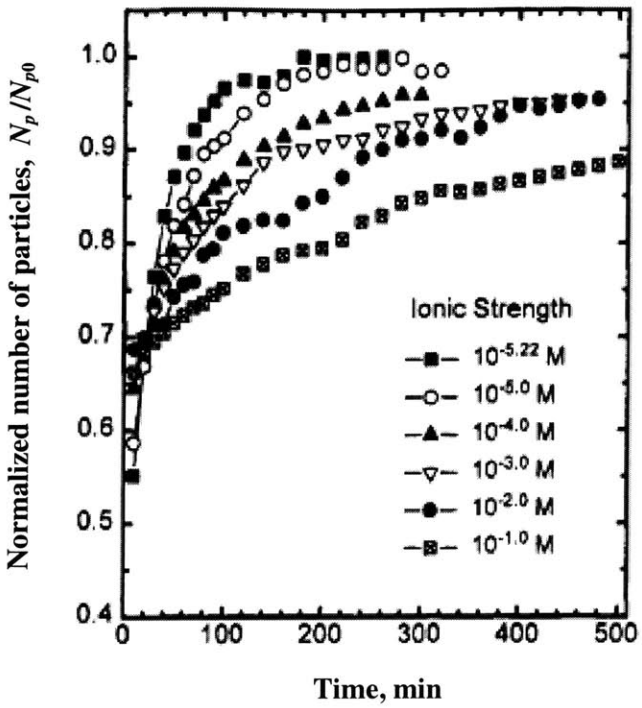

(a) Experimental breakthrough concentrations at different solution ionic strengths

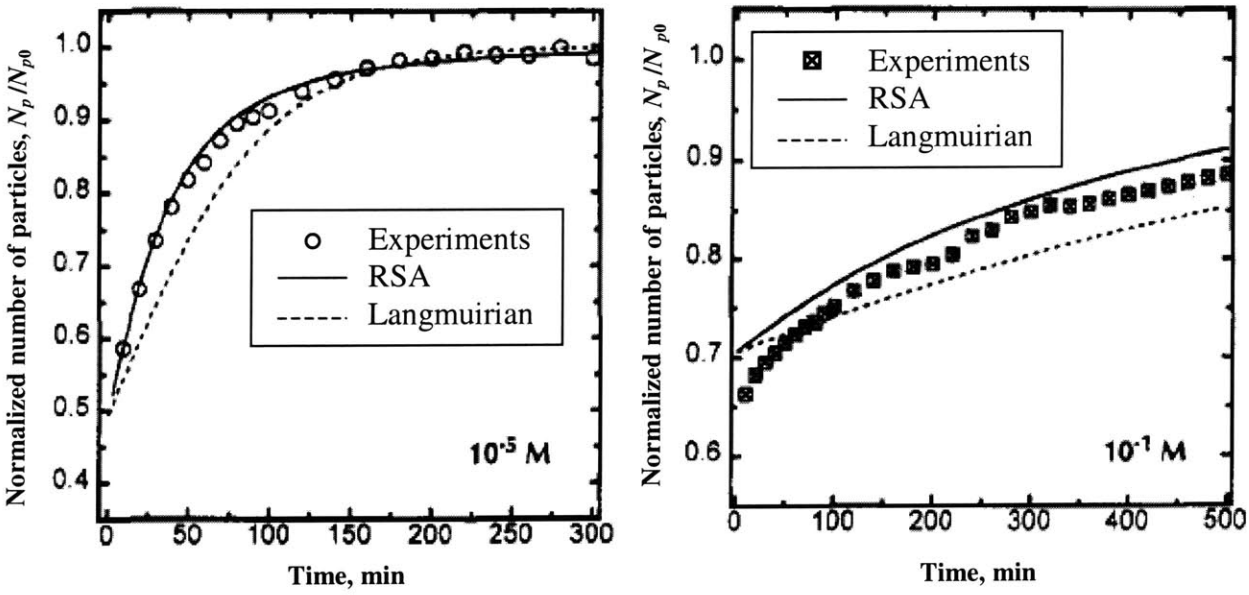

(i) Low concentration (ii) High concentration

(b) Comparison of experimental and theoretical breakthrough curves

Figure 2.1 Measured and theoretical breakthrough curves at different solution ionic strengths (Johnson and Elimelech, 1995)

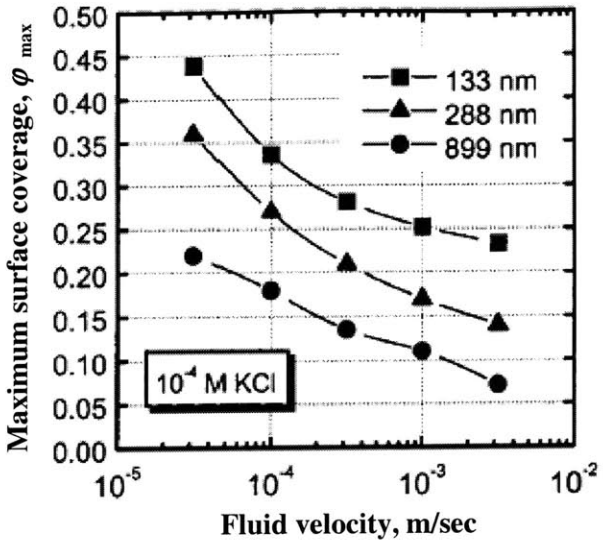

Figure 2.2 Maximum surface coverage, φ_{max} changes with fluid velocity and suspension particle radius (Ko and Elimelech, 2000)

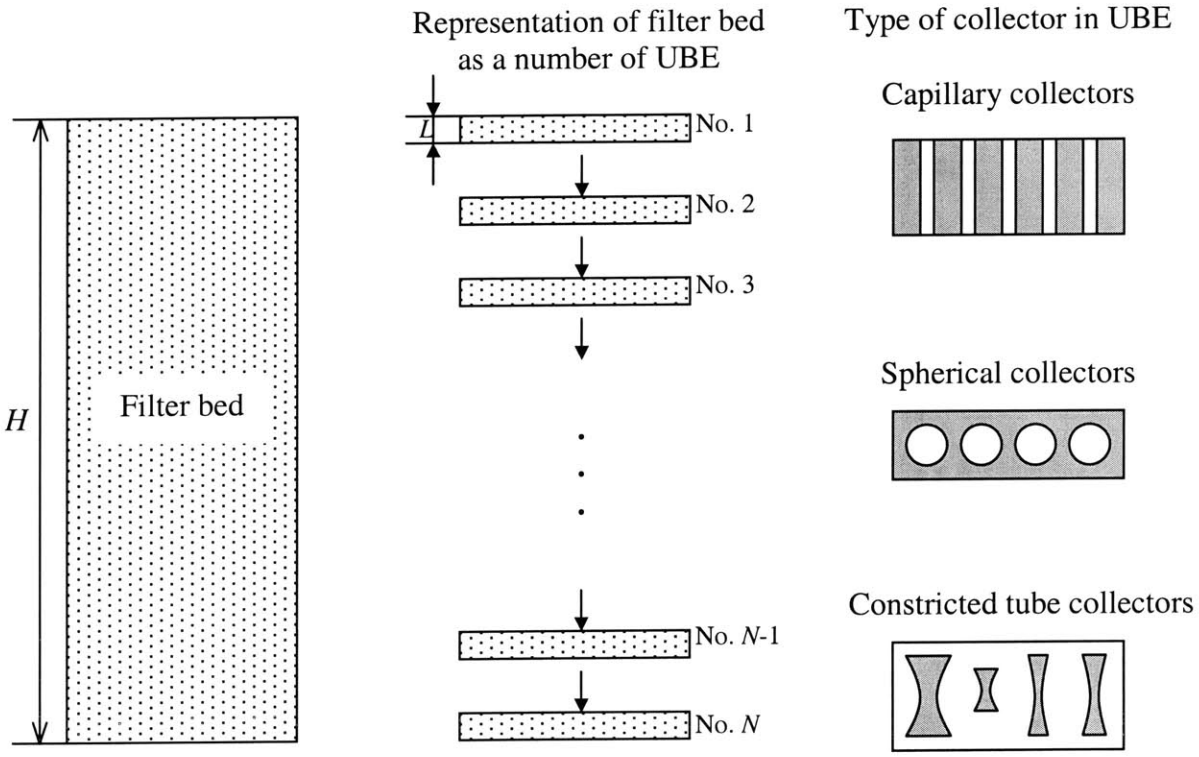

Figure 2.3 UBE representation of granular filter

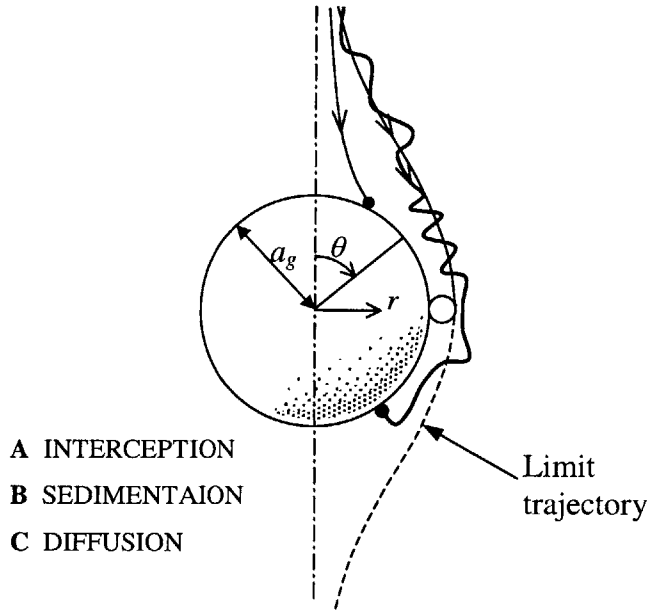

Figure 2.4 Isolated sphere collector and deposition mechanisms by Yao et al. (1971)

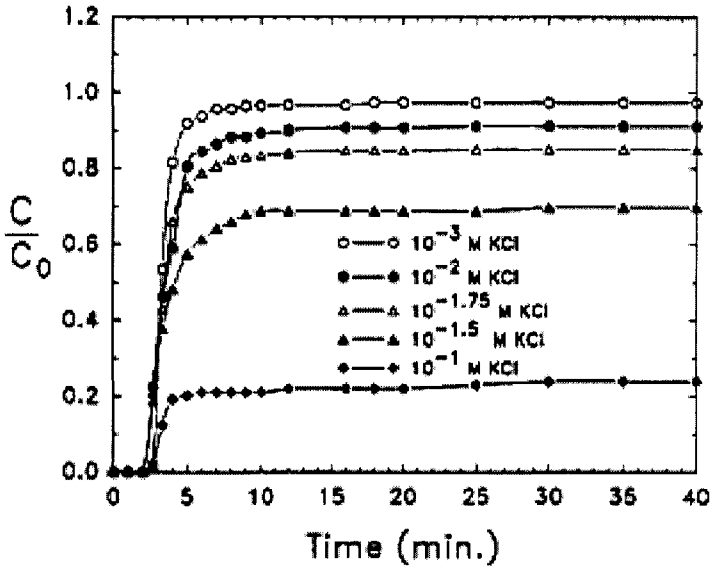

Figure 2.5 Particle breakthrough curves of the 0.753 micron latex particles with various concentrations of KCl: by Elimelech and O'Mella (1990)

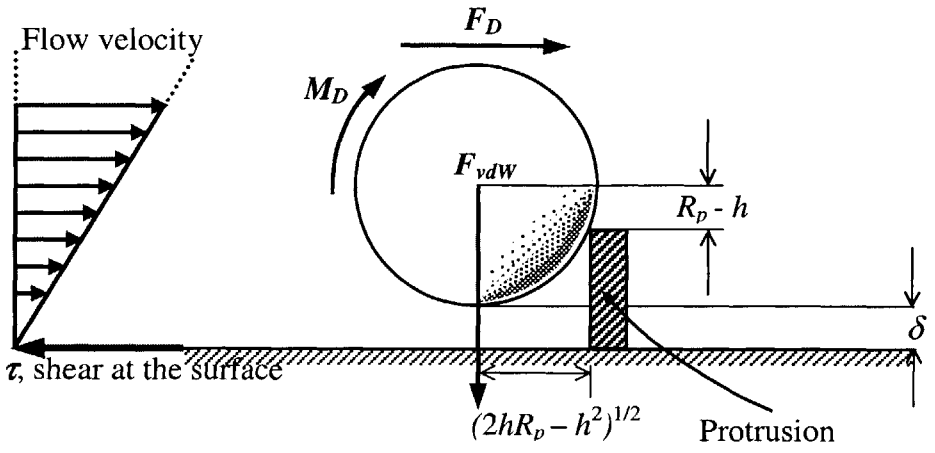

Figure 2.6 Adhesion theory with a protrusion model for roughness of the pore surface (Varidyanathan and Tien, 1988)

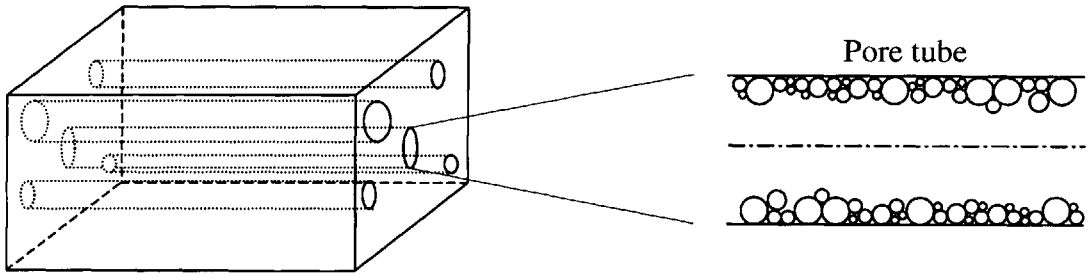

Figure 2.7 Capillary tube representation of porous medium proposed by Reddi and Bonala (1997)

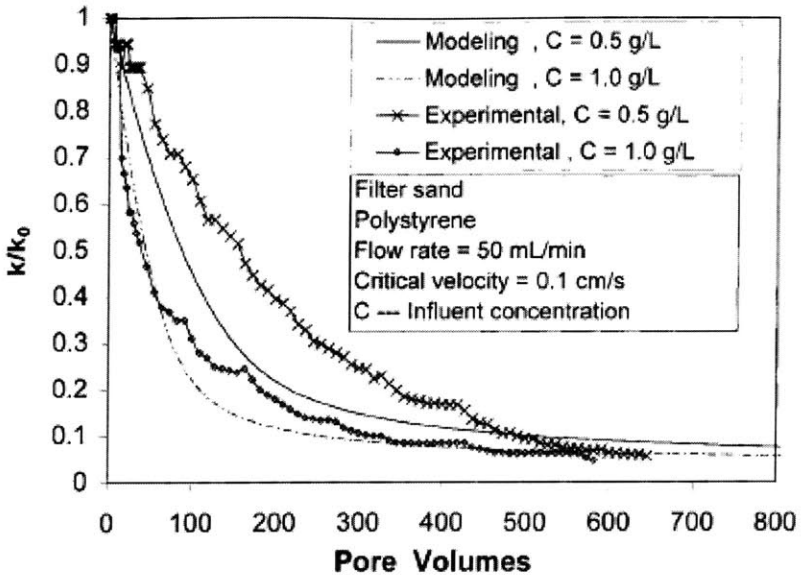

Figure 2.8 Simulated and experimental permeability evolution due to kaolinite filtration: by Reddi et al. (2000)

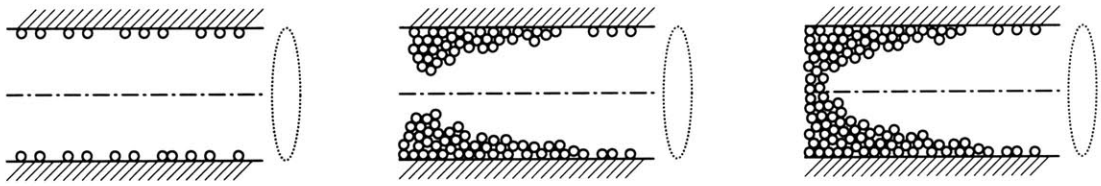

(a) First stage (b) Second stage (c) Third stage

Figure 2.9 Three stages of particle deposition by Choo and Tien (1995)

Table 2.1 List of expressions proposed for the deposition rate function, $F(\sigma) = \lambda/\lambda_0$

Expression	Adjustable Parameters	Reference
$F(\sigma) = 1 + b\sigma$	b	Iwasaki (1937)
$F(\sigma) = 1 - b\sigma$	b	Stein (1940), Ornatski et al. (1955)
$F(\sigma) = \dfrac{1}{(1+b\sigma)^m}$	a, m	Mehter et al. (1970)
$F(\sigma) = \left(1+\dfrac{b\sigma}{n_0}\right)^{m_1}\left(1-\dfrac{\sigma}{n_0}\right)^{m_2}$	b, m_1, m_2	Mackrle et al. (1965)
$F(\sigma) = 1 + b\sigma - \dfrac{a\sigma^2}{n_0 - \sigma}$	a, b	Ives (1960)
$F(\sigma) = \left(1+\dfrac{b\sigma}{n_0}\right)^{m_1}\left(1-\dfrac{\sigma}{n_0}\right)^{m_2}\left(1-\dfrac{\sigma}{\sigma_u}\right)^{m_3}$	b, m_1, m_2, m_3	Ives (1969)

Table 2.2 List of expressions for flow gradient enhancement function, $G(\sigma) = i/i_0$

Expression	Adjustable Parameters	Reference
$G(\sigma) = 1 + d\sigma$	d	Mehter et al. (1970)
$G(\sigma) = 1 + d\dfrac{\sigma}{n_0}$	d	Mints (1966)
$G(\sigma) = \dfrac{1}{(1-d\sigma)^m}$	d, m	Mehter et al. (1970)
$G(\sigma) = \left(1+\dfrac{d\sigma}{n_0}\right)^{m_1}\left(1-\dfrac{\sigma}{n_0}\right)^{m_2}$	d, m_1, m_2	Ives (1969)
$G(\sigma) = 1 + f\left((\lambda_0 + dn_0)\sigma + \left(\dfrac{e+d}{2}\right)^2 + dn_0^2 \ln\left(\dfrac{n_0-\sigma}{n_0}\right)\right)$	f, d, e	Ives (1961)

CHAPTER 3. NETWORK MODELS

3.0 INTRODUCTION

Most problems regarding transport of fine particle-laden fluid through porous media involve multiple length scales. For example, at the largest scale, fines migration related to oil extraction can easily reach the scale of kilometers while construction problems of grouting can range up to tens of meters. In contrast, soil pores have a length scales in the range of microns to millimeters. This is the scale where fundamental interactions occur between particles and soil grains. Major practical issues of filtration involve predicting the macroscopic changes in porous media due to deposition of particles within the pores, (e.g. extent of transport or decrease in permeability due to filtration). Nevertheless, these macroscopic phenomena are ultimately dependent on pore-level processes. The previous chapter has shown that particle filtration depends on pore-level phenomena, and that continuum models focusing on macroscopic scales are often not appropriate. This is ultimately because heterogeneity in the pore structure plays an important role in the process. Modeling the pore scale process is an essential step to transfer microscopic filter efficiency to macroscopic filtration rate. The unit bed representation method with various forms of unit collectors presented in Chapter 2 are examples of basic pore space modeling. This chapter reviews more advanced network models for porous media, and describes in detail the implementation of a simple network model, referred to as the bubble model, that is later used in the Chapters 6 and 7.

3.1 BRIEF HISTORY OF DEVELOPMENT OF NETWORK MODELS

Network models represent the pore space in a medium as a network of pore bodies (referred to as 'sites') connected by pore throats ('bonds'). Network modeling aims to find a mathematical framework for constructing configurations that can represent statistically the heterogeneous medium. The first development of a network model is credited to Fatt (1956) who proposed a regular two-dimensional lattice of tubes of randomly assigned radii to be applied to wetting/imbibition problems (e.g. flow of wetting fluid into a dry medium). Prior to this work, porous media were generally modeled as bundles of parallel tubes, (i.e. capillary model Section 2.4). Although these capillary models have been used in many studies (e.g. interpretation of soil-moisture characteristic curves; Arya et al., 1999) owing mainly to their simplicity, they have also been widely criticized for not representing the connectivity of the pore space within the medium. Fatt's two-dimensional lattice model soon brought about development of three-dimensional lattices. Chatzis and Dullien (1977) pointed out that bicontinua (two continuous phases) could not exist in two dimensions and hence, three-dimensional analyses were necessary for two-phase flow problems. Furthermore, they proposed a modified lattice network in which intersections of pore throats (tubes in lattice) were independently assigned finite volumes. These 'ball-and-stick' type network models are still widely used, having been justified by many researchers who observed that most of the void space is contained in the pore bodies rather than the pore throats (Chatzis and Dullien, 1977; Koplik, 1982).

A popular application of network models is for oil extraction through fractured rock reservoirs. They are also extensively used in chemical and environmental engineering fields when analyzing problems such as centrifuging, drying and multiphase flow in packed columns as well as deep-bed filtration. There are also abundant studies using network models in soil, mostly for wetting/imbibition and other porosimetric problems (e.g., Yanuka, 1989; Zhou & Stenby, 1993). Other important applications, including pore-scale events (such as entrapment of non-wetting phase liquids during

wetting) and dispersion of contaminants, are thoroughly reviewed by Berkowitz and Ewing (1998).

Recently, network models have been successfully applied for simulation of fracture processes in heterogeneous materials (summarized in, for example, Sahimi, 1998). Many heterogeneous materials, such as soils, rocks, fibrous composites, ceramics and concrete, have complex fracture mechanisms strongly related to their microstructures that classical fracture mechanics based on continuum mechanics have limited power to explain. Since network models enable selection of the length scale in which the heterogeneity of the interested material is represented (i.e. for properties such as strength or elastic modulus) by assigning using suitable statistical processes, they work as alternative to the continuum models. Examples of these can be found in Sahimi and Goddard (1986), Duxbury and Leath (1994), and Wu and Leath, (1999).

3.2 TYPES OF NETWORK MODELS

The primary classification of network models depends on the lattice arrangements. Different arrangements generate different coordination numbers (i.e. the number of bonds connected to each site). Although the prevalent network models are two- and three- dimensional square and cubic lattices, there are variations using other regular geometries (such as hexagonal or triangular grids) and random grids based on Voronoi and Delaunay tessellations. Bryant and Blunt (1992) first started to use random-close-packing of mono-dispersed spheres as a network for representing the physical properties of granular soil. This 'physically representative' network model is superior to conventional lattice networks in the sense that it includes the spatial correlations of pore sizes naturally (Thompson and Fogler, 1998). In order to apply such a physically representative network model, however, detailed statistics are needed to characterize the packing of the porous medium and to formulate corresponding network model simulation of the topology. The model of Bryant and Blunt (1992) is based on the 'Finney pack', a set of measurement of 8,000 random closed-packed ball bearings (Finney, 1968). Random packings of regular-shaped particles other than spheres, (i.e. spheroids, ellipsoids, cylinders, and parallelepipeds) have also been studied in physics and soil

science (e.g. see Coelho et al., 1997 and Pilotti, 1998) although it is hard to find equivalent studies on natural porous media. There are more published studies that applied physically representative network models for soil: Stepanek et al. (1999) studied liquid-vapor interface moving; Thompson and Fogler (1997) dispersion; Thompson and Fogler (1998) in situ gelation of an immiscible invading fluid. Figure 3.1 shows some examples of two dimensional lattice and random-packed particle models.

3.3 APPLICATION OF NETWORK MODELS TO FILTRATION PROBLEMS

Continuum models presented in Chapter 2 focus on averaging all microscopic phenomena in pores at the macroscopic scale. For example, the approach of Reddi and Bonala (1997) presented (Section 2.4) takes into account the structure of the pores using a capillary model. These details at the pore level are eventually condensed into a few empirical parameters (such as the deposition coefficient, λ) by averaging, in order to describe the evolution of the host medium and/or filtering material. These empirical parameters represent averaged characteristics of a process which is intrinsically transient and are bound to change as the process advances. Thus, it is often impossible to find a set of parameters that can represent the whole process. Consequently, continuum models have limited predictive power. In order to overcome this limitation, a pore-level scale modeling of the filtering process is required. Discrete network models describe porous media as networks of pore bodies connected by pore throats so that the scale of analysis reduces to the level of pore bodies. As each link in the network represents a pore space, it is possible to model directly the microscopic mechanisms with a network model. Many investigators (Rege and Fogler, 1988, Imdakm and Sahimi, 1991, Datta and Redner, 1998a,b, and Lee and Koplik, 2001) have agreed that network models are more suitable for modeling filtration problems. In their studies, regular lattices of straight tubes were used. While random networks such as the Voronoi network appear to be closer to real porous media, Imdakm and Sahimi (1991) commented that: 'Previous studies (e.g. Jerauld et al., 1984) have shown that, as long as the average coordination number of a

disordered network...is the same as that of a regular network (e.g. a cubic network used in this paper), transport processes in the two networks and their effective properties are, for all practical purposes, identical.'

Two- and three- dimensional lattices of constricted tubes (i.e. tubes with varying radius, maximum at the inlet and outlet and minimum at the middle) are used by Burganos et al. (1991) and Burganos et al. (2001), using the trajectory analysis results of Payatakes (1973) and Tien and Payatakes (1979). The constricted tube shape, provides a better description of the pore space geometry than the straight capillaries.

Burganos et al. (2001) also modeled detachment of large flocs of particles due to hydrodynamic forces and their re-deposition. This has been reported as an important process to cause clogging in filters (Payatakes et al., 1981). In both studies, the deposit layer was assumed to form another constricted tube inside the pore so that the geometry (of the tube with deposit) is also defined analytically (saving computational time).

3.4 BUBBLE MODEL

3.4.1 Principles of bubble model

The bubble model, Figure 3.2, is a quasi-one-dimensional network model first used for filtration problems by Datta and Redner (1998). Each bubble is a bundle of straight circular tubes (bonds) whose radii are described by a probability density function representing the distribution of the pore-radii. The bubble model can be viewed as a two-dimensional square lattice in which all perpendicular bonds are connect to a single site, which corresponds to a homogeneous state at a given time (i.e. has a single pressure and density). The lengths of all bonds in a bubble are identical and they can be thought as representing the length scale between two pressure points.

If a bubble model comprising B- bubbles, each with W- bonds is to be constructed, the length of all B- bubbles and the radii of $B \times W$ bonds should be assigned by a random process equivalent to the pore radius distribution in a grain filter. For example, if a cumulative distribution function for the pore radii distribution is given as a function $F(R)$,

a random generator for bond radii can easily be found by using a random variable, Z, that is uniformly distributed between zero and one.

$$Z = F(R) \tag{3.1}$$

which, in turn, will give the corresponding pore radius:

$$R = F^{-1}(R) \tag{3.2}$$

where F^{-1} is the inverse function of $F(R)$.

Therefore, it is desirable to have an analytical function that is invertible as the distribution function of the pore radius.

It is reasonable to assume that particles are distributed among the bonds with a probability proportional to the flow rate in each bond. If Poiseuille flow is assumed in a bond of radius R, the flow rate is proportional to R^4, and the gradient of the pressure is then:

$$Q = -\frac{\pi R^4}{8\mu}\nabla p \tag{3.3}$$

where μ is the absolute viscosity of the Newtonian fluid.

For particle collection, there are two different mechanisms considered, straining and infiltration. If a particle is larger than the bond, it will be considered collected by the site. This process is often referred to as sieving or straining. A particle smaller than the bond, on the other hand, can become collected inside the pore through deposition and subsequent adhesion (i.e. infiltration). Particles that are not collected are assumed to flow with the fluid. Therefore, the fluid velocity in the bonds is the same as that of the particles. For a time-dependant process such as filtration, the time step small compared to the rate of evolution of the process. The time step in a filtration problem, therefore, needs to be less than the time increment required for a particle to move from one site to the next site, which is referred to as the 'travel time'. The seepage velocity of the fluid in a bond of radius R is:

$$v = \frac{Q}{\pi R^2} \sim -R^2 \nabla p \tag{3.4}$$

The current bubble model assumes a single bond length, L_b, with a constant pressure gradient hence, the time step is defined as the smallest travel time. This time step is inversely proportional to the square of the maximum bond radius, i.e.:

$$\Delta t = \frac{L_b}{v_{\max}} \sim \frac{1}{R_{\max}^2} \tag{3.5}$$

Some of the suspended particles (i.e. those not collected) in the smaller tubes move more slowly than those in larger tubes and do not reach the next site while all of those in the largest tubes move into the next bubble. It becomes complex to evaluate the positions of particles in all bonds with varying radii. A simplified approach is taken by forcing particles to always be at a site for each time step (Hwang and Redner, 2001). Under this assumption, the ratio of the travel distance in a bond, $v\Delta t$, to the total bond length, L, ($v\Delta t/L$) can be considered as the probability for a particle to advance to the next site while the rest remains at the entrance. This concept of particle partitioning to sites is shown schematically in Figure 3.3.

3.4.2 Algorithm for particle transport through bubble model

Once the bond radii are specified, particles are injected into the model. The distribution of particles can be modeled by introducing a probability density function (PDF) for the volume fraction corresponding to the size of the influx particles. The algorithm presented here is similar to that of Hwang and Redner (2001), but also includes the straining mechanism.

For numerical implementation, the PDF should be a discrete, stepwise function. For example, if the particle size distribution is represented by M size fractions, the corresponding PDF is then defined:

$$P[r_{pa}^m] = f_m \times (r_p^m - r_p^{m-1}),\ m = 1\text{-}M \tag{3.6}$$

where f_m is the value of the probability density assigned for radius in the range of $r_p^{m-1} < r_p \leq r_p^m$ whose average radius is given as $r_{pa}^m = (r_p^m + r_p^{m-1})/2$.

For a specified volumetric flow rate, Q, the number of particles in given time, Δt, that belong to each particle size group can then be determined as:

$$\Delta N_{in}^m = \dot{N}(r_{pa}^m)\Delta t,\ m = 1\text{-}M \tag{3.7a}$$

where the particle number injection rate, $\dot{N}(r_{pa}^m)$ is given by:

$$\dot{N}(r_{pa}^m) = Q\,P[r_{pa}^m]/(4\pi(r_{pa}^m)^3/3) \tag{3.7b}$$

Then the total number of particles input for time-step Δt will be the summation of ΔN_{in}^m for all particle size groups in the filtering medium:

$$\Delta N_{in} = \sum_{m=1}^{M} \Delta N_{in}^m \tag{3.8}$$

The fraction of ΔN_{in}^m to this total number of particles, defines the probability density function for the number of particles that belong to the size group (i.e. "the number PDF", g):

$$g_{in}(r_{pa}^m) = \frac{\Delta N_{in}^m}{\Delta N_{in}} = \frac{P[r_{pa}^m]/(r_{pa}^m)^3}{\sum_{m=1}^{M} P[r_{pa}^m]/(r_{pa}^m)^3} \tag{3.9}$$

The number of particles injected from the source, ΔN_{in}, defines the number of input particles to the first site, N_1^{in}. Particles at each site are subdivided among the bonds

exiting. If we assume that the particle density is homogeneous within a site, the number of particles in each bond is only dependent on the flow rate through each bond (i.e. is proportional to R^4, equation 3.3). The number of particles is assumed proportional to the flow rate in each bond and hence, the number of particles advanced to each bond from the input site is controlled by the proportion of the flow carried in each bond. Thus, if the number of particles in j^{th} bond in the first bubble is characterized as $N_{1,j}^{in}$:

$$N_{1,j}^{in} = N_1^{in} \frac{R_{1,j}^4}{\sum_j R_{1,j}^4}, \; j = 1\text{-}W \tag{3.10}$$

where $R_{1,j}$ is the bond radius, and W are the total number of bonds.

The particles in each bond are divided into three groups as follows:

(1) The fraction of remaining particles at the input site

$$N_{1,j}^{reman} = N_{1,j}^{in}\left(1 - \frac{v_{1,j}\Delta t}{L_1}\right) \tag{3.11a}$$

where L_1 is the length of the bonds in the first bubble. The total sum of the remaining particles from every bond gives the number of particles remaining at the first site, $N_1^{reman}(t_1) = \sum_{j=1}^{W} N_{1,j}^{reman}$. The remainder of injected particles will leave the site to the bonds:

$$N_{1,j}^{leave}(r_{pa}^m, t_1) = N_{1,j}^{in}(r_{pa}^m, t_1)\frac{v_{1,j}\Delta t}{L_1} \quad ,m = 1\text{-}M \tag{3.11b}$$

where M is the number of particle size fractions considered (equation 3.5), and the number of injected particles per particle size group can be given as:

$$N_{1,j}^{in}(r_{pa}^m, t_1) = N_{1,j}^{in} g_{in}(r_{pa}^m), \; m = 1\text{-}M \tag{3.11c}$$

(2) The fraction of particles collected by straining

$$N_{1,j}^{strain}(r_{pa}^{m},t_1) = N_{1,j}^{leave}(r_{pa}^{m},t_1)\,P[r_{pa}^{m} > R_{1,j}] \quad , m = 1\text{-}M \tag{3.12}$$

where $P[r_p^m > R_{1,j}]$ is the probability of a particle to be larger than the concerned pore.

(3) The fraction of particles collected by infiltration

$$N_{1,j}^{\inf}(r_{pa}^{m},t_1) = N_{1,j}^{leave}(r_{pa}^{m},t_1)\left(1 - P[r_{pa}^{m} > R_{1,j}]\right)P[\text{infiltration}],\ m = 1\text{-}M \tag{3.13}$$

where P[infiltration] denotes the probability of a particle to be collected thorough infiltration.

In order to assure mass continuity, the number of particles advancing to the second bubble is

$$N_{1,j}^{adv}(r_{pa}^{m},t_1) = N_{1,j}^{in}(r_{pa}^{m}) - N_{1,j}^{reman}(r_{pa}^{m}) - N_{1,j}^{strain}(r_{pa}^{m}) - N_{1,j}^{\inf}(r_{pa}^{m}) \tag{3.14a}$$

Then the total number of particles that will be advanced to the next site can be determined as the total sum:

$$N_{1,j}^{adv}(t_1) = \sum_{m=1}^{M} N_{1,j}^{adv}(r_{pa}^{m},t_1) \tag{3.14b}$$

The radii of bonds from the first bubble should be updated to account for the number of collected particles. The procedure will be further explained in the next section. As a result, the time increment, Δt, which is a function of the maximum tube radius as shown in equation 3.5, is also updated such that $\Delta t = \Delta t_2$.

At the second time step, at $t = t_2 = t_1 + \Delta t_2$, equations 3.8 and 3.9 will be used to update the number of injected particles, $\Delta N_{in}(t_2)$ that corresponds to the new time step, Δt_2. Added to the particles remained at the first site from the previous time

step, $N_1^{reman}(t_1)$, the number of particles injected to the first bubble at the second time step will be:

$$N_1(t_2) = N_1^{in}(t_2) + N_1^{reman}(t_1) \tag{3.15}$$

For the second bubble, particles passed through the first bubble from the first bubble, i.e., $N_2^{in}(t_2) = \sum_{j=1}^{W} N_{1,j}^{adv}$ is injected, with corresponding number PDF function,

$$g_2(r_p^m, t_2) = \frac{\sum_{j=1}^{W} N_{1,j}^{adv}(r_{pa}^m, t_1)}{N_2^{in}(t_2)} \tag{3.16}$$

This way, the last site will be reached after B time steps, the same as the number of bubbles. Eventually, after time $t = T$, for the i^{th} bubble, $N_i(T)$, with corresponding $g_i(r_{pa}^m, T)$ will be known. In addition, the total number of particles collected on the bubble either by straining or infiltration will be given:

$$N_i^{strain}(T) = \sum_{it} \sum_{j=1}^{W} N_{i,j}^{strain}(r_{pa}^m, t_{it}) \tag{3.17a}$$

$$N_i^{\inf}(T) = \sum_{it} \sum_{j=1}^{W} N_{i,j}^{\inf}(r_{pa}^m, t_{it}) \tag{3.17b}$$

which will add up to give the total number of collected particles:

$$N_i^c(T) = N_i^{strain}(T) + N_i^{\inf}(T) \tag{3.18}$$

Figure 3.4 presents this bubble model algorithm as a flow chart.

3.5 COLLECTION MECHANISM IN A BOND AND CHANGES IN BOND RADIUS

In network simulations, the probability of infiltration, P[infiltration], as defined in equation 3.13, is the key parameter that determines the quantity of particles that will be collected in the bonds and affect the subsequent flow (by changing the bond radii). In previous network model simulations, the values of the probability were usually obtained by applying the trajectory analysis results (e.g. Burganos et al., 2001), or empirical relations (e.g. Rege and Fogler, 1988). Again, the influence of the straining process is rather straightforward, because any particle larger than the bond will clog it, and remain trapped at the preceding site. In a probabilistic sense, this means that the probability of flow is the same as that of straining, i.e.:

$$\text{If } N_{i,j}^{strain}(r_{pa}^{m}, t_{it}) \geq 1, \text{ then } R_{i,j} = 0 \tag{3.19}$$

Particles collected by infiltration are smaller than the bond radius, and remain in the bond causing a change in the flow field whose effects can be coupled through separate calculations. For example, Suchomel et al. (1998a and b) used a cubic network of straight pipes to simulate transport of bacteria in porous media. It was assumed that the filtered bacteria would be distributed uniformly around the wall in a given bond. Then, the radius $R(t)$ of the bond corresponding to the specific deposit, $\sigma(t)$ can be obtained by a simple volume-mass balance:

$$R(t) = R(0)\sqrt{1-\sigma(t)/\rho_b} \tag{3.20}$$

where $R(0)$ is the initial bond radius, and ρ_b the bulk density of deposit. The specific deposit accumulation in the bond was calculated with the attachment-detachment kinetics as given in equation 2.14.

Imdakm and Sahimi (1990) used an analytical approximation to estimate the pressure change by single particle deposition. They used the concept of the effective

radius, by introducing a fictitious radius of the cylindrical pore that gives the same hydraulic resistance as the pore and deposited particles. Therefore, the effective radius of the pore with flow rate, Q, and length, L, should satisfy the following relation for Poiseuille flow in equation 3.3.

Using this concept, they treated the pores with deposited particles as an equivalent cylindrical pore with reduced radius. In a clean cylindrical pore, when one particle is attached and exerts a drag force F_D, the new pressure drop, Δp_a, has the following relation with the current pressure drop, Δp_b:

$$\pi R_a^2 \Delta p_a = \pi R_b^2 \Delta p_b + F_D = x \tag{3.21}$$

where R_b is the radius of the clean cylindrical pore before the particle attachment and R_a is the equivalent pore radius after the attachment. When equation 3.21 is substituted into equation 3.3,

$$\frac{8\mu LQ}{R_a^2} = x \tag{3.22}$$

Imdakm and Sahimi (1991) used the expression by Goldman et al. (1967a,b) in equation 2.30a to compute the drag force, F_D, and updated the pressure drop as particles attach to the pore wall, although the solution is strictly only applicable for infinite space bounded by the wall as explained in Section 2.3.2. In order to use Goldman's solution, the wall shear force at the plane, τ_w should be known *a priori*. However, this is not detailed by Imdakm and Sahimi (1990). Therefore, a further assumption is made on the wall shear force, that τ_w can be obtained from another Poiseuille flow relationship:

$$\tau_w = \frac{R}{2}\nabla p \tag{3.23}$$

Therefore, if the length of bond is L and the pressure gradient is assumed constant over the entire bond, equation 3.22 and Goldman's solution in equation 2.30a can be combined to give an expression for the radius after one particle of radius, r_p attached.

$$R_a^2 = \frac{R_b^4}{R_b^2 + \frac{10.205 r_p^2 R_b}{2L}} \tag{3.24}$$

As explained earlier, this method is based on the assumption that the bond with deposited particle can be approximated as a tube with reduced radius, keeping the same geometry as a straight tube, as Suchomel et al. (1998a and b) did. However, assumption is not generally valid, especially when there is substantial deposition. Rigorous solutions of the flow equations with modified boundaries due to deposition should provide a better correlation for the changes in bond radii.

Chapter 4 presents a simulation method for computing particle flow and deposition in model pore tube. Results of this pore model are described in Chapter 5 (including comparisons with equation 3.22). The pore tube model enables a detailed parametric study on effects of inflow velocity, particle density, size and orientation of the pore in order to improve the prediction of deposition probability.

3.6 CONCLUSIONS

Discrete network models provide a framework for analyzing the mechanics of filtration at microscopic scales. A brief history of development of network model as a discrete model of porous media has been presented as an alternative to continuum models reviewed in Chapter 2. A detailed explanation of the quasi-one-dimensional bubble model has illustrated the construction of the particle transport algorithm. This model will be used in later chapters in junction with real-scale parametric study results on particle deposition in cylindrical tubes (model pore), which directly represents the microscopic mechanisms in each bond as will be explained in the next chapter.

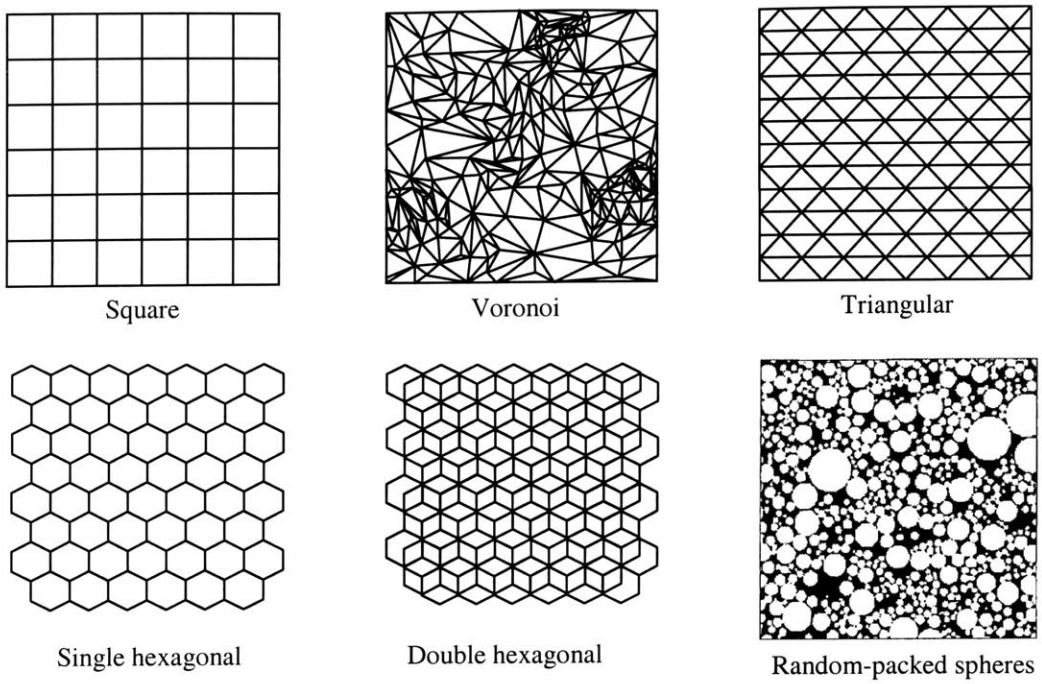

Figure 3.1 Types of two dimensional network models

Symbol	
●	Sites: Suspension in homogeneous conditions
——	Bonds: A cylindrical tube with same length

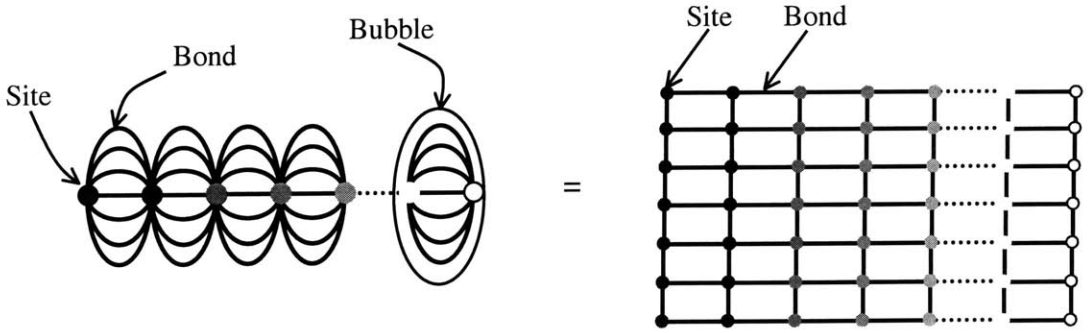

Figure 3.2 Sketch of a bubble model compared with a lattice model

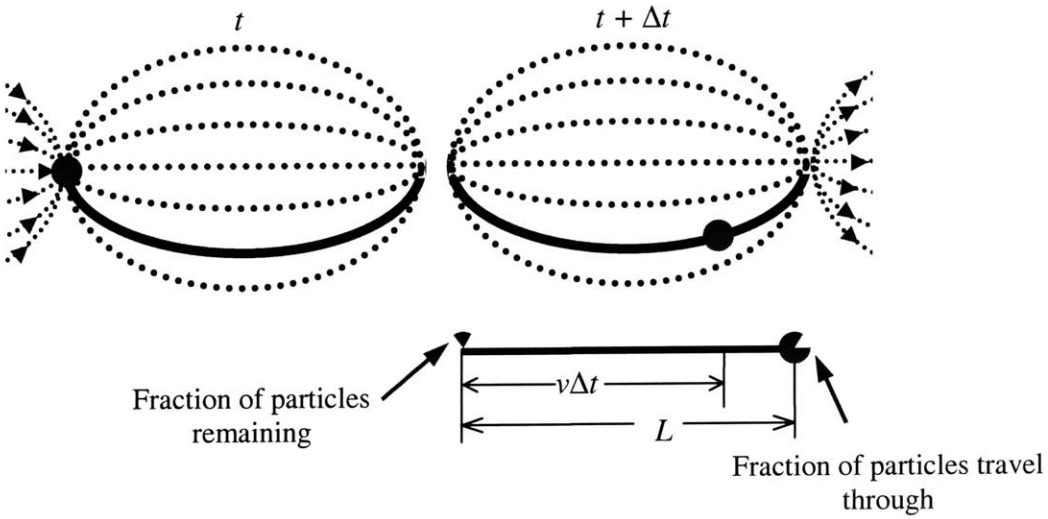

Figure 3.3 Concept of particle partitioning to sites

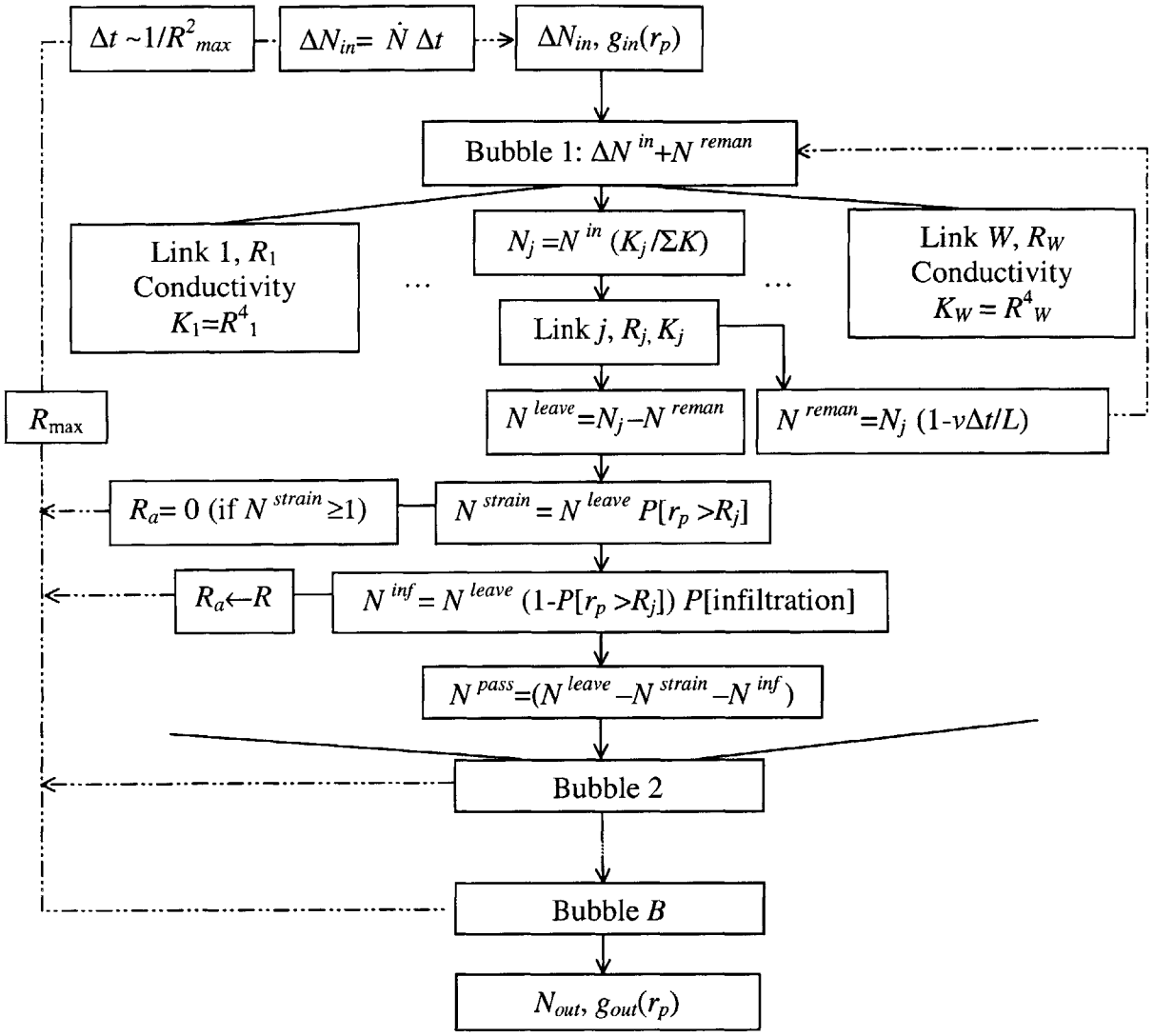

B,W	Number of bubbles, number of bonds in a bubble
Δt	Time step
R_{max}, R_1, R_W	(Maximum, 1st , W st, after filtration) bond radii
v	Fluid velocity in bond
L	Length of bubble
ΔN_{in}	Number of particles input at the time step Δt
$\dot{N}$	Particle injection (number) rate
K	Bond conductivity
N_{leave}	Number of particles injected into bonds
N_{reman}	Number of particles remains at site
N_{pass}	Number of particles pass through to next site
N_{inf}	Number of particles captured by infiltration
N_{strain}	Number of strained particles
N_{out}	Total number of particles passing through the model
g_{in},g_{out}	Input and output particle probability density function (number)

Figure 3.4 Flow chart of particle transport through a bubble model

CHAPTER 4. PORE-SCALE SIMULATION OF PARTICLE-LADEN FLOW

4.0 INTRODUCTION

A network model of a porous medium enables the pore-scale characteristics to be incorporated in the simulation of particle transport problems. Hydrodynamics of particle transport at the pore scale are fundamental when investigating the filtration process of suspensions in porous media. This chapter presents a simulation method that identifies particles that settle out inside a model pore (i.e. become separated from the fluid suspension) and quantifies the effects of these particles on subsequent flow. Simulation of particle motions suspended in a fluid has been known to be a challenging problem due to the technical difficulties of handling complex boundaries and the long-range character of hydrodynamic forces. These long range force interactions make the problem non-convergent especially as the number of injected particles increase and hence, prevents approximation based on simpler systems. Therefore, most existing models of pore-scale filtration mechanism are severely limited when representing the collection of large numbers of particles (i.e. advanced stages of filtration). Despite this complexity, particle-laden flows have been intensively studied since problems involving many particles immersed in fluid are found widely in many engineering and scientific fields. The current study uses a method of solving the flow equations based on a fixed grid, finite difference approximation adapted from Höfler and Schwarzer (2000).

4.1 EXISTING MODELS

The deposition mechanism of particles on the surfaces of grains of the filtering media is impossible to observe directly in most cases[5]. Instead, the process has been indirectly quantified by measuring the effluent concentration or pumping pressure at the injection point, using filtration laws as summarized in Chapter 2. Although this approach is well suited for continuum models that are based on the mass conservation equation of the suspension, a microscopic approach based on network model requires modeling the physical process of particle deposition. There exist a number of theories on the dynamics of deposition for particle suspensions. They can be categorized into two kinds: internal flow and external flow models. External flow models describe a spherical grain within a shell that represent the porosity of the medium, and models flow around the grain. These models are also known as the sphere-in-cell models. On the other hand, internal flow models represent the pore flow as flow through a model tube. Two of the existing models, one from the external flow model and the other from the internal flow model, are discussed in more detail here.

4.1.1 Happel's model

Happel's model, was briefly explained in Chapter 2, and is the most frequently applied external flow model. The Happel's model comprises a solid sphere of radius, a_g, surrounded by a fluid envelope of radius, b, which represents a porous medium with initial porosity, n_0:

$$\frac{a_g}{b} = d = (1-n_0)^{1/3} \tag{4.1}$$

The stream function, ψ_H, of Newtonian viscous flow around a sphere of radius a_g was calculated by Happel and Brenner (1965) using a spherical coordinate system, (r, θ):

[5] An exception can be found in Yoon et al. (2004), which is introduced in more detail in Chapter 6.

$$\psi_H(r,\theta) = A\left(\frac{K_1}{r'} + K_2 r' + K_3 r'^2 + K_4 r'^4\right)\sin^2\theta$$

$$A = \frac{v}{2}a_g^2,\quad K_1 = \frac{1}{w},\quad K_2 = -\frac{3+2d^5}{w},\quad K_3 = \frac{2+3d^5}{w} \text{ and } K_4 = -\frac{d^5}{w} \tag{4.2}$$

where $r' = \frac{r}{a_g}$, $w = 2 - 3d + 3d^5 - 2d^6$ and v is the far field velocity.

Particles can be separated from the streaming fluid and deposited on the surface of a grain due to attractive forces. Mackie et al. (1987) determined the trajectory of particles under the action of gravitational and hydraulic drag forces, which are known to be the most important for larger (i.e. non-colloidal) particles. A particle of radius, r_p, has the following set of stream functions, or trajectories, ψ:

$$\psi = \psi_H(r,\theta) + AN_G r'^2 \sin^2\theta \tag{4.3a}$$

$$N_G = \frac{2(\rho_s - \rho)g r_p^2}{9\mu v} \tag{4.3b}$$

where N_G is a non-dimensional factor for the gravitational force, ρ_s and ρ are the density of particles and fluid respectively, and μ is the fluid viscosity.

Equations 4.3a, b are obtained by balancing the gravitational force with the Stokes drag force, i.e. $F_D = 6\pi\mu\,(v\text{-}u)\,r_p$, applied to a spherical particle of radius, r_p, moving with a constant velocity, u. The velocity of the particle has the following relationship with that of the fluid, v:

$$u = (1 + N_G)v \tag{4.4}$$

Once the particle trajectory equation is determined, the limiting trajectory of the particle that passes tangent to the grain can be specified. This forms a boundary of flow within which the particles will be deposited on the grain surface. Figure 4.1 shows that for a particle of radius, r_p, the limiting trajectory of the streamlines given by equation 4.3

corresponds to the one passing the location, $(a_g + r_p, \pi/2)$, i.e. $\psi\ (a_g + r_p, \pi/2)$. This trajectory, due to the nature as a stream function, gives the volume rate of flows within its boundary as $2\pi\psi\ (a_g + r_p, \pi/2)$.

The efficiency of a unit collector or the rate of particle collection is the fraction of volume flow rate passing inside the limiting trajectory compared to the overall particle influx rate (πub^2).

Thus, the collection efficiency, η, for mono-dispersed particles of radius, r_p, is given as:

$$\eta(r_p) = \frac{2\pi\psi_L}{\pi\, ub^2} = \frac{2d^2\psi_L}{a_g^2(1+N_G)} \tag{4.5}$$

where ψ_L is the limiting trajectory, $\psi_L = \psi\ (a_g + r_p, \pi/2)$.

4.1.2 Constricted tube model

A constricted tube has a curved wall in order to model more realistically the converging-diverging character of pore space within granular material. Different geometries can be considered to describe the wall geometry (parabolic, sinusoidal and hyperbolic). Creeping flow in these types of constricted tubes were evaluated either numerically or analytically by various researchers including Payatakes et al. (1973b), Neira and Payatakes (1978), Fedkiw and Newman (1979) and Venkatesan and Rajagopalan (1980).

Once the flow field is given, the trajectory equation of a particle can be calculated with known forces describing the particle movement. The most general particle trajectory analysis for a particle under the effect of gravitational, double-layer and van der Waals forces including the effect of change in the tube orientation has been presented by Paraskeva et al. (1991) for a sinusoidal tube. Figure 4.2 illustrates a constricted tube with the limiting trajectory of a particle. With known trajectory equation, ψ, the collection efficiency of the tube can be given as a function of stream function, since the difference between stream functions gives the flow rate.

$$\eta = \frac{\psi(R_L, 0.5L) - \psi(R_i, 0.5L)}{\psi(0, 0.5L) - \psi(R_i, 0.5L)} \tag{4.6}$$

where R_i is maximum radius at the inlet (Figure 4.2) and R_L the inlet radius of the limiting trajectory.

4.1.3 Discussion

All existing theories, including the two kinds presented here, are based on the assumption of a well-defined model pore geometry, (either a sphere or a tube). In other words, the presence of previously deposited particles is not taken into account. Consequently, they can be used only for clean filters before the structure of the filter is severely changed by the deposition process. As mentioned in Chapter 2, there are some studies on methods of amending the models to include the effect of these deposits. Mackie et al. (1987) developed a mathematical model to describe deposits shaped as a thin cap in Happel's model (representing an average effect of deposited particles on the collection efficiency) and reported good qualitative agreement with experimental data. Later, Choo and Tien (1995) have developed a similar but more advanced mathematical model that allows flow through the deposit layer. However, representation of the deposits as a thin layer limits the use of these models to relatively small amounts of deposits. Putnam and Burns (1997) modeled individual deposited particles and their hindering effect on the further depositions using a sphere-in-cell model. However, only monolayer deposition was allowed in the analysis assuming particles have double-layer thick enough to prohibit other particles from collecting. Burganos et al. (2001) used a method of continually updating the collection efficiency of the sinusoidal constricted tube models as deposits accumulate, using trajectory equations presented by Paraskeva et al. (1991). They assumed that the deposit should be curved as the sinusoidal tubes, which enabled modeling the tube with deposit with a new sinusoidal surface. They also assigned a specific porosity to the deposit, as Choo and Tien (1995) did, to allow flow through the deposited material.

4.1.4 Explicit numerical model of particle deposition mechanism

Biggs et al. (2003) realistically modeled particles flowing through a) a pore throat composed of two circular half grains, and b) a model two-dimensional porous medium composed of randomly located rectangular grains. They used a lattice-gas automata (LGA) method, which approximates fluid behavior as the product of many fictitious microscopic 'particles' in a lattice and hence, the fluid has only finite number of possible velocity vectors. A fluid particle can move with any of these vectors, but must choose its direction following certain rules when it collides with another particle. These collision rules, is selected such that the average motion of fluid particles approximates that governed by Navier-Stokes equation. The power of LGA methods arises from simple basic equations that allow fine discretization and hence, better mapping of boundaries.

Biggs et al. (2003) applied an LGA method to simulate flow of circular particles through model pore space, composed of randomly placed rectangles. The particles were uniform-sized and neutrally buoyant. They were assumed to be collected upon contact with the pore walls. They discussed the importance of effect of deposition on the flow, which had been neglected in most traditional trajectory studies.

4.3 PARTICLE DEPOSITION IN A CYLINDRICAL PORE

In order to study changes in the deposition rate and flow field due to particle collection, direct modeling of the flow field is needed. However, this approach introduces complex boundaries of the deposited particles and can only be solved through extensive numerical simulations. Particle motions through a finely meshed cylindrical model pore are then formulated and solved simultaneously with the fluid flow.

4.3.1 Fluid

The suspension fluid is formulated with the Stokes equation (i.e. an approximation of Navier-Stokes, for flows where inertial forces are negligible; typically $Re < 1$) described by:

$$\nabla^2 \mathbf{v} = \frac{1}{\mu}(\nabla p - \mathbf{f}) \tag{4.7}$$

where $\mathbf{v}$ is the fluid velocity vector, p is the pressure, $\mathbf{f}$ is the force density vector. In addition, the continuity equation for incompressible fluids applies such that:

$$\nabla \cdot \mathbf{v} = 0 \tag{4.8}$$

Due to the incompressibility condition, the divergence of the equation 4.7 becomes a Poisson's equation for the pressure:

$$\nabla^2 p = \nabla \cdot \mathbf{f} \tag{4.9}$$

Therefore, the three-dimensional Stokes equation is equivalent to a set of four Poisson's equations (three for components of the fluid velocity and one for pressure), equations 4.7, 4.9.

4.3.2 Particles

The suspension is considered stable except for a portion that will be separated within given time duration. A sedimentation test can provide the information needed to predict this fraction. The separated particles move under the influence of hydrodynamic forces and gravity. The hydrodynamic forces on the suspended particles are not explicitly calculated but are indirectly invoked by assuming the particles move at the same velocity as the suspension fluid. No rotation is considered. The gravitational force, on the other hand, is introduced by specifying a constant settling velocity, $\mathbf{v}_s$, according to Stokes Law[6]:

$$\mathbf{v}_s = \frac{2}{9}\frac{(\rho_s - \rho)}{\mu}\mathbf{g}r_p^2 \tag{4.10}$$

[6] This is strictly limited to spherical particles.

A separated particle will settle at this velocity until it contacts either the pore wall or other previously deposited particles.

When a particle comes in contact with the pore wall, a binary (on, off) random process is used to decide whether the particle becomes attached (on) or not (off) according to a predefined probability of attachment. The probability imitates the condition where only certain fraction of the pore wall surface is considered 'rough' enough to hold the deposited particles (i.e. a probability of 0.5 corresponds to a pore wall half of whose surface is rough). Particles that are deposited but not attached will be moving solely by gravity as the no slip boundary condition is applied to the fluid. On the other hand, a particle deposited on top of other particles will continue to move under the action of gravity until it achieves a stable position with at least three contact points.

4.3.3 Fluid-particle coupling

Fluid particle coupling is an essential part of modeling particle-laden flow. The hydrodynamic drag force exerted on a particle of radius, r_p, stems from the no-slip boundary condition of the viscous fluid surrounding the particle:

$$\mathbf{v} = \mathbf{u}(\mathbf{x}_p), \text{ when } \left|\mathbf{x} - \mathbf{x}_p\right| \leq r_p \tag{4.11}$$

where $\mathbf{u}$ is the particle velocity, $\mathbf{x}$ is the coordinate system and $\mathbf{x}_p$ is the coordinates of the center of the particle.

Finding a solution that satisfies this boundary condition when multiple particles exist is a classic problem of particle-laden flow. A variety of different solution methods have been proposed, see for example Ladd and Verberg (2001) and Brady and Bossis (1988). Among these, Höfler and Schwarzer (2000) developed a method based on a fixed grid system. In this approach, the particle is represented by grid points located inside the particle volume. These nodes, named 'embedded nodes', can be thought of as combination of solid and fluid in which the fluid moves with the solid part. Figure 4.3 shows a sketch of particle located in a cubical grid system with nodes embedded in the particle. Thus, the solid has a submerged particle density (i.e. particle density reduced as

much as the fluid density so that the density of the whole volume is that of the particle). This idea was first introduced by Fogelson and Peskin (1988) and later adopted in Höfler and Schwarzer (2000). Numerically, the no-slip condition of the fluid on the particle can be approximately achieved by making the embedded nodes have the same velocity as the particle. To do this, the velocities of the particle and each of the corresponding embedded nodes are compared and the difference between them is used to generate a force density vector for the node.

If $\{i_e\}$ refers to the set including indices of the embedded nodes in a particle denoted as i, the flow field values for the nodes should trace the velocity of the particle, namely, $\mathbf{u}_i$. If the current fluid velocity at a node j, $\mathbf{v}_j$ is different from the target value $\mathbf{u}_i$, a coupling force density should be applied to the node in the opposite direction, i.e.:

$$\mathbf{f}_j^0 = -K(\mathbf{v}_j - \mathbf{u}_i) \quad j \in \{i_e\} \tag{4.12}$$

where K is a constant stiffness parameter (corresponding to the stiffness of the embedded fluid), which will be selected for numerical efficiency. The sum of the coupling force vectors of all embedded nodes belonging to N_c collected particles forms the total force density vector of the problem:

$$\mathbf{f}^0 = \sum_{i=1}^{N_c} \sum_{j \in \{i_e\}} \mathbf{f}_j^0 \tag{4.13}$$

This force vector is then fed to the Stokes equation in equation 4.9:

$$\nabla^2 p = \nabla \cdot \mathbf{f}^1 \tag{4.14}$$

and to the Poisson's equation in equation 4.7:

$$\nabla^2 \mathbf{v} = \frac{1}{\mu}\left(\nabla p - \mathbf{f}^1\right) \tag{4.15}$$

The solution of these new equations will generate a new velocity vector for the embedded nodes. In order to ensure that the embedded nodes match the target velocity of the particle, $\mathbf{u}_i$, iterations are performed. The updated force density vector $\mathbf{f}_j^{k+1}$ can be obtained after the $(k+1)^{\text{th}}$ iteration step with the velocity field vector $\mathbf{v}_j^k$ from the previous iteration step:

$$\mathbf{f}_j^{k+1} = -K(\mathbf{v}_j^k - \mathbf{u}_i) + \mathbf{f}_j^k \tag{4.16}$$

With an appropriate value of the stiffness, K, and sufficient iterations, the relative velocities between solid and fluid part in embedded nodes will become negligible compared to the average flow velocity. The flow field is kept unchanged until the next particle collection occurs. The final coupling force density vector obtained after I iterations can be written:

$$\mathbf{f} = \sum_{i=1}^{N_c} \sum_{j \in \{i_e\}} \mathbf{f}_j^I \tag{4.17}$$

The total drag force, $\Sigma\mathbf{F}_D$ exchanged between collected particles and the fluid can be approximated if the volume represented by each embedded node, v_{pj} is known.

$$\Sigma\mathbf{F}_D = \sum_{i=1}^{N_c} \sum_{j \in \{i_e\}} \mathbf{f}_j^I v_{pj} \tag{4.18}$$

where v_{pj} can be obtained by dividing particle volume by the number of embedded nodes (as the particle volume is considered uniformly distributed to the embedded nodes).

4.3.4 Simulation of constant-flow-rate in pore tube

Constant-flow-rate is the boundary condition generally applied in experimental studies of filtration processes. In the context of the current formulation, the constant-flow-rate condition should be invoked by adjusting pressure conditions at the ends of the

model pore. Whenever the new collection of particle occurs, the force density is updated, producing a change in the velocity field, which, in turn, will require updating of the pressure conditions.

Let's consider the case when a Newtonian fluid with a viscosity μ is flowing through a tube of radius, R, and length, L, with a constant flow rate of Q_0:

$$Q_0 = U_{flav}(\pi R^2) \tag{4.19}$$

where U_{flav} is the average flow velocity.

If there are no collected particles, the force density vector is zero and the solution of the Poisson's equation in 4.9 will be the constant pressure gradient, i.e., $\nabla p = C$ (where C is an integration constant).

Substituting this to the Stokes equation in 4.7 generates:

$$\nabla^2 \mathbf{v} = \frac{C}{\mu} \tag{4.20}$$

Equation 4.20 with the constant flow rate condition (4.19) has an analytical solution:

$$\mathbf{v} = U_{flav}\left(1 - \frac{r^2}{R^2}\right)\mathbf{i}_z \tag{4.21a}$$

$$C = \frac{dp}{dz} = -\frac{8U_{flav}\mu}{R^2} \tag{4.21b}$$

where $\mathbf{i}_z$ is the unit vector parallel to the axis. Therefore, if the pressure at the exit is set to be zero, the pressure field will be given by:

$$p = \frac{8U_{flav}\mu}{R^2}(L - z),\ 0 \le z \le L \tag{4.22}$$

The Poiseuille flow stays unchanged until particle collection begins. Once a particle is collected, the embedded fluid nodes can be distinguished and the iteration scheme invoked to find the force density vector presented in the previous section.

Let's assume the first collection happens at the n-th time-step, and refer to the set including indices of the embedded nodes as $\{i_e\}$ as before. From the previous time-step, the velocity vector at an embedded node j, $\mathbf{v}_{j,n-1}$, is known, and the velocity of the collected particle should be zero. Therefore, the force density vector in equation 4.13 becomes:

$$\mathbf{f}^0 = -K \sum_{j \in \{i_e\}} \mathbf{v}_{j,n-1} \tag{4.23}$$

To solve Stokes' equation in equation 4.15 with the coupling force, boundary conditions are needed for the pressure. However, the conditions to ensure the specified flow rate are not known *a priori*. Therefore, the pressure boundary condition has to be included in an iterative scheme. The pressure at the entrance and exit corresponding to Poiseuille flow (in equation 4.22) is used as an initial approximation:

$$p = 0, \text{ at } z = L \tag{4.24a}$$

$$p = p_0 = \frac{8U_{flav}\mu}{R^2} L, \text{ at } z = 0 \tag{4.24b}$$

which gives the initial pressure drop across the model pore, $\Delta p = p_0$.

Then, from equation 4.15, the new velocity field $\mathbf{v}^1$, can be calculated. However, this velocity field is not consistent with the assumed, considering as the pressure boundary condition (in equation 4.24b) is incorrect. The pressure boundary condition is then updated to match the required flow rate. For this purpose, flow rate at the middle of the tube, i.e., at $z = L/2$ is evaluated from the updated flow field.

$$Q^1 = \int_{r=0}^{r=R} \mathbf{v}^1(r, z = L/2)(2\pi r\, dr) \tag{4.25}$$

The difference between Q_0 and Q^1 can then be compensated by a differential pressure correction, p_c^1, applied at the tube entrance:

$$p_c^1 = \frac{8\mu L}{\pi R^4}(Q_0 - Q^1) \tag{4.26}$$

Adding this to the initial pressure boundary condition in equation 4.24b, the new pressure boundary condition for the next iteration step will be given

$$p = \Delta p = p_0 + p_c^1 \quad \text{at} \quad z = 0 \tag{4.27}$$

which will be used for the next step of iteration, to keep the prescribed constant-flow-rate condition.

4.4 NUMERICAL IMPLEMENTATION

4.4.1 Multigrid solver

The three-dimensional Stokes equation is solved as a set of four Poisson equations (equation 4.7 and 4.9). For an equilateral lattice with spacing, h, the finite difference discretized Stokes equation for the velocity components are given by:

$$\begin{aligned} &\frac{\mathbf{v}_{i+1,j,k} - 2\mathbf{v}_{i,j,k} + \mathbf{v}_{i-1,j,k}}{h^2} + \frac{\mathbf{v}_{i,j+1,k} - 2\mathbf{v}_{i,j,k} + \mathbf{v}_{i,j-1,k}}{h^2} + \frac{\mathbf{v}_{i,j,k+1} - 2\mathbf{v}_{i,j,k} + \mathbf{v}_{i,j,k-1}}{h^2} \\ &= \frac{1}{\mu}\left(\frac{p_{i+1,j,k} - p_{i-1,j,k}}{2h} - \mathbf{f}_{i,j,k}\right) \end{aligned} \tag{4.28}$$

where i, j and k are indices of the nodes that are increasing in x, y and z directions respectively. A similar discretization for the pressure is given by:

$$\frac{p_{i+1,j,k}-2p_{i,j,k}+p_{i-1,j,k}}{h^2}+\frac{p_{i,j+1,k}-2p_{i,j,k}+p_{i,j-1,k}}{h^2}+\frac{p_{i,j,k+1}-2p_{i,j,k}+p_{i,j,k-1}}{h^2}$$
$$=\left(\frac{f_{xi+1,j,k}-f_{xi-1,j,k}}{2h}+\frac{f_{yi,j+1,k}-f_{yi,j-1,k}}{2h}+\frac{f_{zi,j,k+1}-f_{zi,j,k-1}}{2h}\right) \quad (4.29)$$

There are many solvers available for these discretized three-dimensional Poisson equations. For the current simulator, a solver named 'MUDPACK' is used. MUDPACK is a collection of Fortran 77/90 subprograms of a solver for linear elliptic partial differential equation utilizing finite-difference approximation and multigrid iterations (Adams, 1989 and 1990).

A multigrid method is a relaxation scheme that combines classical iterative techniques, such as Gauss-Seidel relaxation and sub-grid refinement procedures. The term multigrid came from the characteristic of the method that uses a coarser grid to get the initial approximation of the finer grid system. For example, for a two-dimensional discretization using an n by n grid, equations for an $n/2$ by $n/2$ grid is solved prior to provide the approximate solution. This idea can be applied recursively (i.e. the $n/2$ by $n/2$ system can be approximated using an $n/4$ by $n/4$ system). This procedure is called a restriction scheme (Briggs et al., 2000). Multiple correction schemes can be used for an analysis, in which case the solution at the finer grid will be used back for the coarser grid to improve the solution, and this process is called a correction scheme. The numerical relaxations transferring procedure in the multiple grid system reduces storage requirements and improves computational efficiency compared to direct solution methods.

There are different algorithms of combining the correction and restriction schemes, which differ in the effectiveness and the precision. MUDPACK solver uses a full multigrid W-cycle. A full multigrid, namely, FMG-W cycle is a nested iteration algorithm that uses coarse grids to obtain improved initial guess for fine-grid problems. Therefore, the solution at the coarsest level with initial guess will be restricted to an upper lever to provide the initial guess of relaxation at the level. Correction scheme will be followed back to the coarsest level. Relaxation will be done at the coarsest level with this corrected initial guess, and the solution will be restricted until two levels up this time for relaxation. This process will be applied until the finest grid is reached for the

relaxation. Figure 4.4 shows a schedule for the FMG-W scheme is drawn. In the figure, h denotes the size of the grid. More details on the full multigrid cycle and multigrid methods can be found in Briggs et al. (2000).

4.4.2 Adaptation for circular pore boundary

As explained in the previous section, a cubic grid is chosen for the finite-difference approximation. However, the cubic grid must be adapted to represent the circular cross-section boundary of the pore tube. Figure 4.5 shows the approximation of the pore boundary by nodes that lie right inside the cross-sectional circle, which comprise a jagged boundary enclosing the actual boundary when connected. For the boundary nodes, the grid spacing, h, should be adjusted so that the known values of thc fluid velocity, which are zero with no-slip condition, can be incorporated into the finite-difference equation. For example, for the boundary node A in Figure 4.5c:

$$\begin{aligned}&\frac{0-2\mathbf{v}_{i,j,k}+\mathbf{v}_{i-1,j,k}}{h_x^{\,2}}+\frac{0-2\mathbf{v}_{i,j,k}+\mathbf{v}_{i,j-1,k}}{h_y^{\,2}}+\frac{\mathbf{v}_{i,j,k+1}-2\mathbf{v}_{i,j,k}+\mathbf{v}_{i,j,k-1}}{h^2}\\&=\frac{1}{\mu}\left(0-\mathbf{f}_{i,j,k}\right)\end{aligned} \tag{4.30}$$

where h_x and h_y are the length in x and y-directions to the real boundary from the boundary nodes, as illustrated in Figure 4.5c. The boundary condition of the pressure equation on the circular boundary is that its gradient is zero, for the boundary node A,

$$\begin{aligned}&\frac{-p_{i,j,k}+p_{i-1,j,k}}{h_x^{\,2}}+\frac{-p_{i,j,k}+p_{i,j-1,k}}{h_y^{\,2}}+\frac{p_{i,j,k+1}-2p_{i,j,k}+p_{i,j,k-1}}{h^2}\\&=\frac{0-f_{x\,i-1,j,k}}{2h_x}+\frac{0-f_{y\,i,j-1,k}}{2h_y}+\frac{f_{z\,i,j,k+1}-f_{y\,i,j,k-1}}{2h_y}\end{aligned} \tag{4.31}$$

4.4.3 Particle motion

(1) Suspended particles

As explained in the previous section, suspended particles are assumed to settle at velocities according to Stoke law. Therefore, only a fraction of the complete particle velocity vector[7], $\mathbf{v}_f$, is deduced from the flow field. For a particle whose center is located at $\mathbf{x} = \mathbf{x}_p = (x_p, y_p, z_p)$, the fluid part of the velocity, $\mathbf{v}_f(\mathbf{x}_p)$ can be approximated from velocities of 8 neighboring points of the center:

$$\mathbf{v}_f = \sum_{i=1\sim 8} w_i \mathbf{v}_i \tag{4.32}$$

where w_i is a weight given as a descending function of the distance between the center of the particle and the node of index i at (x_i, y_i, z_i):

$$w_i = \left(1 - \frac{|x_i - x_p|}{dx}\right)\left(1 - \frac{|y_i - y_p|}{dy}\right)\left(1 - \frac{|z_i - z_p|}{dz}\right) \tag{4.33}$$

so that the sum of weights for all 8 nodes becomes 1. Finally, the total particle velocity is given as:

$$\mathbf{u}(\mathbf{x}_p) = \mathbf{v}_f + \mathbf{v}_s \tag{4.34}$$

The coordinate of the particle center, in turn, should be updated after a given time step, Δt, at time $t + \Delta t$:

$$\mathbf{x}_p(t + \Delta t) = \mathbf{x}_p(t) + \mathbf{v}(\mathbf{x}_p^k)\Delta t \tag{4.35}$$

(2) Collected particle

When a particle is collected either by the pore wall or by other collected particles, it becomes a collected particle, and no longer moves with the suspension. However, the

[7] The total particle velocity vector is $\mathbf{v}=\mathbf{v}_f+\mathbf{v}_s$

collected particle is assumed to keep moving under the influence of gravity until it finds a stable position resting on least three points of contact. Due to limitations in the time-steps, particle contacts can only be detected after partial overlap occurs between particles. At each time step, the positions of suspended particles are scanned to see if they have any overlap with deposited particles. Each particle is then characterized by the number of contact points.

The position of one-contact particles must be corrected to eliminate overlaps. This is done by moving the particle backward in the direction of its current velocity until it finds the point of apparent first contact. In mathematical form, when the current position of the particle is $\mathbf{x}_p$, and its velocity during the time step Δt, is $\mathbf{u}_p$, the corrected position of particle $\mathbf{x}_{corrected}$, will be found by computing the value α,

$$\mathbf{x}_{corrected} = \mathbf{x}_p + \alpha \mathbf{u}_p dt \tag{4.36}$$

that makes contact with a deposited particle located at $\mathbf{x}_d$:

$$\left|\mathbf{x}_{corrected} - \mathbf{x}_d\right| = r_p + r_d \tag{4.37}$$

where r_p is the particle radius, and r_d is that of the deposited particle. One-contact particles can move in gravity direction as long as do not penetrate the contacting particle. Once they move far enough from the contact, however, they can become suspended again until it finds more contacts.

A particle is considered as a two-contact particle either when it is found with two other overlapping particles, or there is a single overlap for a particle already in contact with one other particle. The position of a two-contact particle can be determined by putting all three particles in a plane (i.e. the corrected position $\mathbf{x}_{corrected}$ should be in the same plane with both contact particles, $\mathbf{x}_a$ and $\mathbf{x}_b$):

$$\mathbf{x}_{corrected} - \mathbf{x}_a = \beta(\mathbf{x}_b - \mathbf{x}_a) + \gamma \tag{4.38}$$

while it makes contacts with these particles with radii r_a and r_b, respectively:

$$\left|\mathbf{x}_{corrected} - \mathbf{x}_a\right| = r_p + r_a \tag{4.39a}$$

$$\left|\mathbf{x}_{corrected} - \mathbf{x}_b\right| = r_p + r_b \tag{4.39b}$$

When a particle is to have three contacting particles whose coordinates are $\mathbf{x}_a$, $\mathbf{x}_b$ and, $\mathbf{x}_c$ its position can be decided by making it satisfy three contact conditions:

$$\left|\mathbf{x}_{corrected} - \mathbf{x}_a\right| = r_p + r_a \tag{4.40a}$$

$$\left|\mathbf{x}_{corrected} - \mathbf{x}_b\right| = r_p + r_b \tag{4.40b}$$

$$\left|\mathbf{x}_{corrected} - \mathbf{x}_c\right| = r_p + r_c \tag{4.40c}$$

The simulator comprises three parts: 1) fluid motion, for which the MUDPACK (Adams, 1989) solver used adapted for circular pore boundary, 2) particle-fluid coupling and 3) particle motion[8].

4.5 VALIDATION OF PARTICLE-FLOW SIMULATOR

Validation of the particle-flow simulator can be achieved by considering the transport of a single spherical particle in a viscous fluid flow through an infinitely long circular tube. The geometry and coordinate system for this problem are defined in Figure 4.6. A spherical particle of radius, r_p, is located within the cylindrical pore of radius, R and positioned at an offset distance, b, from the axis of the pore. The governing equation of the fluid is the Stokes equation and the boundary conditions are no slip conditions on the wall of the tube and on the particle:

$$\mathbf{v} = 0 \text{ on } r = R \tag{4.41a}$$

[8] The Fortran source code for the particle simulator can be obtained by request to Professor Andrew J. Whittle at Massachusetts Institute of Technology (ajwhittl@mit.edu) or from the author (geoysk@alum.mit.edu).

$$\mathbf{v} = \mathbf{u} \text{ on } \left|\mathbf{x} - \mathbf{x}_p\right| = r_p \tag{4.41b}$$

where $\mathbf{x}_p$ is the coordinates of the center of the particle and $\mathbf{u}$ the particle velocity. As indicated in the figure, the flow is Poiseuille flow in the far-field when undisturbed by the particle:

$$\mathbf{v} = U_{flav}\left(1 - \frac{r^2}{R^2}\right)\mathbf{i}_z \text{ as } z = \pm\infty \tag{4.42}$$

where $\mathbf{i}_z$ is the unit direction vector for the z-axis that also makes up the centerline of the tube.

There is an approximate analytical solution for this boundary value problem by Haberman and Sayre (1958), whose procedures and results have been summarized in Happel and Brenner (1965). There are also numerical computations reported by Higdon and Muldowney (1995), and Wang and Parker (1998). The solutions are usually presented as the ratio of the magnitude of the drag force exerted by the particle, $\mathbf{F}_D$, to the Stokes drag force (i.e. the solution of the Stokes equation for a particle in an unlimited flow field), which is referred to as the wall correction factor and denoted as K_p:

$$K_p = \frac{\left|\mathbf{F}_D\right|}{6\pi\mu\, r_p \left|\mathbf{u}_r\right|} \tag{4.43}$$

where $\mathbf{u}_r$ is relative velocity between the fluid and the particle.

A model tube size R = 0.5 mm and L = 1 mm has been chosen for the validation exercise. A particle of specific density, G_s = 1.1 is considered suspended in water of viscosity μ = 1 centi poise. The far-field condition in equation 4.42 cannot be directly applied for this finite model tube. Instead, constant-pressure boundary conditions are applied to the ends of the numerical model with a finite length, L:

$$p = \Delta p = p_0 \text{ at } z = 0 \tag{4.44a}$$

$$p = 0 \text{ at } z = L \tag{4.44b}$$

where the value of the pressure p_0 should be decided during iterations to a value that gives an approximately constant volume flow rate result. A similar method was used for Higdon and Muldowney (1995).

4.5.1 Stationary particle on the axis of the cylindrical pore

The first validation example is the case of a stationary particle (i.e. $\mathbf{u} = 0$) located on the centerline of the cylindrical tube. The tube is discretized to 64×64×64 cubes, which results in mesh size $h = 0.015625 = 1/2^7$ mm. Then, for a particle size $r_p = 0.25$, the number of embedded nodes becomes 17,365. The iterative procedure in 4.3.3 is applied to obtain the fluid-particle coupling force, i.e., the drag force $\mathbf{F}_D$. For 300 iterations (with stiffness constant, $K = 1$), the resulting wall correction factors for five different ratios of particle radius to the tube radius, r_p/R ranging 0.1 to 0.5 are plotted in Figure 4.7. The numerical solutions are in excellent agreement with analytical solutions of Haberman and Sayre (1958). However, the accuracy does reduce for large ratios, $r_p/R \rightarrow 0.5$ where there is a 9% difference between numerical and analytical solutions.

4.5.2 A stationary particle contacting the wall

Next, the particle is moved off-axis and placed on the tube wall, (similar to initial collection conditions). The mesh size, stiffness and the number of iterations are the same as in the first case. For this asymmetric case, there are no analytical solutions. Figure 4.8 compares the current analyses with numerical simulations with reported Higdon and Muldowney (1995) using a boundary element method. The comparison shows a close match between two results with less the maximum error of less than 5.8 %.

4.6 MULTIPLE PARTICLE FLOW SIMULAITONS

For modeling filtration processes, multiple particles in suspension must be modeled. The simulation of particle-laden flows introduces a specific number of particles at the entrance at the beginning of given time-step.

Figures 4.9a, b and c present a sequence of 3-D snapshots of a model pore of the same size used in the previous validation problems. The particles injected have a uniform radius, $r_p = 0.05$mm. In the simulation, a random number generator produced a uniform distribution of input particles at the inlet at a rate of 10 particles per second. Other input parameters used are the same as those used in single particle simulations. Given grid size ($h = 1/2^7$mm) resulted in 147 nodes embedded in each particles. The motion of particles and fluid were updated at every time step, $\Delta t = 0.01$ seconds. The particles were tracked until they either passed through the tube or were collected. Whenever a new particle was collected, the iteration scheme presented in 4.3.3 was applied for all collected particles (including the newly collected particle) for 50 iteration steps to achieve a convergent fluid field.

The streamlines in Figure 4.9 clearly show that how the flow is subdued along the boundaries of the deposited particles and the fluid field becomes distorted from the initial Poiseuille flow.

Figure 4.10a and b show a second example using smaller particles with radius, $r_p = 0.025$mm, each approximated by 19 embedded nodes. The figures show snapshots at an earlier stage of the filtration (a) and at a more advanced stage (b), where most of the fluid finds its way out at the top part of the pore tube where it is not covered by the particles. Figures 4.9 and 4.10 show that the mound of collected particles is highest at the inlet of the pore, which was expected from the fact the driving force of the filtration is gravity. When the opening at the entrance is effectively covered by particles (Figure 4.9c), the pressure difference between the ends of the model pore starts to increase very rapidly, eventually reaching a point where the calculation has to be stopped (corresponding to full clogging of the pore).

Figure 4.11 shows the total drag force by collected particles obtained by equation 4.18 during these two simulations. The values of total drag force are given normalized by

that of single particle on the wall, F_{Ds}, that can be obtained through the same procedure given in Section 4.5.2. It is noticeable that the larger particles (r_p = 0.05mm) produce higher total drag force than smaller particles (r_p = 0.025mm). Drag force increases unconditionally after the number of deposited particles becomes more than 154, at which point the tube inlet is almost completely blocked as shown in Figure 4.9c. It is also interesting to see that drag force initially increases with a smaller increment than the single drag force (slope of the curves are less than 1). For the small particles, the slope of the curve keeps decreasing until around 194 particles are collected, (i.e. case shown in Figure 4.10b). This trend must be due to reduction in local fluid velocity around the deposited particles at the initial stage of particle collection. As collected particles accumulate, however, the average fluid velocity keeps increasing and the increased average fluid velocity will eventually negate these local reductions. This explains the reason for the total drag force rapidly increasing after 194 particles are collected. The two phases of decreasing and increasing slope are shown with the larger particles although the deflection point is not as clear as with the small particles.

The effect of increasing drag forces results in an increase in the pressure drop across the pore tube, Δp, as the deposits accumulate under the current constant-flow rate condition as explained in Section 4.3.4. Figure 4.12 shows the pressure drop, Δp, normalized by the initial value, Δp_0, plotted against the number of deposited particles. As the drag force initially increases at a slow rate and then later accelerates, the pressure drop also increases non-linearly. The rate of pressure change is much higher for the larger particles, as they are more effective in blocking the flow.

During multiple-particle simulations, the collected particles were found to foster the filtration process and result in higher collection efficiency. This observation is presented in Figure 4.13 which shows the number of collected particles as a function of the number of injected particles obtained in simulations with and without particle-fluid coupling. Without particle-fluid coupling, flow remains Poiseuille regardless of the deposited particles. In this figure, it is clear that the simulation results with coupling forces produce more collected particles for the same number of injected particles than for Poiseuille flow (i.e. without coupling forces), for both small and large particles. This must be caused by the reduced fluid velocities above the filtered deposit layer of particles,

effectively increasing the duration of the particle retained in the pore tube. Detailed discussion on conditions affecting the deposition process inside pore is given in Chapter 5.

The reason that larger particles collected faster than smaller particles is due to higher settling velocity (v_s / U_{flav} = 0.54, 0.14 for r_p/R = 0.05 and 0.025 respectively). Extended study on the rate of particle collection (collection efficiency) as well as pressure drop change due to collected particles is presented in Chapter 5.

4.7 CONCLUSIONS

This chapter has presented a new numerical simulator for modeling particle-laden flow in a cylindrical model pore. Using a fine cubical mesh, the simulator can track multiple particles separated from the suspension and settling out due to gravity, while it solves the discretized Stokes equation with a multi-grid solver, MUDPACK. The drag forces exchanged between collected particles and the suspension are evaluated through an iterative scheme that uses relative velocity between nodes encompassed by the particle (embedded nodes) and the fluid as residual. The simulator was validated with a problem with known analytical solution. Then it was applied for multiple-particle case, whose results have showed the effect of deposited particles on fluid. The simulator provides a tool to study the filtration process, which can incorporate effects of previously collected particles (particle modeling), a key part of the physics that has not previously been studied in detail.

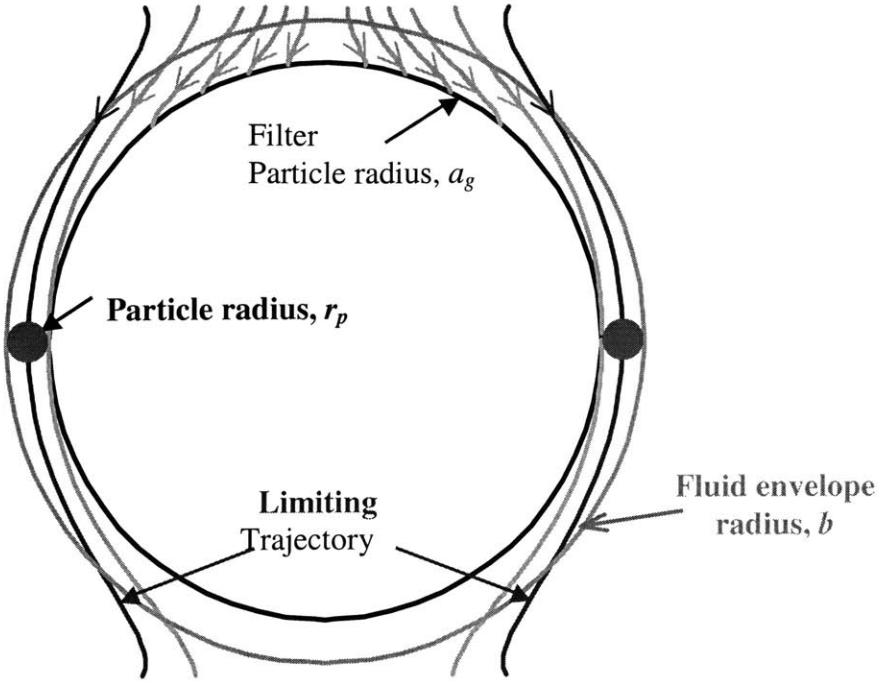

Figure 4.1 Sketch of the Happel's model and the limiting trajectory

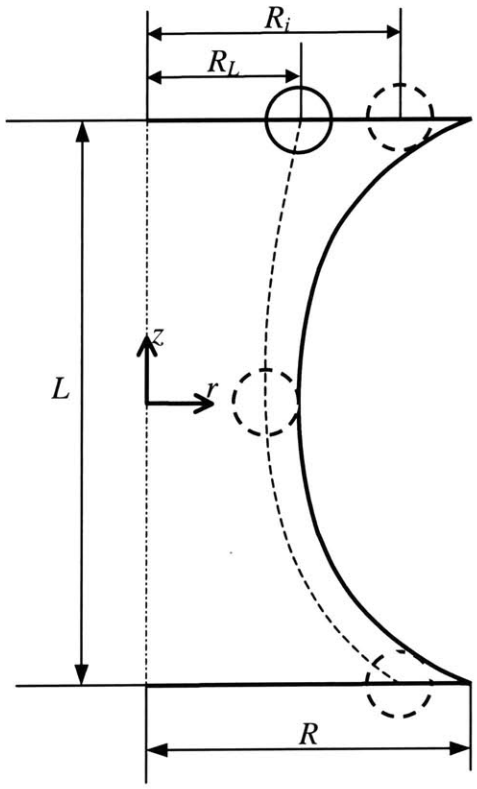

Figure 4.2 A schematic representation of a constricted tube and limiting trajectory

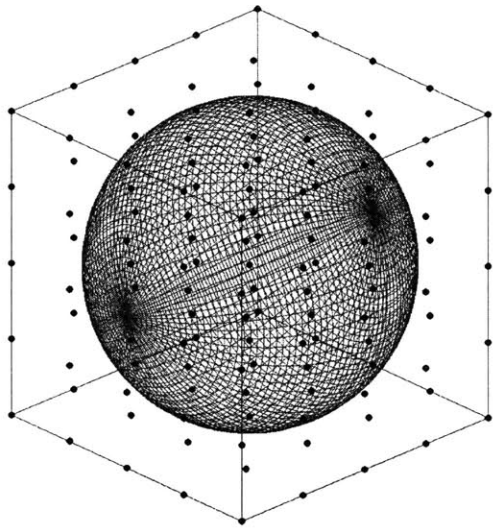

Figure 4.3 A particle in a grid system and embedded nodes

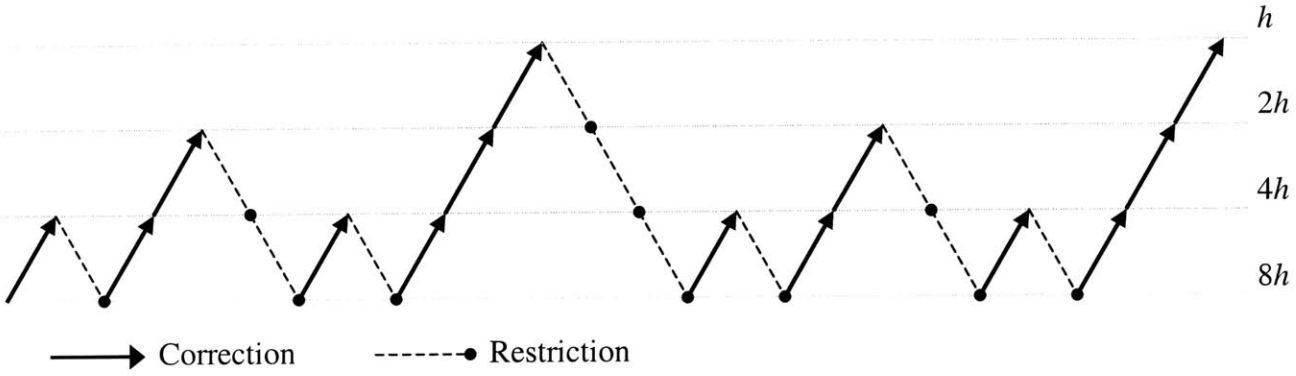

Figure 4.4 Schedule of grids for the full multigrid W-cycle used in MUDPACK

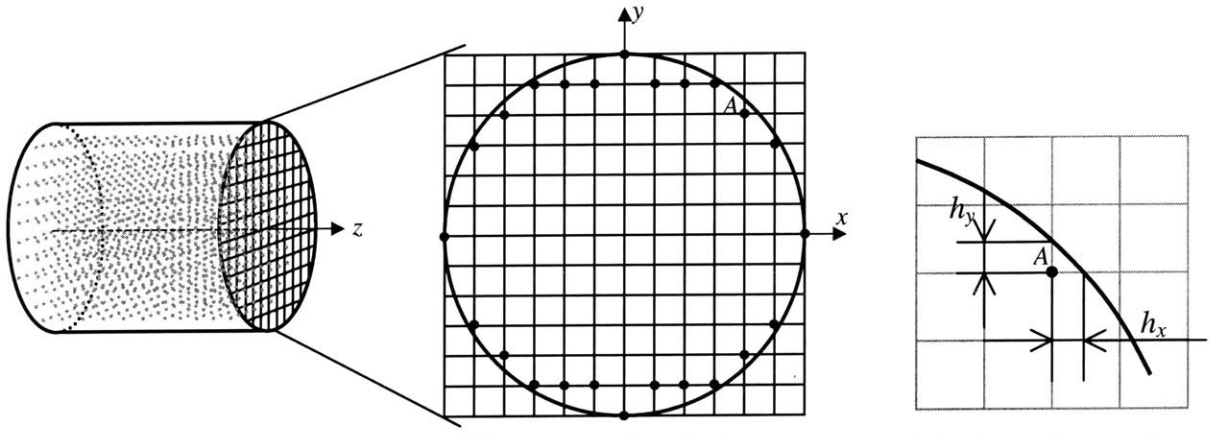

(a) all nodes (b) cross-sectional view (c) a boundary node

Figure 4.5 Approximated circular boundary in rectangular grid system

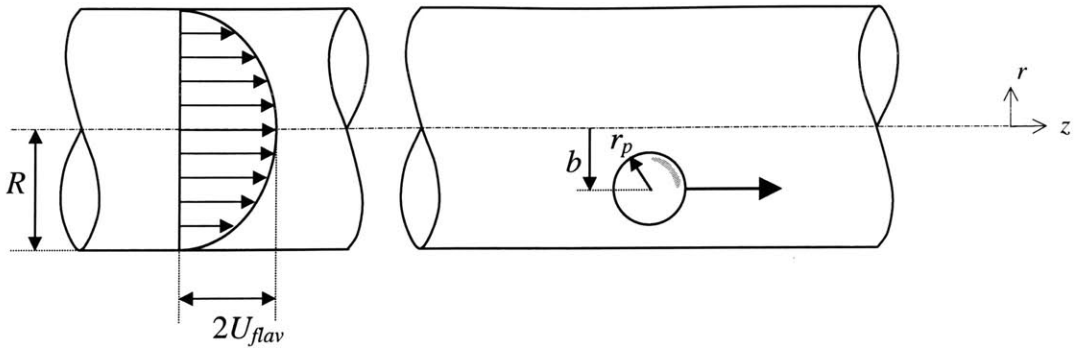

Figure 4.6 Validation problem configuration

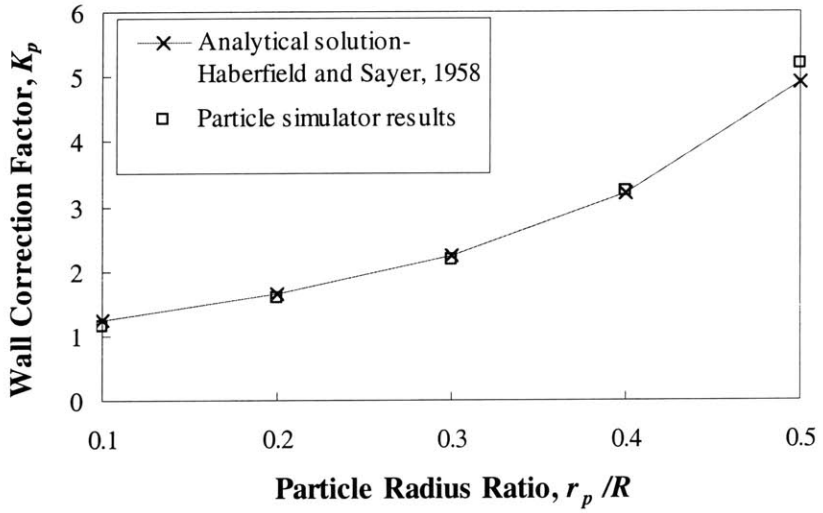

Figure 4.7 Wall correction factors for a stationary particle at the center of the tube

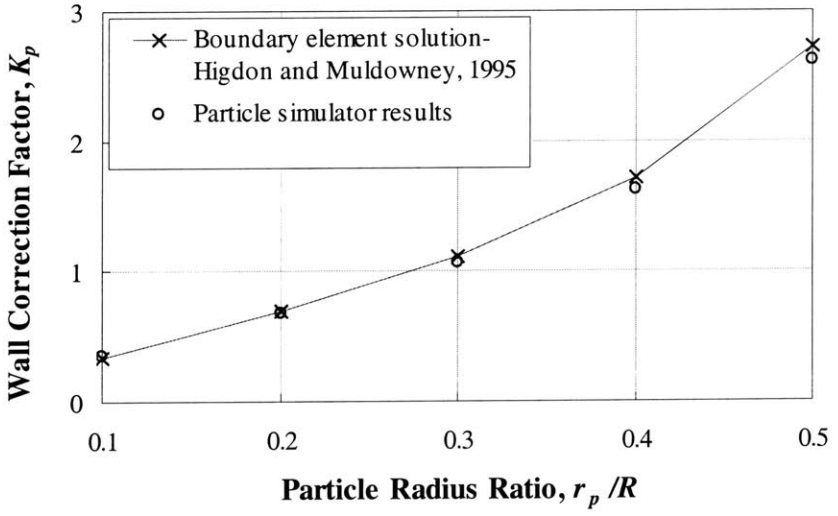

Figure 4.8 Wall correction factors for a stationary particle contacting the tube wall

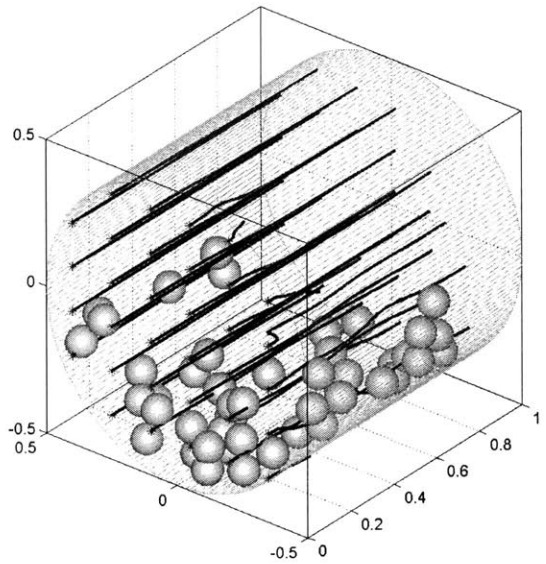

(a) 45 particles collected

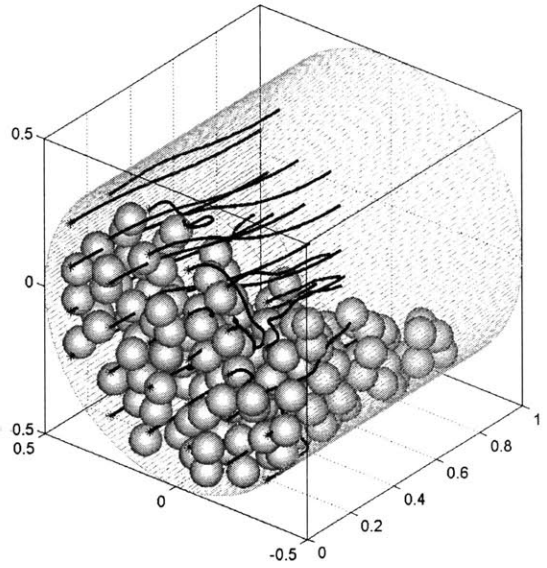

(b) 143 particles collected

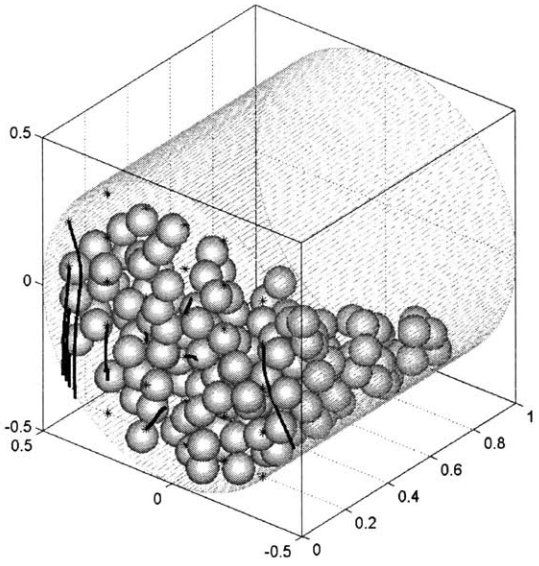

(d) 154 particles collected

Figure 4.9 Snapshot of pore tube during multiple particle simulation, $r_p = 0.05$ mm (dimension in mm)

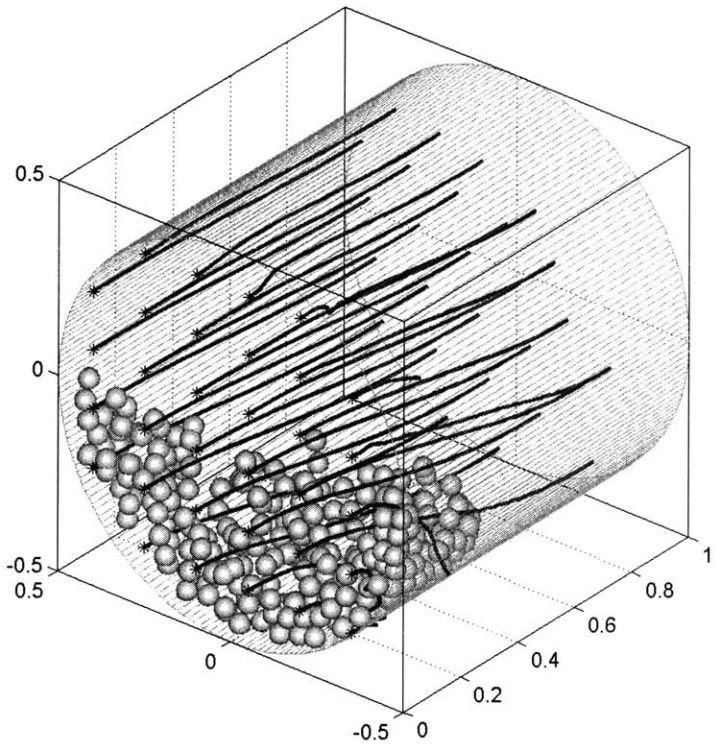

(a) 194 particles collected

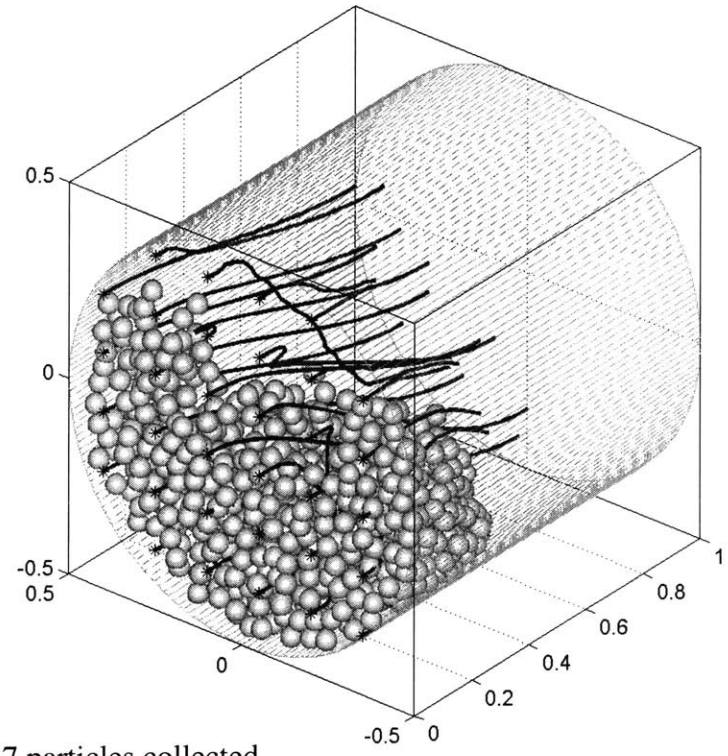

(b) 487 particles collected

Figure 4.10 Snapshot of pore tube during multiple particle simulation, $r_p = 0.025$ mm (dimension in mm)

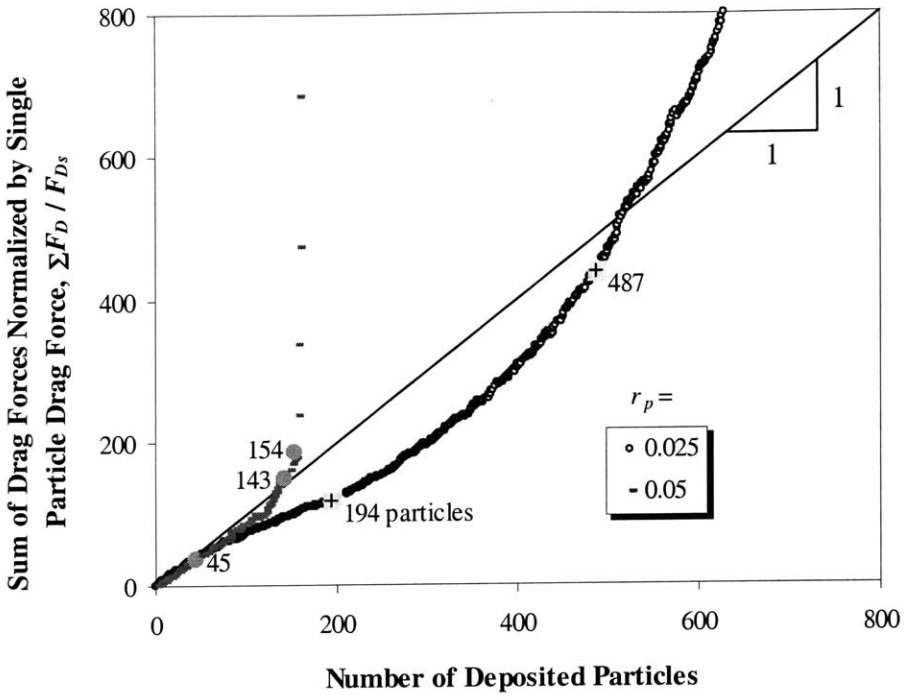

Figure 4.11 Total drag force increase with collected particles

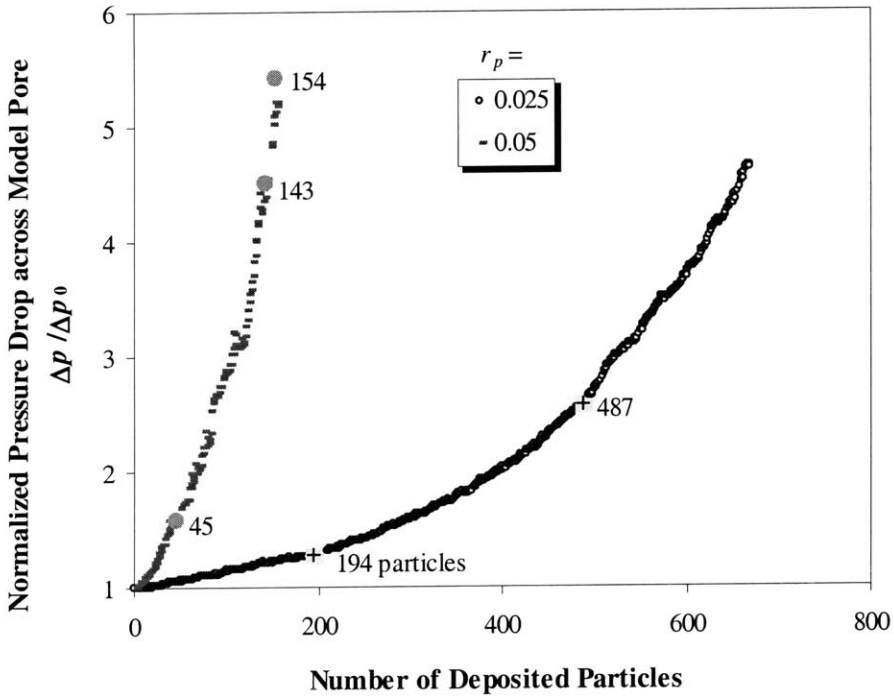

Figure 4.12 Pressure increase with collected particles

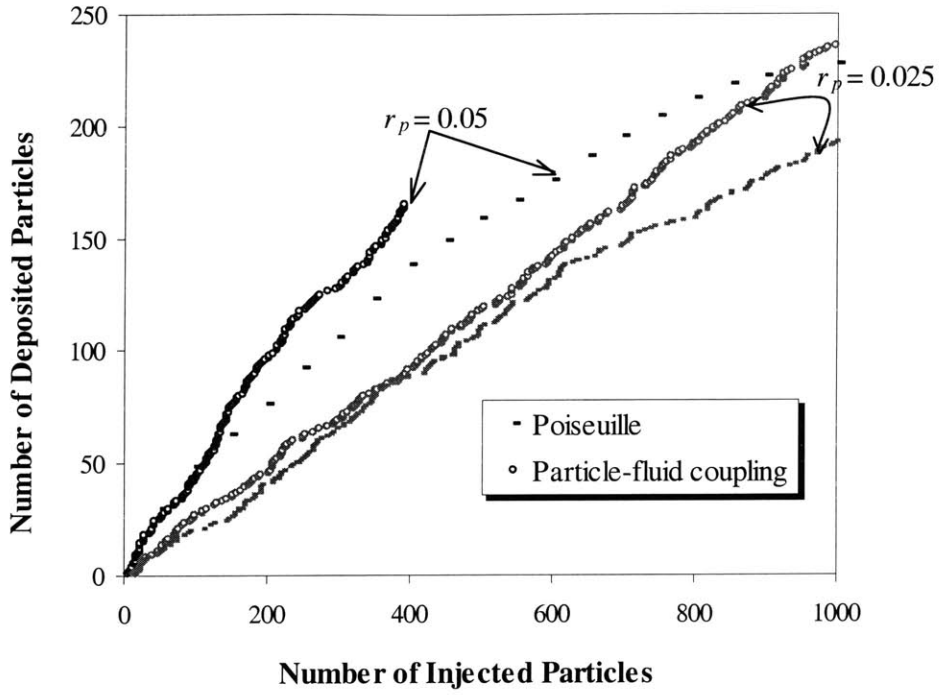

Figure 4.13 Effect of particle-fluid coupling on particle collection

CHAPTER 5. PARAMETRIC STUDY

5.0 INTRODUCTION AND KEY PARAMETERS

The previous chapters have proposed the use of network models to provide a method of scaling pore scale filtration processes to the macroscopic behavior. A key component of network models, such as the bubble model (Section 3.4), is the development of a particle flow simulator for the deposition of particles within a pore throat in the granular medium. Chapter 4 has presented details of the formulation for a particle flow simulator in a cylindrical model pore. This chapter describes results of parametric analyses that have been performed using this simulator. The particle flow simulator represents the deposition of particles on the wall of a model pore under the action of hydrodynamic and gravitational forces.

The calculations consider suspensions with mono-dispersed particles that are injected at constant flow rate. The model pore comprises a cylinder of diameter D, and length, L, and assumes a constant ratio, $L/D = 1$. A fixed number of particles of a chosen radius, r_p, are generated at the inlet of the pore tube at a random position[9]. Fluid motion is modeled by the Stokes equation so that the undisturbed flow (i.e. no deposit present) corresponds to Poiseuille conditions. Initially, the pore tube is considered oriented perpendicular to the gravitational field (i.e. maximizing effects of gravity on particle depositions). Subsequent calculations consider filtration for the tube inclined at a dip angle, θ, to the horizontal, as defined in Figure 5.1.

The settling velocity of the particles is determined by Stokes' law (equation 4.9). When a particle settles, it either becomes attached or can slide along the pore wall (i.e. with zero velocity normal to the pore wall), depending on a pre-defined attachment probability, A_p. The attachment probability, $A_p = 1$, corresponds to the case of full attachment where all particles that contact the pore wall become attached (i.e. are

[9] i.e. sequence of random numbers used changes at every realization

deposited or collected). The notion of attachment probability and its effect on the filtration process will be later explained in detail in Section 5.5. The ratio of attached to injected particles defines the efficiency of the pore for collecting suspended particles, η (same notations as in deep bed filtration theories presented in Chapter 3). As the deposit accumulates, some of the incoming particles will be blocked by previously deposited particles. The ratio of these 'rejected particles' divided to the total number of injected particles is defined as the rejection efficiency, η_{reject}.

The extent of the deposit accumulation can be characterized by the volumetric ratio of the deposited particles to the pore volume, V_d. Alternatively, the maximum depth of the deposit, $d_{\max}$, can be used to characterize the effect of the deposited particles on the remaining flow in the pore.

Table 5.1 summarizes the parameters selected for the base case calculations. The pore tube has diameter D = 1mm (= L). The pore walls are considered to have full attachment condition, (A_p = 1). The suspension has a viscosity 3 times higher than that of water and a density, ρ/ρ_w = 1.2. These values represent the typical conditions for permeation grouting, using microfine cements (with water-cement ratio, W/C = 3). For a suspension of this density, containing 25μm spherical particles of density ρ/ρ_w = 3 (typical cementitious grout), the number of particles in one pore volume (0.785mm^3), $N \cong 1000$.

Particle injection rate was fixed at 10 particles per pore volume for all simulations. This is equivalent to only 1% of the total number of particles from the suspension. The injection rate does not affect the result unless particles are very concentrated and interfere with each other while suspended. The effect of this interference will be discussed in Chapter 7.

The flow rate introduced to pore tube volume is set to 0.785 mm^3/sec (equivalent to 1 pore volume/sec) such that the average flow velocity, U_{flav} = 1.0mm/sec. For a characteristic length, 1mm, this velocity gives a Reynolds number, Re = 0.5, which is within the range of creeping flow for which Stokes equation is applicable. Numerical simulations are done with a time step, Δt = 0.01 sec. Whenever a particle is collected on the pore wall, the iteration scheme explained in Section 4.3.3, is applied to update the coupling forces between collected particles and the suspension. The number of iterations

is set at 50, which is found to be sufficient to achieve numerical accuracy in the validation trials of the simulator. The simulation with total of 1000 particles injected is equivalent to 100,000 time steps.

5.1 COLLECTION EFFICIENCY, η

5.1.1 Effect of settling velocity, v_s

For the full attachment condition (A_p = 1), the collection efficiency can be estimated from simple considerations of the particle trajectory. If the settling velocity of a particle is v_s, the maximum gravitational fall during its transit through the pore is:

$$\Delta z_{max} = v_s \, t_{travel} \tag{5.1}$$

where t_{travel} is the time needed for the particle to travel through the pore tube (unless it is deposited on the pore wall). If Δz_{max} is smaller than the distance between the initial position of the particle and the bottom of the deposit, d, the particle will be deposited and collected. Therefore, the collection efficiency can be defined as

$$\eta = P\,[d \le \Delta z_{max}] \tag{5.2}$$

where $P\,[d \le \Delta z_{max}]$ denotes the probability injected particle at an initial position at which d is smaller than Δz_{max}.

As particles are distributed uniformly distributed at the inlet, this probability is just the area where $d \le \Delta z_{max}$, divided by the total entry area, A_t, for the suspended particles:

$$\eta = \frac{A(d \le \Delta z_{max})}{A_t} \tag{5.3}$$

For a clean pore, $A_t = A_{t0}$, where A_{t0} is given by:

$$A_{t0} = \pi(R - r_p)^2 \tag{5.4}$$

However, once deposits begin to form part of the cross-section becomes blocked such that:

$$A_t = A_{t0} - A_{deposit} \tag{5.5}$$

The blocked cross sectional area at the inlet by the deposit, $A_{deposit}$, is likely to be a function of the maximum depth of the deposit, $d_{\max}$.

In conclusion, the collection efficiency of the pore tube can then be written in the following functional form:

$$\eta = \eta\,(v_s, t_{travel}, R, r_p, d_{\max}) \tag{5.6}$$

Among these parameters, the travel time, t_{travel} is the hardest to predict because it varies depending on the trajectories of the particles, and is strongly affected by the local fluid field around the deposits. Therefore, it is highly unlikely that an analytical expression can be found for the collection efficiency.

A series of simulations were carried out in order to establish principal factors affecting the collection efficiency. A series of 16 simulations were performed using particles of radius r_p/R = 0.04, with random uniformly distributed locations of injected particles at the pore inlet. The results of the simulations are summarized in Figure 5.2a. This figure shows that the deposited particle volume is proportional to the number of particles injected, V_d/V_{in} = 0.58 with regression coefficient R^2 = 0.9951. This result implies that the collection efficiency of the pore remains constant throughout the simulation. Among the parameters listed in equation 5.6 (i.e. v_s, t_{travel}, R, r_p, $d_{\max}$), R and r_p were fixed in these simulations. The travel time, t_{travel} and $d_{\max}$ change according to changes in the flow field, due to particle deposition (although change in t_{travel} must be

much smaller than those for d_{max}). Therefore, it is most likely that the settling velocity, v_s is the principal factor controlling the collection efficiency at a given radius ratio, r_p /R. Figure 5.2b shows similar sets of (sixteen) simulations for the different specified values of v_s /U_{flav} = 0.60, 0.12 and 0.03. All three cases show higher rates of particle accumulations. As anticipated, the higher settling velocity causes more deposition of particles in a given timeframe.

When the settling velocity is increased further to v_s/U_{flav} = 1.21, 3.02, there is a marked retardation in the deposition rate with time as shown in Figure 5.3a. It is clear from this figure that the collection efficiency of the pore decreases as the deposit builds up at higher settling velocity. This effect can be explained by a corresponding increase in the rejection efficiency, η_{reject}, as v_s/U_{flav} increases. Therefore, the reduced rate of deposit observed in Figure 5.3a may be caused by the reduced number of particles that actually pass into the pore. This effect can be isolated by modeling a constant number of particles passing into the pore volume (i.e. by constraining the input positions to prevent particle rejection at the inlet). Figure 5.3b compares this 'no-rejection' injection method for v_s /U_{flav} = 3.02, with the unconstrained injection results (from Figure 5.3a). This figure confirms proportionality between injected and collected particles. This refined injection method defines the collection efficiency, η, at higher settling velocities, (v_s/U_{flav} = 1.21 and 3.02).

At slow settling velocities, the rate of particle accumulation increase as the process advances. This phenomenon of improvement in filtrate quality and decreasing effluent concentration is often referred as 'ripening' in DBF theories. Figure 5.4 shows two of these cases, when v_s/U_{flav} = 0.01 and 0.005. Ripening seems to occur as the slower settling particles require a longer time to reach the pore wall. As they are retained inside the pore longer, the population of suspended particles increases with time and hence, the increase in the accumulation rate. Among the ten different values of settling velocities used in the simulations (see Table 5.2), ripening was noticed prominently in the case with the five lowest settling velocities (v_s /U_{flav} < 0.12). However, all the results can be approximated by linear regression curves (i.e. constant η) with good correlation (the worst case with v_s/U_{flav} = 0.005 produces R^2 = 0.6855). Thus, the linear regression curves

were used to define collection efficiencies for the full range of settling velocities used in the simulations.

Figure 5.5 summarizes the collection efficiency, as a function of the settling velocity for the simulations with r_p/R = 0.04 (note that the horizontal axis is in logarithmic scale). In this figure, values represented by circles are obtained by regressions of the entire data of all 16 simulations. The minimum and maximum of these values are obtained through separate regressions on each of the simulations and drawn in the same figure to show the ranges of simulated collection efficiencies.

5.1.2 Effect of particle size

Figure 5.6 presents results of deposit/collection rates for larger injected particles with, r_p/R = 0.1(all other parameters are held constant, Table 5.1). There is a larger rejection rate in these simulations (i.e. larger blockage effects at the inlet) and hence, the constrained rejection is used throughout (i.e. to avoid spurious results due to particle rejection) for all settling velocities reported in the figure for each settling velocity, v_s/U_{flav} . Figure 5.6 shows a well-defined time limit before the pore inlet becomes clogged. The results show that the final clogging time increases with the settling velocity. Prior to clogging, there is almost a linear rate of particle deposition, confirming previous results showing constant collection efficiency, η for a given settling velocity.

Comparison of simulation results obtained with various particle sizes show that the collection efficiency at a given settling velocity, v_s, is largely independent of the particle size (see values of η in Table 5.2). This is highlighted in Figure 5.7, where results of three sets of sixteen simulations, each with three different particle sizes r_p/R = 0.04, 0.06 and 0.1 are overlaid for the same settling velocity, v_s/U_{flav} = 0.60. Values of collection efficiencies from linear regression for simulations with six different size groups are plotted against the settling velocities in a log-log scale as in Figure 5.8. This figure includes results from 56 combinations of r_p/R and v_s/U_{flav}, producing 896 simulations (sixteen simulations per case). The values of η and the corresponding R^2 values are shown in the Table 5.2. The results from different sized particles overlap

almost completely in this figure, suggesting that the particle size, r_p, only affects collection efficiency indirectly through the settling velocity.

5.1.3 Effect of travel time, t_{travel}

Travel time (t_{travel}) is certainly a factor that should affect collection efficiency. In order to quantify this effect, simulations have been performed with different lengths of pores. Figure 5.9 shows the accumulation of deposits for model pores length-diameter aspect ratios, L/D = 0.5, 2.0, and 4.0. The particle size used in these analyses, r_p/R = 0.06, and the settling velocity, v_s/U_{flav} = 0.06. It is clear that the collection efficiency increases with increase in the aspect ratios of the pores.

Figure 5.10a summarizes collection efficiencies from these simulations at settling velocities ranging from v_s/U_{flav} = 0.06 to 0.60. (each data point in this plot represents the average from a set of sixteen simulations). Figure 5.10b normalizes the collection efficiency relative to the reference collection efficiency η_1, obtained at L/D = 1 shown in Figure 5.8. These normalized efficiencies η/η_1 form a unique correlation with L/D independent of settling velocity v_s/U_{flav}, except at the highest settling velocity, v_s/U_{flav} = 0.60. The latter reach full efficiency η = 1 at L/D >2 (Figure 5.10b) and hence, reach a maximum ratio η/η_1 = 1.4 at L/D = 2. Figure 5.11 compiles the normalized collection efficiency values from simulations with various particle sizes, r_p/R = 0.05, 0.06, and 0.12 at constant settling velocity, v_s/U_{flav} = 0.06 and pore lengths, L/D = 0.5, 0.8, 1.0, 1.5, 2.0, 3.0 and 4.0. These results confirm a direct correlation of efficiency with travel time.

5.1.4 Correlation for collection efficiency

The complied simulation data in Figure 5.8 can be characterized by the following correlation equation for the collection efficiency at L/D = 1:

$$\eta_1 = \min\left[0.75\left(\frac{v_s}{U_{flav}}\right)^{0.49}, 0.9\right] \tag{5.7}$$

where the settling velocity is a function of the particle size, $v_s(r_p)$, according to equation 4.10.

The data shown in Figures 5.10 and 5.11 can be fitted by a power law function of the pore aspect ratio, *L/D*:

$$\eta = \eta_1 \left(L/D\right)^{0.57} \tag{5.8a}$$

with regression coefficient $R^2 = 0.9509$. Hence, overall we find:

$$\eta = 0.75\left(\frac{v_s}{U_{flav}}\right)^{0.49}\left(\frac{L}{D}\right)^{0.57} \quad \text{for } 0< \eta <0.9 \tag{5.8b}$$

5.1.5 Effect of gravitational field

In the preceding sections, the model pore had its axis perpendicular to the gravity. Since the driving force for particles to separate from the suspension is gravity, the pore orientation must also influence the filtration efficiency. Three sets of simulations have been performed to evaluate particle collection at $\theta = 0°$ (horizontal), 40° and 80°, using a reference particle size, $r_p/R = 0.06$, and settling velocity, $v_s/U_{flav} = 1.21$. Figure 5.12 shows the volume of accumulated deposits against the input particle volume, (both volumes being normalized by the pore volumes as in previous figures). The results show that the collection efficiency decreases with increasing dip angle as the pore becomes more aligned the gravitational field. At a given dip angle, one component of the gravitational force with ($\mathbf{g}\cos\theta$) acts to cause particle deposition while the other ($\mathbf{g}\sin\theta$) reduces the travel time.

Figure 5.13 shows simulated trends in collection efficiency, η as a function of dip angle, θ for $r_p/R = 0.06$ and $r_p/R = 0.1$ (each of these data points was obtained as the average of 16 simulations at $v_s/U_{flav} = 1.21$). Figure 5.14 shows a plot of collection efficiency normalized to the horizontal reference case, η_0, at ($\theta = 0°$) for the cases presented in Figure 5.13. These data support a single correlation for the normalized

collection efficiency values with the dip angle θ °, which can be well represented by a quadratic equation shown in the Figure 5.14:

$$F(\theta) = M_0 - M_1\theta - M_2\theta^2 \tag{5.9}$$

where $M_0 = 1.0$, $M_1 = 2.8\times10^{-3}$, $M_2 = 9.2\times10^{-5}$ when θ is given in degrees.

Using this equation, the average value of the normalized efficiency is evaluated:

$$\eta_H = \frac{\int_{\theta=0}^{90^\circ} F(\theta)d\theta}{90^\circ}\ ^{10} \tag{5.10}$$

which gives the resulting average value of efficiency,

$$\eta_H = \frac{\eta}{1.6} = 0.625\eta_{(\theta=0^\circ)} \tag{5.11}$$

This average value, η_H, can be used as a representative value of collector efficiency for porous media with homogeneous pore orientation, replacing η in equation 5.8.

5.2 PRESSURE CHANGE ACROSS MODEL PORE

5.2.1 Significance of the pressure change

The consequence of particle deposition in the pore is a change in the flow field (i.e. the newly imposed stationary boundary conditions on the deposited particles will result in overall changes in the suspension flow). Changes in the flow field generate an increase in the pressure difference between the ends of the model pore to achieve the condition of constant flow rate. The pressure boundary condition is updated for each particle deposited (to compensate for the corresponding reduction in flow). Full details of

[10] It was found that the sign of the dip angle had minimal effect and hence, the range was limited to $0\ ^\circ \le \theta \le 90\ ^\circ$. More details are given in Section 5.3.5.

solution procedure including the iteration scheme to evaluate pressure changes were given in Chapter 4.

In Section 3.5, Imdakm and Sahimi (1990)'s method of estimating the pressure change by collected particles, through reduction in pore radius, R, was explained. As noted there, the key assumptions of the method are a) flow remains Poiseuille and b) drag force exerted by a collected particle can be estimated by Goldman et al. (1967)'s solution (equation 2.30a) with approximated wall shear stress, τ_w.

In contrast to this approximate procedure, the current particle simulator computes pressure changes and drag forces directly from numerical simulations enabling the relationships to be found through numerical calculations. Figure 5.15a shows the pressure development across the pore tube as a function of the total drag force exerted by the deposited particles. The results corresponded to a set of sixteen simulations with particle size (r_p/R = 0.06 and 0.10) and settling velocity v_s/U_{flav} = 0.60. The relationship between the total drag force ΣF_D and the normalized pressure drop $\Delta p/\Delta p_0$, appears to be unique, and independent of the particle size. Therefore, the pressure drop is most appropriately characterized using the computed drag forces directly.

Equation 3.22 has been used to generate an artificial set of pressures based on the computed drag forces from the numerical simulations shown in this figure so as to compare the numerical simulations with approach used by Imdakm and Sahimi (1990). The values of flow rate, Q, and fluid viscosity, μ were the same as used in numerical simulations. The results presented in Figure 5.15b show that equation 3.22 generates much higher values of pressure at a given drag force then use computed from the numerical analyses. Therefore, employing equations 3.21 and 3.22 will result in significant overestimation of the pressure drop caused by deposition.

5.2.2 The maximum mound height, h_{max} and deposit depth, d_{max}

Figure 5.16 shows numerical simulations of the pressure drop across the model pore as functions of the normalized deposit volume, V_d for three different particle sizes, r_p/R = 0.05, 0.09 and 0.12. It is apparent that the deposit volume is not the only parameter controlling pressure changes. This dependency on particle size indicates

structural difference of deposits formed with different sized particles. Small particles form a deposit, which is more effective in blocking the pore than the same volume of deposits with larger particles, and also induce higher pore pressure change across the model pore tube.

Therefore, the deposit volume does not provide an adequate representation of the sum of the forces. The force acting on a suspended particle (if all other fluid characteristics are unchanged) depends only on the fluid velocity surrounding the particle. In the pore model simulations, changes in the fluid velocities are best represented by the cross-sectional area covered by the deposit. Following this reasoning, a new parameter the maximum deposit depth, d_{max}, has been selected. The deposit depth is measured as the distance between the tops of a deposited mound of particles to the pore wall directly beneath it, Figure 5.17, (i.e. in the same cross-section). The pressure drop data from the Figure 5.16 have been plotted against the maximum deposit depth, d_{max} in Figure 5.18. These results show improved correlations effectively reducing the dependence of the pressure drop on particle size. However, it is still apparent that deposits with specified d_{max} generate higher pressure drop for smaller size particles. This trend is particularly noticeable at later stages of filtration (i.e. high values of d_{max}/D). A second parameter, referred to as the maximum mound height, h_{max}, was also been considered. Mound height, h, relative to the central base axis is defined as the vertical coordinate of the top of a particle mound of the tube in Figure 5.17. Due to the difference in the reference datum, the maximum height of the deposit will be the height of a particle located at the highest point in the tube whereas the maximum depth of the deposit will be the depth of a particle that is farthest from the bottom pore wall. To illustrate the difference between h_{max} and d_{max}, a typical pore tube with deposited particles are shown in Figure 5.19, (this shows an axial view of 155 deposited particles). The particle marked as p_1 in this figure, is characterized by $h_{max}/D = 0.84$, while particle p_2 controls the depth, $d_{max}/D = 0.8$. Comparing these two particles, p_1 is in a position to induce more drag force (i.e. larger impact on pressure change), than p_2. This is because the fluid that will be replaced by p_1 has higher velocity. For this reason, h_{max} is expected to work better as a variable to parameterize the pressure drop when the mound covers more than half the depth of the pore tube.

This expectation is proven when the same pressure drop data (from Figure 5.16) are re-plotted against their corresponding h_{max} values in Figure 5.20, showing improved correlation for all particle sizes compared to d_{max} in Figure 5.18.

Finally, two different correlation equations are proposed to characterize the pressure drop, one as a function of the deposit depth d_{max}, and the other for maximum mound height, h_{max} as shown in Figures 5.21a, b

$$\frac{\Delta p}{\Delta p_0} = 7.0\left(\frac{d_{max}}{D}\right)^3 + 1.5\left(\frac{d_{max}}{D}\right)^2 + 1 \quad \text{for } d_{max}/D < 0.5 \tag{5.12a}$$

$$\frac{\Delta p}{\Delta p_0} = 15\left(\frac{h_{max}}{D}\right)^3 - 6.0\left(\frac{h_{max}}{D}\right)^2 + 1 \quad \text{for } d_{max}/D \geq 0.5 \tag{5.12b}$$

In order to get this correlation, sixteen different particle sizes ranging from $r_p/R = 0.04$ to 0.12 was used. Twenty base case simulations were done per each size with corresponding Stokes velocity ($v_s/U_{flav} = 0.005$-3.02).

5.3 MOUND HEIGHT, h_{max} AND MAXIMUM DEPOSIT DEPTH, d_{max}

5.3.1 Correlation for β, the increase rate

Figures 5.22a, b show the maximum mound height as a function of normalized deposit volume, V_d, for cases with a) $r_p/R = 0.05$ and $v_s/U_{flav} = 0.03$; and b) $r_p/R = 0.11$ and $v_s/U_{flav} = 1.00$. The data were obtained from sixteen base-case simulations. These figures show that there are two distinct regions of behavior: The initial phase involves a rapid mounding of particles in a relatively loose structure, while at later stages there is greater coordination number (contact point per particle). The results have been fitted using a bi-linear function between h_{max}/D and V_d.

$$h_{max}/D < 0.45: \; h_{max}/D = 2r_p/D + \alpha V_d \tag{5.13a}$$

$$h_{max} / D \geq 0.45: \; h_{max} / D = h_0 / D + \beta V_d \tag{5.13b}$$

where α, β are defined in Figure 5.22a. The constants α, β are equal at $h_{max}/D = 0.45$:

$$\alpha = \beta \frac{(0.45 - 2r_p / D)}{(0.45 - h_0 / D)} \tag{5.14}$$

Figure 5.23 shows similar results for the maximum deposit depth, d_{max}, from simulations with two particle sizes (r_p/R = 0.05, 0.11) and v_s/U_{flav} = 3.02. In this case, it is more difficult to identify the initial phase of deposition, while the later phase can be described by the new relation:

$$d_{max} / D = d_0 / D + \beta V_d \tag{5.15}$$

The parameter β is practically identical using either the mound height, h_{max}, or deposit depth, d_{max}.

A series of simulations have been performed at different settling velocities and particle sizes to characterize the parameter, β. Table 5.3 summarizes the linear regressions from sets of 16 simulations for each combination of r_p/R and v_s/U_{flav} (This corresponds to 108 separate cases and a total of 1728 simulations). The correlation coefficients range from R^2 = 0.6-0.9.

Figure 5.24a summarizes β values for smaller particle sizes, r_p/R = 0.04, 0.05, 0.06, and 0.07 as function of the specified settling velocity. The figure also shows the settling velocity expected for each particle size according to Stokes equation. The results show β increasing with settling velocity in the range v_s/U_{flav} = 1.00-3.02. At small settling velocities v_s/U_{flav}<1, β is either constant or exhibits a small increase as v_s/U_{flav} approaches 0 (depositions purely dependent on hydrodynamic forces). As a result, β parameter is at a maximum when the settling velocity is approximately equal to the average flow velocity. The slow increase in depth of the deposit implies low deposit porosity or a densely structured deposit. Thus, the occurrence of a minimum β value (at a

certain settling velocity) implies that the velocity is at an optimum condition for forming a dense deposit. For larger particles (r_p/R = 0.08-0.12) optimal density is achieved for $v_s/U_{flav} \leq 1.0$. This result is also physically reasonable as there is limit on the density of packing for larger particles. For this reason, two different bi-linear correlation equations are used for β depending on the particle size:

$$r_p/R < 0.08$$

$$\beta = -1.16\left(\frac{v_s}{U_{flav}} - 1\right) + 3.90 \text{ for } \frac{v_s}{U_{flav}} < 1 \tag{5.16a}$$

$$\beta = 1.70\left(\frac{v_s}{U_{flav}} - 1\right) + 3.90 \text{ for } \frac{v_s}{U_{flav}} \geq 1 \tag{5.16b}$$

$$r_p / R \geq 0.08$$

$$\beta = 3.60 \text{ for } \frac{v_s}{U_{flav}} < 1 \tag{5.17a}$$

$$\beta = 1.70\left(\frac{v_s}{U_{flav}} - 1\right) + 3.60 \text{ for } \frac{v_s}{U_{flav}} \geq 1 \tag{5.17b}$$

5.3.2 Correlation for h_0 and d_0

The parameter, h_0, introduced in the regression equation 5.13b, is the intercept at zero deposit volume for estimating the mound height, h_{max}. Naturally, its value should be affected by the size of particles. Values of h_0 are summarized in Table 5.3 are plotted in Figure 5.25a and b as functions of the settling velocity and particle size. It can be seen that h_0 is approximately constant for the range of settling velocities, v_s/U_{flav} = 0.03 –3.02 used in simulations. However, there is a clear dependency on the particle size, as presented in Figure 5.25b, which shows a well defined linear correlation based on average values of h_0/D :

$$h_0 / D = \max\left\{0.45 - 0.59\, r_p / R,\ 2r_p / D\right\} \tag{5.18}$$

with $R^2 = 0.9189$. Substituting this result into equation 5.14,

$$\alpha = \beta \max\left\{0.76\frac{R}{r_p} - 1.7, 2r_p / D\right\} \tag{5.19}$$

The intercept, d_0, for the maximum depth does not vary as much as h_0. An average value, $d_0/D = 0.15$, is suitable for the range of particle radii considered in the simulations.

Substituting equation 5.18 to equation 5.13b, the difference between h_{max} and d_{max} can be analytically given:

$$\frac{h_{max} - d_{max}}{D} = \max\left\{0.3 - 0.59\frac{r_p}{R}, \frac{r_p}{R} - 0.15\right\} \tag{5.20}$$

According to this equation, difference between h_{max} and d_{max} is larger for a smaller size of particle group than for a larger size group as expected, proving that the larger particles tend to form loose structures that result in higher mounds than for the same volume of small particles.

5.3.3 Effect of pore tube length

Pore length has previously been shown to affect collection efficiency, it should also influence the deposit depth. Figure 5.26 shows values of d_{max}/D plotted against the normalized volume of deposit V_d, for $r_p/R = 0.1$ and $v_s/U_{flav} = 0.06$ for three different pore aspect ratios, $L/D = 1.0$, 2.0 and 4.0. The results show that the rate of formation of deposit depth increases with pore aspect ratio. This means that the deposits in shorter pores tend to be spread more evenly than those in longer tubes, which is logical considering that the particles settle mainly in the vicinity of the inlet. The correlation between rate of deposit depth, β, and the pore aspect ratio is presented in Figure 5.27 based on the 68 simulation cases previously shown in Figure 5.11. It seems the relationship between β and L/D is very similar to that between the collection efficiency η

and L/D and has been fitted by similar power law functions with exponent 0.57 with $R^2 = 0.8977$:

$$\beta = \beta_1 (L/D)^{0.57} \tag{5.21a}$$

$$\alpha = \alpha_1 (L/D)^{0.57} \tag{5.21b}$$

where α_1 and β_1 are reference values of α and β value for $L/D = 1$.

5.3.4 Effect of pore dip angle

Figure 5.28 compares the volume of collected particles with dip angles: θ = 20° and -20°. The collection efficiency values for both cases are almost identical until later stages of filtration where the case with θ = -20° shows a reduced collection rate (η remains almost constant for θ = 20°). Figure 5.29, shows the deposit depths for the two sets of simulations. In both simulations, the same component of gravitational ($\mathbf{g}\cos\theta$) force promotes settling. However, the other component ($\mathbf{g}\sin\theta$) acts in the direction of flow at θ = 20° tube and opposes the flow for θ = -20°. The forces opposing the flow direction (θ = -20°) cause the particles to mound near the inlet, which result in faster increases in d_{max}. As expected, the β parameter is higher for dip angle θ = -20° than with θ = 20°. This result confirms that the sign of θ has little influence on the collection efficiency, but is an important factor affecting the deposit depth (and hence the pressure change).

Figure 5.30 summarizes computed values of the rate of deposit depth, β, from linear regressions of simulations with dip angles $-60° < \theta < 80°$ and various particle sizes (r_p/R = 0.06, 0.08, and 0.1) and settling velocities (v_s/U_{flav} = 0.06, 0.60 and 1.21). The total number of cases is 44. The resulting β values can be characterized by a quadratic function of the dip angle:

$$\frac{\beta}{\beta_0} = 1.5\times10^{-4}\ \theta^2 - 0.01\,\theta + 1 \tag{5.22}$$

The average of this correlation over the range of θ = -90° to 90° gives the equivalent β value when the pore orientation is uniformly distributed denoted with subscription H, β_H:

$$\beta_H = 1.4\beta \tag{5.23}$$

5.4 THE REJECTION EFFICIENCY, η_{reject}

5.4.1 Linear function of deposit volume

The preceding sections are all based on a constant rate of particle injection (as explained in Section 5.2). This approach ignores the particles that are rejected due to the deposit growing at the pore inlet. These 'rejected particles' are filtered through a different mechanism, and must be accounted for in the simulation for injection. The rate of rejection is characterized by the rejection efficiency, η_{reject}. Figure 5.31a shows the normalized volume of rejected particles, V_{reject} as a function of the normalized total volume of injected particles, V_{in}. The reference particle size in the case is r_p/R = 0.07 with a settling velocity, v_s/U_{flav} = 1.65, (and a total of 17 simulations). In contrast to the particles collected in the pore (c.f. Figure 5.2), the rejected particle volume increases non-linearly with the total volume of input particles. This occurs because the volume of rejected particles is controlled by the deposit volume. In other words, as the filtration advances, the accumulated deposit volume increases and particle rejection occurs more frequently at the inlet. Therefore, the rejection efficiency, η_{reject} is hypothesized to be a linearly increasing function of the normalized deposit volume, V_d:

$$\eta_{reject} = \gamma V_d \tag{5.24}$$

where γ is a constant.

The value of γ should be determined by fitting the simulation results. The number of particles input per given time step, ΔN_{in} is known. The rejection probability, η_{reject}, can

then be evaluated from the known value of collected particles, V_d. Then the fraction of input particles that will be rejected during the time step, ΔN_{reject} can be evaluated as:

$$\Delta N_{reject} = \eta_{reject}(V_d)\, \Delta N_{in} \tag{5.25}$$

Adding ΔN_{reject} values, the total number of rejected particles can be predicted

$$\overline{N}_{reject} = \sum \Delta N_{reject} \tag{5.26}$$

By comparing the simulated values of N_{reject} with this predicted value of $\overline{N}_{reject}$, the value of γ can be estimated.

Figure 5.31b superimposes values of $\overline{V}_{reject}$, which can be calculated from $\overline{N}_{reject}$, on top of the computed volume of rejected particles (Figure 5.34a). There is an excellent match between the computed results, confirming that the hypothesis for equation 5.24 is satisfactory.

Further comparisons have been made for all 123 cases, with r_p/R ranging from 0.04 to 0.12 and v_s/U_{flav} ranging from 0.006 to 3.02. The resulting γ values are plotted in Figure 5.32. Each point in the plot represents the result of regressions for sixteen different simulations. The solid black line in the same figure shows the selected correlation equation of γ to the settling velocity, v_s/U_{flav}:

$$\gamma = -1.3\left(\frac{v_s}{U_{flav}} - 1.0\right) + 6.7, \quad \frac{v_s}{U_{flav}} < 1.0 \tag{5.27a}$$

$$\gamma = 2.7\left(\frac{v_s}{U_{flav}} - 1.0\right) + 6.7, \quad \frac{v_s}{U_{flav}} \geq 1.0 \tag{5.27b}$$

5.4.2 Correlations between rejection efficiency and deposit depth pore dip angle and aspect ratio

Both η_{reject} and $d_{\max}$ are correlated with the deposit volume V_d in equations 5.24 and 5.15 respectively. Therefore, it should be possible to set an equivalent direct correlation between η_{reject} and $d_{\max}$ (i.e., by substituting equation 5.15 into equation 5.24),

$$\eta_{reject} = \gamma \left[\frac{d_{\max} - 2r_p}{D\beta} \right] \tag{5.28}$$

By similar reasoning, the effects of gravitational orientation (dip angle) and pore length on $d_{\max}$ should also affect the rejection efficiency:

$$\eta_{reject} = \eta^1_{reject} (L/D)^{0.57} \tag{5.29}$$

where η^1_{reject} denotes the η_{reject} value when $L/D = 1$.

$$\eta^H_{reject} = 1.4\eta_{reject} \tag{5.30}$$

where η^H_{reject} denotes the average η_{reject} value for homogeneously oriented pore system.

5.4.3 Effect of rejected particles on flow

Rejected particles are considered part of the filtered mass along with particles collected inside the pore tube. Therefore, the effect of the rejected particles on the flow should be considered. It is not possible to determine the drag force numerically for rejected particles that are outside the boundary of the flow calculations. Instead, the flow rate is increased to compensate for the volume of rejected particles in a given time step:

$$\Delta Q_{reject} = \frac{\Delta N_{reject}\left(4/3\pi r_p^3\right)}{\Delta t} \tag{5.31}$$

The rationale for this equation is that the rejected particles should force the replaced fluid volume into the pore tube. This increment can be added to the total flow rate so that the next step can be computed with (slightly) increased flow rate. The increase in flow rate will then also influence the pressure drop. The Poiseuille flow equation 5.12 can be used to decide the corresponding increase in pressure drop. This is because the linearity of the implemented Stokes equation allows superposition of the solutions, and the solution of Stokes equation without force vector is the Poiseuille flow. Therefore, the equivalent pressure change due to rejected particles is:

$$\Delta p_{reject} = \Delta Q_{reject} \frac{8\mu L}{\pi R^4} \tag{5.32}$$

5.5 EFFECT OF ATTACHMENT PROBABILITY OF THE PORE WALL, A_p

The preceding simulations have all been conducted under the assumption of perfect attachment ($A_p = 1$ in equation 5.4) in which all particles contacting the pore wall are collected. However, in reality many researchers have reported that only a fraction of these particles are captured by the grains of a pore system. Inefficient attachment reflects the limited capacity of the grains and related roughness of the material. The adhesion model first introduced by Varidyanathan and Tien (1988) and later used by Imdakm and Sahimi (1991) was summarized in Section 2.3 (filter coefficient models). According to this model, the density and the height of protrusions are assumed to represent the degree of the roughness of the surface. If a particle settles onto a smooth pore surface, it will roll along until it encounters a protrusion. In order to observe the effect of reduced particle capture probability by the pore wall, the attachment probability, A_p is introduced. The parameter A_p defines the fraction of particles that will be attached to the pore wall among

all particles deposited. In other words, if the total number of particles that are settled on the pore wall during a given time step Δt was ΔN_{settle}, only a fraction, ΔN_{attach}, of it will become attached by the wall:

$$\Delta N_{attach} = A_p \Delta N_{settle} \tag{5.33}$$

The remainder, $(1\text{-}A_p)\Delta N_{settle}$ will be considered the same as the suspended particles that are transported with the fluid. The limiting cases, $A_p = 1$ and $A_p = 0$ represent perfect attachment and zero attachment conditions, respectively. It should be noted that the attachment probability is only applied to particles directly contacting the wall. Particles in contact with previously collected particles (i.e. mounded particles) are considered unconditionally collected as before. A series of simulations have been carried out with varying A_p values. Figure 5.33a compares the results of two sets of simulations (each with sixteen simulations) with $r_p/R = 0.04$ and $v_s/U_{flav} = 0.03$ for $A_p = 0.1$ and 1.0. The particle collection rate is much lower for $A_p = 0.1$ than $A_p = 1.0$. However, the collection efficiency is constant for both cases (at the selected settling velocity). Collection efficiency becomes non-linear only at higher settling velocity, $v_s/U_{flav} = 0.30$ as shown in Figure 5.33b. In this case, the collection efficiency increases as the process advances, reaching a constant value only after enough particles become attached to the wall. A comparison with simulations for $A_p = 1.0$ (full collection condition) shows that the long-term collection efficiency is independent of A_p. Indeed, reduced collection efficiency is proportional to the attachment probability, A_p:

$$\eta = \eta_{full} A_p \tag{5.34}$$

As the deposit volume increases, the settled particles become increasingly likely to mound on top of previously collected particles and hence, the behavior reverts back to the case with $A_p = 1$. The probability of a particle mounding on previously deposited particles depends on the surface area of the pore tube covered by particles. Accordingly, it can be hypothesized that the collection efficiency, η is a power-law function of deposit volume until reaching the collection efficiency, η_{full}:

$$\eta = \eta_{full} S(V_d) \tag{5.35a}$$

where the function $S(V_d)$ is defined as

$$S(V_d) = \left(\left(\frac{V_d}{V_d^L} \right)^{2/3} (1 - A_p) + A_p \right) \quad \text{for} \quad \frac{V_d}{V_d^L} < 1 \tag{5.35b}$$

$$S(V_d) = 1 \text{ for } \frac{V_d}{V_d^L} \geq 1 \tag{5.35c}$$

In this equation V_d^L is the 'surface saturation' at which value the collection efficiency reaches the full value, η_{full}.

Exponent value of 2/3 in equation 5.35b is the dimensional ratio of surface area to volume for the cylindrical pore. In Figure 5.34a, the data in the previous figure are compared with the regressed value using equation 5.35, with a limit deposit volume, V_d^L = 0.0043 and full efficiency, η_{full} = 0.43. In this case, the equation provides a good first approximation to widely scattered simulation data. Figures 5.34b and c show simulations with the same particle size and settling velocity and A_p = 0.2, 0.5 respectively. The same function (equation 5.35) is used with the same limit deposit volume value and previously computed η_{full} values. In Figure 5.34c, the effect of A_p becomes minimal and the deposit volume increases linearly. The good agreement between simulated and analytically computed values in these figures confirms the basic hypothesis for effects of A_p.

Given that the same limit value V_d^L applies for all A_p values, it can also be summarized that once a certain amount of deposit is accumulated the attachment probability has no further effect on filtration rate. The value V_d^L = 0.0043 is rather small (implying only 0.43% of the pore tube volume). A possible explanation for this is that the settling of the particle occurs mainly in a confined region of the tube for particle trajectories sharing the same settling velocity, although released at different initial

elevations (with respect to the base of the tube) do not differ much. Thus, the value is not affected by the settling velocity.

When the settling velocity is increased to v_s / U_{flav} = 3.02 with η_{full} = 0.89, analytical calculations with V_d^L = 0.0043 also give the same good agreement as shown in Figure 5.35a. However, the particle size does have an effect on the surface saturation value. In Figures 5.35b, and 5.35c the values V_d simulated and analytically obtained are plotted together for r_p/R = 0.06 and 0.1 cases, with settling velocities v_s / U_{flav} = 0.24, 0.30, and attachment probability, A_p = 0.1. The resulting surface saturation values are found to be V_d^L = 0.0144 and 0.0667, respectively. In each case, these values of V_d^L correspond to 100 collected particles (for r_p/R = 0.04, 0.06 and 0.1). This means that the number of particles, rather than their volume, determines the surface saturation value. This result is reasonable considering the fact that the probability a particle will meet previously deposited particles must depend on the surface area covered by them. Although equation 5.35 is reasonably successful, further simulations are needed to investigate conditions where there is minimal wall attachment. This becomes especially important for polydispersed particles, where the surface area covered by deposited particles is much harder to define.

5.6 IMPLEMENTING OF SIMULATION RESULTS INTO NETWORK MODEL

Chapter 3 has provided the background theories of network models and the procedure for performing network simulations. It was assumed that microscopic modeling of particle laden flow through a model pore could provide the correlations for the key parameters required in the model (i.e. the probability of particle capture and the capacity of each individual link in a network). The probability of particle capture in a pore is equivalent to its collection efficiency. As discussed in detail in previous sections, a particle can be collected by a pore in two ways, either by rejection at the inlet (i.e. blockage by pre-existing deposits), or by accumulation inside the pore. While interpreting the simulation results, the particles collected by the former mechanism were counted

separately from those of the latter, and each was accounted for by efficiencies: η_{reject} and η, respectively. The efficiency η, was best parameterized with the settling velocities of the particles, v_s that has presented in Section 5.1. As the settling velocity of a particle can be estimated by Stokes equation, which is solely a function of the particle size, r_p. Hence, the efficiency, η is a function of r_p. On the other hand, the rejection efficiency, η_{reject} was found to be a function of both the deposit volume and the settling velocity, v_s, as explained in Section 5.4.

For each network node, calculations from the previous time step (Figure 3.4 flow chart) generates the number of particles per each size group left and ready to be fed to the next set of bonds (i.e. model pores). Given a network bond with radius, R, the number of input particles is defined by $\Delta N_{in}^{k}(r_{pi})$, i = 1-N_r particles fed into the link for a given time step, Δt, where k is the time-step index, N_r is the number of particle size groups and r_{pi} denotes the radius of each size group. The link has a deposit layer of normalized volume V_d^{k-1}, from previous filtration (particle collection). Then the collection efficiency for each size group of particles can be determined using equations 5.7, 5.8, and 5.11. The input parameters required are, the pore length, L, diameter, D, dip angle, θ, the attachment probability A_p, the surface saturation, V_d^L, and the average flow velocity, U_{flav}. The rejection efficiency, η_{reject}, can be decided using equation 5.24, and equations 5.27 to 5.30. Then the particles that will end up in one of the following three categories can be determined.

1. Particles that are size excluded by the pores (i.e. bonds): $\Delta N_{in}(r_{pi})P\left[r_{pi} > R\right]$

2. Particles that will be collected by the pores:

(1) Rejected at the inlet: $\Delta N_{reject}(r_{pi}) = \Delta N_{in}(r_{pi})P\left[r_{pi} \le R\right]\eta_{reject}(r_{pi})$

(2) Collected inside the pores: $\Delta N_{collect}(r_{pi}) = \Delta N_{in}(r_{pi})P\left[r_{pi} < R\right](1-\eta_{reject})\eta(r_{pi})$

3. The remainder of particles will break through (transported without filtration)

In addition, the deposit volume after the current time step k, V_d^k can be determined:

$$V_d^k = V_d^{k-1} + \frac{4}{3R^2}\sum_{i=1}^{N_r} r_{pi}^3 \Delta N_{collect}(r_{pi}) \tag{5.36}$$

Once the current deposit volume is known, the reduced capacity of the pore (due to filtration) can be evaluated. First, the maximum deposit depth, $d_{\max}$ and height $h_{\max}$ are evaluated using equations (5.13), (5.15) to (5.18), and (5.21). Collected particles affect the fluid body by exerting drag forces on it. The drag forces slow down the flow rate if the pressure difference stays constant or raise the pressure difference for the same flow rate.

In the parametric study described in this chapter, the flow rates are kept constant and the effect of drag forces by deposited particles were observed indirectly by an increase in the pressure difference across the ends of the model pore. The pressure drop in the current time step Δt_k, Δp^k can be obtained from equation 5.124. There is a further increment in pressure change drop increase due to the rejected particles, which can be estimated from equation 5.32. In order to be used in network model simulations, the change in pressure drop increase has to be linked to the flow capacity of the link (i.e., the flow rate a link can produce with given pressure drop). This can easily be computed as the capacity of a given link is computed from the Poiseuille flow equation given in equation 3.3 whereas the flow rate, Q, is given as a function of tube size, (R and L), transporting fluid viscosity, η, and pressure difference, Δp. Therefore, the capacity of the bond, K_k can be updated from the previous value, K_0:

$$K_k = \frac{\Delta p_k + \Delta p_{reject}}{\Delta p_0} K_0 \tag{5.37}$$

where the capacity K is proportional to the fourth power of the radius, i.e. $K \propto R^4$. Therefore, the current bond radius, R_k will have the following relationship with the initial radius, R_0:

$$R_k = \frac{\Delta p_k + \Delta p_{reject}}{\Delta p_0} R_0 \tag{5.38}$$

5.7 CONCLUSIONS AND LIMITATIONS

An intensive parametric study has been performed using the particle flow simulator described in Chapter 4. The correlations developed from the numerical simulations provide a quantitative framework for simulations in model pore tubes. The current study has been restricted to uniform (mono-disperse) particle populations. However, there are no conceptual barriers to further explorations with polydispersed systems. The other key assumption is that only gravity forces are considered to act on the particles. Finally, it should be noted, that some parameters, such as the viscosity, average fluid velocity and the density of the fluid were included in the study but found to have trivial effect on the simulation results and accordingly, they are omitted from discussed in this chapter.

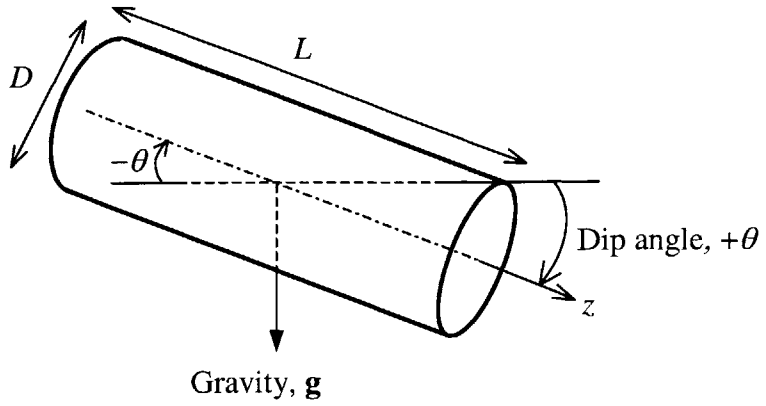

Figure 5.1 Sign convention of pore tube dip angle

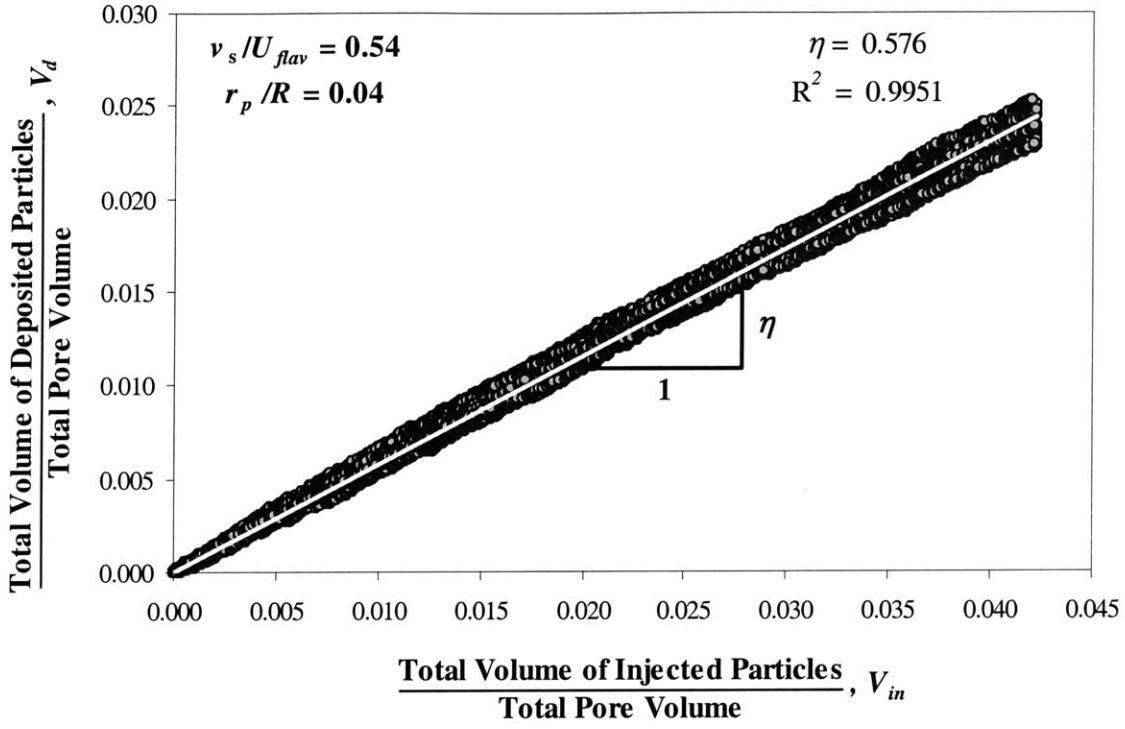

(a) $r_p/R = 0.04$ and $v_s/U_{flav} = 0.537$

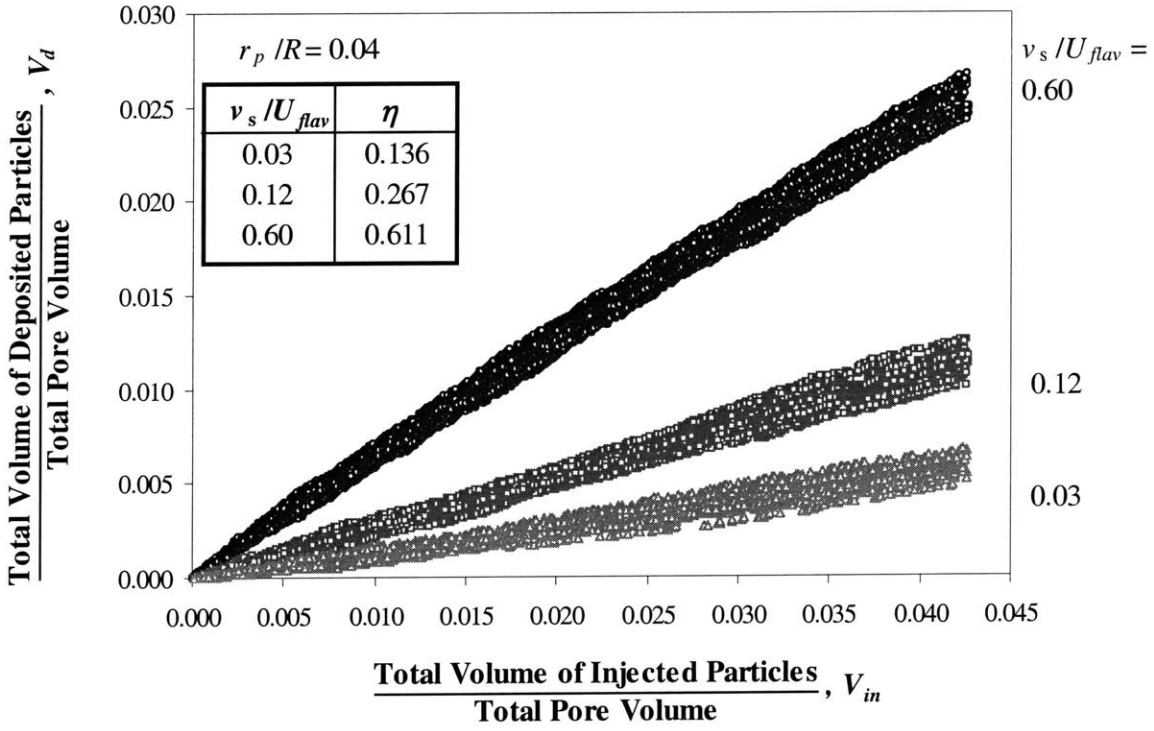

(b) With higher settling velocities

Figure 5.2 Normalized volume of collected particles for cases with $r_p/R = 0.04$

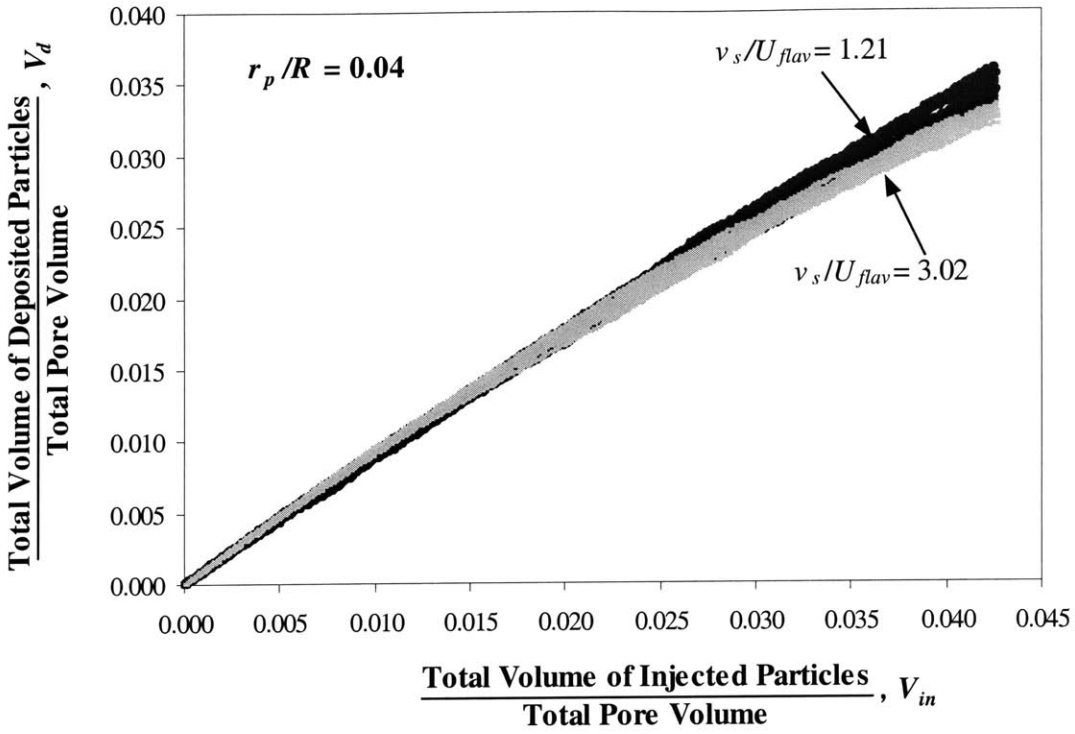

(a) Nonlinear increase for v_s/U_{flav} = 3.02

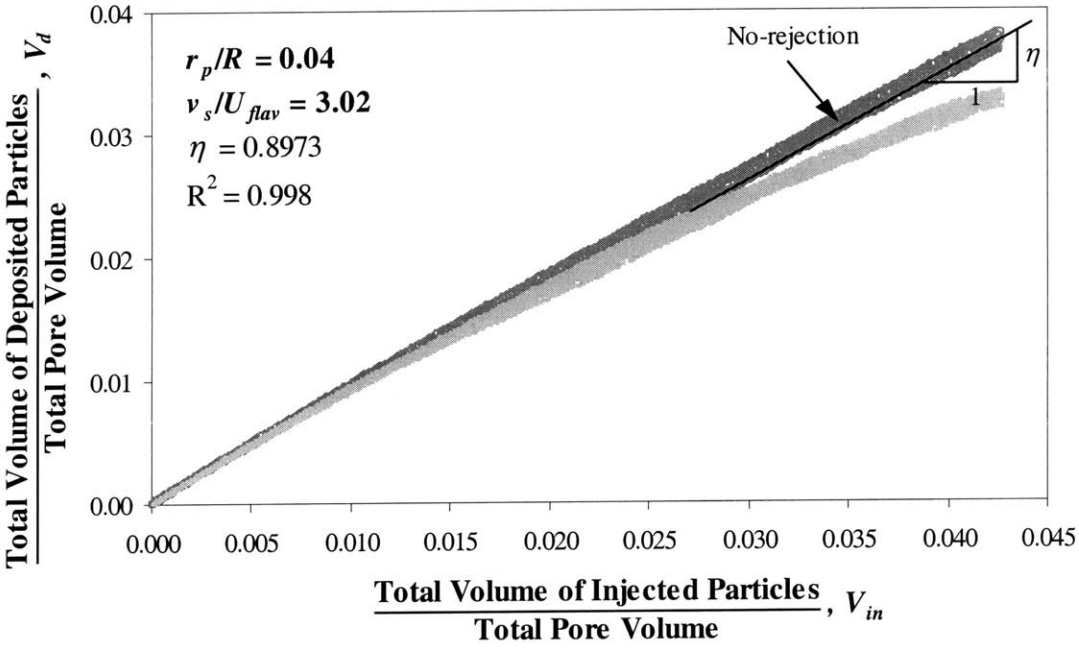

(b) Linear increase rate with the 'no-rejection' simulation

Figure 5.3 Increase in normalized deposit volume for simulations with r_p/R = 0.04

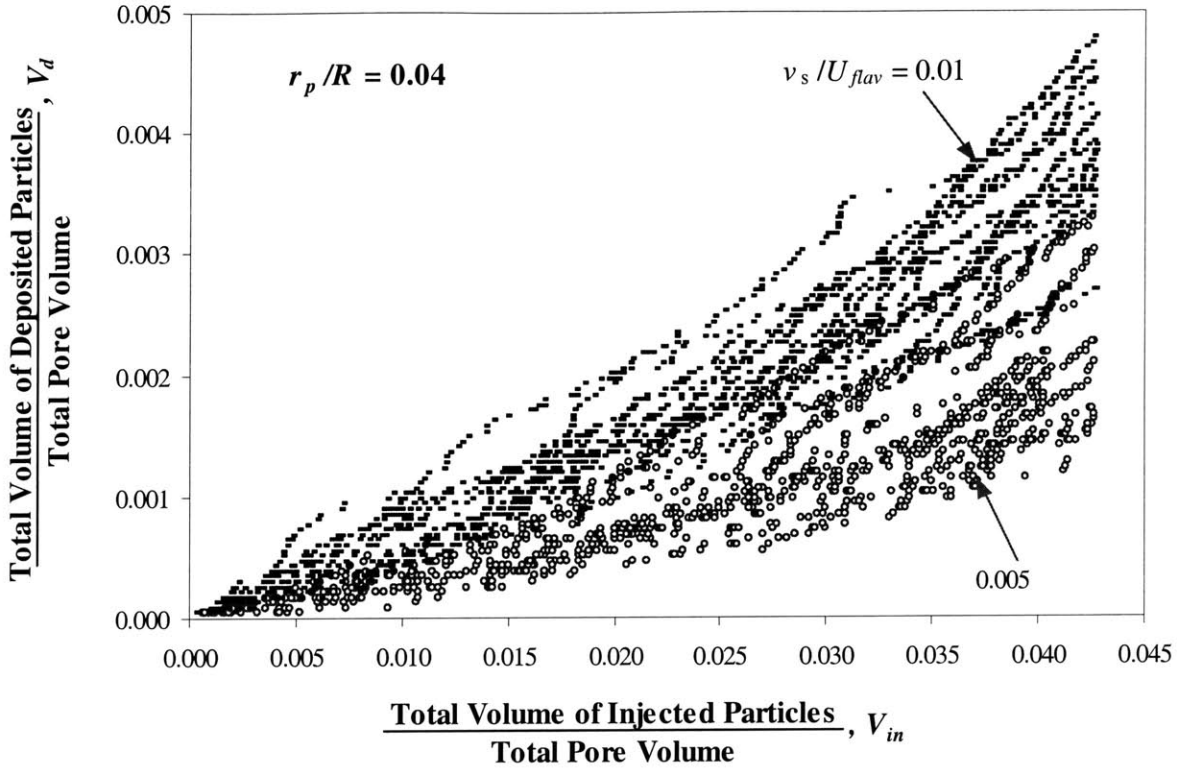

Figure 5.4 Ripening of collection efficiency at low settling velocities for simulations with r_p/R = 0.04

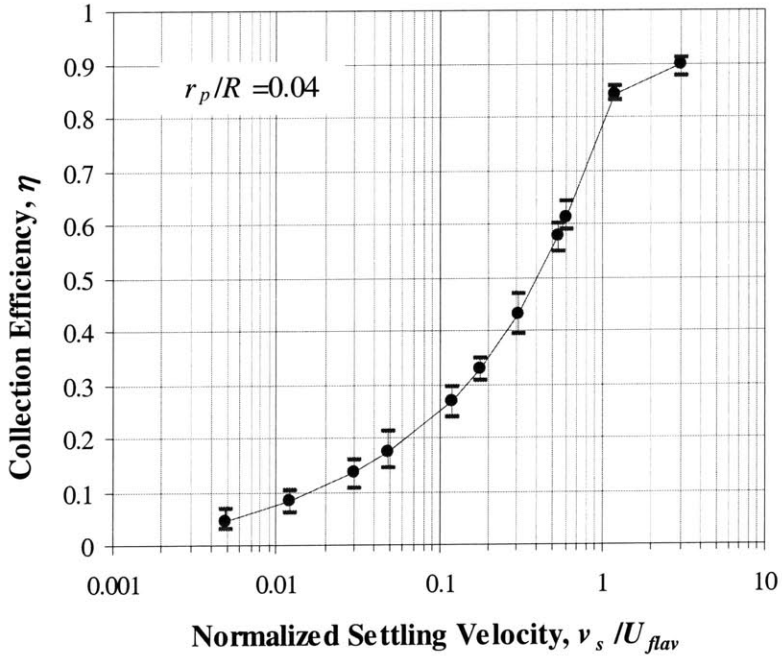

Figure 5.5 Collection efficiency and the settling velocity for r_p/R = 0.04

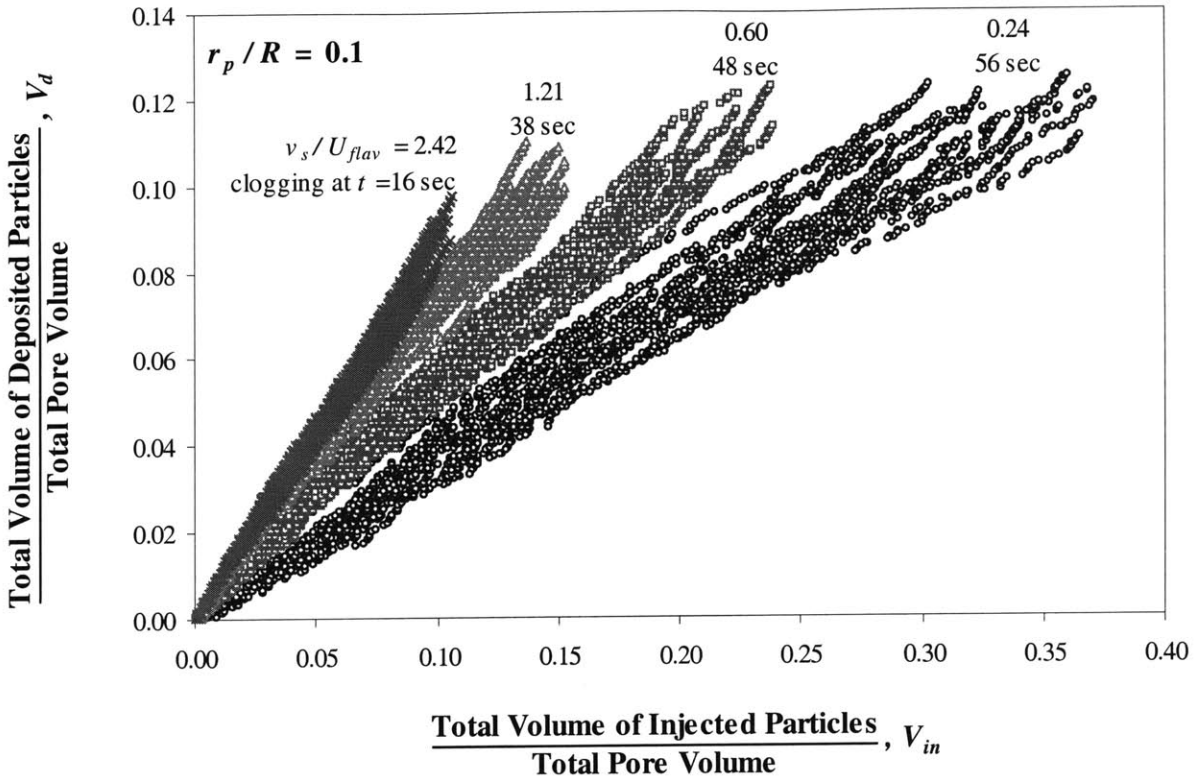

Figure 5.6 Normalized volume of particles collected for $r_p/R = 0.1$

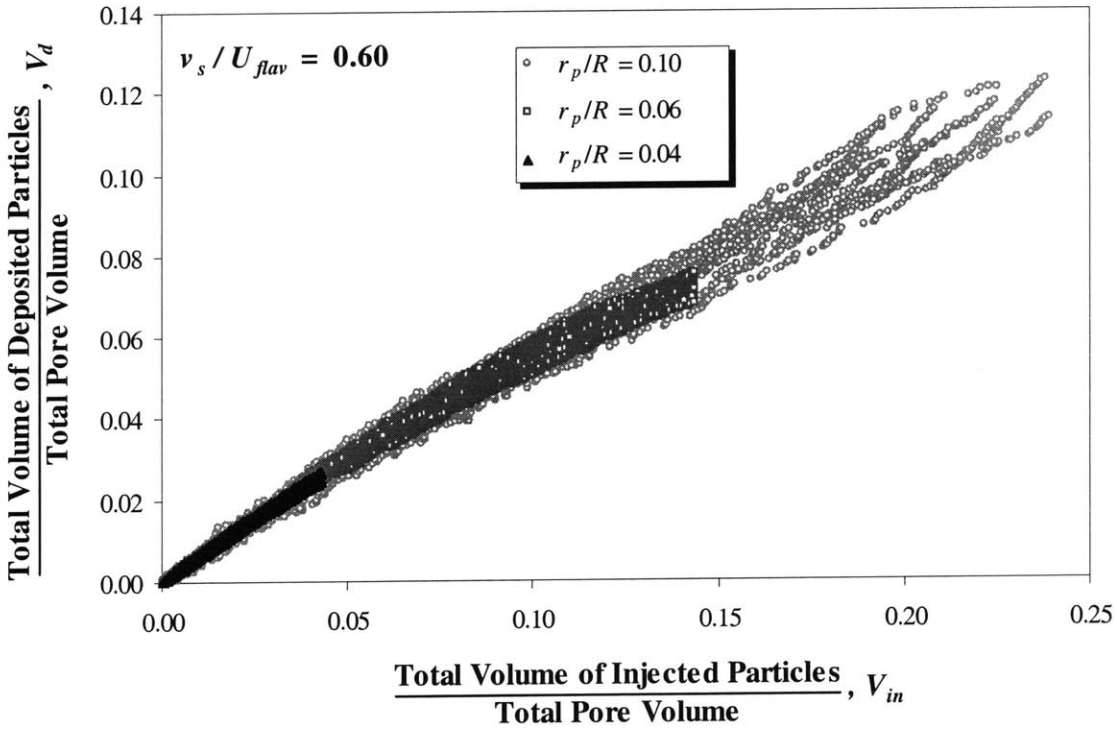

Figure 5.7 Same efficiency for three different sizes of particles with a same settling velocity

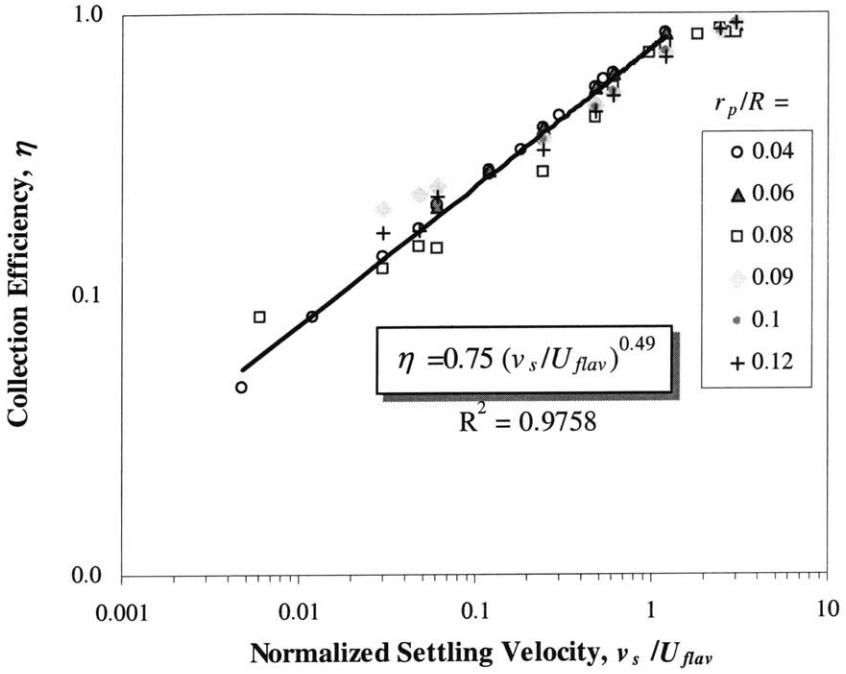

Figure 5.8 A log-linear relationship between the collection efficiency and the settling velocity for various sized particles

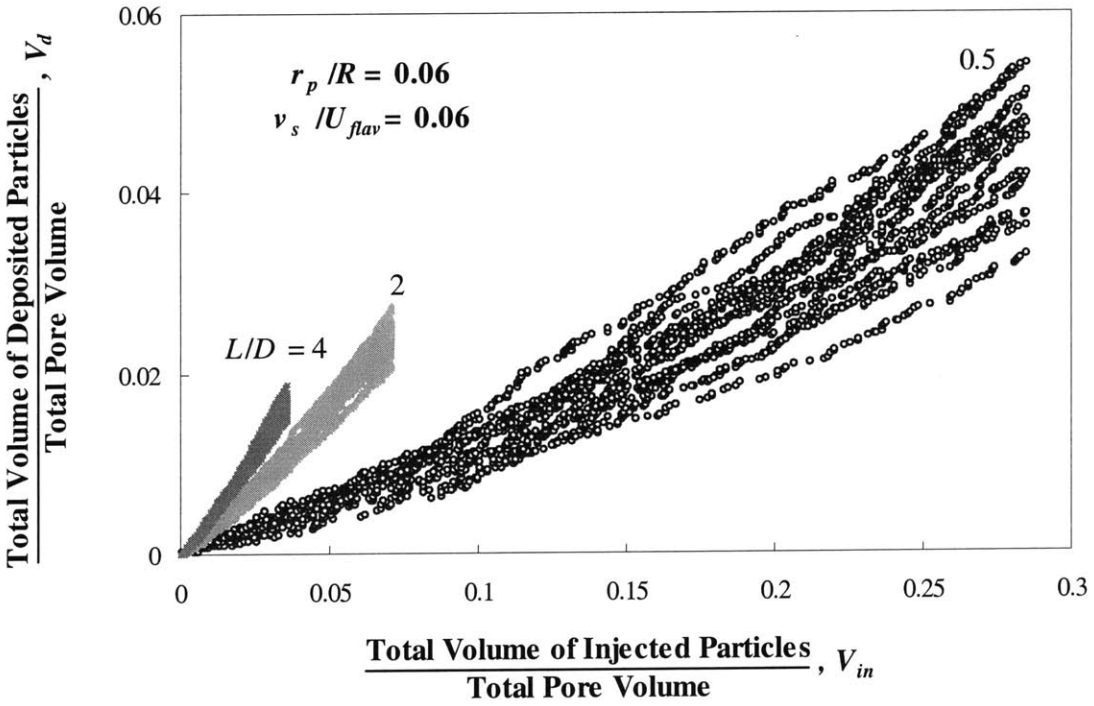

Figure 5.9 Effect of pore length on collection efficiency for $r_p/R = 0.06$

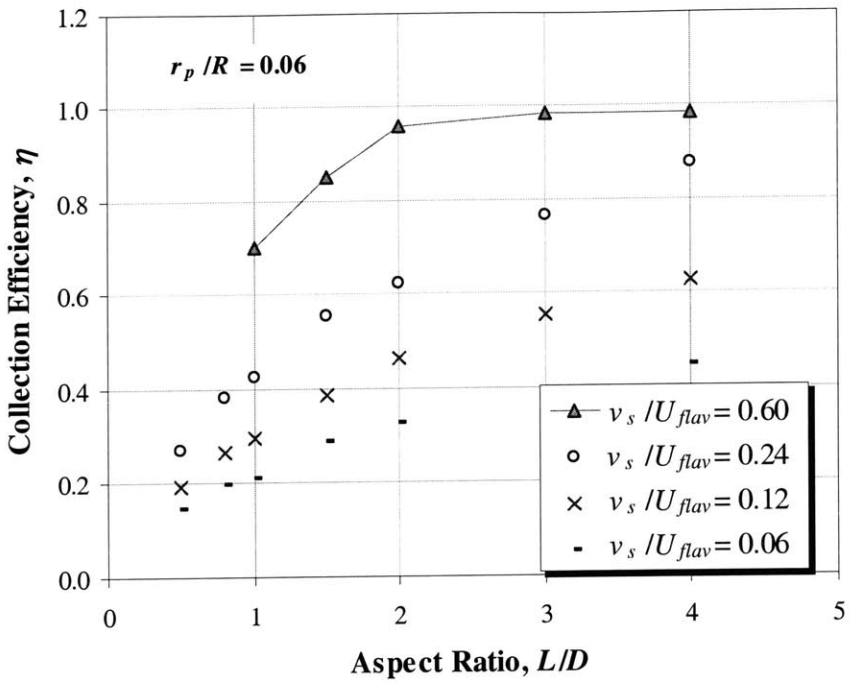

(a) Not normalized

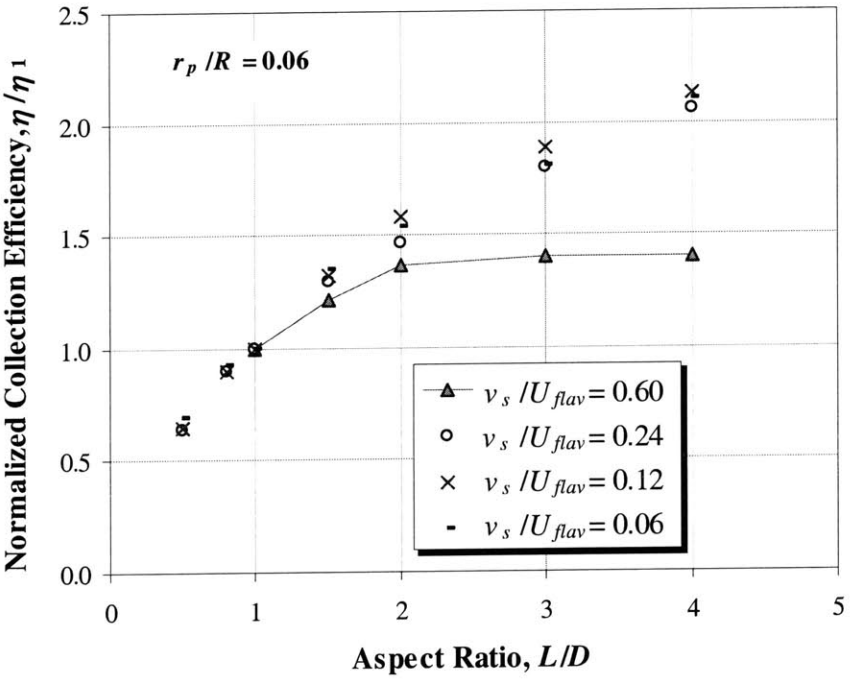

(b) Normalized with values at $L/D = 1$

Figure 5.10 Collection efficiency pore aspect ratio for various settling velocities

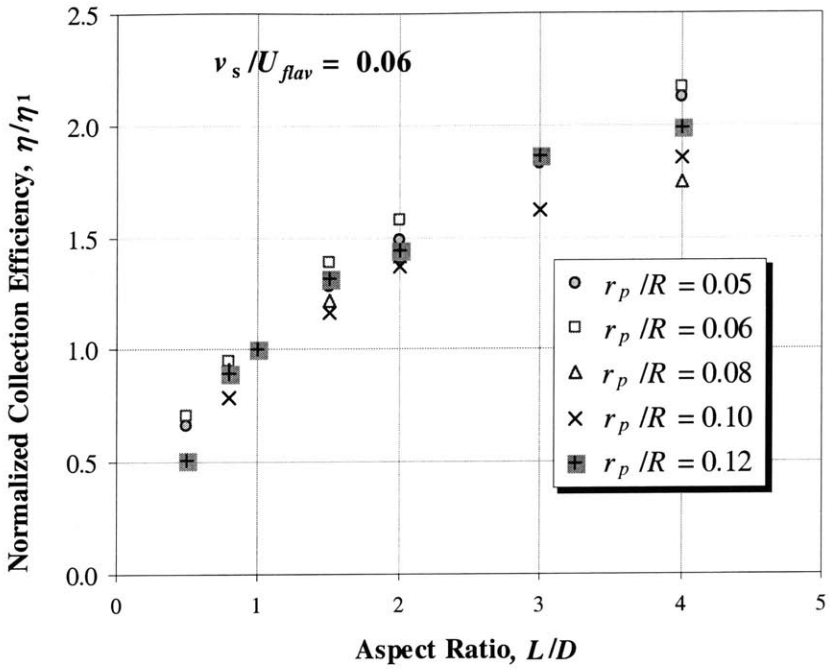

Figure 5.11 Collection efficiency versus *L/D* for various sized particles

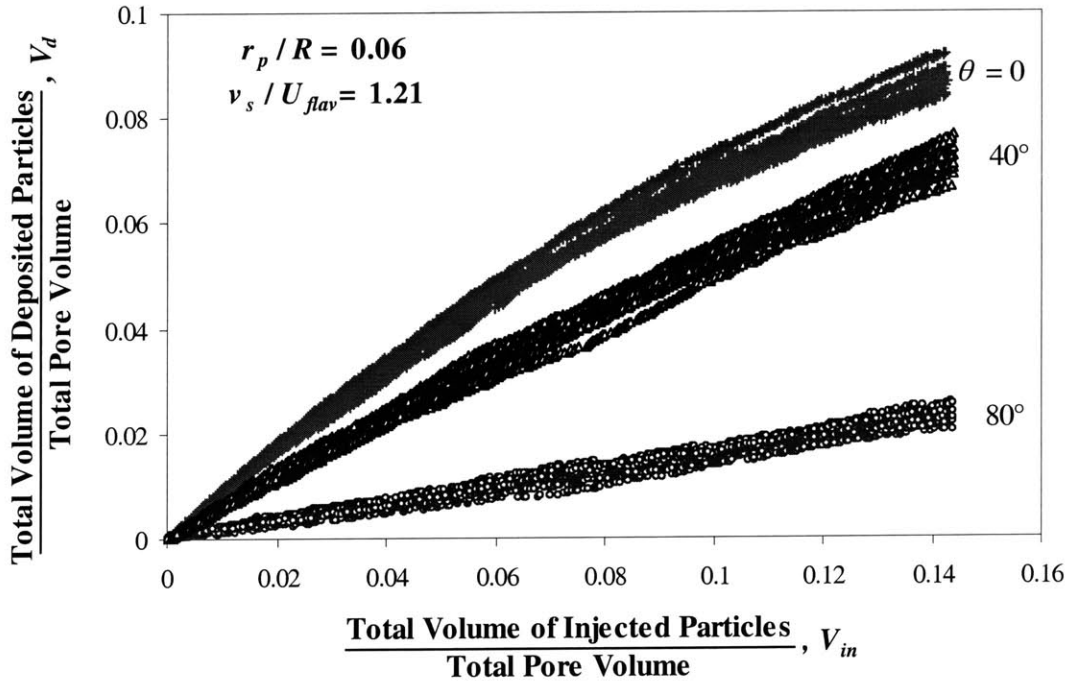

Figure 5.12 Effect of pore dip angle on particle collection

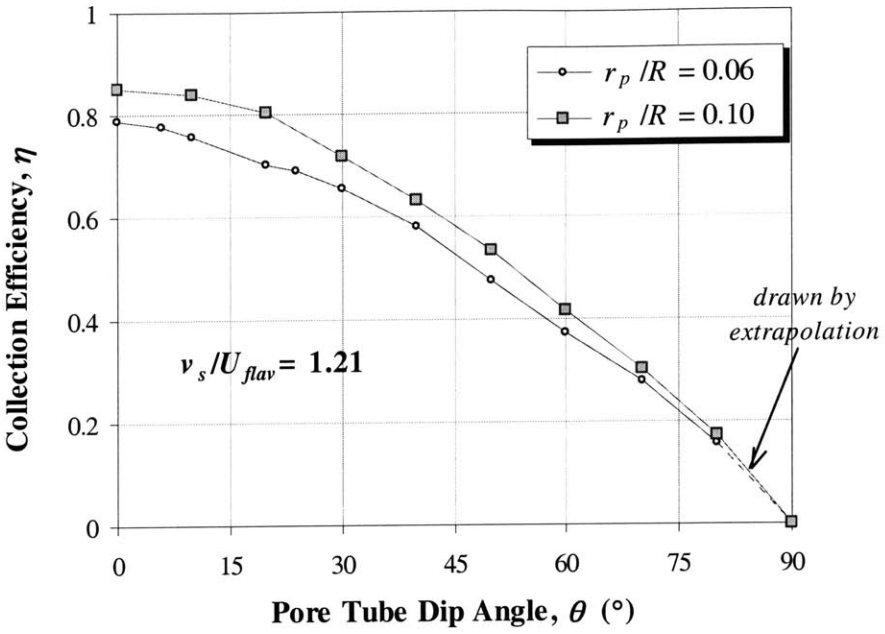

Figure 5.13 Effect of particle size and dip angle on particle collection

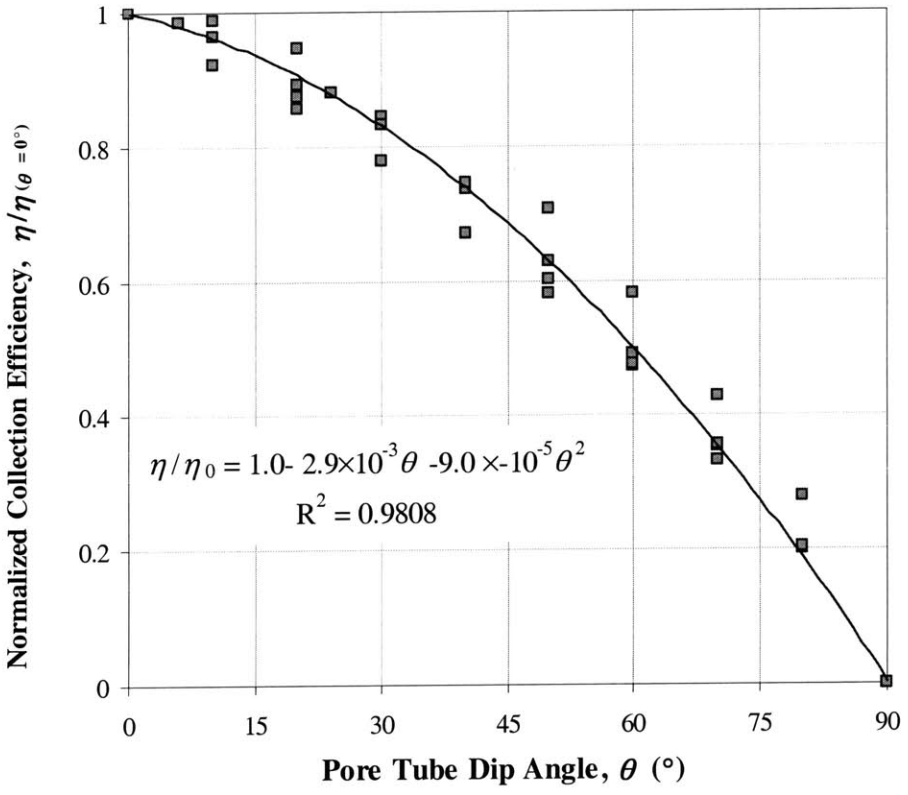

Figure 5.14 Correlation of particle efficiency with dip angle

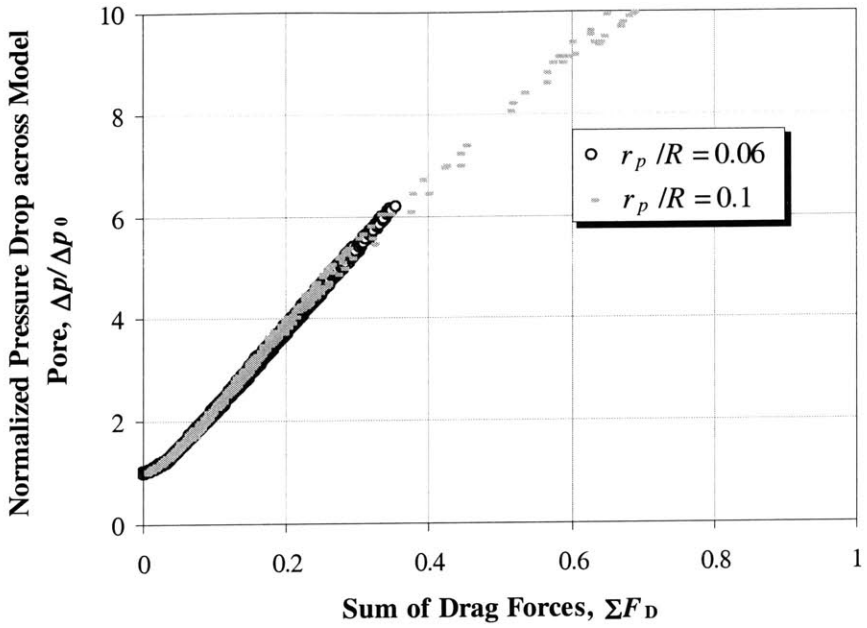

(a) From simulations

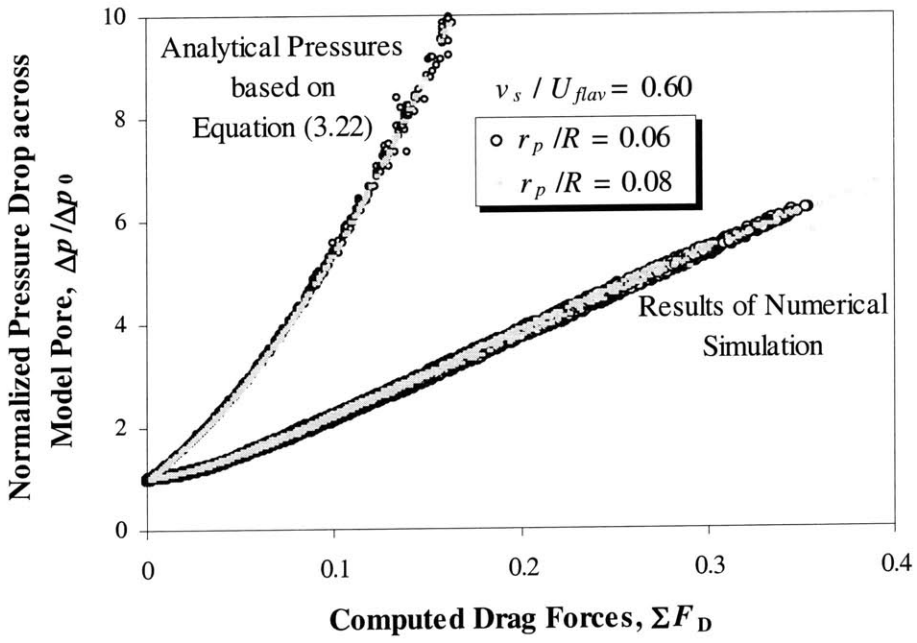

(b) Compared with equation 3.22

Figure 5.15 Normalized pressure drop $\Delta p/\Delta p_0$ versus the total drag force ΣF_D

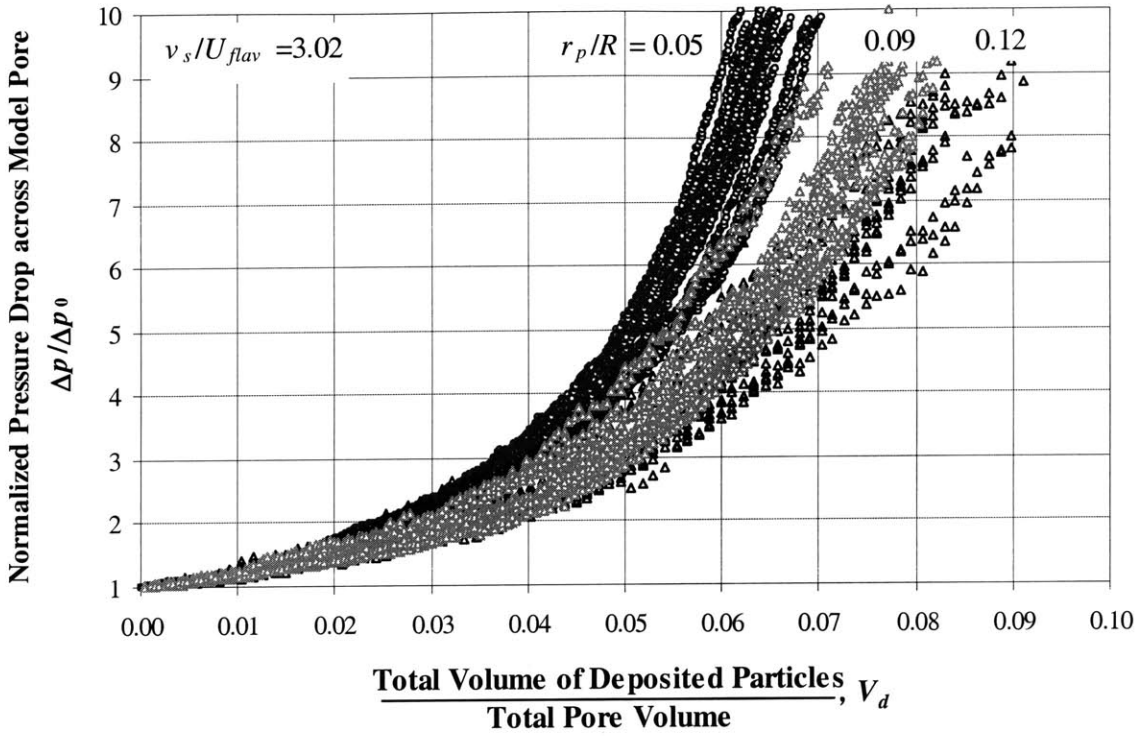

Figure 5.16 Normalized pressure drop

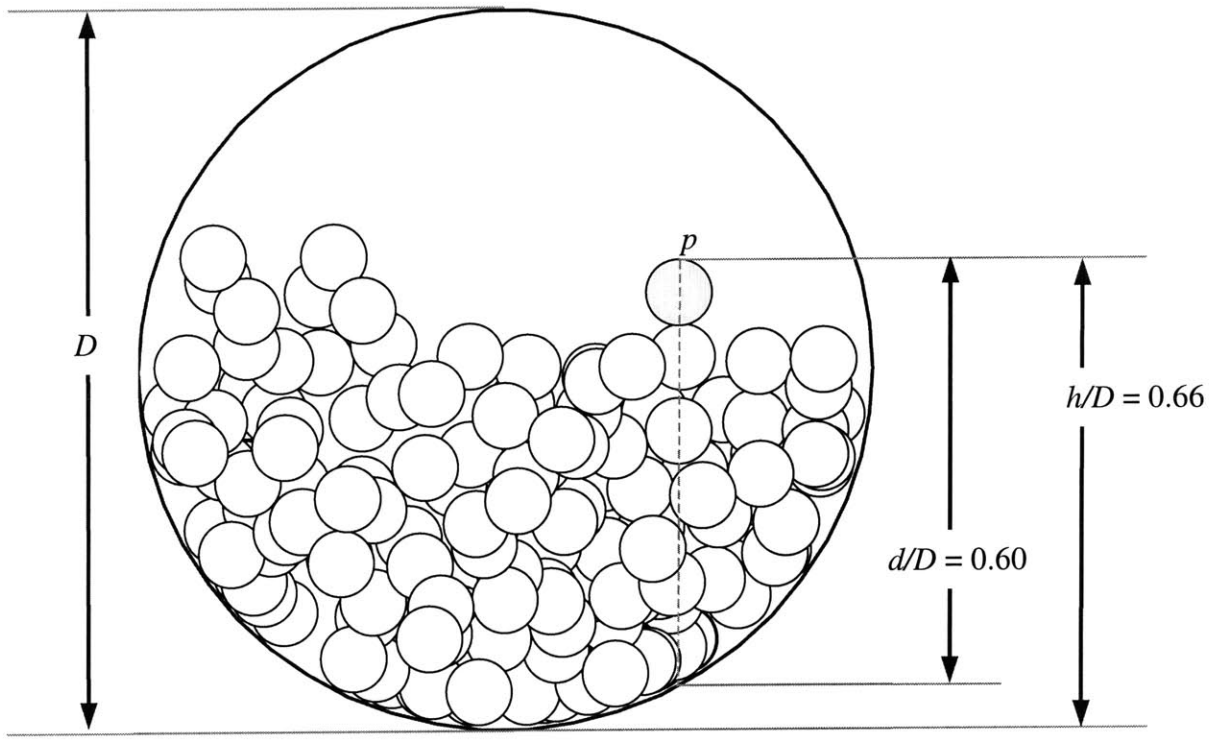

Figure 5.17 Definition of deposit depth, d , and mound height, h

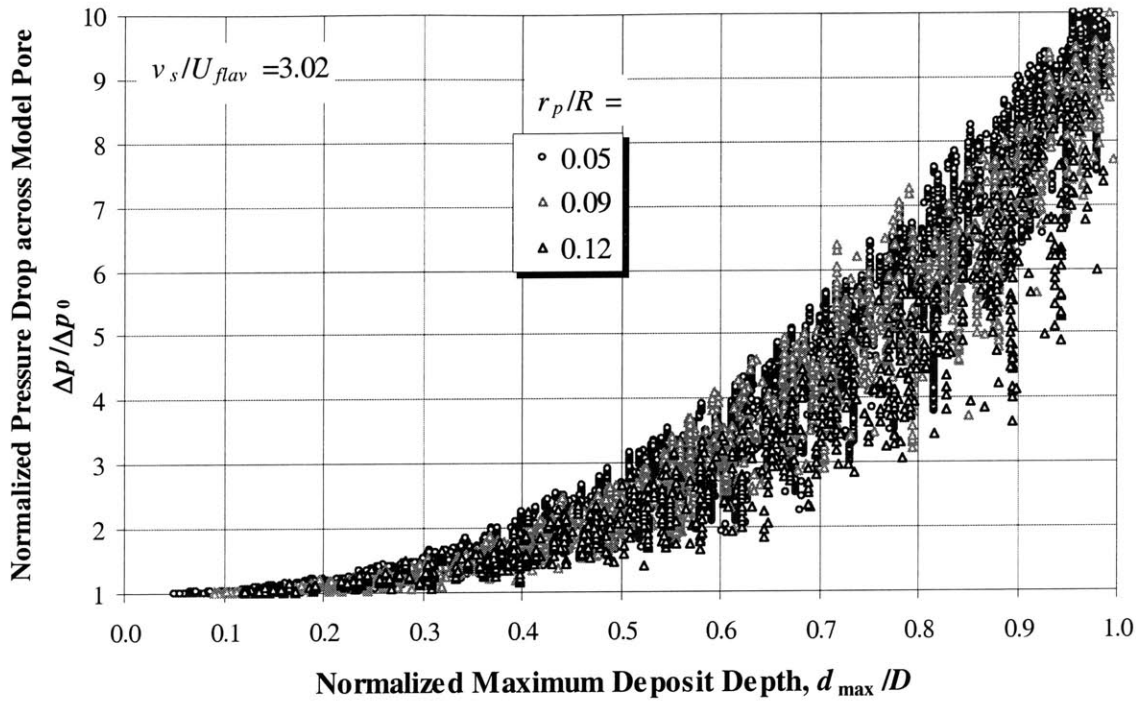

Figure 5.18 Correlation of normalized pressure change with maximum deposit depth, d_{max}

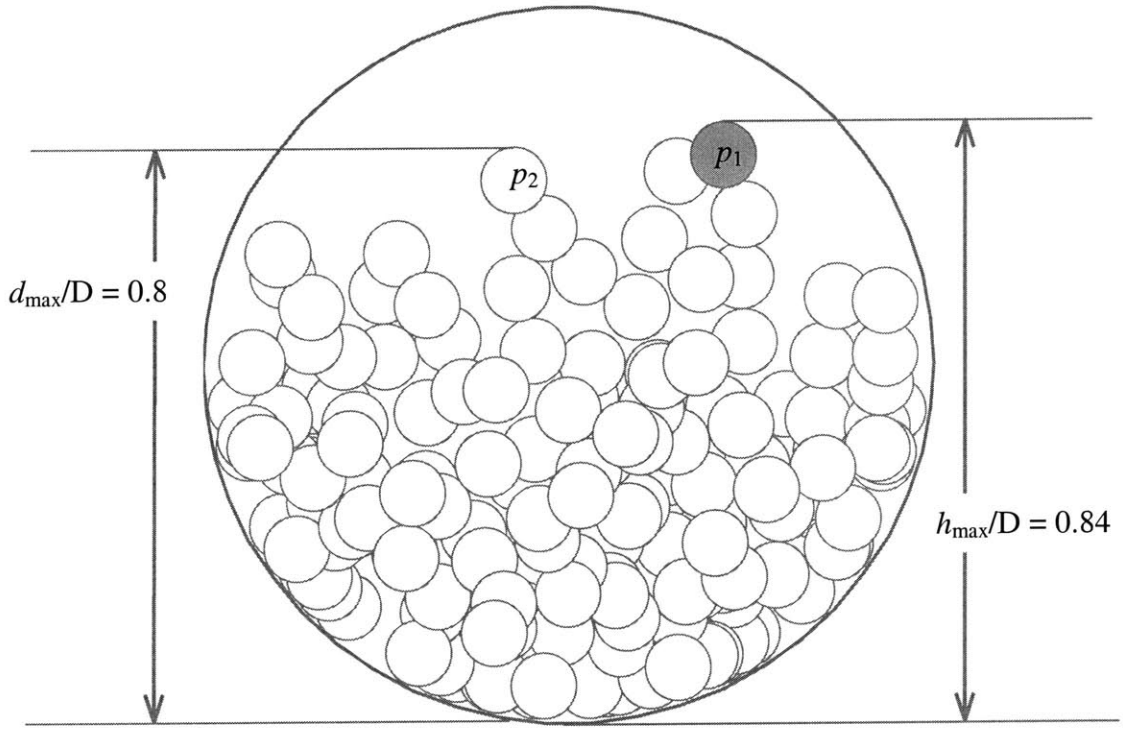

Figure 5.19 Illustration of maximum mound height, h_{max}, and maximum deposit depth, d_{max}

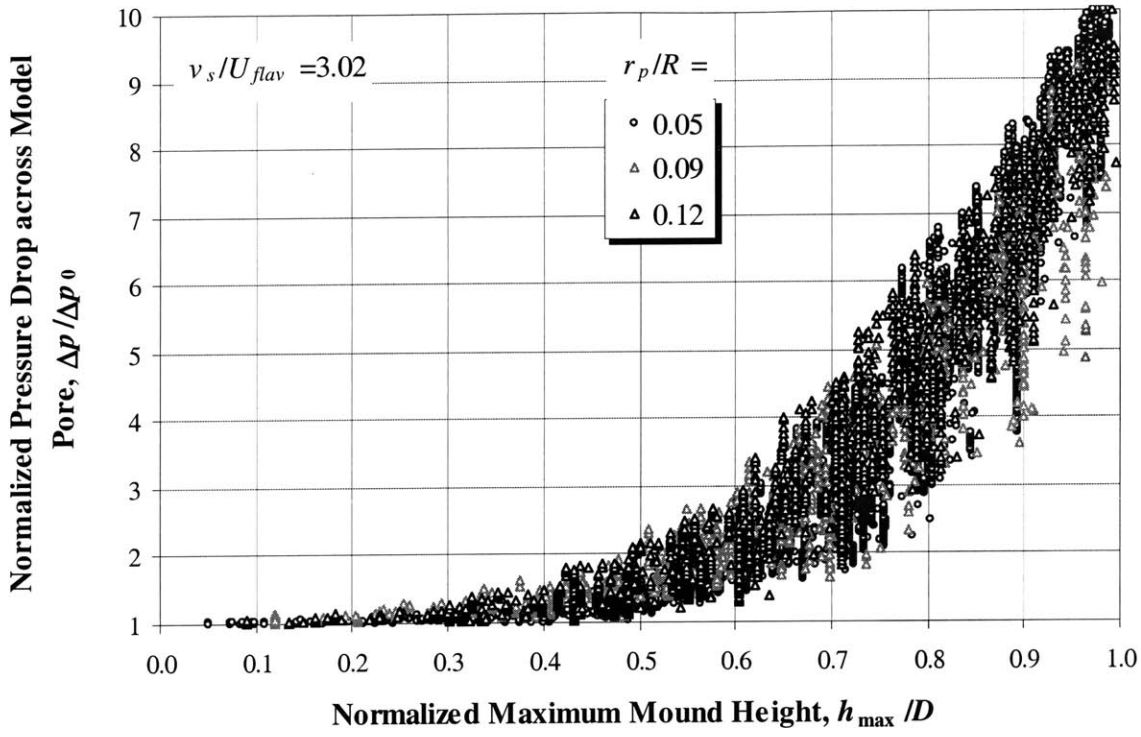

Figure 5.20 Normalized pressure drop against the maximum mound height, h_{max}

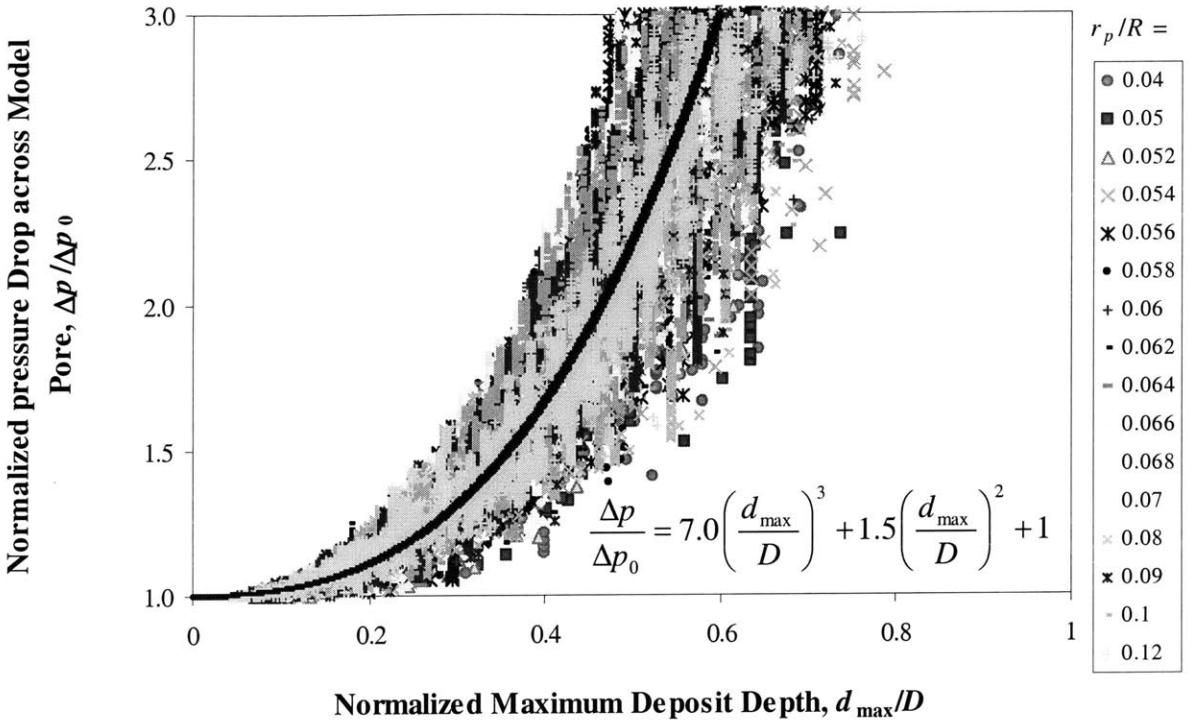

(a) Function of maximum deposit depth

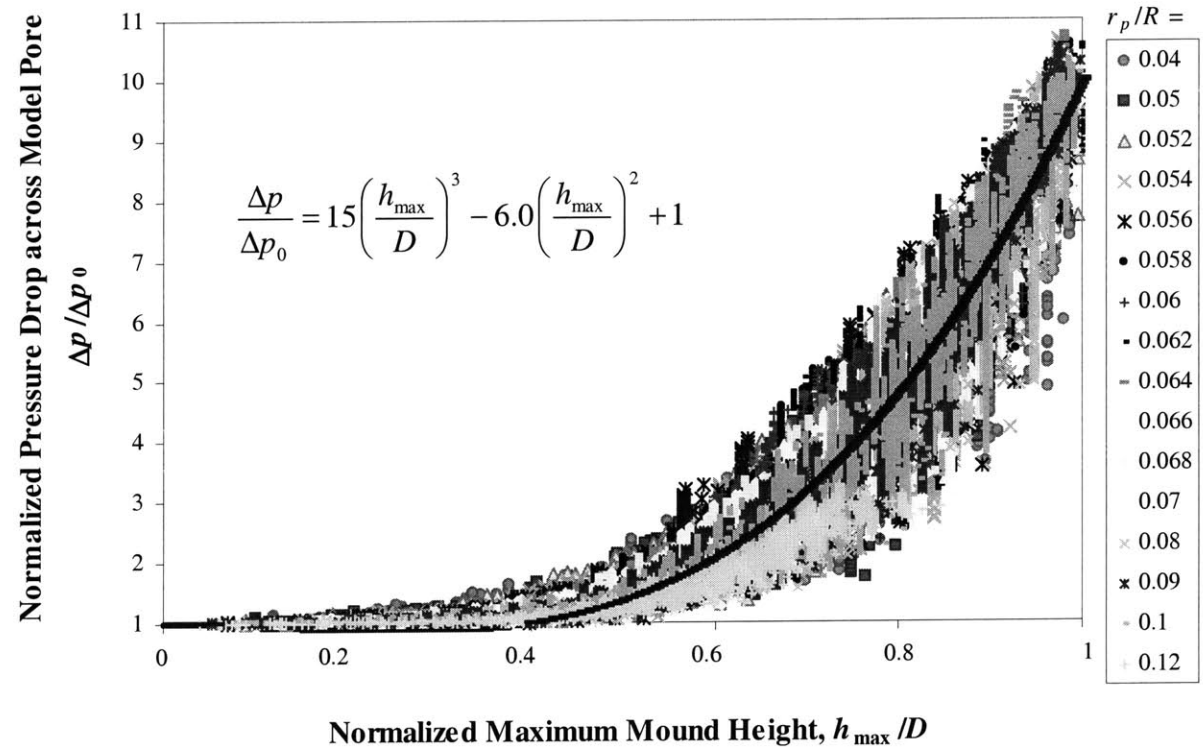

(b) Function of maximum mound height

Figure 5.21 Proposed correlations for pressure changes in the model pore

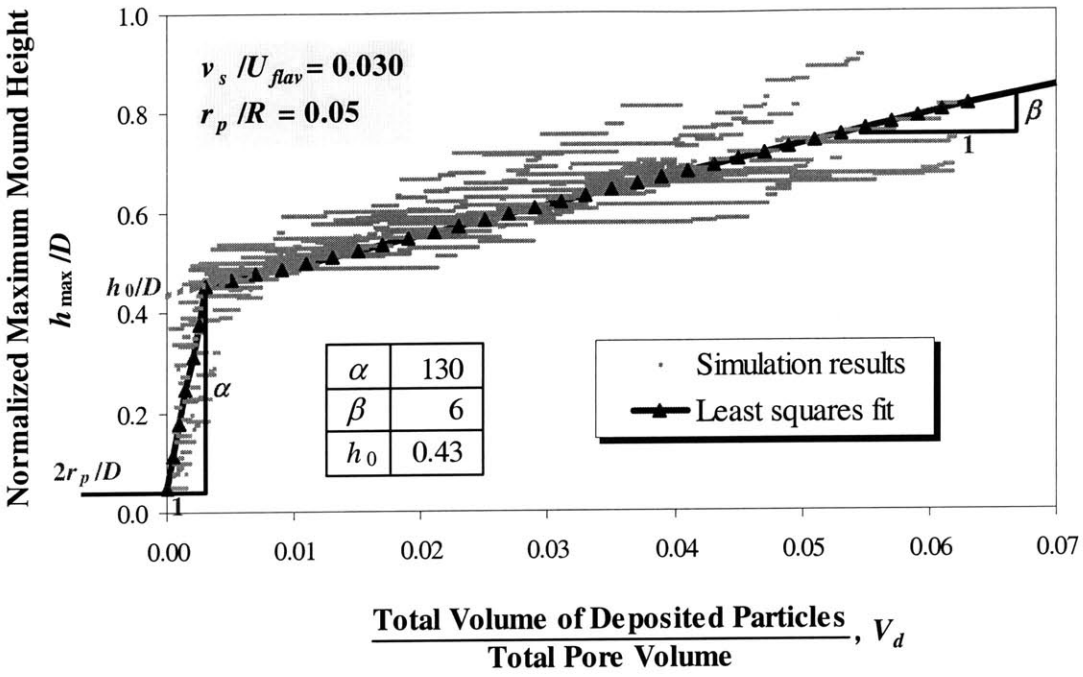

(a) r_p/R = 0.05, and settling velocity, v_s/U_{flav} = 0.03

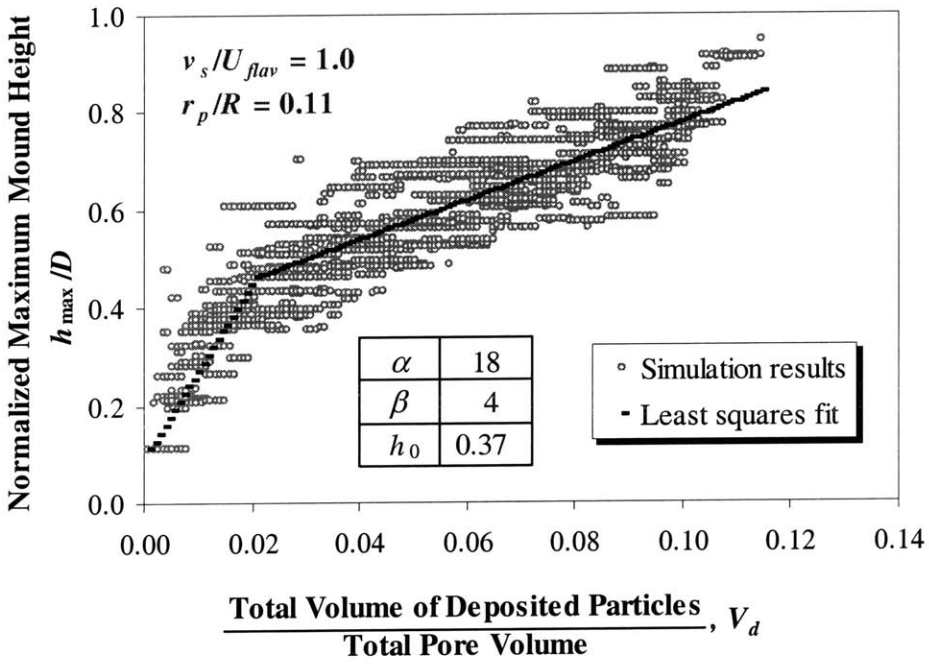

(b) r_p/R = 0.11, and settling velocity, v_s/U_{flav} = 1.0

Figure 5.22 Maximum mound height increases as a function of the total volume of deposited particles

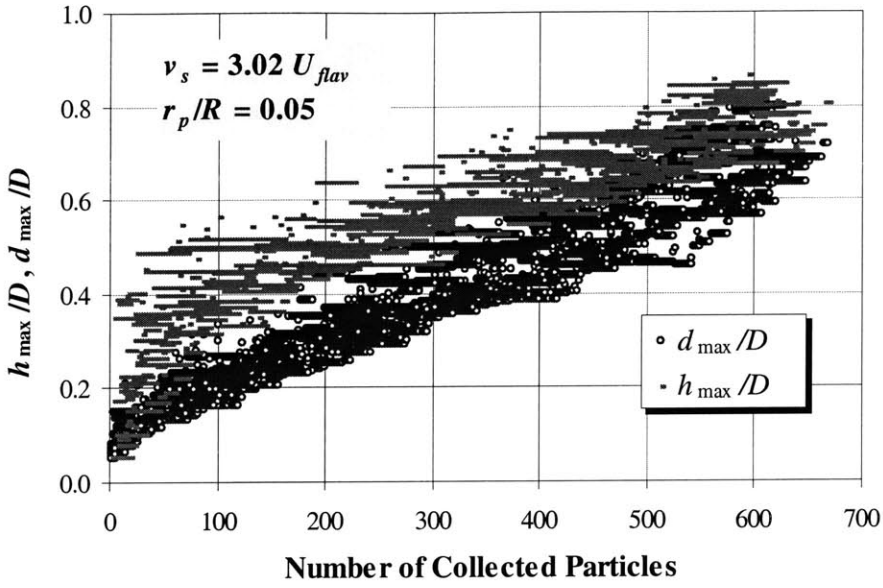

(a) r_p/R = 0.05, and settling velocity, v_s/U_{flav} = 3.02

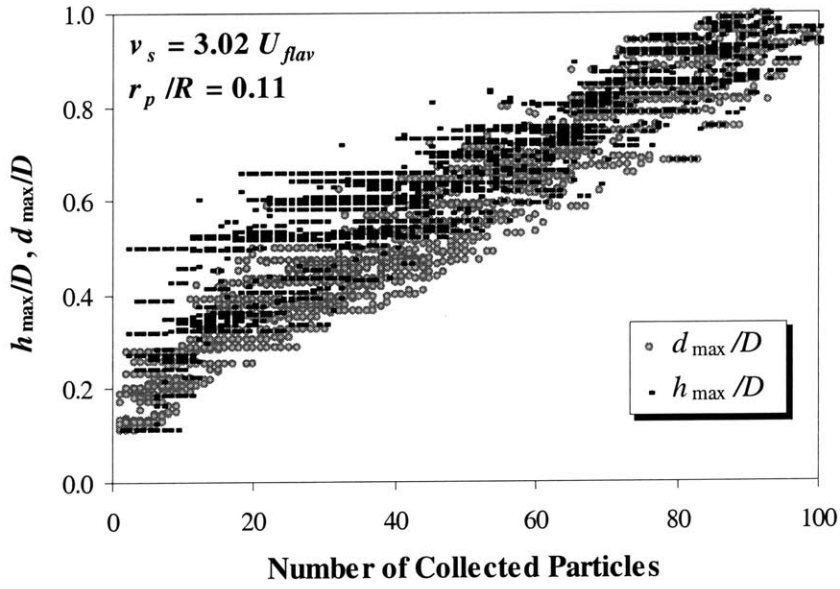

(b) r_p/R = 0.11, and settling velocity, v_s/U_{flav} = 3.02

Figure 5.23 Comparison of maximum mound height and deposit depth as functions of the total number of deposited particles

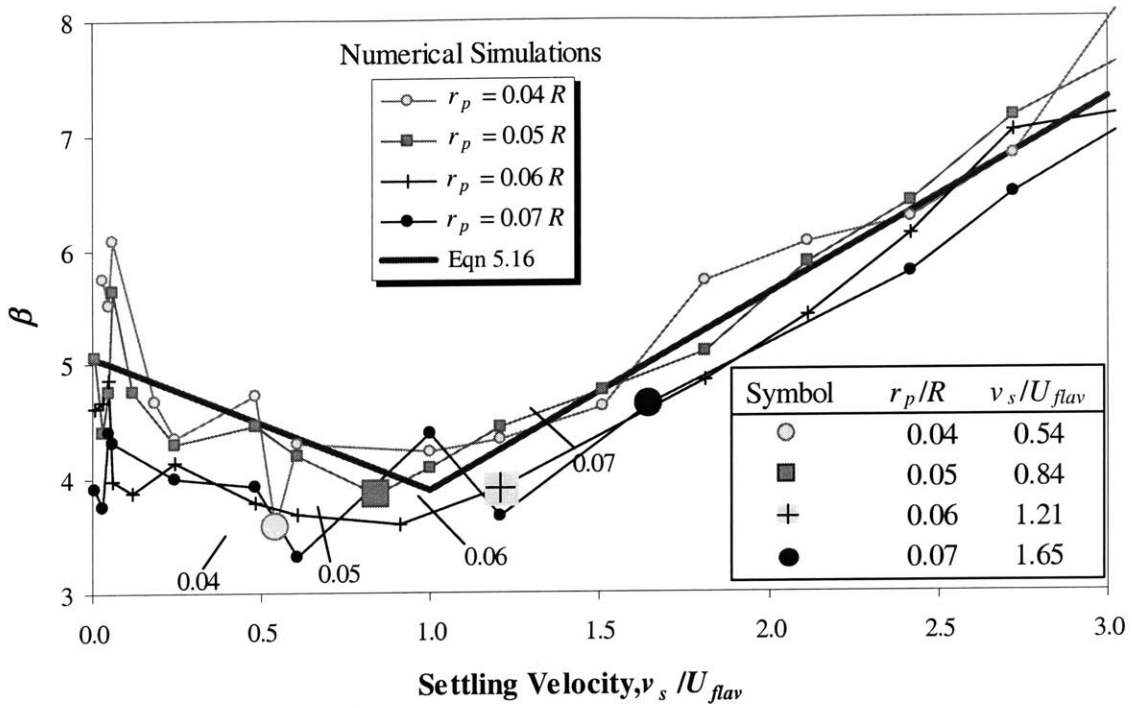

(a) r_p/R ranging 0.04 to 0.07

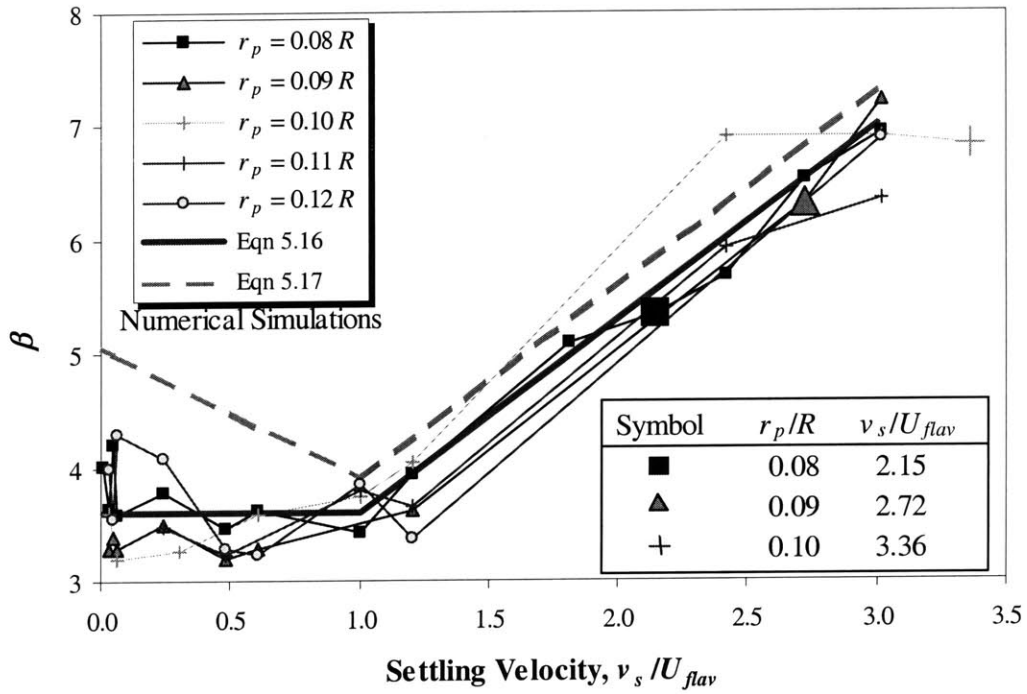

(b) r_p/R ranging 0.08 to 0.12

Figure 5.24 Correlations for empirical parameter β in equation 5.13b

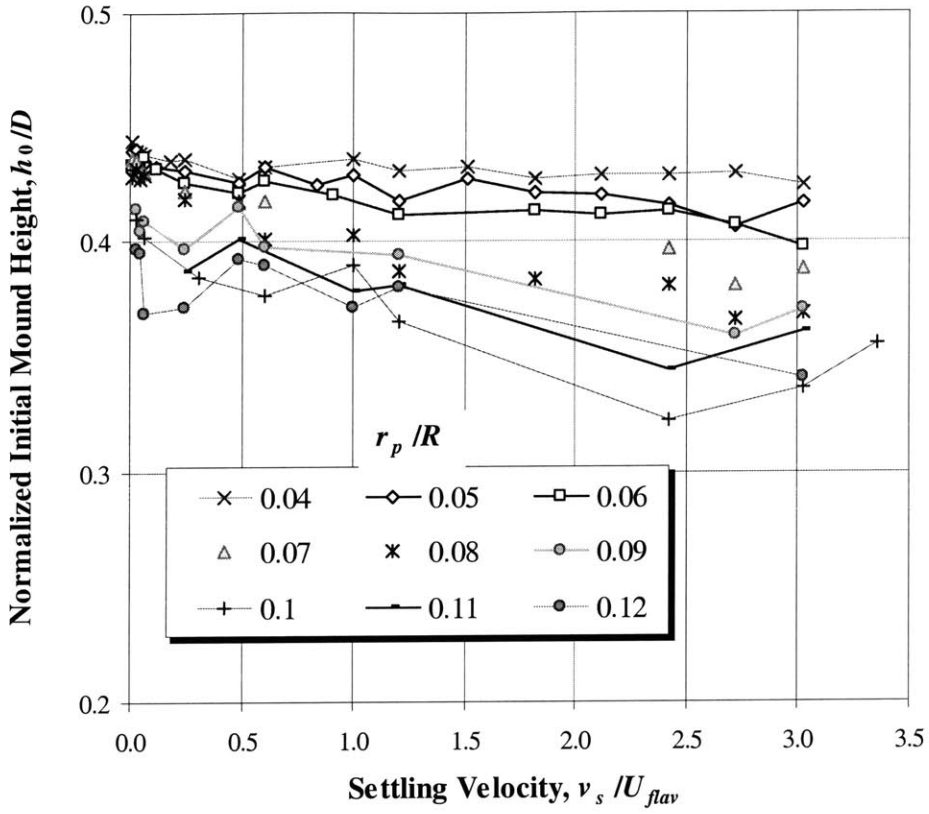

(a) h_0 versus settling velocity

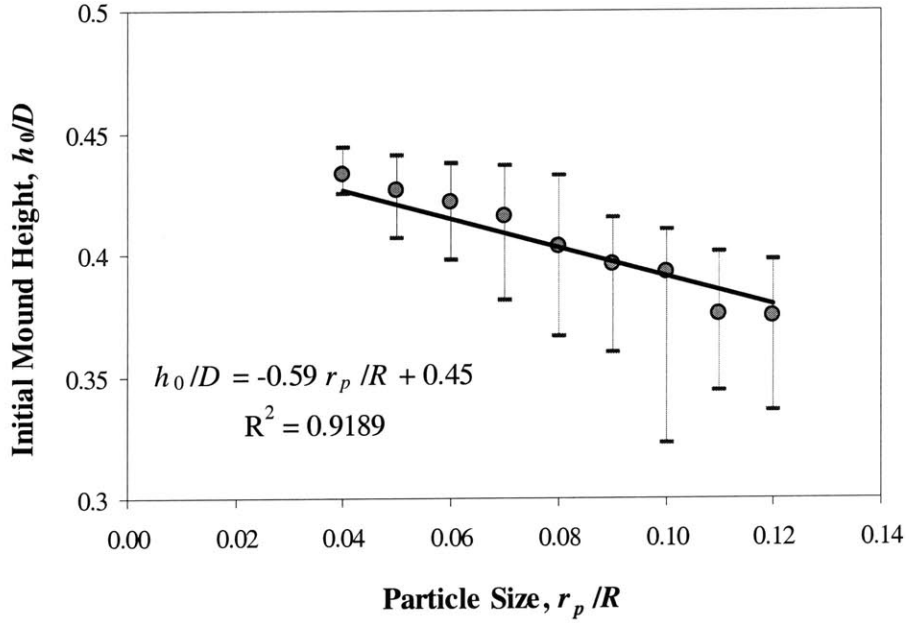

(b) Average h_0 values for the particle radius

Figure 5.25 Correlations for initial mound height parameter, h_0/D

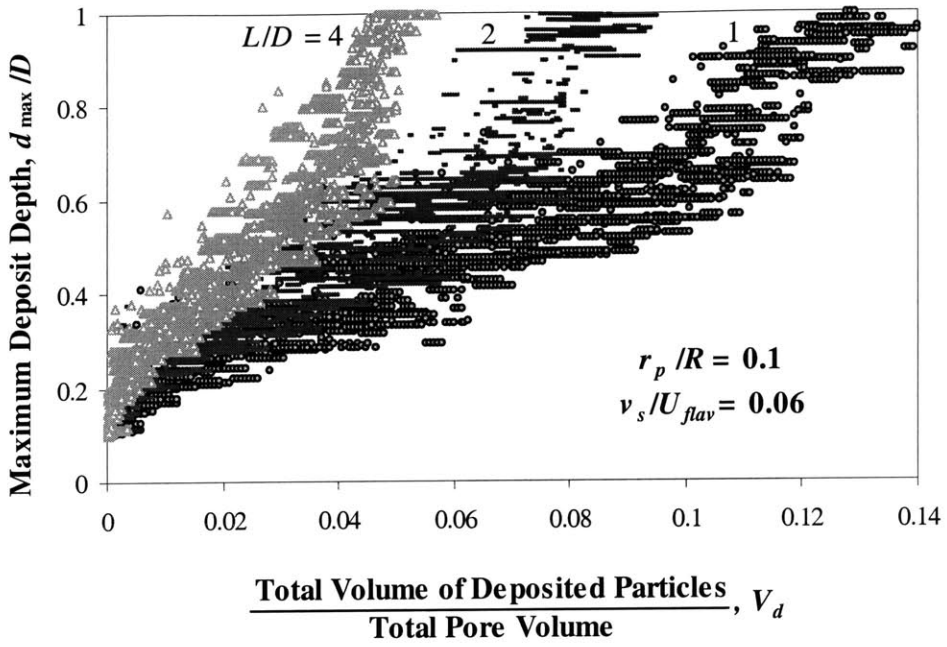

Figure 5.26 Effect of pore tube aspect ratio on deposit depth

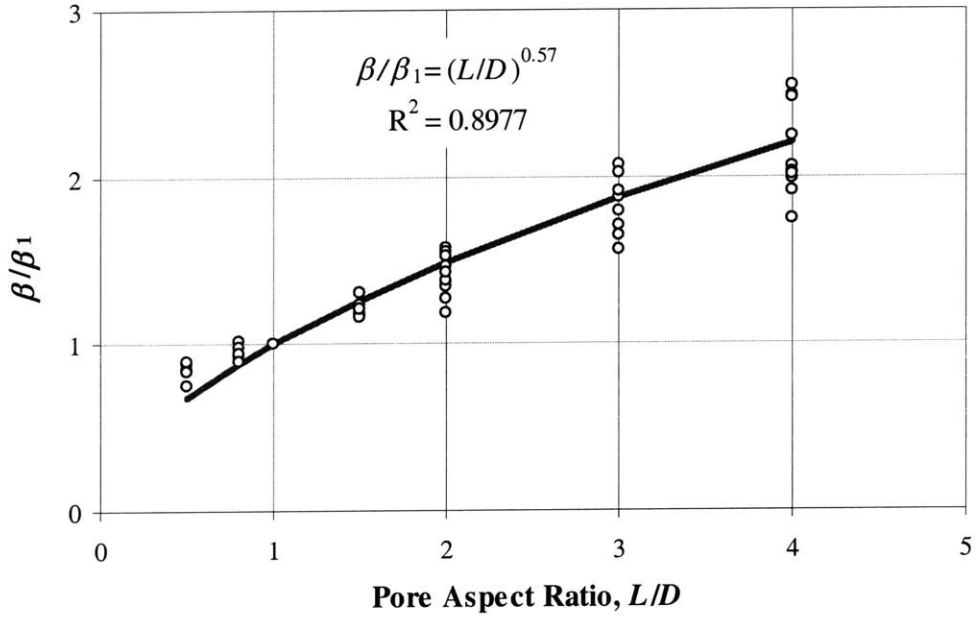

Figure 5.27 Effect of pore aspect ratio on rate of deposition depth, β

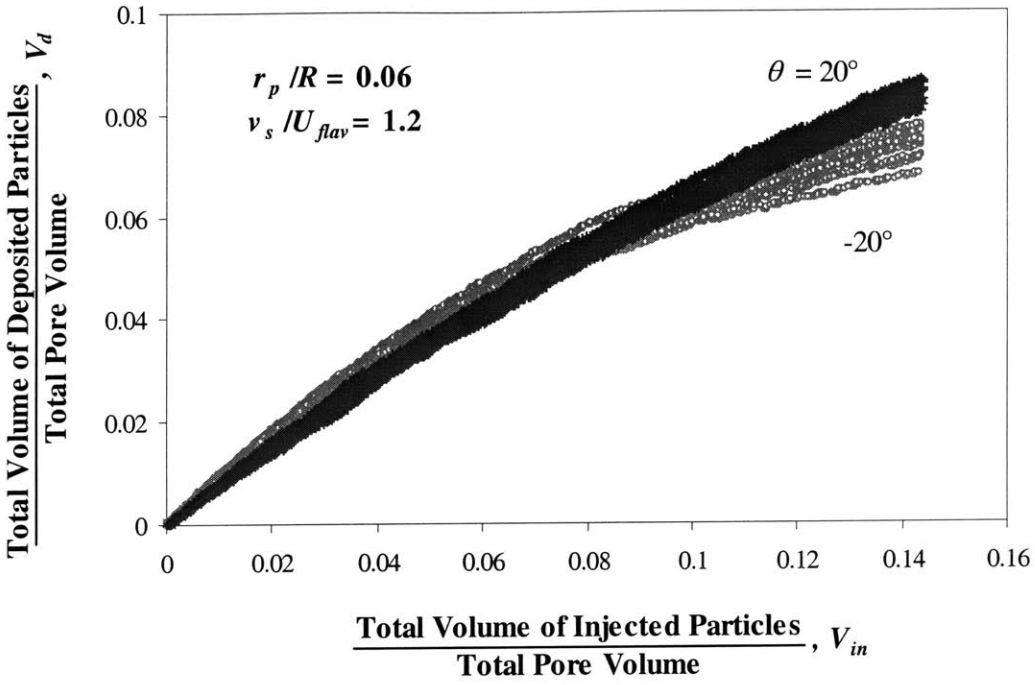

Figure 5.28 Effect of dip orientation on particle deposition

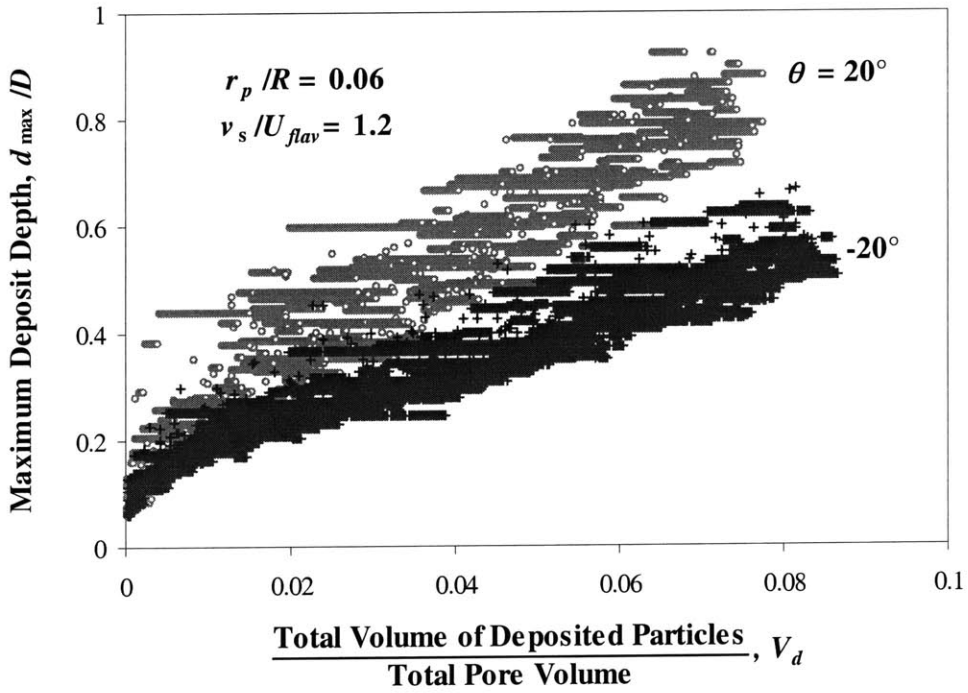

Figure 5.29 Effect of dip orientation on deposit depth

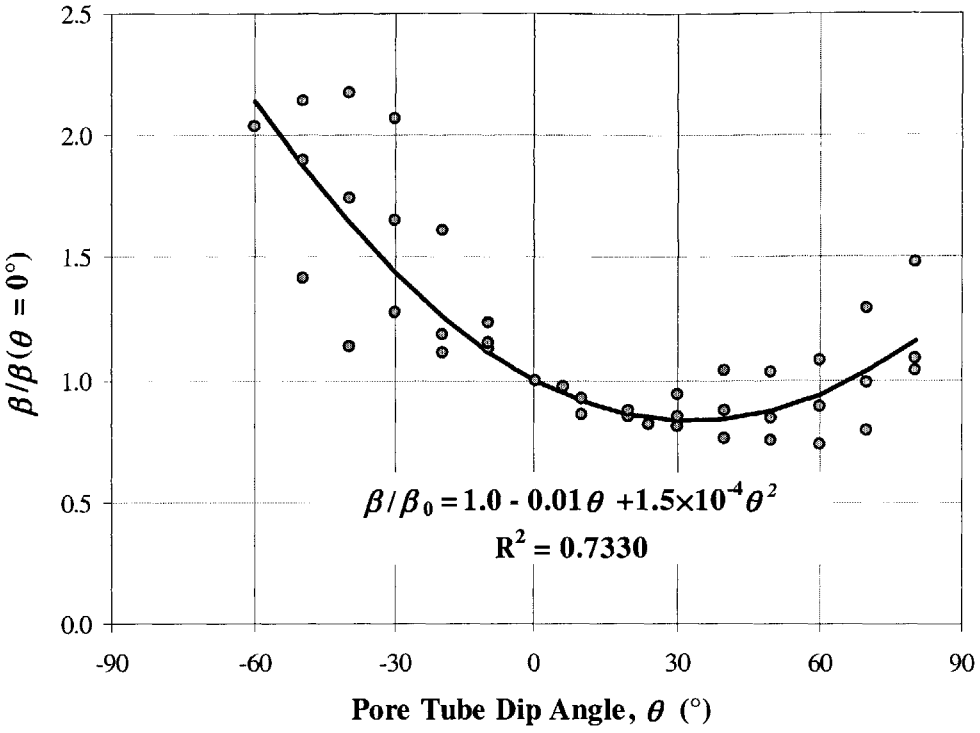

Figure 5.30 Correlation for rate of deposit depth as a function of pore dip angle

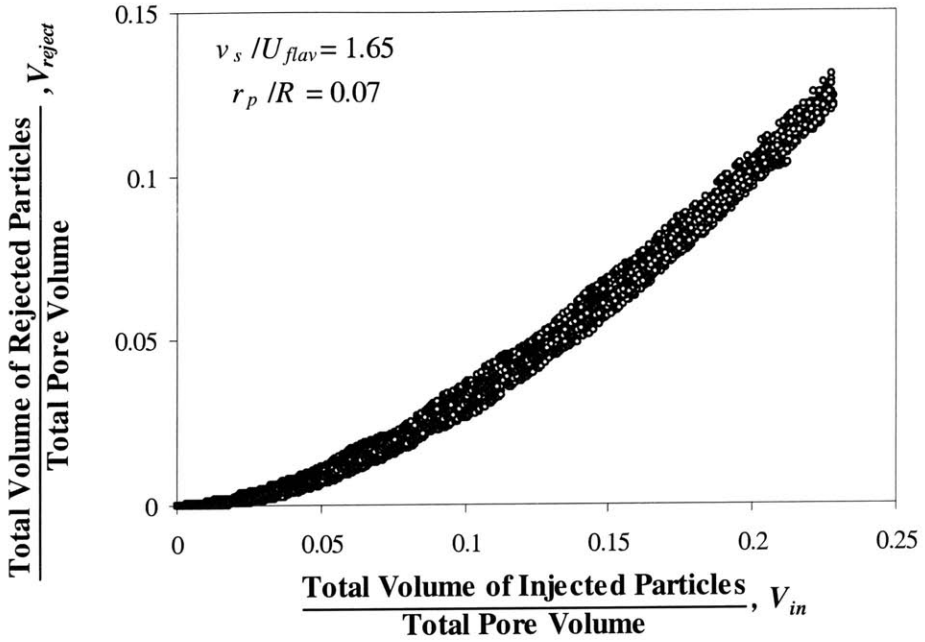

(a) Simulated results

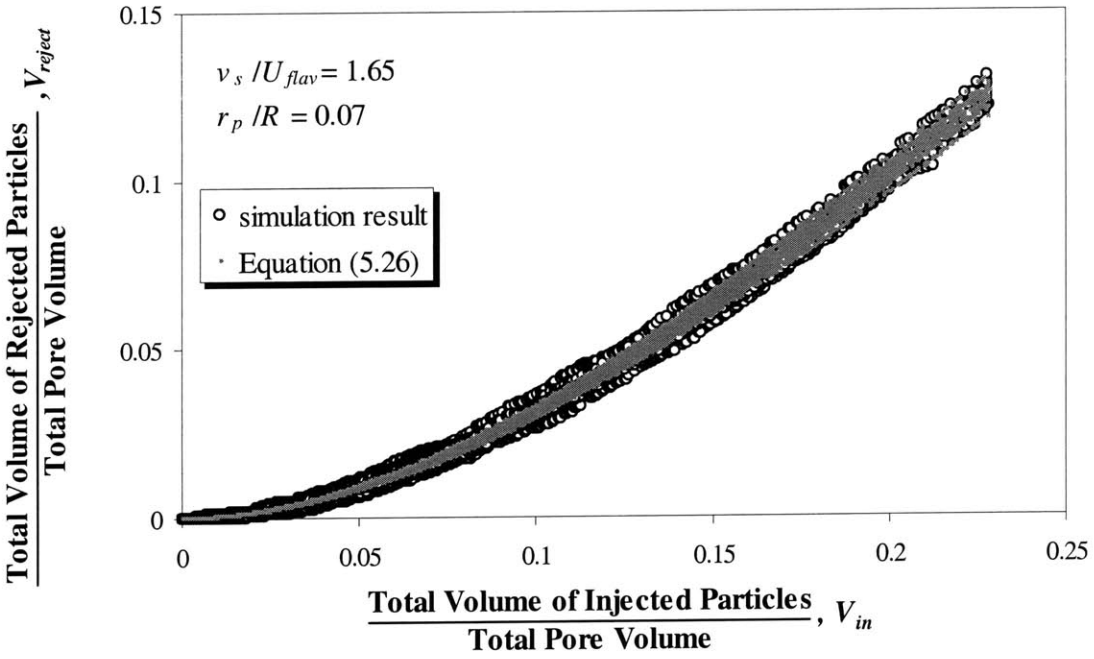

(b) Comparison with analytical estimates of V_{reject}

Figure 5.31 Accumulation of rejected particles at the pore inlet

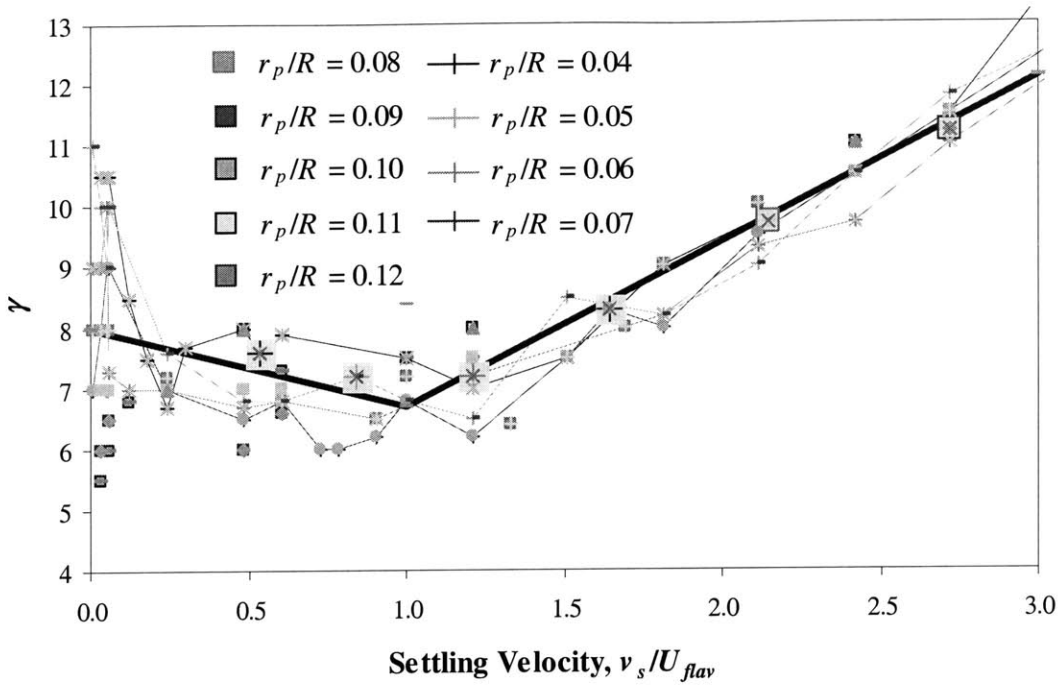

Figure 5.32 Correlations for rejection efficiency parameter, γ

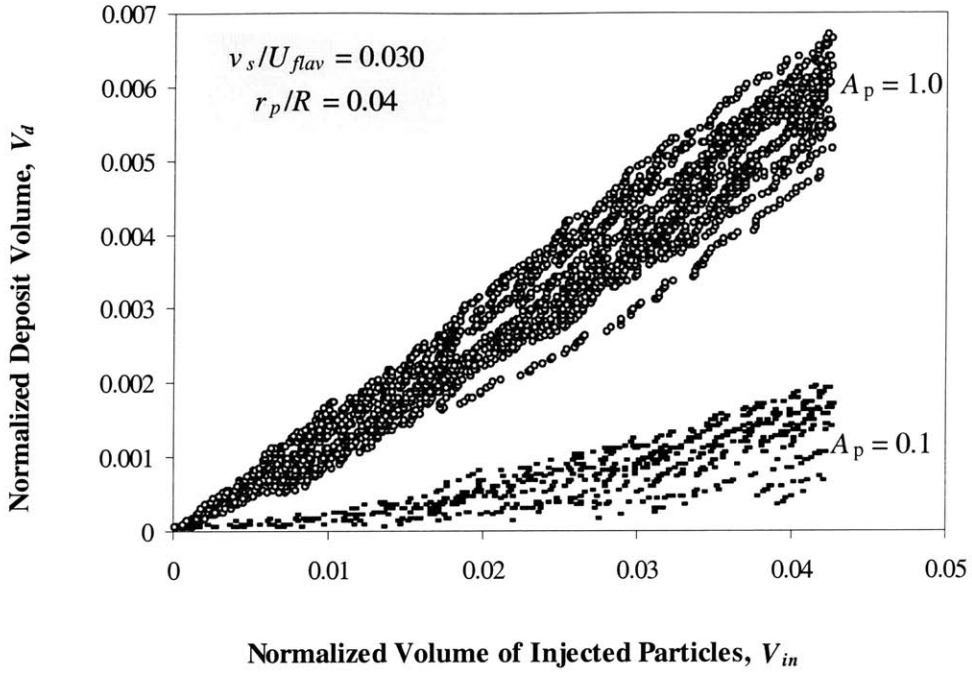

(a) Linear relationship with V_{in}

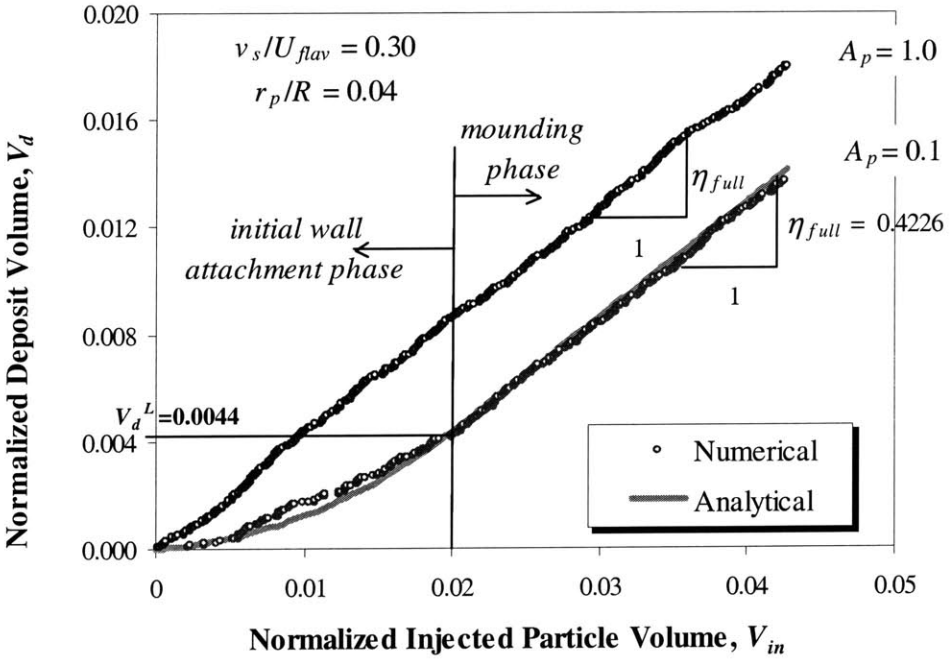

(b) Nonlinear relationship with a higher settling velocity

Figure 5.33 Effects of attachment probability on particle collection in model pore tube

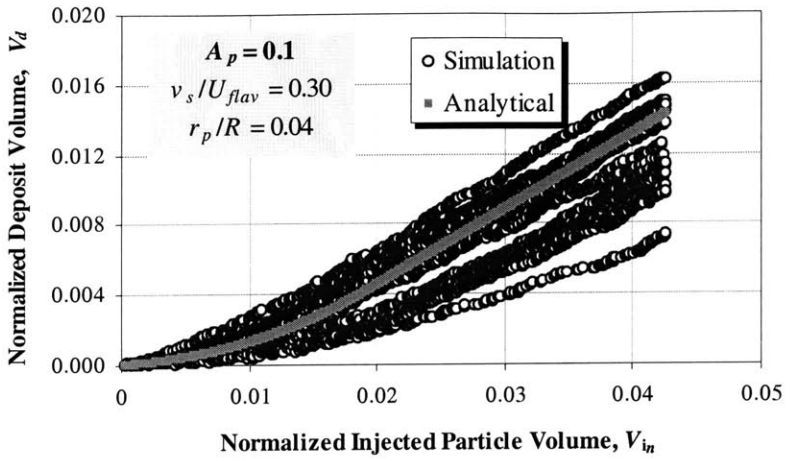

(a) $A_p = 0.1$

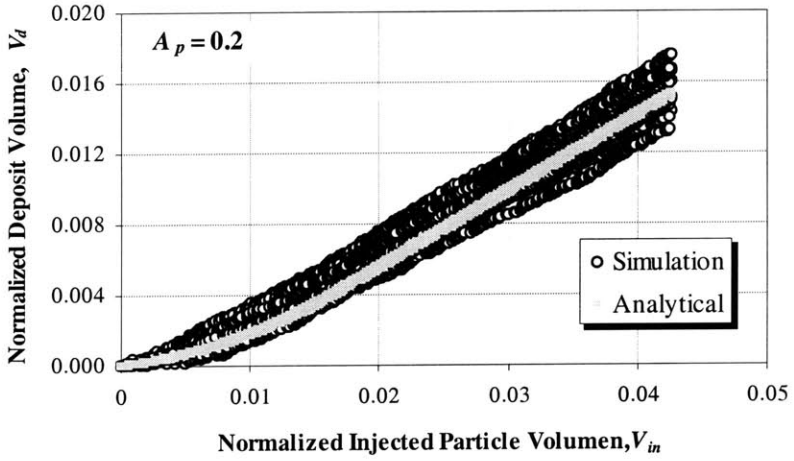

(b) $A_p = 0.2$

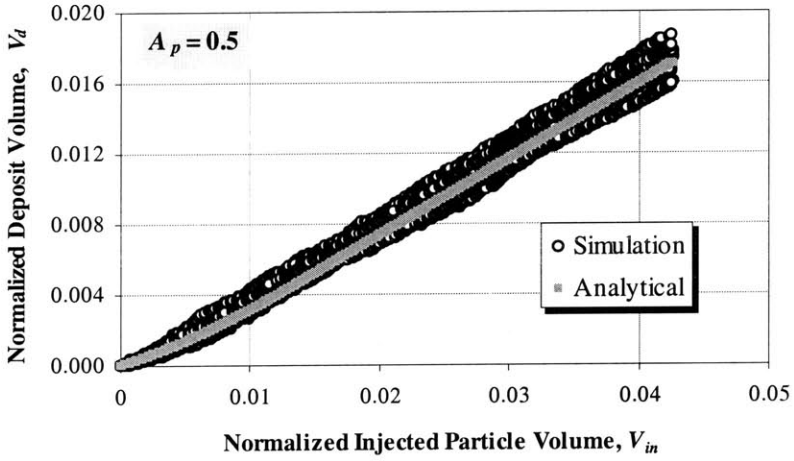

(c) $A_p = 0.5$

Figure 5.34 Comparison of simulated and analytically computed deposit volumes for selected attachment probabilities

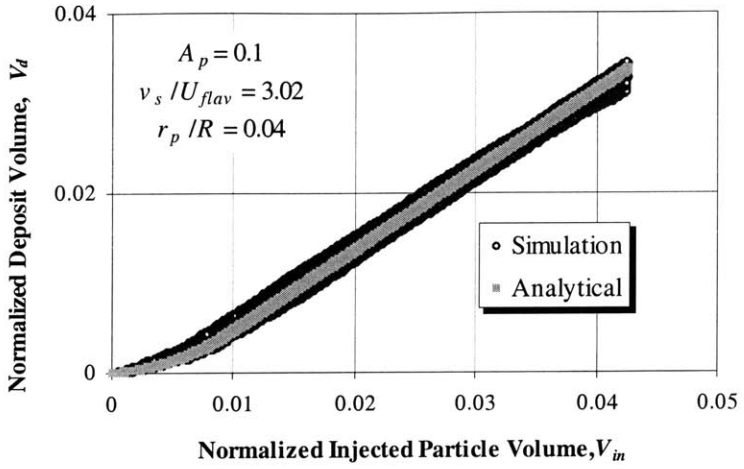

(a) $r_p/R = 0.04$

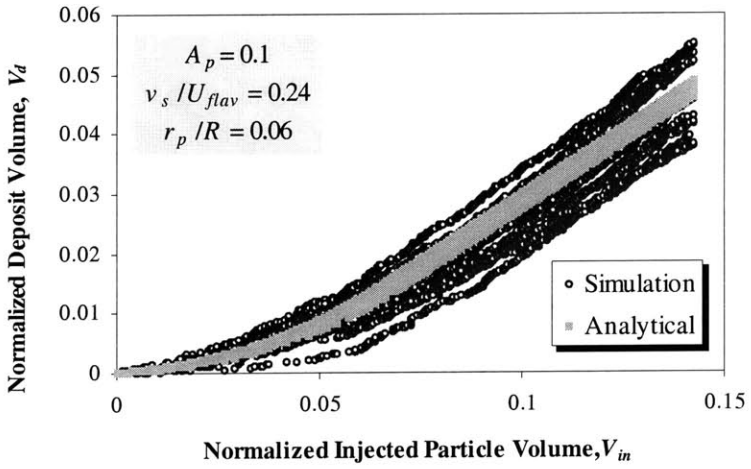

(b) $r_p/R = 0.06$

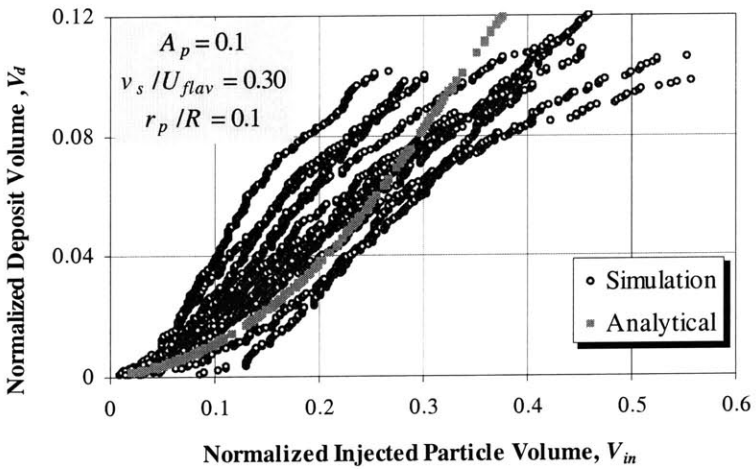

(c) $r_p/R = 0.1$

Figure 5.35 Effect of particle size on surface saturation, V_d^L

Table 5.1 Parameters for base-case simulations

Pore diameter, D	[mm]	1.0
Pore tube aspect ratio, L/D	[-]	1
Dip angle, θ	[°]	0°
Attachment probability, A_p	[-]	1
Viscosity of suspension, μ/μ_w	[-]	3
Density of the suspension, ρ/ρ_w	[-]	1.2
Particle concentration		10 particles/pore volume
Flow rate, Q	[mm^3/sec]	0.785
	[pore volume/sec]	1
Average flow velocity, $U_{flav} = Q/A$	[mm/sec]	1.0
Time step, Δt	[sec]	0.01
Number of iterations		50
Total particles injected		1000

Table 5.2 η values from linear regression and R^2 values

r_p/R	v_s/U_{flav}	η	R^2
0.04	0.00	0.047	0.6855
	0.01	0.083	0.8841
	0.03	0.136	0.9458
	0.05	0.172	0.9476
	0.12	0.267	0.9806
	0.18	0.327	0.9909
	0.30	0.429	0.9885
	0.54	0.576	0.9951
	0.60	0.611	0.9934
	1.21	0.842	0.9961
	3.02	0.897	0.998
0.06	0.06	0.206	0.9465
	0.12	0.275	0.9659
	0.24	0.389	0.9877
	0.48	0.542	0.9869
	0.60	0.605	0.9944
	1.21	0.853	0.9974
	3.02	0.899	0.9974
0.08	0.01	0.083	0.6749
	0.03	0.122	0.8212
	0.05	0.147	0.7946
	0.06	0.145	0.8941
	0.24	0.271	0.9184
	0.48	0.425	0.9613
	0.60	0.546	0.9794
	0.97	0.722	0.9742
	1.21	0.765	0.9792
	1.81	0.839	0.9843
	2.42	0.872	0.9863
	2.72	0.852	0.9846
	3.02	0.848	0.9859

r_p/R	v_s/U_{flav}	η	R^2
0.09	0.03	0.201	0.8372
	0.05	0.225	0.9414
	0.06	0.240	0.9196
	0.24	0.361	0.9805
	0.48	0.470	0.9575
	0.60	0.519	0.9628
	1.21	0.721	0.978
	2.42	0.868	0.9919
	3.02	0.925	0.9968
0.1	0.06	0.208	0.8989
	0.24	0.354	0.9593
	0.48	0.463	0.9632
	0.60	0.524	0.9773
	1.21	0.730	0.9781
	2.42	0.860	0.9879
	3.02	0.922	0.9905
0.12	0.03	0.166	0.8385
	0.05	0.168	0.8151
	0.06	0.224	0.8909
	0.24	0.325	0.8963
	0.48	0.442	0.9348
	0.60	0.509	0.944
	1.21	0.700	0.9593
	2.42	0.876	0.9804
	3.02	0.924	0.9865

Table 5.3 Values of β and h_0 from regression with corresponding R^2 values

r_p/R	v_s/U_{flav}	β	h_0	R^2
0.04	0.01	4.27	0.444	0.7131
	0.03	5.75	0.440	0.8080
	0.05	5.52	0.439	0.7013
	0.06	6.07	0.438	0.7675
	0.18	4.67	0.435	0.7762
	0.24	4.36	0.436	0.5533
	0.48	4.73	0.428	0.8461
	0.60	4.31	0.433	0.7133
	1.00	4.23	0.436	0.7146
	1.21	4.34	0.431	0.7485
	1.51	4.62	0.433	0.8308
	1.81	5.71	0.427	0.8934
	2.12	6.04	0.429	0.7374
	2.42	6.25	0.429	0.8896
	2.72	6.80	0.430	0.8751
	3.02	8.06	0.425	0.7599
0.05	0.01	5.05	0.439	0.6955
	0.03	4.41	0.440	0.6655
	0.05	4.76	0.438	0.7602
	0.06	5.63	0.434	0.6209
	0.12	4.76	0.433	0.7245
	0.24	4.31	0.431	0.6755
	0.48	4.46	0.426	0.7206
	0.60	4.20	0.433	0.7545
	0.84	3.87	0.425	0.6455
	1.00	4.09	0.429	0.6946
	1.21	4.45	0.418	0.7815
	1.51	4.76	0.428	0.7206
	1.81	5.09	0.421	0.7920
	2.12	5.87	0.420	0.8066
	2.42	6.39	0.416	0.9105
	2.72	7.14	0.406	0.8936
	3.02	7.60	0.417	0.8845

Table 5.3 continued

r_p/R	v_s/U_{flav}	β	h_0	R^2
0.06	0.01	4.62	0.434	0.5666
	0.03	4.67	0.434	0.6188
	0.05	4.86	0.434	0.8347
	0.06	3.99	0.437	0.7344
	0.12	3.88	0.432	0.8066
	0.24	4.15	0.425	0.7786
	0.48	3.79	0.421	0.7759
	0.60	3.68	0.426	0.8771
	0.91	3.61	0.420	0.7186
	1.21	3.92	0.412	0.7309
	1.81	4.84	0.414	0.8190
	2.12	5.42	0.412	0.8940
	2.42	6.11	0.414	0.8606
	2.72	7.02	0.408	0.8631
	3.02	7.15	0.397	0.9030
0.07	0.01	3.92	0.436	0.6052
	0.03	3.76	0.435	0.7514
	0.05	4.40	0.431	0.6069
	0.06	4.32	0.430	0.6597
	0.24	4.01	0.422	0.6724
	0.48	3.93	0.417	0.6956
	0.60	3.32	0.418	0.7386
	1.00	4.40	0.419	0.8024
	1.65	4.65	0.399	0.8458
	2.42	5.78	0.397	0.8529
	2.72	6.48	0.381	0.8528
	3.02	6.99	0.388	0.8480

Table 5.3 continued

r_p/R	v_s/U_{flav}	β	h_0	R^2
0.08	0.01	4.01	0.428	0.6308
	0.03	3.63	0.432	0.6761
	0.05	4.20	0.428	0.6859
	0.06	3.59	0.429	0.8266
	0.24	3.77	0.418	0.6857
	0.48	3.47	0.418	0.7311
	0.60	3.63	0.401	0.8640
	1.00	3.43	0.403	0.6960
	1.21	3.93	0.388	0.7845
	1.81	5.09	0.383	0.8339
	2.15	5.33	0.385	0.8397
	2.42	5.68	0.381	0.8359
	2.72	6.52	0.366	0.8505
	3.02	6.93	0.369	0.8546
0.09	0.03	3.28	0.414	0.6687
	0.05	3.38	0.405	0.5476
	0.06	3.29	0.409	0.5083
	0.24	3.51	0.397	0.7459
	0.48	3.19	0.415	0.7976
	0.60	3.29	0.397	0.7081
	1.21	3.62	0.394	0.8016
	2.72	6.32	0.359	0.8591
	3.02	7.22	0.370	0.8647

Table 5.3 continued

r_p/R	v_s/U_{flav}	β	h_0	R^2
0.1	0.03	3.60	0.410	0.5563
	0.06	3.19	0.402	0.6100
	0.30	3.27	0.384	0.7394
	0.60	3.58	0.377	0.6870
	1.00	3.74	0.390	0.7139
	1.21	4.05	0.365	0.7541
	2.42	6.90	0.322	0.8376
	3.02	6.90	0.337	0.8222
	3.36	6.83	0.356	0.8445
0.11	0.24	3.48	0.387	0.6331
	0.48	3.23	0.401	0.5858
	1.00	3.79	0.379	0.6681
	1.21	3.65	0.381	0.6497
	2.42	5.92	0.344	0.8074
	3.02	6.35	0.361	0.8162
0.12	0.03	4.00	0.397	0.1838
	0.05	3.54	0.395	0.5289
	0.06	4.29	0.368	0.6288
	0.24	4.09	0.372	0.6757
	0.48	3.28	0.393	0.6041
	0.60	3.23	0.390	0.6497
	1.00	3.86	0.371	0.6415
	1.21	3.38	0.381	0.6278
	3.02	6.89	0.341	0.8189
	4.83	8.17	0.336	0.8746

CHAPTER 6. SIMULATION OF DISCRETE PARTICLE TRANSPORT EXPERIMENTS

6.0 INTRODUCTION

This chapter describes the application of the pore filtration simulations (Chapter 5) and bubble model (Chapter 4) to interpret high quality experimental measurements of particle transport reported by Yoon et al. (2004). The laboratory-scale experiments were performed in a 16.5cm long water saturated granular filter bed comprised of spherical glass beads (4mm diameter). Dilute suspensions of acrylic particles (diameter ranges 1-25μm) were transported through the filter at a range of flow velocities. An ionic surfactant (Alconox®) was added at a concentration of 0.05% of weight of acrylic particles to prevent aggregation between particles. Figure 6.1 shows a schematic of the experimental set-up with dimensions of the filter bed. The key feature of this experimental study was the development of a high resolution visualization technique that enables direct observation of particles within the filters. The visualization technique uses a laser source, which excites the particles and causes them to fluoresce under blue-green light. During the experiments, images of the filter bed are obtained by a digital camera and later analyzed by an image processor. The resulting light intensity data (emitted by the particles) are converted to an equivalent concentration of particles by calibrating for a system of saturated particles suspended in the water.

Yoon et al. (2004) report measurements of filtration in experiments performed at three different flow rates. Each test comprised two stages: 1) injection of suspension and

2) flushing with clean water. Table 6.1 summarizes the seepage velocities and other material parameters related to the experiments. The seepage velocity is defined as:

$$v = \frac{Q}{An_0} \tag{6.1}$$

where A is the cross sectional area of the glass bead bed, and n_0 its initial porosity.

Table 1 distinguishes between tests using "rough" and "smooth" beads. The beads supplied by the manufacturer are considered to have a "rough" surface based on SEM images reported by Yoon et al. (2004), with surface roughness of the order of 2μm. After repeated cleaning by ultrasonification, the glass beads have abnormally smooth surfaces in SEM pictures, and they are referred as "smooth" beads.

The effluent concentrations were recorded continuously during each experiment. The results are conveniently reported as functions of the fluid volume injected in units of pore volumes, pV, where the initial volume of the sample is:

$$pV = AHn_0 \tag{6.2}$$

If the porosity does not change significantly during the time frame of the injection, the initial pore volume will also remain constant. Thus, the breakthrough time required for one pore volume to pass through the sample can be calculated as:

$$t_{br} = \frac{AHn_0}{Q} = \frac{H}{v} \tag{6.3}$$

Figure 6.2 shows the breakthrough (i.e. effluent) concentration, C_{out}, normalized by the initial concentration, C_0, as a function of the pore volume for the one of the three tests with 'slow' seepage velocity, v = 1.24×10^{-2} cm/sec on rough beads, referred to as 'RS2' in Table 6.1. The effluent concentration starts to increase after the initial breakthrough at 1 pV and increases rapidly until about 2pV and then more slowly until it reaches a stabilized at C_{out}/C_0 = 0.75-0.80 at 5pV - 8pV. If no filtration had occurred, the

stabilized effluent concentration should reach, $C_{out}/C_0 = 1.0$. Therefore, it is clear that filtration does occur during transport of the acrylic particles. After 10 pV, the injection was flushed through at the same flow rate, causing a gradual decrease in effluent concentration. The washing was added to the experiments in order to study the effects of the particle detachment process on the collected particles.

The population of acrylic particles can be retrieved by analyzing the photographic records of laser intensity. As the camera detects fluorescence from both mobile particles in the suspension and immobile ones collected by the beads, the relative concentration corresponds to the sum of the suspension concentration, C, and deposit concentration, S. Figure 6.3 shows the evolution of the relative concentration, $(C+S)$ at one point within the sample, at z = 1.8 cm, for the 'RS2' test. This particular observation elevation is near the top of the sample and hence, the relative concentration rises almost immediately after the start of injection. The relative concentration increases at a decreasing rate with pore volume injection and with constant rate for injections beyond 5 pV (until the end of the injection stage at pore volume of 10 pV). The decrease in concentration due to subsequent water flushing reduces the relative concentration to a residual value of filtered material (i.e. $C+S/C_0$ =3.4 at 15pV). Figure 6.4 shows the profile of relative concentration based on measurements at 7 elevations at 10pV (equivalent to $t = 10t_{br}$ = 1371 secs).

6.1 EXPERIMENTAL OBSERVATION AND CONTINUUM MODEL

During the experiments, Yoon et al (2004) observed that particles that had been deposited at certain locations were released after a while, during both injection and flushing stages. They refer to this type of filtration process followed by detachment as *hindrance*. The remaining fraction of filtered material is referred to as *entrapped* particles. By including the detachment process, the continuous increase in breakthrough concentration observed in output concentration measurement in Figure 6.2 can be explained since the process will effectively decrease filtration rate until a stabilized value is reached. The increase in effluent concentration between 1pV and 8pV in Figure 6.2 was

attributed to hindrance because it temporarily delays the breakthrough of particles (due to the time required for the hindrance -detachment process).

In magnified snapshots of grains taken during experiments, collections occur both on the surface of the beads and close to parts of contact between beads (solid-solid contact points). Yoon et al. (2004) refer to these collections on the surface or near contact points as *surface* entrapment/hindrance or *contact* entrapment/hindrance respectively. They hypothesized that the surface entrapment occurs mainly due to roughness on surface. The role of surface roughness was investigated by Yoon et al. (2004) through evaluation of the experimental results with smooth and rough beads. Figure 6.5a compares the relative concentration profiles at $10pV$ (after injection stage is finished), average values from all slow tests with rough (RS1-3) and those from smooth glass beads (SS1-3) with error bar indicating their standard deviations. Except for minor changes in porosity (from 0.367 to 0.374 in average) and seepage velocity (from 1.36×10^{-2} cm/sec to 1.38×10^{-2} cm/sec in average), all experimental conditions were identical.

The large difference in concentration profile clearly shows the important role of the surface roughness on particle collection. Figure 6.5b compares the deposit concentration profiles (S/C_0) after the wash stage is completed (note suspension concentration $C = 0$ in wash stage). These profiles indicate the amount of collected particles that survived the flushing stage, and therefore, are most firmly attached to the grains. Microscopic images during the 'Smooth Slow' tests clearly showed the particle collections on bead surfaces during the injection stage are almost completely lifted away at the end of the washing stage, leaving only particles deposited near solid-solid contact points. This suggests that the particles positioned on relatively smooth surface are only temporarily attached (i.e. by surface hindrance) and all firm collections are purely by contact entrapment. Therefore, the difference between rough bead and smooth bead results should specify the amount of particles firmly collected due to surface roughness (i.e. surface entrapment). This observation on the role of surface roughness in the attachment process agrees well with the adhesion model presented in Chapter 2, where the fate of a particle impinging on a protrusion is obtained through analytical calculations of driving and resisting moment. However, it is unclear what fraction of the particles

collected near contact points were detached. In short, it is difficult to distinguish contact hindrance from contact entrapment.

Yoon (2004) applied a continuum model to simulate the tests. The one-dimensional mass conservation equation applies:

$$\frac{\partial(nC)}{\partial t} + n\frac{\partial C}{\partial z}v - \frac{\partial}{\partial z}\left(nD\frac{\partial C}{\partial z}\right) = -\frac{\partial nS}{\partial t} \tag{6.4}$$

where z is the coordinate measured from the top of the column (Figure 6.1), C is the concentration of particles, and S, the concentration of the filtered material (defined as the mass of filtrates per unit pore volume). Equation 6.4 can be compared directly with equation 2.4 where the specific deposit σ and the deposit concentration S are related as follows:

$$S = n\sigma \tag{6.5}$$

where σ is the specific deposit (i.e. the mass of filtered particles per unit medium volume).

The detachment of deposited particles has been observed in the colloid transport literature (e.g. see Harvey and Garabedian, 1991) and is commonly modeled as a two-site adsorption/desorption process as explained in Section 2.4. A first order adsorption-desorption law in equation (2.14) can be re-written for the deposit concentration S:

$$\frac{\partial S(z,t)}{\partial t} = k_f C - k_r S \tag{6.8}$$

where k_f and k_r are the forward and reverse adsorption rate constants, respectively.

Hendry et al. (1997) propose a slightly different model in which desorption occurs only with the reversible deposit of concentration S_r (as distinct from the irreversible deposit, S_{irr}).

$$\frac{\partial S(z,t)}{\partial t} = \frac{\partial S_{irr}}{\partial t} + \frac{\partial S_r}{\partial t} \tag{6.9}$$

$$\frac{\partial S(z,t)}{\partial t} = k_{irr} C + k_d C - k_r S_r \tag{6.10}$$

In this model, k_d denotes the filtration rate for reversible (i.e., detachable) deposit and k_{irr} for irreversible deposit, k_r is referred to as detachment rate, rather than the reverse adsorption rate.

This 'two-site' model has been used for latex spheres (Yan, 1996), bacteria (Hendry et al. 1997) and clay particles (Compère, 2001). Yoon (2004) has applied equations 6.9 and 6.10 to interpret the breakthrough curve and the normalized relative concentration profile in Figures 6.6a and b.

The rate of entrapment seems to remain constant and control the stabilized filtration rate. Contact entrapment process that happens at contact points between grains should intrinsically be a process that is limited by the number of contacts (coordination number). Both contact and surface entrapment can be limited by the number of protrusions/capacity of contact points in nature and leads to decreasing filtration rate unless the previously collected particles replace protrusions. Therefore, it seems that the extent of filtration during the tests were well within the capacity of the filter and no significant change in filtration process had occurred.

The rate parameters (k_{irr}, k_d, k_r) appearing in equation 6.10 were obtained by fitting the breakthrough curve (Figure 6.6a) during the injection stage. Thus, the analytical solution matches the measured values very well up to $10pV$, but is less accurate in predicting the subsequent flushing stage. However, the relative concentration profile is not matched as well by the two-site model. Specifically, the analytical solution fails to predict the nonlinear spatial distribution of relative concentration values with depth. The two-site model predicts smaller changes in relative concentration through the filter bed than are measured, but does achieve better agreement closer to the source. Although the combined concentration of deposit and suspension, (C+S) is shown, the nonlinear profile in Figure 6.6b is controlled by the deposit concentration, S, since the suspension concentration does not differ much (i.e. the output concentration is 0.8 of the initial

concentration C_0). Therefore, it can be deduced that the attachment rate is higher near injection point and decreases with depth in the filter bed. This feature can apparently not be described by even quite sophisticated continuum models.

6.2 SELECTION OF PARAMETERS FOR NETWORK MODEL SIMULATIONS

This section describes the application of the network model presented in Chapter 3 to model the filtration process of the particles. Individual links in the network model are based on results of simulations of particle collection for the model pore presented in Chapter 5. It has also been assumed that the orientation of pores is uniformly distributed and the average value of collection efficiency (i.e. η_H in equation 5.11) is used throughout.

6.2.1 Pore size distribution

The granular bed used in the experimental study by Yoon et al. (2004) was made with uniform glass beads. The size distribution of pores and pore throats of the granular system with uniform spheres has been evaluated inspected by several studies. Yanuka et al. (1986) studied a reconstructed porous medium using randomly packed ellipsoids. The pore space was described by an orthogonal three-dimensional system as shown in Figure 6.7. They described the pore space for three different kinds of regular packings: uniform spheres (with diameter, D_g) the simple cubic, orthorhombic and rhombohedral. The unit cells of these three packings are sketched in Figure 6.8. Table 6.2 shows the porosity and the average pore sizes (calculated analytically by Kruyer, 1958) of all three packs quoted from Yanuka et al. (1986).

The throat radius, R_{throat} (referred to as 'neck' radius by Yanuka et al., 1986) indicates the radius of the largest circle that can be inscribed in the narrow passage of the sphere packing. The porosity of the glass bead bed, $n = 0.38$, is close to the value for the simple orthorhombic packing. With given grain diameter, D_g = 4mm, this gives the

average pore body size, $2a = 2b = 2c = 2.11$ mm, and the throat radius, $R_{throat} = 0.57$ mm. Based on this information, the mean pore and pore throat radii were chosen $R_{mean} = 1$ mm and $(R_{throat})_{mean} = 0.57$mm.

The ratio between mean pore size and mean pore throat size is known as the aspect ratio of the pore space and quoted to be 2 for unconsolidated porous media by both Payatakes et al. (1980) and Jerauld and Salter (1990). Hilpert et al. (2003) also performed a study on the calibration of a pore network using a pore-morphological analysis for a random spherical packing with the same grain-size statistics and porosity as the current material of interest. One of the materials was relatively uniform glass bead. They reported an average pore body radius of 0.03 mm for a system made of 0.1156 mm diameter beads with a porosity n= 0.372. The ratio between pore radius to the glass bead radius (0.51) is similar to the value (0.5275) by Yanuka et al. (1986) shown in Table 6.3.

The distribution of pores and pore throat size are approximated with a Hertzian distribution with following probability density function:

$$F(R) = 1 - \exp(-\alpha R^2) \tag{6.11}$$

where $\alpha = 1/R_{mean}^2$. This distribution has been reported to fit other geological filter materials (Hwang and Redner, 2001) and is also analytically convenient. Figure 6.9 shows the pore and pore throat (number) distributions obtained based on equation (6.11), which clearly shows two distinctive distributions for throats and pores.

6.2.2 Filter coefficient

The parametric study in Chapter 5 has provided relationships for the collection efficiency of particles with radius, r_p in a pore tube of known diameter, D (= $2R$), and length, L, in equations 5.7, 5.8 and 5.11:

$$\eta_1 = \min\left[0.75\left(\frac{v_s(r_p)}{U_{flav}}\right)^{0.49}, 0.9\right] \tag{5.7bis}$$

$$\eta = \eta_1 \left(L/D\right)^{0.57} \tag{5.8bis}$$

$$\eta_H = \frac{\eta}{1.6} \tag{5.11bis}$$

Yoon et al. (2004) measured the velocities of free falling latex particles immersed in a column filled with still water by comparing the fluorescence from bursts of laser energy. By analyzing the intensity profile of the column, Yoon et al (2004) are able to define the fraction of particles with settling velocities in a certain range. The measured settling velocity ranges from $v_s = 1.26\times10^{-4}$ cm/sec to 2.01×10^{-3} cm/sec, which correspond to 1/6 to 1/100 of the seepage velocity of the 'slow' test, $v = 1.36\times10^{-2}$ cm/sec. The particle sizes, however, cannot be back-calculated from Stokes law in (equation 4.10) because of uncertainties related to the density of the particles and their non-spherical shapes. Instead, particle size distribution and particle population numbers were measured using a commercial electric particle size analyzer (Multisizer 3 Coulter Counter by Beckman Coulter, Inc.). The measurements produced 256 ranges of particle sizes (each represented by a single average value) and number of particles in each range. Assuming that the particles are spherical, this measurement can be interpreted as a volumetric distribution of the particle size, as shown in Figure 6.10a, with $d_{50} = 7\mu$m ($r_{p50} = 3.5\mu$m). Figure 6.10b shows the results of the sedimentation tests as a plot of cumulative volume versus settling velocity, v_s. By comparing directly the measured particle sizes in Figure 6.10a with those back-calculated from measured velocities using Stokes law, it was found that the particle density from ρ_s =1.07g/cm^3 to 1.18 g/cm^3, (increasing with particle radius).

Figure 6.11 presents the collection efficiency as a function of particle diameter based on equations 5.7, 5.8 and 5.11. With r_{p50} =3.5μm and mean pore throat radius, R_{mean} = 1 mm (i.e. D = 2mm) and pore length L = 2mm, the collection efficiency is found to be, $\eta = 0.066$ for the 'slow' injection test seepage velocity of $v = 1.36\times10^{-2}$ cm/sec.

The same graph also shows values of collector efficiency using trajectory analysis in Happel's unit collector model (equation 4.2) and limit analysis only considering gravitational force, (after Mackie et al., 1987) using the same parameters $r_p = 3.5$ μm, a_g (grain radius) = 2mm, $n = 0.367$, and $v = 1.36\times10^{-2}$ cm /sec.

$$\eta(r_p/a_g)=0.014 \tag{6.12}$$

The unit collector model predicts a much smaller collection efficiency due, in larger part, to the different geometries used in the two models (cylindrical for the model pore simulator versus flow around a sphere in Happel's model). However, it is worth mentioning that the model pore simulator predicts that the collection efficiency increases much faster with particle size than Happel's model. This trend is later borne out by the experimental results with simulations in Section 6.3.

6.2.3 Attachment probability

As previously explained in Chapter 2, it has been noticed that the unit collector theory often fails to predict the collection efficiency, η, especially when repulsive double layer interactions predominate (see, for example, Elimelech and O'Melia, 1990). The easiest and hence, most widely used method to deal with this problem is to introduce an empirical collision (attachment) efficiency to describe the fraction of collisions with filter grains that result in attachment.

$$\eta = \alpha\eta_{full} \tag{6.13}$$

where η is the current efficiency, α the collision efficiency, and η_{full} the 'full' efficiency when all the collisions result in particle collection.

The collision efficiency is comparable to the attachment probability, A_p introduced in Chapter 5, which defines the fraction of particles that will be attached to the pore wall among all particles deposited. However, the attachment probability is limited to particle collection on the pore wall (perfect attachment with A_p = 1 is assumed for mounding particles). Accordingly, the collection rate in the parametric study was found to increase as the deposits accumulates (cf. Figure 5.34). The related correlation, equation 5.35, defines η to increase with the deposit volume, V_d until it reaches a limit value, V_d^L, the surface saturation. However, the assumption of perfect attachment between particles

is too simplistic, not accounting for surface forces acting on particles and the resulting repulsive and attractive interactions between them (which control the particle collections by deposit layer). Surface forces are known to become significant relative to hydrodynamic forces for colloidal sized particles (less than hundred microns) (Russell et al., 1989). Considering that the maximum diameter of acrylic particles used in the tests is 27 μm, and surfactant was used, which further increases repulsive forces between particles, full attachment between particles is unlikely. Accordingly, particle collection for the bubble model is assumed to occur with attachment probability $A_p < 1$, assuming the same empirical format proposed in equation 6.13:

$$\eta = \eta_{full} A_p \tag{6.14}$$

6.3 UNIT BED ELEMENT (UBE) SIMULAITON ON 'SMOOTH SLOW' TESTS

The simplest network model represents the glass bead filter by a single model pore tube. This is identical to the UBE method proposed by Payatakes et al. (1973), Section 2.2.2. The results from this UBE model provide a reference for subsequent bubble model simulations and by comparing UBE and bubble models, it is then possible to appraise the effects of the pore size distribution. For the UBE model, the pore is assumed to have a radius equal to the mean pore throat radius selected in Section 6.2.1 (i.e. $R = R_{mean}$ = 1mm) while the length of the pore, L = 4mm, is assumed equal to the grain diameter, such that the pore tube aspect ratio, L/D = 2. For this model, a total of 43 model tubes are needed to represent the full height of the glass bead filter bed, (i.e. ~17 cm, Table 6.1).

(1) Procedure

The particles follow the propagation rules of a network model presented in Chapter 3 (Figure 3.4). The measured particle size distribution in Figure 6.10a is used, as a form of stepwise function comprising 256 particle size bands. For each size band, the

particle settling velocity, v_s, corresponds to the volume fraction found from the measured settling velocities shown in Figure 6.10b. The time step in the network model is selected to be the travel time of the link of the maximum radius and hence, is equal to the maximum flow velocity. As all model pores are identical in the UBE simulation, the time step is defined by:

$$\Delta t = L/v \tag{6.15}$$

where v is the pore velocity, whose initial value is set as the seepage velocity.

The number of input particles (for the first tube) can be calculated from the known concentration and the assumed particle radii distribution shown in Figure 6.10a using a simple mass balance. For the m^{th} particle size, $r_{p,m}$, the fraction of the particles corresponding to this size is, $F(m+1)$-$F(m)$. Thus the number of particles belonging to the size group per given time step Δt, ΔN_{in}^{m} can be given as:

$$\Delta N_{in}^{m} = C_0 \pi R^2 v \frac{\left(F(m+1) - F(m)\right)}{\frac{4}{3}\pi r_{p,m}^3 \rho_s} \qquad \text{For, } m = 1,\ldots,256 \tag{6.16}$$

For each size band, the collection efficiency is given so that the number of particles that will be collected by the current link can be calculated:

$$\Delta N_{c}^{m} = \eta(r_{p,m}, R, L)\Delta N_{pass}^{m} \tag{6.17}$$

The volume of the filtered deposits at time step T, $V_c\Big|^{T}$, can be obtained from the known number of accumulated particles,

$$N_c^m\Big|^{T} = \sum_{it=1}^{T} \Delta_{it} N_c^m \tag{6.18}$$

$$V_c\Big|^T = 4\pi/3 \sum_{m=1}^{256} r_{p,m}^3 N_{filtered}^m \Big|^T \tag{6.19}$$

Dividing the collected volume with the total volume of particles injected per given time-step, V_{in}, the concentration of the filtered particles for the i^{th} element is given as:

$$S_i(T\Delta t) = \frac{V_c\Big|_i^T}{V_{in}} \tag{6.20}$$

The parameters used for the simulation of the 'Smooth Slow' tests (SS1,2,3) are summarized in Table 6.3.

(2) Detachment rate, k_r

The particles deposited but not yet not attached are considered as hindered particles that can be recaptured by the flow. This detachment ratio, k_r is assumed in the two-site continuum model (equation 6.10). If the number of passing particles in a certain link at a given time step is denoted as ΔN_{in}, the number of entrapped particles, ΔN_{irr} is expressed by:

$$\Delta N_{irr} = \Delta N_{in} \eta A_p \tag{6.21}$$

The remainder of the deposited particles will be considered 'hindered particles', whose number is denoted by ΔN_r, i.e.;

$$\Delta N_r = \Delta N_{in} \eta (1\text{-}A_p) \tag{6.22}$$

The total number of hindered particles will be stored in memory at every element as N_r, and the number detached during a given time step can be given:

$$\Delta N_d = \Delta t N_r k_r \tag{6.23}$$

Consequently, the total number of hindered particles should be updated to $N_{r,\text{new}}$:

$$N_{r,\text{new}} = N_r + \Delta N_r - \Delta N_d \tag{6.24}$$

If $k_r = 1$, all hindered particles will be instantly detached, as if there are no reversible collections. This condition will be referred to as 'full detachment' condition. Accordingly, smaller k_r values cause more hindrance and hence, increase the total deposition of particles. This will, in turn, reduce the concentration of the suspended particles, resulting in a lower breakthrough concentration. However, the breakthrough concentration will increase continuously due to detachment, until a balance between hindered particles and detachment is achieved.

Figure 6.12a shows the breakthrough curves computed by the UBE model with various k_r values for slow tests done with smooth beads (SS1,2,3). The same attachment probability, $A_p = 0.02$ was applied for all simulations. The effect of detachment is clearly manifested by a delayed breakthrough due to prolonged retention of suspended particles. The value of $k_r = 0.0045\text{sec}^{-1}$ gives the best-fit curve although it slightly underestimates breakthrough concentrations during wash stage. Actually, both continuum and discrete model simulations consistently underestimate the breakthrough concentrations during wash stage even when matching closely the injection stage. Yoon (2004) discussed this is due to the reversibility of the entrapped particles: although entrapped particles more firmly attached to the filter grains, they are not irreversibly attached and hence, can be detached and penetrate through the filter bed. It seems the effect of detachment of entrapped particles is particularly obvious during wash stage because of the low concentration of particles.

Figure 6.12b shows the corresponding relative concentration that increases with decreasing detachment rate, k_r as expected and greatly improves the matching with measured data from the full detachment condition simulation. Figure 6.13b shows the simulated deposit concentration profile after wash stage is completed, consistently overestimating the measured values. It is interesting to note that change in k_r values have minimal effect on the final deposit concentration (except for with $k_r = 0.0022\text{sec}^{-1}$, which gives a slightly higher downstream concentration, $z > 14\text{cm}$). This is because all hindered

particles will be eventually detach no matter what detachment rate is assigned, in long term flushing tests. Therefore, the amount of simulated final deposit concentration is determined only by attachment probability that determines the portion of entrapment from deposited amount of particles. The fact that simulated values are overestimated may indicate that some of the entrapped particles were released back to the flow, supporting the hypothesis by Yoon (2004).

Another possible explanation for the overestimation of relative concentration after the injection stage and deposit concentration after wash stage is the pore size distribution. Larger pores have greater capacity for carrying the pore fluid and have smaller collection efficiency for a given size of transported particle. Therefore, a dispersed pore system will bring out a higher initial breakthrough concentration compared to the UBE model. The following sections present the results of simulations with a bubble model, which simulates this dispersed pore system.

As expected from the very dilute concentration of the suspension as well as the large difference between the pore size and those of particles (R/r_{p50} = 200), hardly any change in pore pressure was produced during the simulations (cf. Chapter 7). In addition, the depth of collected deposit was found minimal so that almost no collections in model tube inlet by blocking the particles introduced i.e., the 'rejected' particles defined in Chapter 5 were found.

6.4 NETWORK MODEL SIMULATION

6.4.1 Construction of a bubble model

A bubble model, as explained previously in Section 3.4, comprises a serial linkage of parallel cylindrical tubes of constant length. In order to represent the pore throats and pores in the granular filter beds, the current analyses introduce two distinctive Hertz distributions, one with mean radius, R_{mean} = 1 mm, to represent the pores and the second with $(R_{throat})_{\text{mean}}$ = 0.57 mm for the pore throats. Half of the bonds are assumed to represent pore throats while the other half are the pore bodies. All model pores have the same length, L = 4mm (as in the previous UBE simulation).

The flow rate to the model, Q, should be determined for the breakthrough time, t_{br} of the model to correspond that of the experiment. In other words, average velocity of the model should match the real value. With the UBE model, it was a straightforward operation as the same pore fluid velocity occurred in each bond. For the bubble model, the pore fluid velocity varies through each bond, detailed calculations are needed. Flow distributes to each bond in bubble, i, in proportion to R^4, i.e. for bond, k, with radius R_k:

$$q_k = Q\frac{R_k^4}{\sum_{k=1}^{N} R_k^4} \quad \text{for } k = 1, 2, 3, \ldots W \tag{6.25}$$

where W is the total number of bonds belongs to each bubble.

The subscript indicating the bubble, i, is omitted for simplicity in equation (6.25). The velocity of the bond, v_k is defined as

$$v_k = \frac{q_k}{\pi R_k^2} = \frac{QR_k^2}{\pi \sum R_k^4} \tag{6.26}$$

The time step in the network simulation is picked as the shortest travel time for all bonds in the model:

$$\Delta t = {L_m}/{v_{\max}} \tag{6.27}$$

where L_m and $v_{\max}$ denote the length and the maximum velocity of the m^{th} bubble where the bond belongs.

At each link, the total volume flow rate given to the link is partitioned between fraction that passes through, q_k^p and the remainder that will stay at the entrance, $(1-q_k^p)$. The ratio between q_k^p and $(1-q_k^p)$ should be proportional to that of the travel time of the given link to the given time step, as explained in Chapter 3.

$$q_k^p = q_k \frac{\Delta t}{L / v_k} \tag{6.28}$$

where L denotes the length of the current bubble. Substituting equations (6.27),

$$q_k^p = q_k \frac{v_k}{v_{\max}} \frac{L_m}{L} \tag{6.29}$$

Then the total flow rate passing through the bubble during the given time Δt can be determined as:

$$Q^p = \sum_{k=1}^{W} q_k^p \Delta t \tag{6.30}$$

This flow rate, Q^p denotes the effective flow rate of the model and its ratio to the total flow rate injected to the model, Q, corresponds to the ratio of the average seepage velocity of the bubble, v_{avg}, to the maximum pore velocity, $v_{\max}$:

$$\frac{v_{avg}}{v_{\max}} = \frac{Q^p}{Q} \tag{6.31}$$

If there are sufficient bonds at each bubble, the seepage velocity will not deviate significantly. The velocity is matched with the known seepage velocity and as a result, the flow rate can be determined.

$$t_{br} = H / v = \sum_{i=1}^{B} \frac{L_i}{v_{avg,i}} \tag{6.32}$$

6.4.2 Effect of pore velocity on attachment probability and detachment rate

In contrast to the UBE model, the bubble model has a distribution of pore size and corresponding pore fluid velocity. Therefore, it is important to decide how the empirical parameters (i.e. A_p and k_r) might be affected by the pore fluid velocity. The effect of injection velocity on filtration is clearly illustrated in Figure 6.13, which compares the measured breakthrough curves during the injection period (upto 10 pV) for three tests with different injection velocities ('slow', 'medium' and 'fast'). The effluent concentration builds up more rapidly and reaches a high plateau in the fast tests.

The previous section has shown (from UBE model simulations in Figure 6.12b) that the rate of initial effluent concentration build-up is controlled by the detachment rate, k_r. Therefore, it is likely that detachment rate increases with the pore velocity:

$$k_r = \bar{k}_0 v \tag{6.33}$$

where $\bar{k}_0$ [1/L] is a constant that will be determined at the reference value of $v_0 = 1.38\times10^{-2}$ cm/sec, used in the 'Smooth Slow' tests, and will be referred to as the 'reference detachment rate'. Therefore, a value of $\bar{k}_0 = k_r/v_0 = 0.33$ cm^{-1} as used in the best-fit UBE simulation given in Figures 6.12.

Figure 6.14a,b present the breakthrough curve and the concentration profiles (at the end of injection period and the wash period) for the 'Smooth Slow' tests. The attachment probability, by definition, partitions the deposited particles into entrapped (either on the surface or at a solid-solid contact point) and hindered fractions. Therefore, it seems reasonable to assume it is less sensitive to seepage velocity. Following this rationale, a constant value of $A_p = 0.02$ was used for the bubble model simulation to match the breakthrough curve, with $\bar{k}_0 = 0.28$ cm^{-1} (vs. $\bar{k}_0 = 0.33$ cm^{-1} for UBE) with these parameters, the bubble model show slightly higher initial rates of concentration build-up despite the decrease in assumed detachment rate.

In the bubble model, hydrodynamic dispersion is intrinsically modeled through distributed bond sizes where flow velocities differ according to equation 6.26. As a result, the average flow velocity in the bubble, v_{avg}, is different from the maximum flow velocity, v_{max}, in an individual bond (equation 6.31). Then, the particles flowing through larger bonds will arrive faster than those in smaller bonds, simulating the real porous media behavior. Therefore, the ratio between v_{avg} and v_{max} is the controlling factor for the first arrival of particles, which is determined solely by the distribution function of the bonds. The first arrival occurs at $0.9pV$ in the current bubble simulation, which is slower than the measured first arrival at $0.6pV$.

The effluent concentration build-up rate progressively slows down in the bubble model, reflecting the effect of decreased overall detachment rate, and producing better agreement with the measured curve during the wash stage was found for the UBE model. The bubble model simulation also matches the trend of measured relative concentration profile both at the end of injection stage and at the end wash stage as clearly shown in Figure 6.14b[11]. This reflects the role of bond size distribution on collection rate for different sized particles.

When the same values of A_p and $\bar{k}_0$ are used to simulate the 'Smooth Medium (SM1,2,3,4,5)' and 'Smooth Fast (SF 1,2,3)' Figure 6.15 and Figure 6.16 were obtained. In both cases, bubble model underestimates the stabilized breakthrough concentration between $6pV$ and $10pV$ very slightly, and those during the wash stage. As a result, simulated concentration profiles (both after injection and wash stages) slightly overestimate the measured data both cases. As noted earlier in Section 6.3, the reason that the simulated breakthrough concentrations are lower than measured values during the wash stage seems to be related to the detachment of some entrapped particles during the wash stage.

In all three cases, when the concentration profiles are compared in Figures 6.14b, 6.15b and 6.16b, it is noticeable that the concentrations near the injection point were consistently overestimated by the simulation, particularly after the wash stage. Considering that larger particles have higher deposition rate (Figure 6.11), deposit

[11] Large scatter in the results of bubble model is due to the changes in total volume of bubble, in which the bond sizes are randomly assigned. The total volume of maximum sized bubble is about 8% larger than that of the smallest.

concentration near injection point should be controlled by that of the larger particles. Therefore, the characteristically low deposit concentration near the injection point (z = 1.2cm) should indicate a lower attachment probability of larger particles than expected, or the ease of reversing larger particles entrapped in contact points. Further observational study, especially the particle size distribution after injection/wash stages to compare the simulated results will be needed to make any assumption on the dependence of reversibility of contact entrapment on the particle size. It was concluded that at this point with given information, the assumption of detachment rate increasing with the pore velocity should be chosen to explain the dependence of measured results on injection velocity.

6.4.3 Effect of surface roughness

The parameter A_p describes the probability that a deposited particle (due to gravity) will remain attached either by the surface roughness or at a solid-solid contact point. Therefore, the correlation between the attachment probability and the pore velocity is more difficult to define than the detachment rate (equation 6.35). In the previous section, it was concluded that the attachment probability related to solid-solid contact points (i.e. contact entrapment) is largely unaffected by the pore velocity. Surface entrapment, on the other hand, must be strongly influenced by hydrodynamic forces and pore fluid velocity.

For one of the 'Rough Slow' test (RS3), Yoon et al. (2004) measured the effluent particle size distribution with a Coulter Counter. Figure 6.17a compares the measured effluent particle volume distribution at $10pV$ with that of inflow shown in Figure 6.10a. It is clear that the population of smaller particles in the effluent is underestimated by the bubble model. In Figure 6.17b, the measured input and output particle volume distribution are compared by plotting discrete (not cumulative) particle volume against size. It is noticeable that the effluent volume of particles that are smaller than approximately 5μm diameter is not changed from injected volume, while that of larger particles is grossly decreased. This observation suggests that particles smaller than a limit size are not collected at all.

The adhesion theory by Varidyanathan and Tien (1988) presented in Chapter 2 describes an adhesion mechanism similar to surface entrapment proposed by Yoon et al. (2004), considering that a particle in contact with a plane boundary will stay in place when it acquires sufficient resisting moment against the moment rolling it over a surface protrusion. The adhesion theory also specifies that the resisting moment mainly comes from van der Waals force, while hydrodynamic drag works as driving force. According to this theory, a particle cannot be collected if the drag force, or equivalently, the flow velocity is high enough to lift it back to flow. Therefore, when the critical velocity is higher for a given particle, the particle should be considered "temporarily collected", or hindered (rather than entrapped) even though it has met a protrusion.

The minimum flow velocity that enables particle to be lifted is termed the 'critical velocity'. Mathematically, the critical velocity should be derived from moment equilibrium in equation 2.30:

$$F_A(2r_p h - h^2)^{1/2} \geq F_D(r_p - h) + M_D \qquad (2.30\text{bis})$$

The adhesive force, F_A that appears on the left hand side can be determined from the known equation for van der Waals force given in equation 2.31. However, the drag force F_D and moment M_D were evaluated from analytical solutions that are only applicable for infinite half space in the original theory. This is unrealistic for application to interstitial pore flow as noted in Chapter 2. An alternative approach uses the results of particle flow simulation for one particle placed on the wall of a cylinder presented in Figure 4.8 to develop a 'wall correction factor', K_p. The wall correction factor gives the drag force acting on the particle when multiplied by the Stokes force (equation 4.43).

Figure 6.18a summarizes values of critical velocity obtained from equation 2.30 with van der Waals force in equation 2.31 and the Stokes force corrected by the wall correction factor when the cylinder radius, R = 1mm. The Hamaker constant, A_H was assumed 3×10^{-13} erg, and the assumed height of the protrusion, $h = 2\mu$m according to the visual observation made in the experimental study as mentioned in Section 6.0. The figure shows that values of the critical velocity increase nonlinearly with the particle size (i.e. it is more difficult to lift larger particles from the wall). The same figure shows the

seepage velocity for the slow test, $v = 1.36\times10^{-2}$ cm/sec which can be interpreted, as the particles are larger, it becomes harder to lift them up from the wall. In the same figure, a line designating the seepage velocity, $v = 1.36\times10^{-2}$ cm/sec is drawn over the entire size range. For a given seepage velocity, this defines a minimum particle size which can be collected in the model pore. According to the criterion, for $v = 1.36\times10^{-2}$ cm/sec (the slow test) 'limit particle radius', $r_{limit} = 3.2\mu$m, slightly larger than the measured $r_{limit} = 2.5\mu$m.

The critical velocity values are affected by many factors. For example, Figure 6.18b shows the curves of critical velocities for different pore tube radii. As pore size increases, the critical velocity also increases because it reduces drag force. The critical velocity will also increase as the height of protrusion increases. Since the size of protrusion must also be distributed, so should the critical velocity. In addition, collected particles can also serve as a protrusion and hence the values of critical velocity will change with time. On the other hand, pore velocity also changes with the pore size (in both the physical experiments and the bubble model) and will affect the limiting collectible particle size. Finally the drag force acting on a particle, as well as pore fluid velocity should be affected by the neighboring collected particles as explained in Chapter 4 and hence, the critical velocity will be dynamic.

It should be noted that the limit particle size is only applicable to collections on the surface (i.e. surface entrapment and hindrance), not to collections at contact points. It was hypothesized, accordingly:

1. No surface entrapment is allowed for particles $r_p < r_{limit}$ and hence, a reduced attachment probability, $A_p = A_{pc}$ is applied. A_{pc} will be referred to as 'contact' attachment probability while A_p will represent a 'total' attachment probability including the surface attachment probability.
2. The rest of particles, with the fraction $(1\text{-}A_{pc})$, are considered as hindered particles.

Unfortunately, there are too many uncertainties involved in the prediction of limit size, r_{limit}, and therefore, the value was included as a calibration parameter similar to the total attachment probability, A_p and the reference detachment rate, $\bar{k}_0$ in numerical simulations. Contact attachment probability, A_{pc} should be equivalent with the attachment

probability for smooth beads since smooth beads do not have any surface roughness. Therefore, $A_{pc} = 0.02$, which was obtained during simulations of smooth tests can be used for rough test simulations.

6.4.4 Bubble model simulation results of 'Rough Slow' test

Figure 6.19 shows three breakthrough curves and corresponding concentration profiles using the proposed bubble model with the total attachment probability, $A_p = 0.09$, contact attachment probability, $A_{pc} = 0.02$, detachment rate, $\bar{k}_0 = 28.2\text{cm}^{-1}$, and varying limit particle size, $r_{limit} = 2.5, 5, 9\mu\text{m}$ for slow, medium and fast tests, respectively. Figure 6.19a shows that the increasing r_{limit} mainly affects the stabilized breakthrough concentration value. With the measured $r_{limit} = 2.5\mu\text{m}$, the best-fit curve and corresponding relative concentration profile was obtained. The characteristic underestimation during the wash stage (observed during simulations of 'smooth' tests) persists, possibly due to the lift-off of less firmly entrapped particles coming out as discussed earlier. However, it seems this underestimation did not affect the concentration at the end of wash stage, as shown in Figure 6.19c.

Figure 6.20 compares the bubble model simulation results with $r_{limit} = 2.5\mu\text{m}$ with the continuum model results, previously shown in Figure 6.6. Continuum model matches the breakthrough concentration. However, bubble model simulation greatly improved the prediction of $(C+S)/C_0$, profile at $10pV$ of higher concentration close to the injection point than that can be projected linearly from downstream in the filter bed. This can be explained by the collection efficiency when is an increasing function of the particle settling velocity relative to the pore fluid velocity, v_s/U_{flav}, (equation 5.7). According to this equation, collection efficiency becomes higher when the particles have a higher settling velocity, (i.e. larger particles flowing pores with smaller pore fluid velocity). Therefore, by including particle and pore size distributions, the bubble model disperses the collection efficiency, produces a nonlinear spatial distribution in the deposit concentration profile. Therefore, it can be concluded that particle and pore size distributions, help to explain the measured concentration profile.

Figure 6.20c compares relative concentration (C+S) values at an observation point near the injection point (at 1.8 cm) from one of the 'Rough Slow' test, RS2. This result also shows greatly improved matching with the measured values compared with the continuum model result.

6.4.5 Bubble model simulations for 'Rough Medium' and 'Rough Fast'

For bubble model simulations of 'medium' and 'fast' tests with rough beads, the empirical parameters, i.e., A_p, A_{pc}, $\bar{k}_0$ and r_{limit} are needed. Through experience of simulating the tests with smooth beads in Section 6.4.2, the same values of A_{pc} and $\bar{k}_0$ can be used to simulate the results with varying seepage velocities, and with the same logic, the $A_p = 0.09$, $\bar{k}_0 = 0.28\text{cm}^{-1}$, and $A_{pc} = 0.02$ can be used for simulation of 'Rough Medium' and 'Rough Fast'. As shown in Figure 6.19, limit radius, r_{limit} controls the stabilized effluent concentration, and it is a function of seepage velocity. Therefore, r_{limit} is calibrated with the average stabilized effluent concentration, C_{out}/C_0 = 0.85 for the medium test and C_{out}/C_0 = 0.95 for the fast test. Table 6.4 summarizes the empirical parameters used in the bubble model simulations.

Figure 6.21a and b present the simulation results for 'Rough Medium' tests (RM1,2,3,4). The calibrated r_{limit} value corresponding to final C_{out}/C_0 was 5μm. Although the simulated values reasonably match the measured values during injection period, the underestimation of wash stage concentration is more pronounced than in 'Rough Slow' simulations. Again, this does not affect the prediction of concentration profile and the simulated and measured concentration profiles match very well as shown in Figure 6.21b. The same trend is observed in the simulations of 'rough fast' tests (RF1,2) shown in Figures 6.22a,b. The r_{limit} value used is 9μm.

6.5 CONCLUSIONS

This chapter has provided a detailed account of the simulations of 1-D particle injection tests performed by Yoon et al. (2004) using analytical and numerical network

simulations, with UBE and bubble model assumptions. The bubble model simulates the particle collection process with three parameters, 1) collection efficiency, η, 2) the normalized detachment ratio, k_r, 3) total attachment probability, A_p, 4) contact entrapment probability, A_{pc}, and 5) the limit particle size, r_{limit}. Among these, the collection efficiency is evaluated using the parametric study result with measured settling velocities of used suspension particles. Based on the comparison of breakthrough concentrations of tests with three different seepage velocities, 'slow', 'medium' and 'fast', it was first hypothesized that the detachment probability k_r is linearly proportional to the pore fluid velocity ($k_r = \bar{k}_0 v$). With this hypothesis, the measured breakthrough curves of 'slow' injection tests with smooth beads were calibrated to find the values of A_{pc} and $\bar{k}_0$. When the obtained parameters were applied to tests with different injection velocities, 'Smooth Medium' and 'Smooth Fast', the results showed reasonable agreements with measured values.

Surface roughness was considered to cause surface entrapment and effectively increasing the overall attachment probability from A_{pc} with smooth beads to A_p with rough beads. The dependence of particle size on the surface entrapment mechanism was discussed and the limit particle size, r_{limit} was defined as the criterion below which only contact entrapment is allowed. Total attachment probability value, A_p was obtained by calibrating the 'Rough Slow' tests results. When the A_p value, together with A_{pc} and $\bar{k}_0$ found from 'Smooth Slow' tests to simulate 'Rough Medium' and 'Rough Fast' tests, good predictions of breakthrough and concentration profiles were obtained.

The simulation results characteristically underestimated breakthrough concentration during the wash stage. This is probably due to release of some entrapped particles, which were assumed firmly collected. However, more detailed experimental study is required to understand the reversibility of the entrapment process.

The collection efficiency, η_H, proposed in Chapter 5 applied in the bubble model was found not predicting the measured filtration rates without help of the empirical parameters. However, it should be noted that the predicted relationship between η_H with particle radius (Figure 6.11) has resulted in capturing the characteristic nonlinear spatial distribution of deposit volume in the bubble model simulations. This suggests that

filtration rates of the tests were directly related to deposition rates of particles, which was successfully predicted by the particle flow simulator presented in Chapter 4.

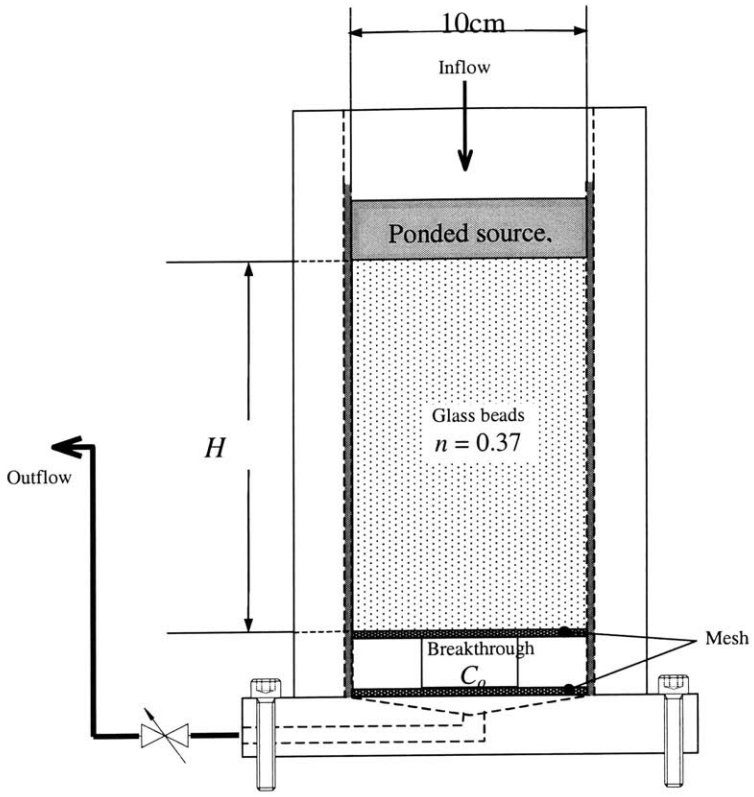

Figure 6.1 Configuration of colloid injection test by Yoon et al. (2004)

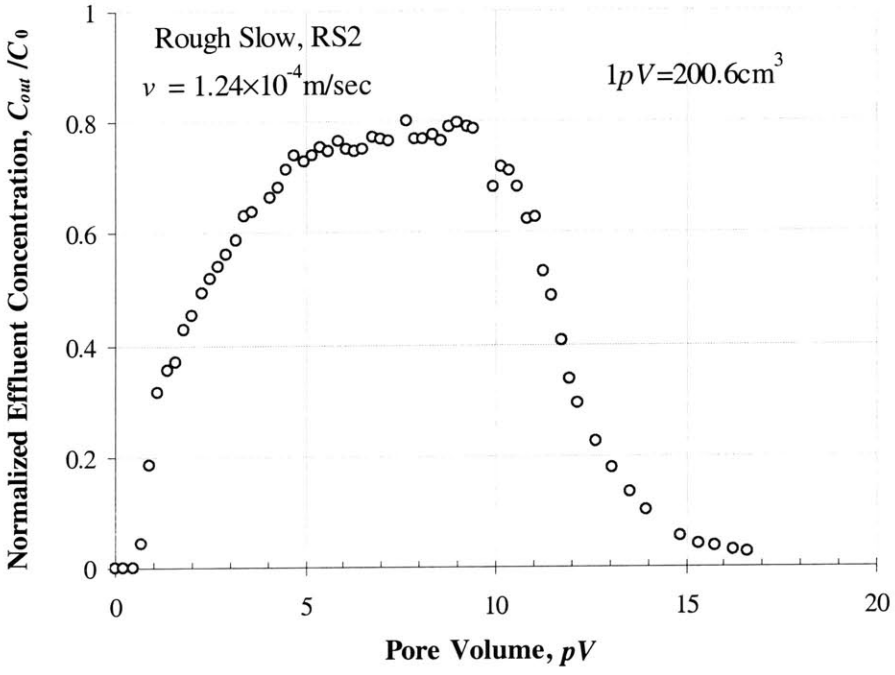

Figure 6.2 Breakthrough curve for a 'Rough Slow (RS2)' test

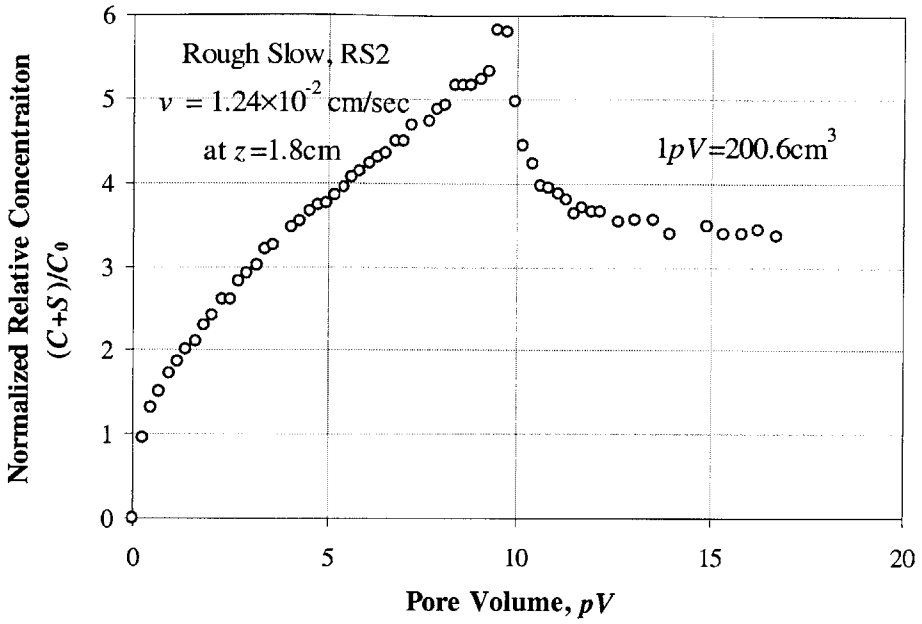

Figure 6.3 Normalized total concentration evolution for a 'Rough Slow (RS2)' test at z = 1.8cm

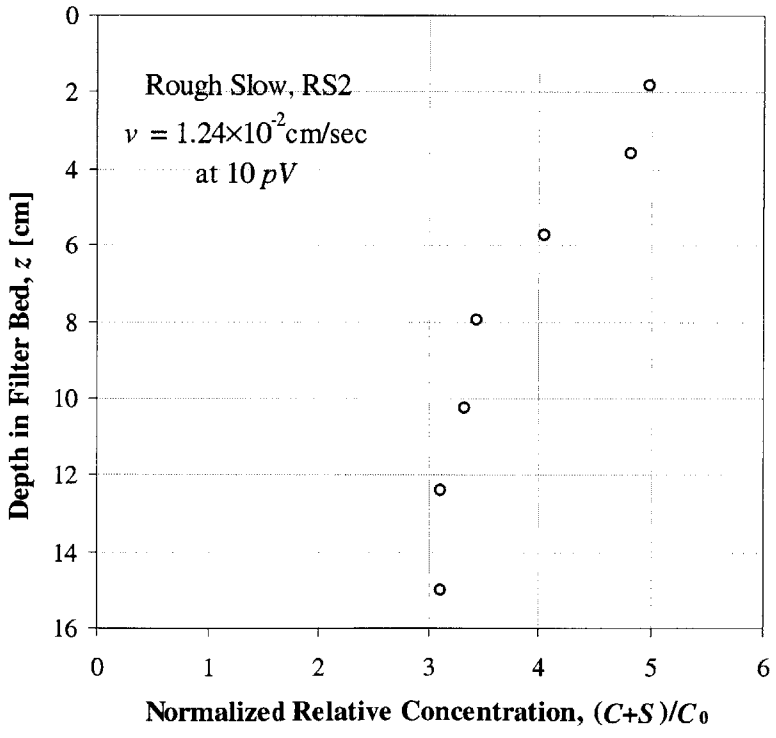

Figure 6.4 Normalized total concentration profile for a 'Rough Slow (RS2)' test at 10 pV

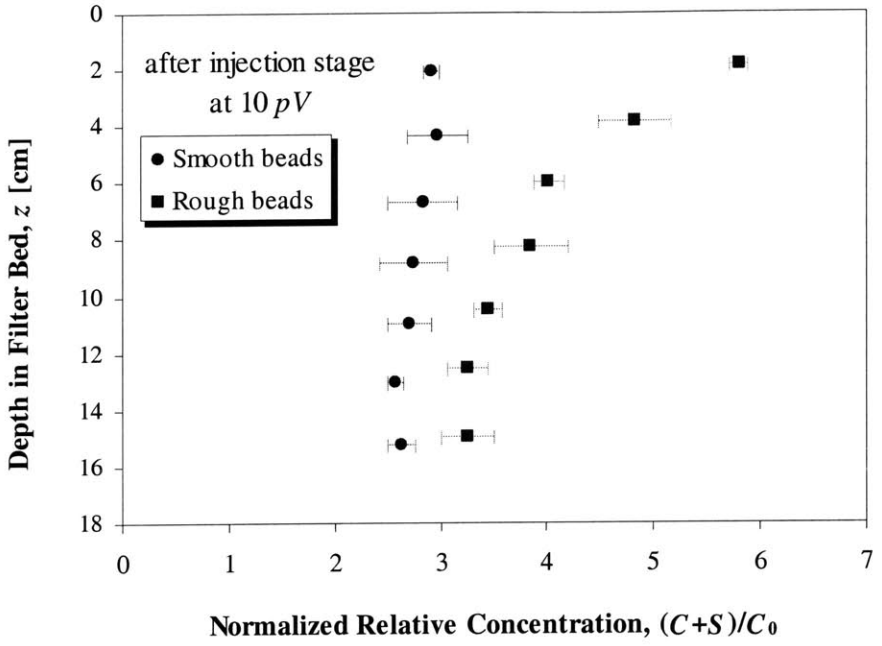

(a) Relative concentration profile at the end of injection stage

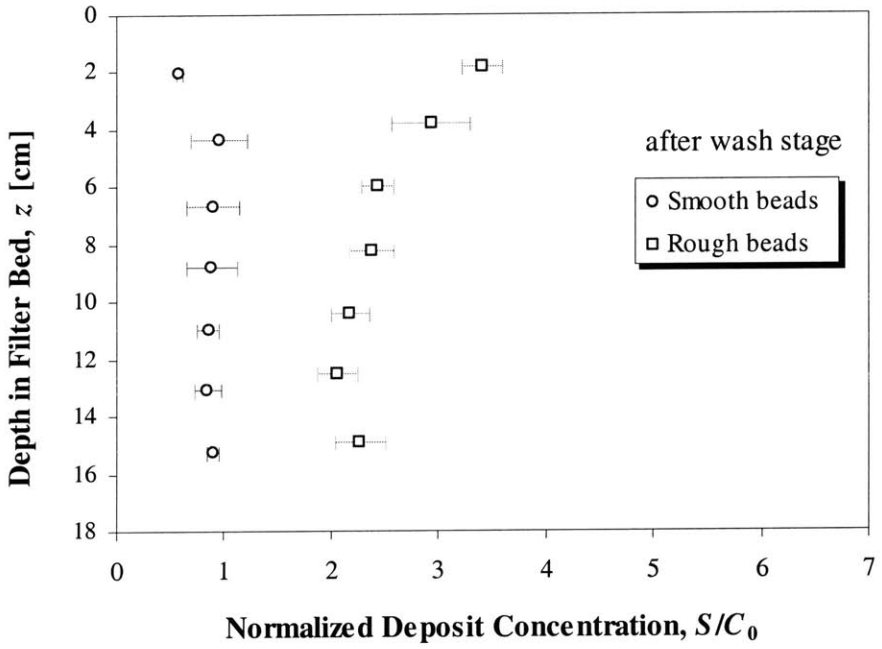

(b) Deposit concentration profile at the end of wash stage

Figure 6.5 Comparison of concentration profiles of tests with 'smooth' and 'rough' beads

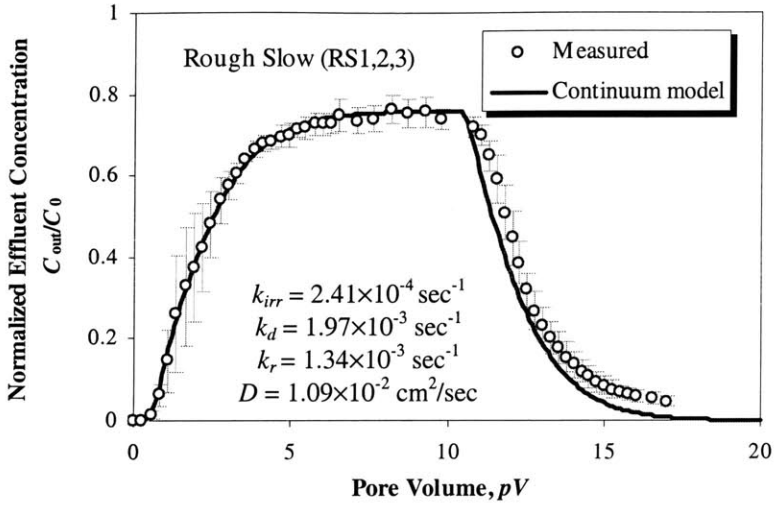

(a) Breakthrough curve

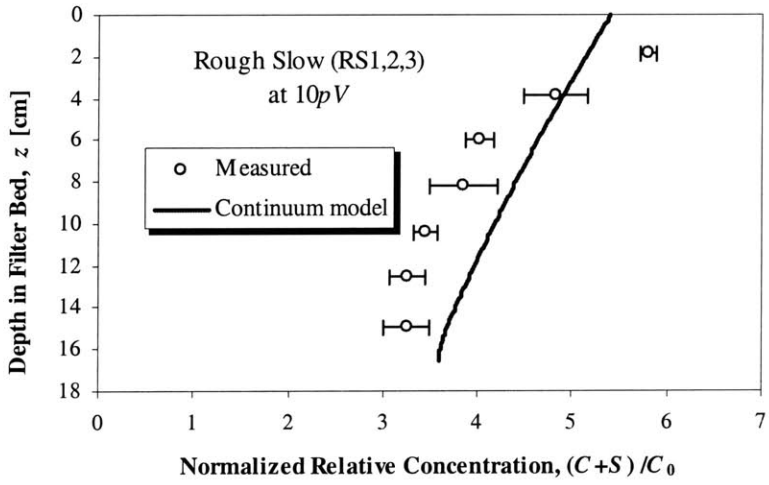

(b) Concentration profile

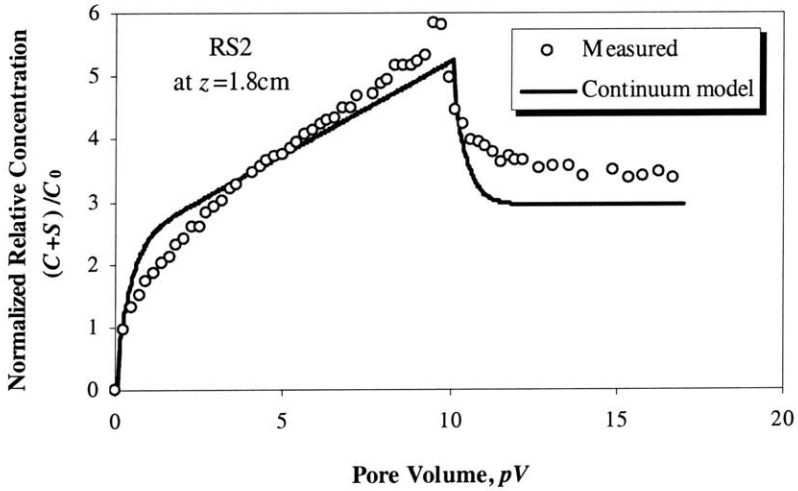

(c) Concentration evolution

Figure 6.6 Comparison of measured data with predictions of 'Rough Slow (RS)' tests with two-site continuum model (Yoon et al., 2004)

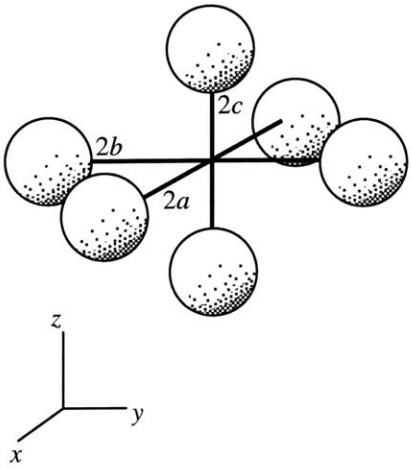

Figure 6.7 Pore measurement coordinate system

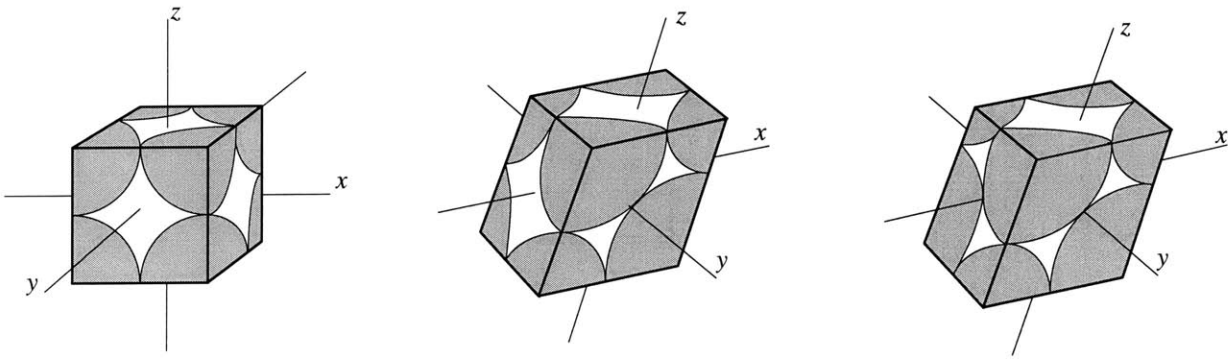

(a) Simple cubic (b) Simple orthorhombic (c) Simple rhombohedral

Figure 6.8 Unit cells of the regular sphere packings

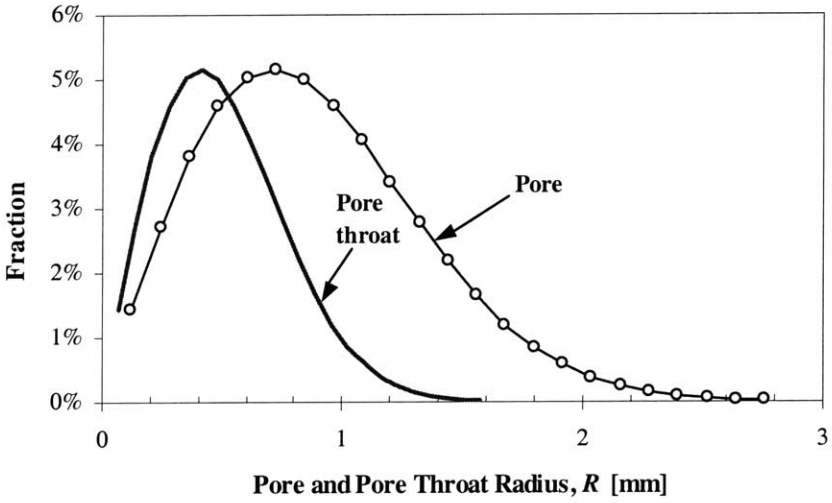

Figure 6.9 Model pore and throat size distribution

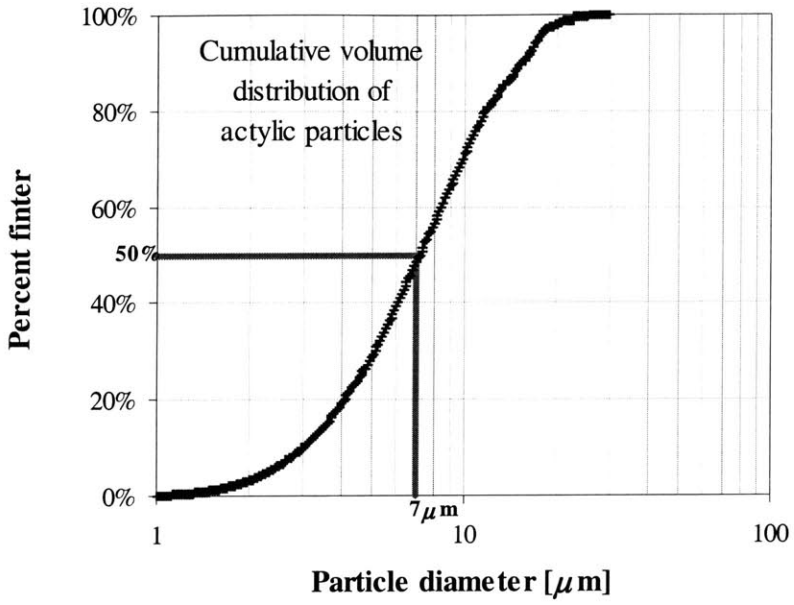

(a) Measured particle distribution by electric particle counter

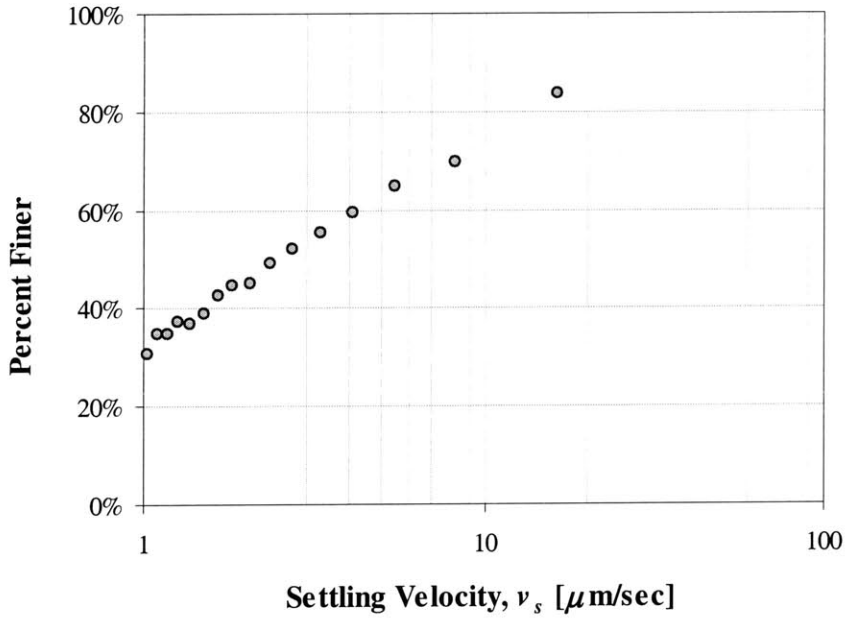

(b) Measured settling velocities from laser fluorescence measurements

Figure 6.10 Suspension particle size and settling velocity distribution (Yoon et al., 2004)

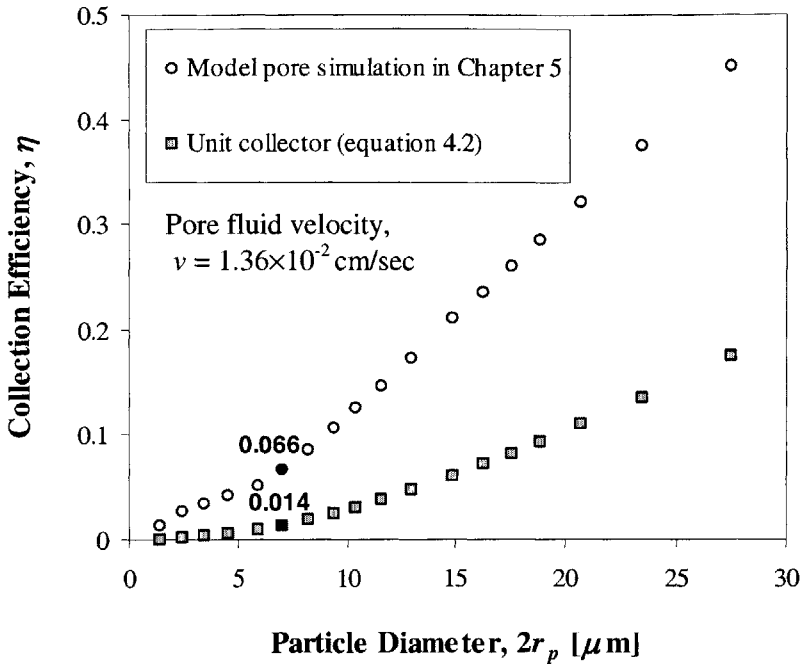

Figure 6.11 Collection efficiency resulted from parametric study

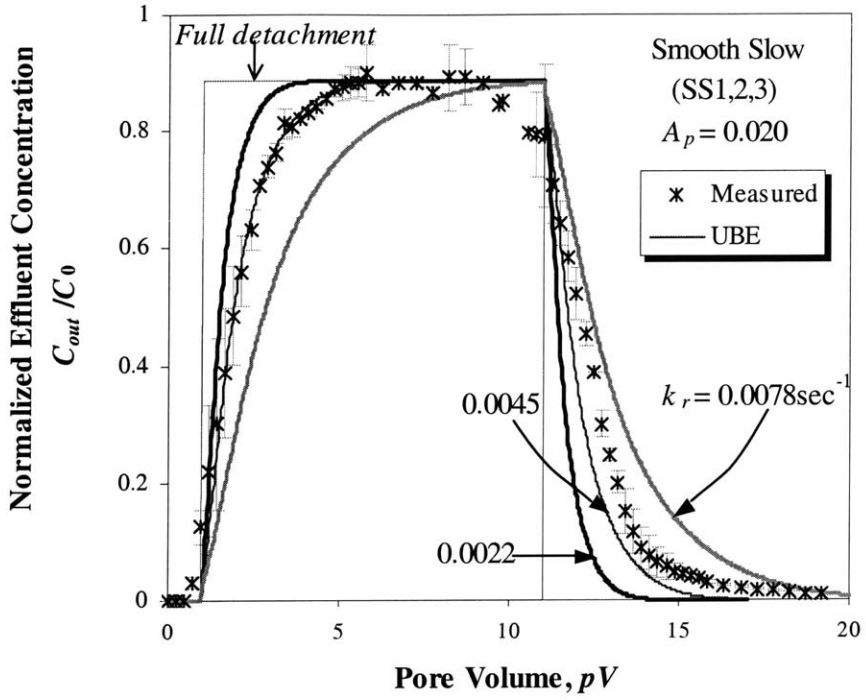

(a) Breaktnrougn curves

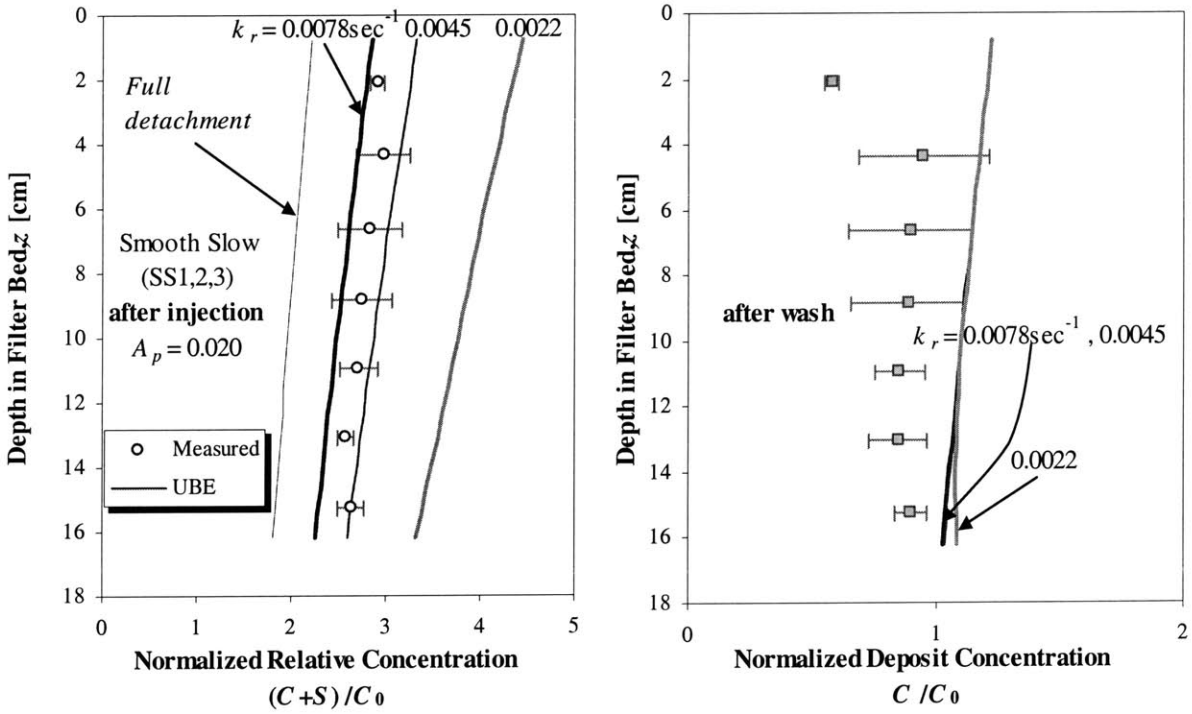

(b) Concentration profile after injection stage (c) Concentration profile after wash stage

Figure 6.12 Effects of detachment ratio on UBE simulation of 'Slow Smooth (SS)' tests

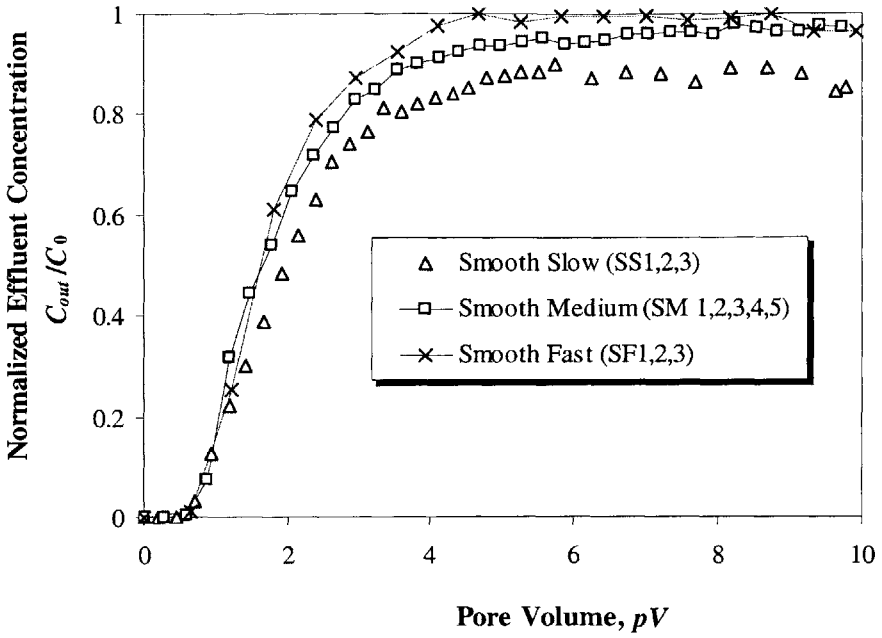

Figure 6.13 Comparison of measured breakthrough curves for slow, medium and fast tests with smooth beads

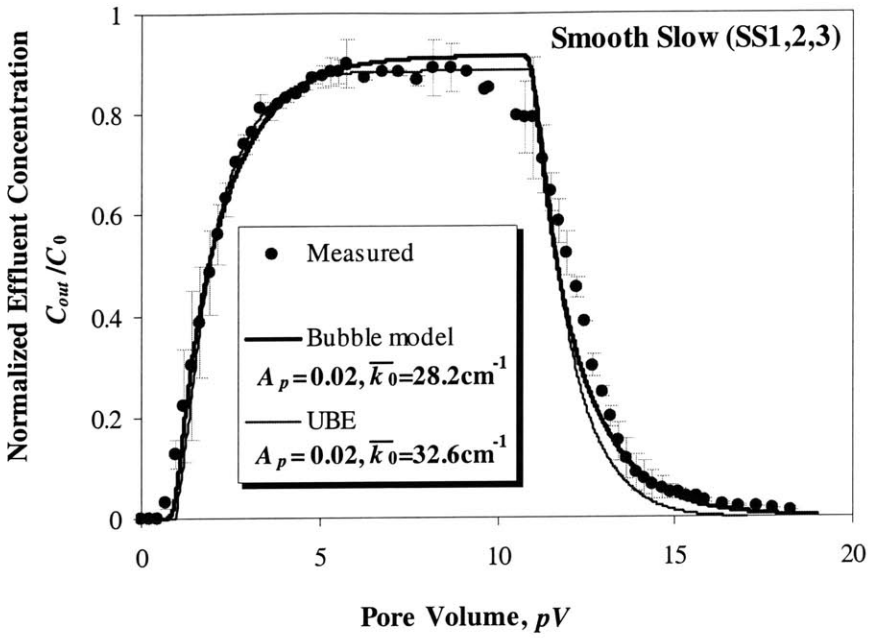

(a) Breakthrough curve

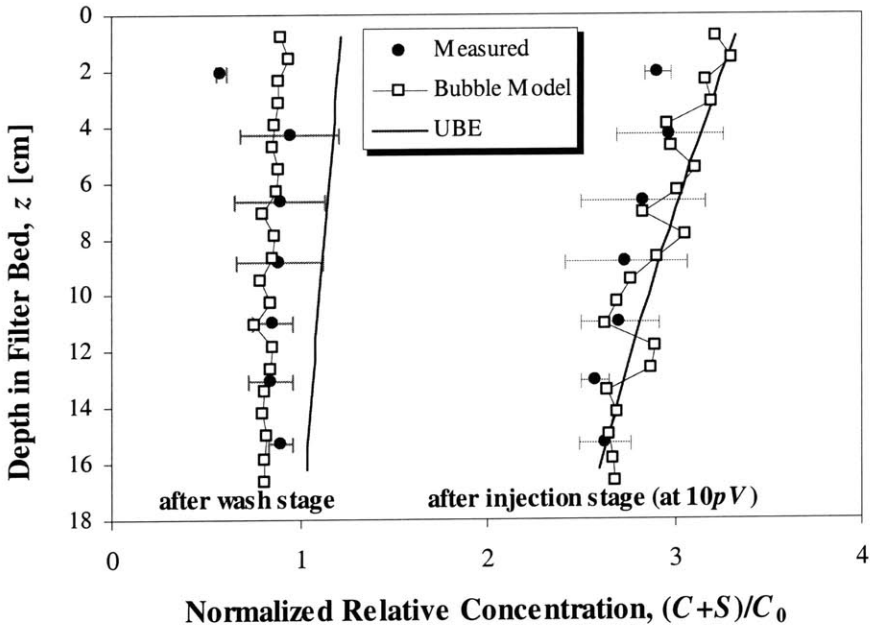

(b) Concentration profile

Figure 6.14 Results of bubble model simulation for 'Smooth Slow (SS)' tests

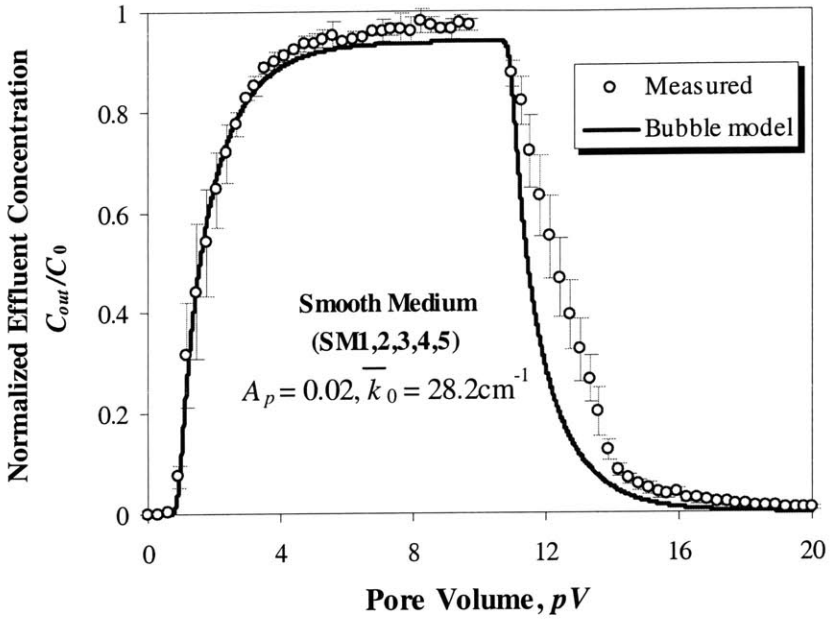

(a) Breakthrough curve

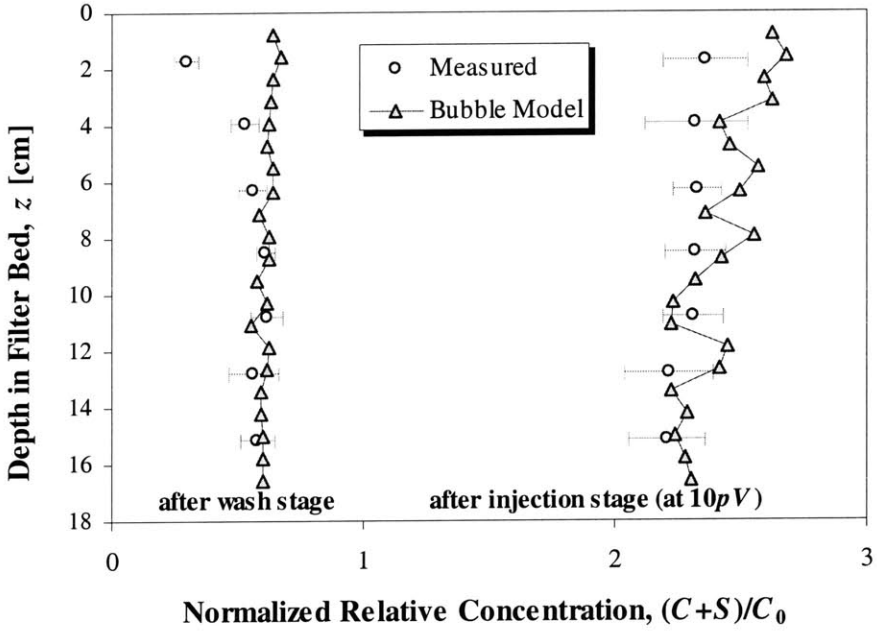

(b) Concentration profile

Figure 6.15 Results of bubble model simulation for 'Smooth Medium (SM)' tests

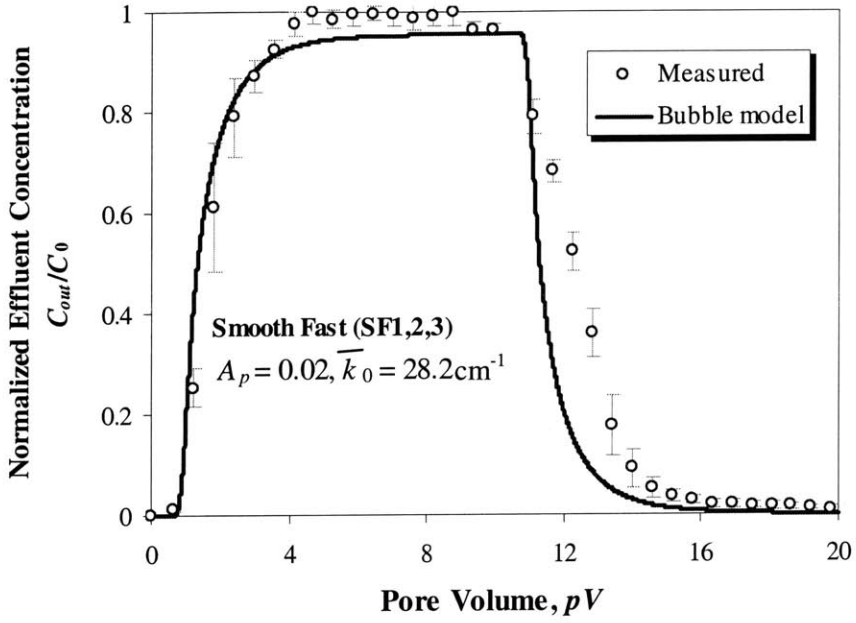

(a) Breakthrough curve

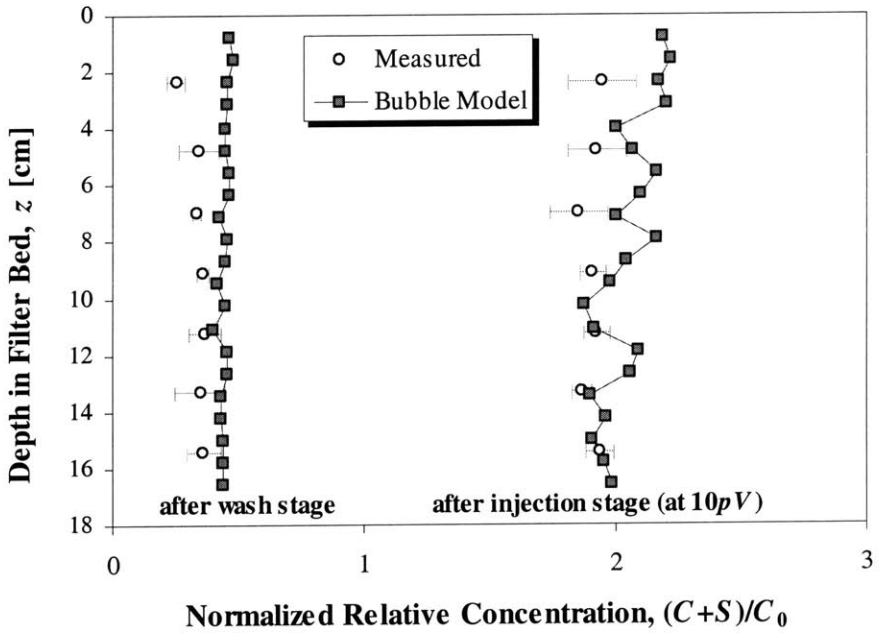

(b) Concentration profile

Figure 6.16 Results of bubble model simulation for 'Smooth Fast (SF)' tests

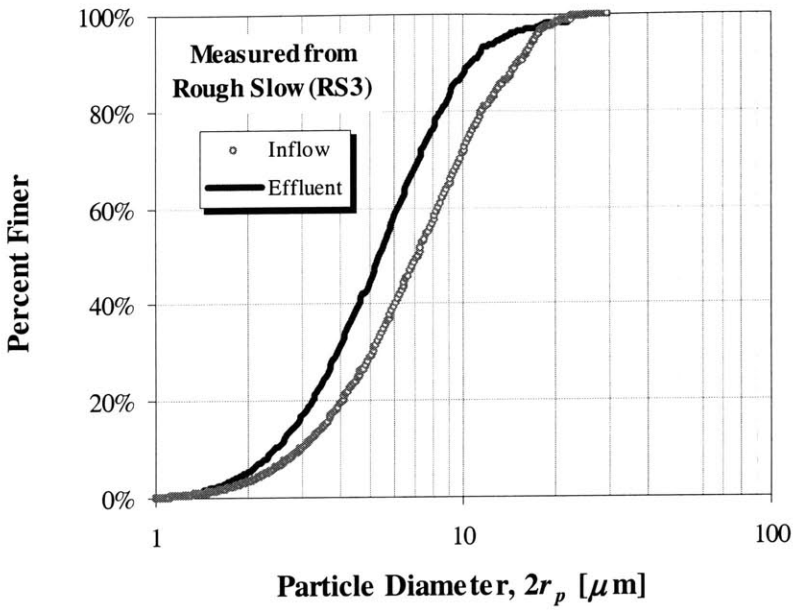

(a) Comparison of measured inflow and effluent cumulative particle size distributions

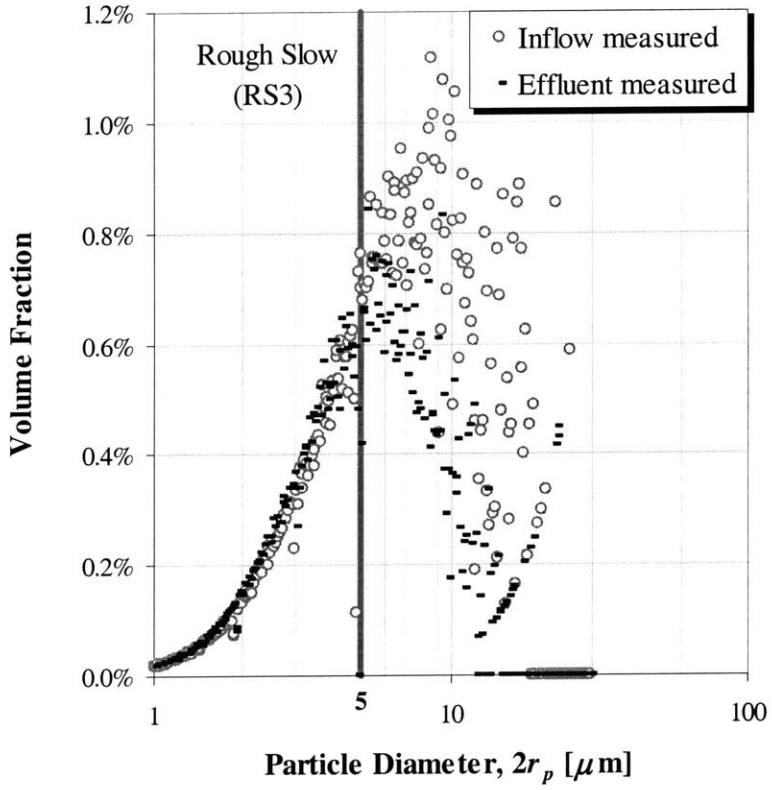

(b) Measured discrete inflow and effluent particle size distributions
Figure 6.17 Measured particle size distribution for RS3 test

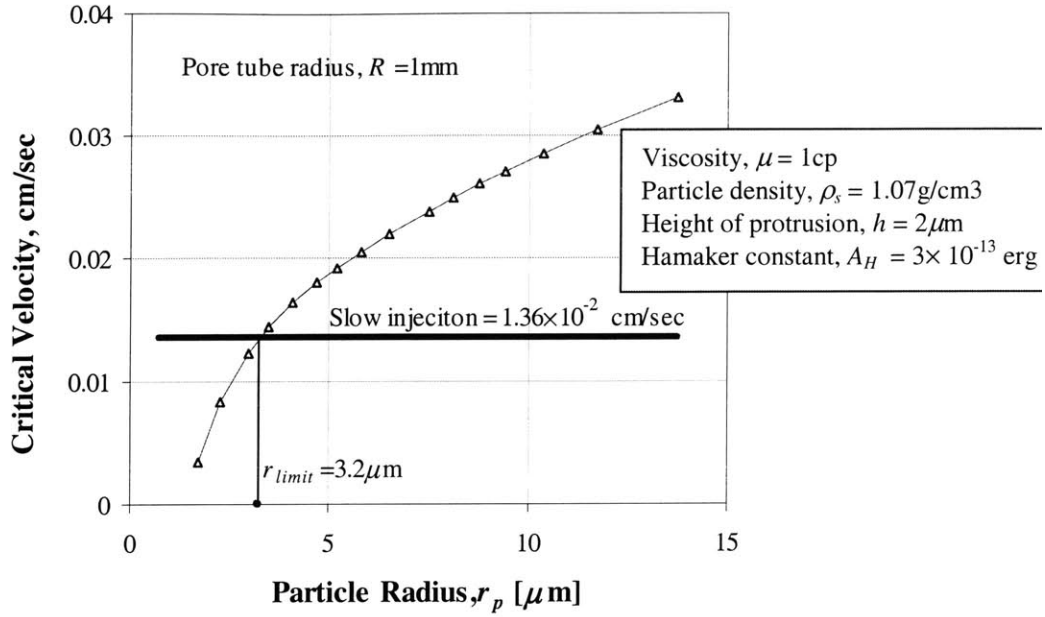

(a) For tube radius R =1mm

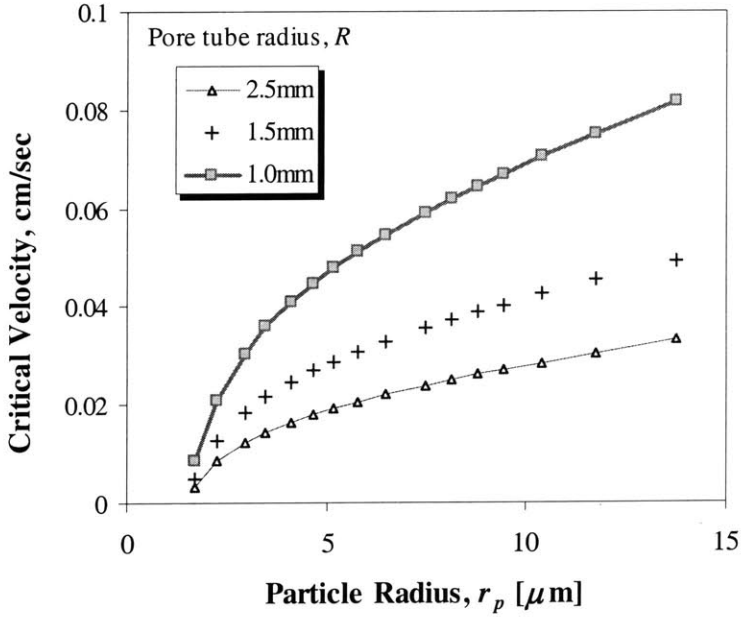

(b) For various pore tube radii

Figure 6.18 Evaluation of critical lifting velocity based on equation 2.30

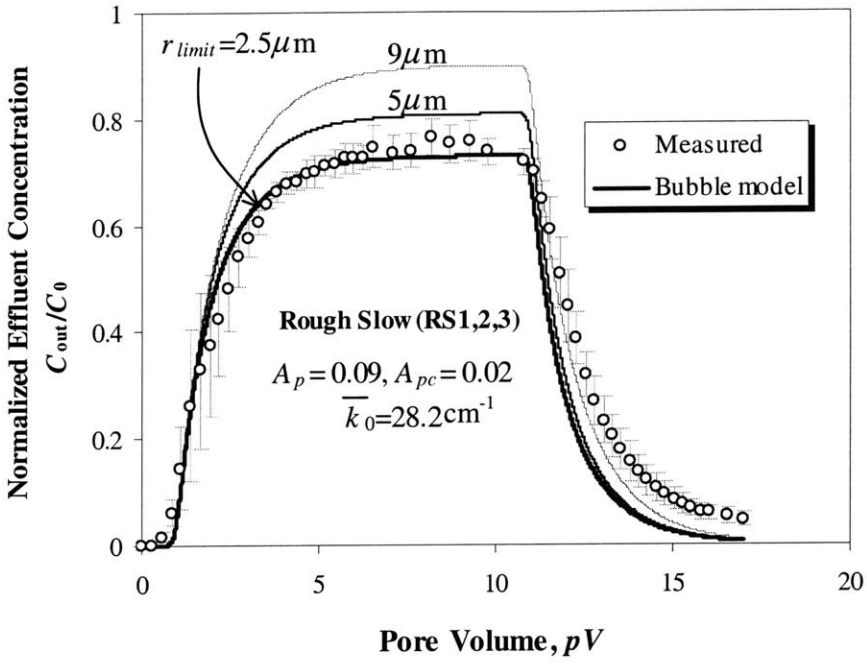

(a) Breakthrough curve

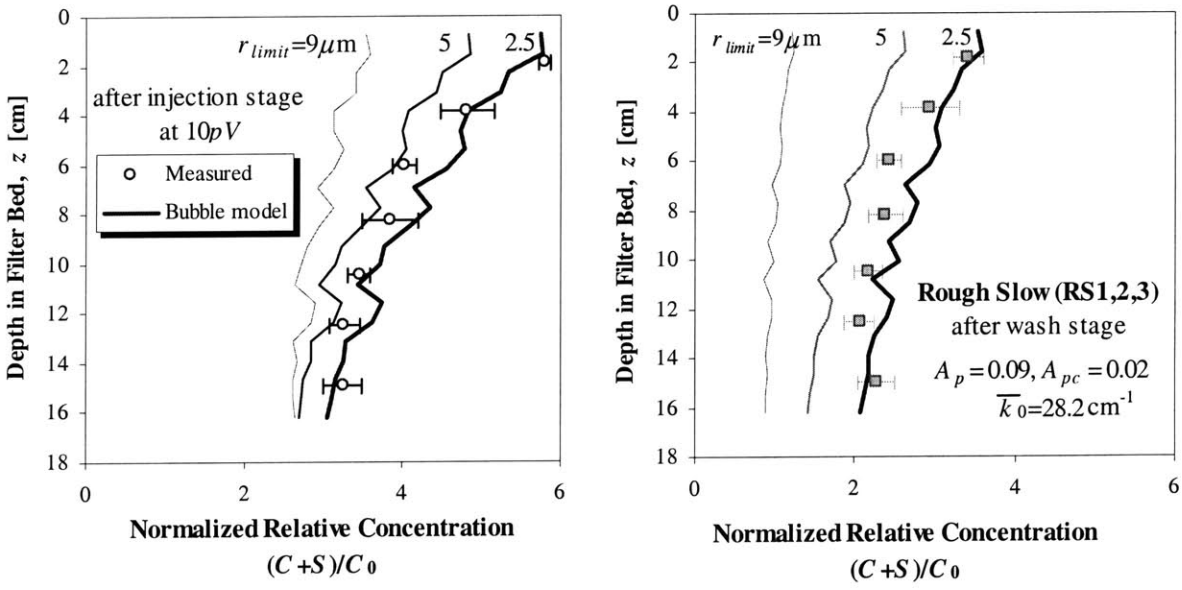

(b) Concentration profile after injection stage (c) Concentration profile after wash stage

Figure 6.19 Bubble model simulations for 'Rough Slow' tests with limit particle size

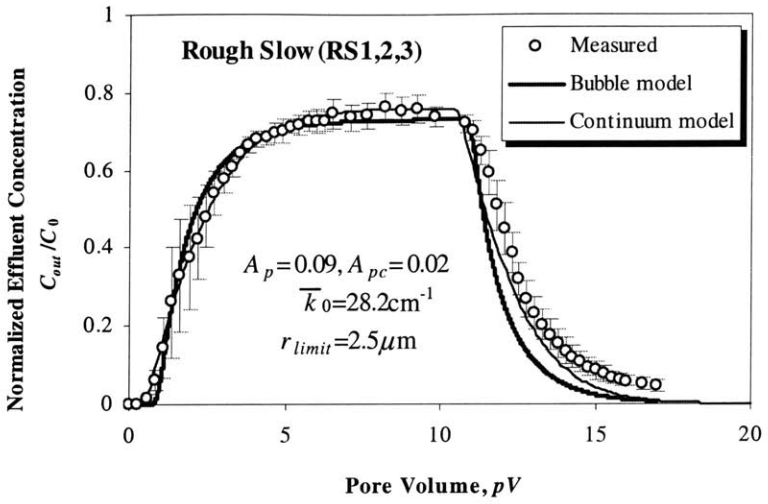

(a) Breakthrough curve

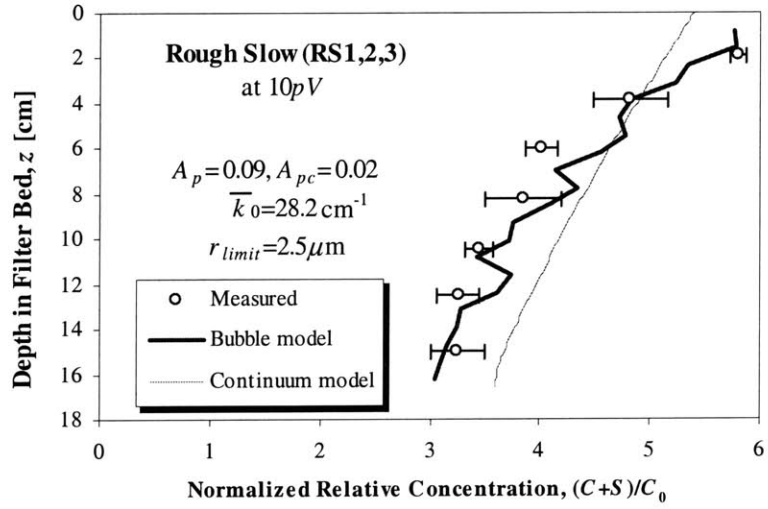

(b) Concentration profile

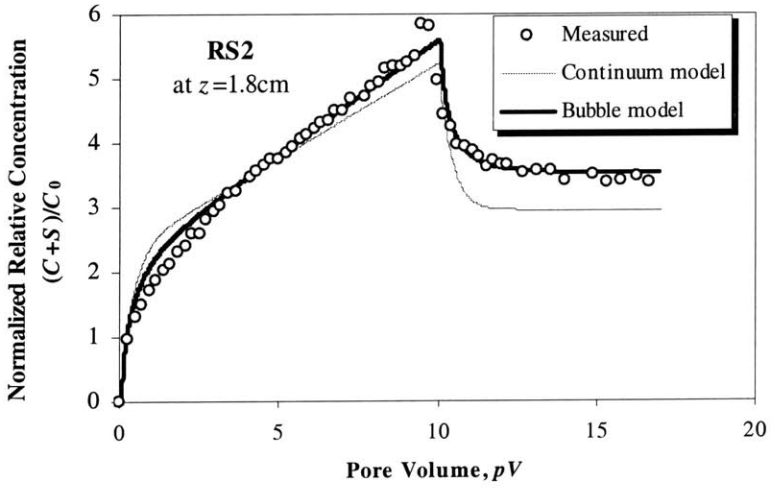

(c) Concentration evolution

Figure 6.20 Comparison of bubble model results with the continuum model results for a 'Rough Slow (RS2)' tests

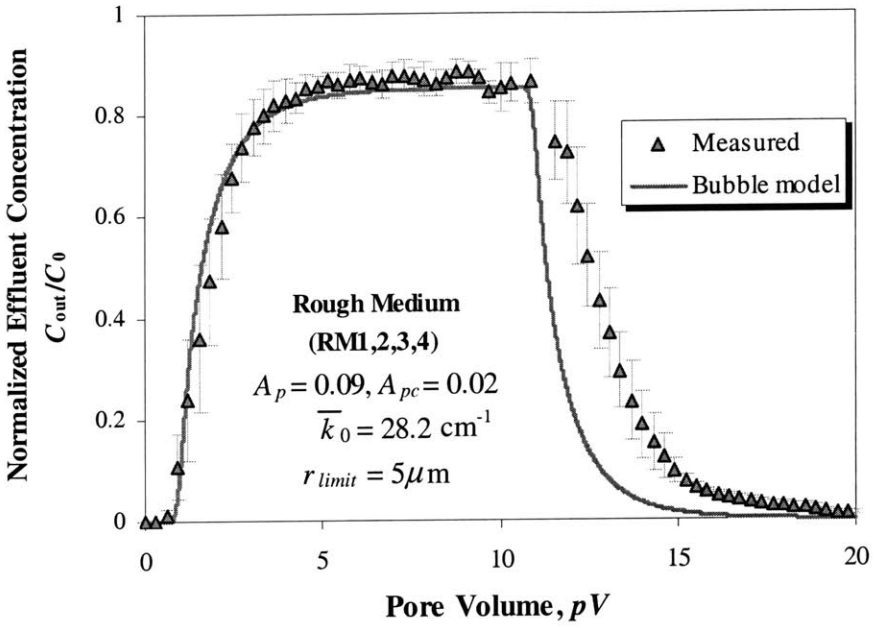

(a) Breakthrough curve

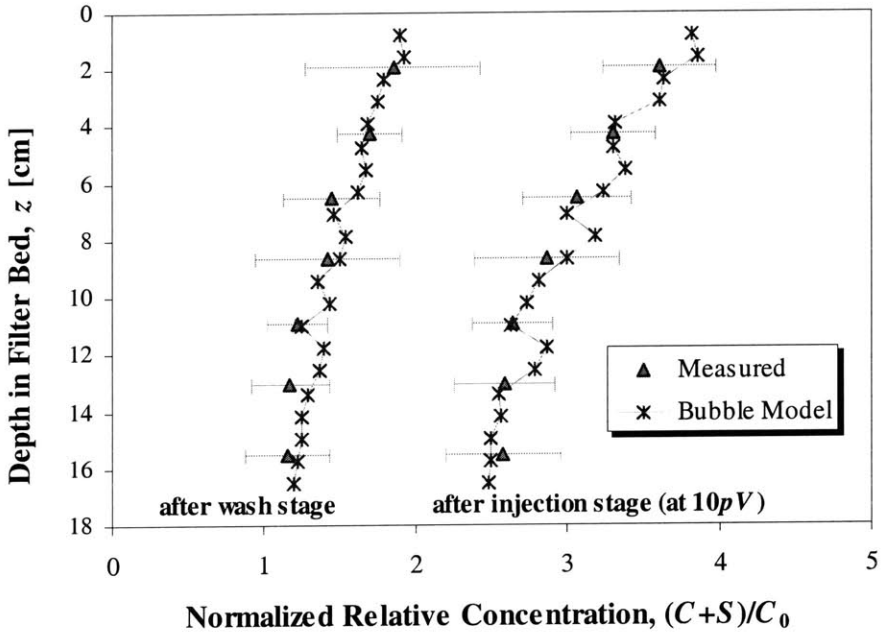

(b) Normalized concentration

Figure 6.21 Bubble model simulations for 'Rough Medium' tests

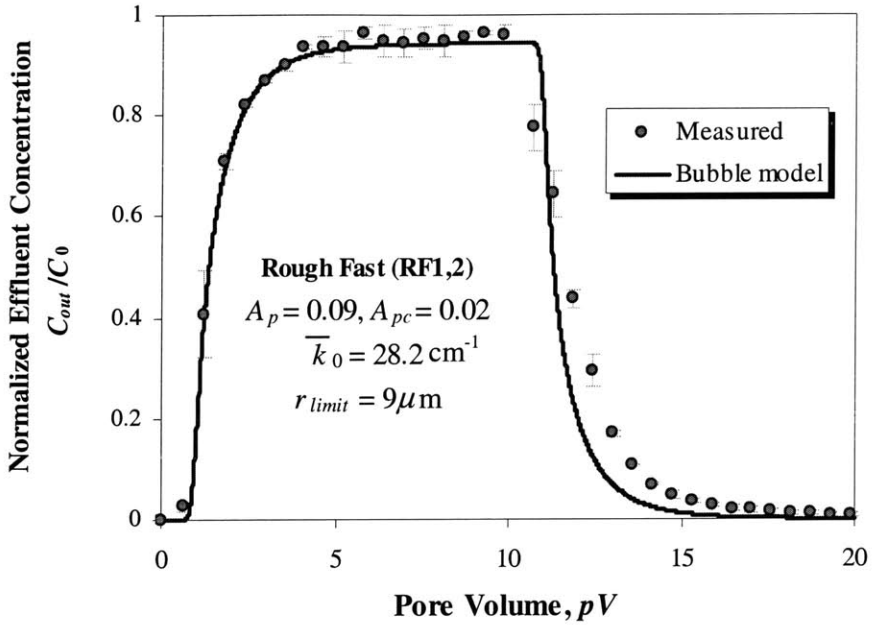

(a) Breakthrough curve

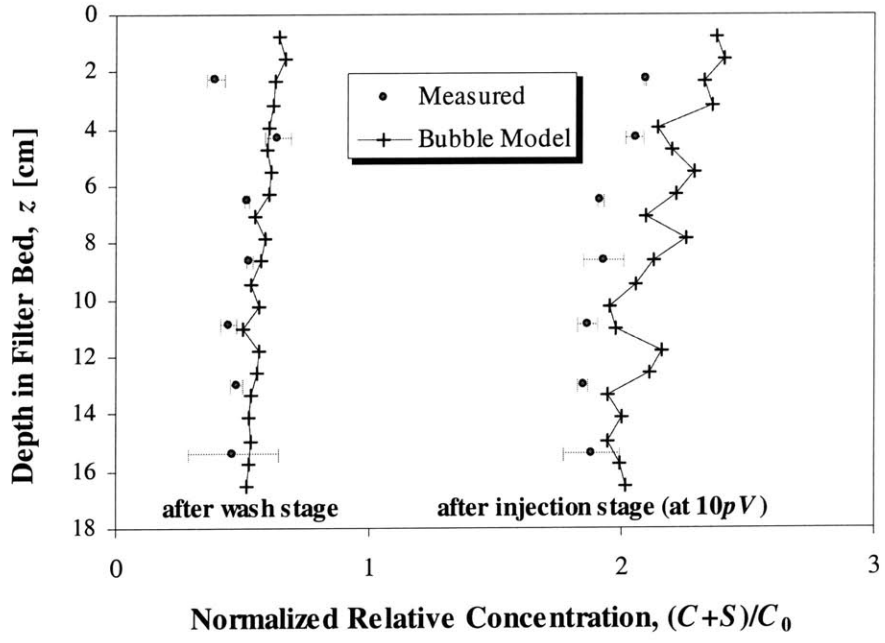

(b) Normalized concentration

Figure 6.22 Bubble model simulations for 'Rough Fast' tests

Table 6.1 Material parameters of experiments by Yoon et al. (2004)

Test Label*	Beads	Seepage velocity, v ** [cm/sec]	Initial porosity, n_0	Filter depth, L [cm]
RS1	Rough	Slow $1.36(\pm 0.13)\times 10^{-2}$	0.367 (±0.007)	16.60 (±0.20)
RS2				
RS3				
RM1		Medium $2.73(\pm 0.24)\times 10^{-2}$	0.376 (±0.004)	16.87 (±0.18)
RM2				
RM3				
RM4				
RF1		Fast $5.31(\pm 0.14)\times 10^{-2}$	0.378 (±0.002)	16.60 (±0.08)
RF2				
SS1	Smooth	Slow $1.38(\pm 0.15)\times 10^{-2}$	0.374 (±0.002)	17.04 (±0.09)
SS2				
SS3				
SM1		Medium $2.76(\pm 0.08)\times 10^{-2}$	0.373 (±0.002)	17.04 (±0.06)
SM2				
SM3				
SM4				
SM5				
SF1		Fast $5.49(\pm 0.16)\times 10^{-2}$	0.379 (±0.003)	17.06 (±0.08)
SF2				
SF3				
Average suspension particle density, ρ_s [g/cm^3]			1.1	
Suspension initial density (mass), C_0 [g/cm^3]			50×10^{-6}	

* R and S represent rough and smooth beads, respectively. F, M, and S represent fast, medium, and slow seepage velocities, respectively.

** The numbers in the parentheses are the standard deviations.

Table 6.2 Average Pore body and throat radii of three types of regular sphere packing

		Type of regular packing		
		Simple cubic	Simple Orthorhombic	Simple Rhombohedral
Porosity		0.4767	0.3954	0.2595
Pore Dimensions (see Figure 6.7)	$2a$	0.7320 D_g	0.5275 D_g	0.4142 D_g
	$2b$	0.7320 D_g	0.5275 D_g	0.4142 D_g
	$2c$	0.7320 D_g	0.5275 D_g	0.2247 D_g
R_{throat}		0.207 D_g	0.142** D_g	0.077 D_g

* D_g = grain diameter

** Averaged: (0.207+0.077)/2

Table 6.3 Parameters used for UBE simulations

Seepage velocity, v	1.38×10^{-4} m/sec
Model pore radius, R	1 mm
Model pore length, L	4 mm
Total number of elements	42

Table 6.4 Parameters used for bubble model simulations

Test Label		Total attachment probability, A_p	Contact entrapment probability, A_{pc}	Reference detachment rate, $\bar{k}_0$ [cm^{-1}]	Limit size, r_{limit} [μm]
Rough Slow	RS1	0.09	0.02	28.2	2.5
	RS2				
	RS3				
Rough Medium	RM1				5.0
	RM2				
	RM3				
	RM4				
Rough Fast	RF1				9.0
	RF2				
Smooth Slow	SS1	0.02			0
	SS2				
	SS3				
Smooth Medium	SM1				
	SM2				
	SM3				
	SM4				
	SM5				
Smooth Fast	SF1				
	SF2				
	SF3				

CHAPTER 7. SIMULATIONS OF MICROFINE CEMENTITIOUS GROUT INJECTION

7.0 INTRODUCTION

As a ground improvement technique first developed 200 years ago (Landry et al., 2000), grouting has proven its effectiveness in modern geotechnical engineering for various purposes ranging from filling natural or artificially created voids in ground; densification, stabilization and strengthening; controlling tunneling or excavation induced settlement; reducing permeability to prevent seepage around tunnels or dam foundations (Nonveiller, 1989, Kutzrer, 1996, Welsh, 1998, and Gouvenot,1998). Grouting has been carried out by various techniques (Henn, 1996). Permeation grouting is primarily used to replace water and/or air voids in the soil mass by injecting a fluid grout at low pressures (in order to prevent fracturing of the soil mass). Permeation grouts include cementitious suspensions and chemical solutions. Cement-based suspensions (cement grouts) are the most commonly applied material in grouting. Although chemical grouts such as sodium silicate have been used successfully for fine-grained substrata in which cement grouts are not penetrable, cement grouts dominate being superior on cost factors, durability and environmental safety (Gause and Bruce, 1997). In addition, the development of microfine cement has allowed application of cement grouts for fine-grained sandy soils with hydraulic conductivity as low as 10^{-3}~10^{-4} cm/sec (Zebovitz et al., 1989). This chapter compares experimental results from a series of microfine cement grout injection tests in fine sand reported by Bouchelaghem and Vulliet (2001) with numerical simulation using a bubble network model using the parametric study from the model pore particle flow simulator in Chapter 5.

7.1 FACTORS AFFECTING PERMEABILITY OF CEMENTITIOUS GROUTS

Cement based suspension grouts, although superior in material properties to chemical solution grouts, have intrinsic characteristics that deteriorate their injectibility. They are 1) hydration and 2) filtration. Hydration refers to a process of solidification that can cause cement grout to accumulate inside pores and inhibit further injection. The main hydration usually begins after an initial induction period (Taylor, 1997) of at least a few hours and can be extended (up to a few days) by the use of retarding agents after mixing. The partial hydration occurring during the induction period can affect the flow by changing the rheological properties of the grout even if it does not produce significant solidification. The effects of hydration on rheological properties of cementitious grout and grout penetration are explained in detail in Appendix A. The other factor adversely affecting the injectibility of cement grout is filtration. Filtration occurs when either the water 'bleeds' out of the grout or solid cement particles are separated from the fluid grout. The former, often referred to as pressure filtration because it particularly occurs during pressure grouting process, is more common when the water-to-cement ratio (W/C) in grout is relatively low, such that the fluid behaves as thick slurry rather than a suspension. Pressure filtration causes a rapid increase in viscosity and reduces penetrability of grout into small pores (Landry et al., 2000). On the other hand, soil grains act to filter cement particles from dilute suspensions at high water-to-cement ratios, decreasing the size of pores and hence, increasing hydrodynamic resistance and ultimately causing clogging. Arenzana et al. (1989) first suggested that this phenomenon is essentially a deep bed filtration process.

Deep bed filtration is often encountered when the water content in the grout mix is increased in order to improve rheological properties of it and acts to negate any real advantage during injection (Bruce et al. 1997). While pressure filtration is relatively easy to prevent by the use of additives. Problems caused by deep bed filtration are pervasive and have not been studied in detail.

7.2 LAB-SCALE INJECTION TESTS OF MICROFINE CEMENT GROUT

Bouchelaghem (2002), Bouchelaghem & Vulliet (2001), and Bouchelaghem et al. (2001) have presented a series of studies on flow and transport of microfine cement grout in soil, using 1-D and 3-D lab-scale tests as well as a continuum model simulations. Figure 7.1 shows the size distributions of the sand the cement particles used in the experiments. As shown in the figure, the diameter of the soil grain (D_{15} = 0.17mm) is much larger than that of the cement particle (d_{85} = 0.008mm), D_{15}/d_{85} = 21.3 satisfying the lenient 'groutability ratio' criterion (Mitchell, 1981): D_{15}/d_{85} >11 although slightly less than the strict criterion of ratio D_{15}/d_{85} >24.

Nevertheless, filtration was observed both in one- and three-dimensional injection tests, manifested by increases in headloss. Figure 7.2 shows a diagram of the experimental apparatus for one-dimensional injection test represented by Bouchelaghem and Vulliet (2001), comprising an 82cm high sand column with a series of four pore pressure tapping points. Table 7.1 lists the material parameters and flow conditions used in the experiments.

7.2.1 Continuum model

The 1-D injection of a cementitious grout within a saturated porous soil and be described by the convection-diffusion governing equation of mass balance for the 1-D transport process can be written as follows:

$$\frac{\partial(nC)}{\partial t} + nv\frac{\partial C}{\partial z} - \frac{\partial}{\partial z}\left(nD\frac{\partial C}{\partial z}\right) = -\frac{\partial \sigma}{\partial t} \tag{7.1}$$

where C is the concentration of particles in the suspension, n is the porosity, v the pore fluid velocity, D the hydrodynamic dispersion coefficient, and σ is the specific deposit, which is defined as the mass of filtered solid per unit porous medium. The main source of difference amongst continuum models lies in the representation of law defining the

filtration process (as described in Section 2.1). The most commonly used expression is the first-order rate law:

$$\frac{\partial \sigma}{\partial t} = \lambda C \tag{2.3bis}$$

where λ is the filtration rate. Bouchelaghem and Vulliet (2001) have used density of suspension ρ, instead of concentration, C in their formulation:

$$\frac{\partial \sigma}{\partial t} = \lambda \rho \tag{7.2}$$

The suspension density, ρ, measures the total mass of suspension per unit volume while concentration, C only measures the mass of solid volume per unit volume of suspension. Therefore, density and concentration has the following relationship:

$$\rho = \rho_w + C\left(1 - \frac{\rho_w}{\rho_s}\right) \tag{7.3}$$

where ρ_w and ρ_s are the densities of water and solid particles respectively.

As filtered material accumulates, the porosity reduces and this will, in turn, affect the permeability of the host medium. The Kozeny-Carman equation is then used to relate changes in porosity to the permeability:

$$\frac{k}{k_0} = \left(\frac{n}{n_0}\right)^3 \left(\frac{1-n_0}{1-n}\right)^{4/3} \tag{7.4}$$

where k and k_0 are the current and initial values of the permeability.

A phase change rule can then link the change in porosity to the specific deposit:

$$n = n_0 - \frac{\sigma}{\rho_s} \tag{7.5}$$

where ρ_s is the solid density of particle for which (ρ_s = 3.0 g/cm^3 is used for cement grout).

Darcy's law is assumed to apply in both the grouted and ungrouted (saturated) zones of the soil:

Grouted zone: $$\frac{k(n)}{\mu}\frac{dp}{dz} = V_a \tag{7.6a}$$

Ungrouted zone: $$\frac{k_0}{\mu_w}\frac{dp}{dz} = V_a \tag{7.6b}$$

where V_a is the apparent velocity, r the pore fluid pressure, μ and μ_w are viscosities for the cement grout suspension and water, respectively.

The filtration rate, λ in equation 7.3 was assumed constant in the study by Bouchelaghem and Vulliet (2001)[12]. It is well known that the filtration rate is very difficult to predict, especially for random porous media such as soil because of the dynamic nature of the filtration process at the pore scale. For this reason, the values of filtration rate are usually obtained through back analysis of experimental results, such as effluent concentration and pore pressure measurements.

Bouchelaghem and Vulliet (2001) have calibrated λ from separate small-scale injection tests in an 8-cm column (instead of the 82 cm column used for the main test). The effluent concentration and pressure gradient data were fitted to results from a continuum analysis. The resulting λ values ranged over more than one order of magnitude during injection. Eventually, through a detailed statistical study, the Authors selected a constant value, $\lambda = 1.5\times10^{-4}$/sec for further numerical simulations.

Figure 7.3a shows an independent analysis of these data using the same material properties and assumed filtration rate. These calculations assume that dispersion is

[12] The Authors admit this is an oversimplification due to lack of information.

negligible (i.e., $D = 0$; equation 7.1) and ignore changes in the viscosity of the suspension as filtration occurs.

The initial pore pressures at each of the four tapping points reflect the injection pressure. The pore pressures then increase as the suspension grout front rises to the elevation of the tapping point. There is a clear change in the rate of pore pressure evolution after the grout front breaks through to the top of the column at time, $t_{br} = 250$ seconds. Although the pressures curves simulated by the continuum model generally match the experimental results well for the two positions closer to the injection point ($z =$ 5 and 15 cm), the model characteristically overestimates the post-breakthrough ($t > t_{br}$) measured pressures further up the column ($z = 45$ and 65 cm).

Bouchelaghem and Vulliet (2001) also noted the discrepancy between measured data and their simulation result, (which are very similar to values in Figure 7.3). They suggested that this could stem from the fact that λ is not constant (as assumed in the continuum model). However, they did not offer an explanation for λ changes as grout penetrates.

This result is actually due in larger part, to the overestimation of the pressure build up from the time when the grout first reaches the observation point, t_1, until t_{br}. As a consequence, the pressure at breakthrough, p_{br}, is higher than the measured value. For example, at $z = 65$cm, $p_{br} = 30$kPa compared to observed 17kPa. Changes in pressure for $t_1 < t < t_{br}$ are mostly due to the increased viscosity of the pore fluid (i.e. for cement grout, $\mu = 3$cp, while water has $\mu_w = 1$cp). Therefore, overestimated pressures for $t < t_{br}$ must be mostly caused by overestimated viscosity. Figure 7.3b shows simulated breakthrough curve (no measured values were available in the publications). Looking closely, it shows that effluent concentration reaches 0.52 of the initial concentration ($C_{out}/C_0 = 0.52$) almost instantly at $t = t_{br} = 250$secs and continues to decrease at a very slow rate to $C_{out}/C_0 = 0.5$ at $t = 600$sec. This must be due to decrease in pore volume and resulting increase in pore fluid velocity, which work to reduce filtration by shortening the travel time of suspension in unit pore volume. This seems a substantial change in concentration enough to induce change in viscosity, and accordingly, a new continuum model including viscosity change due to filtration has to be considered.

7.2.2 Updated continuum model with viscosity change

(1) Viscosity changes with volumetric fraction of solid particles

The microfine cement suspension used in Bouchelaghem and Vulliet (2001) is much more concentrated than the acrylic particle suspension used in Yoon et al. (2004) simulated in Chapter 6. The suspension density, ρ, having the relationship with concentration, C as given in equation 7.3, can be converted to the volumetric fraction of solid particles, ϕ_p, as follows:

$$\phi_p = \frac{\rho - \rho_w}{\rho_s - \rho_w} \tag{7.7}$$

According to this, the microfine cement suspension has volumetric fraction, $\phi_p = 0.075$ while the acrylic suspension of concentration $C = 50 \times 10^{-6}/\text{cm}^3$ has volume fraction of $\phi_p = 4.545 \times 10^{-5}$.

As a suspension becomes more concentrated, interactions between particles become significant and they change the rheological properties of the suspension. Substantial research has been carried out on the rheology of concentrated suspensions (see Probstein, 1994 or Tsai et al., 1992 for review) because it is fundamental knowledge of widespread interest in many industrial applications. Rheological properties of suspensions may depend on many properties of solid particles including particle size distribution, geometry, ionization and volumetric fraction of particles (Raiskinmäki et al., 2000). However, it is well agreed that volumetric fraction of particles is the most important factor controlling the viscosity, since Einstein (1956) derived a formula for viscosity at zero Reynolds number:

$$\mu = \mu_f (1 - 2.5\phi_p) \tag{7.8}$$

where μ_f is the viscosity of the fluid phase. Einstein's formula is derived assuming no hydrodynamic and physicochemical interactions between particles, it is only valid for very dilute ($\phi_p < 5\%$) suspensions (Raiskinmäki et al., 2000).

As the solid volume fraction increases and the interactions between the suspended particles become significant, a nonlinear dependence of shear stress, τ on strain rate, $\dot{\gamma}$ may appear (i.e. non-Newtonian fluid behavior). Especially, it is known that this non-Newtonian behavior is mostly due to small-sized (less than 100 micron) particles (Russell et al., 1989).

In the cement literature, it is widely accepted that fresh mixed cement suspension shows non-Newtonian behavior unless the cement content is very small. Often, especially for extremely dense cement pastes used for structural purposes (water-cement ratio, W/C≅0.3), a Bingham model, with a fixed yield stress, τ_f, at zero shear rate is used (Tattersall and Banfill, 1983):

$$\tau = \mu\dot{\gamma} + \tau_f \quad \text{for} \quad \tau \geq \tau_f \tag{7.9a}$$

$$0 = \dot{\gamma} \quad \text{for} \quad \tau < \tau_f \tag{7.9b}$$

Alternatively, power-law relationships have also been proposed to model the non-Newtonian behavior of cement suspensions (Struble and Sun, 1995).

$$\tau = a\dot{\gamma}^b \tag{7.10}$$

Mittag (2000) carried out a detailed experimental study on the rheology of microfine cement suspensions. The cement particles used in the study have very similar particle size distribution with the one used in Bouchelaghem and Vulliet (2001). Through measurements with microfine cement suspensions at various concentrations (W/C = 3-10), Mittag suggests an empirical relationship for the power-law parameters a and b in equation 7.10:

$$a = 0.001+10.0\ \text{W/C}^{-2.75} \tag{7.11a}$$

$$b = 1.0\text{-}1.13\ \text{W/C}^{-0.53} \tag{7.11b}$$

The measured values of shear stress are shown in Figure 7.4a with the power-law equation 7.10 with these parameters. The water-cement (weight) ratio, W/C has the following relationship with the particle volume fraction, ϕ_p:

$$\phi_p = \frac{1}{1 + \frac{\rho_s}{\rho_w} \text{W/C}} \tag{7.12}$$

The microfine cement grout in Bouchelaghem and Vulliet (2001), according to this relation, has W/C = 4.1.

Figure 7.4b shows shear stress-strain rate relations based on Mittag's correlations for three different W/C values 4.1, 6, and 8 (corresponding to ϕ_p = 0.075, 0.053 and 0.032). The curves clearly show decreasing stress at the same value of strain rate with increasing W/C (i.e. decreasing particle concentration). The measured value of suspension viscosity reported in Bouchelaghem and Vulliet (2001) was μ = 3cp, and the suspension was modeled as a Newtonian fluid. A slope of μ = 3cp can be obtained from the stress curve for W/C = 4.1 if a straight line is drawn from zero to (i.e. $\dot{\gamma}$ = 2750sec^{-1}, τ = 8.24Pa). This is equivalent to approximating the power-law fluid as a Newtonian fluid with an effective viscosity, μ_{Newton} . When straight lines are drawn through the origin at the same shear rate, $\dot{\gamma}$ = 2750sec^{-1} for curves W/C = 6.0 and 8.0, as shown in Figure 7.4, μ_{Newton} = 2.3cp and 1.7cp are obtained respectively.

As shown in Figure 7.3b, the concentration decreases to C_{out}/C_0 = 0.515 by filtration is obtained from continuum model. This is equivalent to the same value of normalized volumetric concentration ϕ_p/ϕ_{p0} and to W/C = 8.3, according to equation 7.12. The power–law fluid with parameters given by Mittag's expression in equation 7.11 predicts substantial changes in viscosity as shown in Figure 7.4.

Although change in viscosity with particle concentration is not modeled by Bouchelaghem and Vulliet (2001), an empirical model of viscosity has been suggested in a more recent publication, Bouchelaghem (2002):

$$\mu = \mu_w \left[1 + \left(\frac{\mu_0}{\mu} - 1 \right) \frac{\phi_p}{\phi_{p0}} \right] \tag{7.13}$$

where $\mu_0 = 3$cp, the initial viscosity at $\phi_{p0} = 0.075$.

Figure 7.5 shows the effective Newtonian viscosities obtained based on Mittag's power law stress-strain relation (equation 7.10, 7.11) and viscosity from equation 7.13 are plotted against the volumetric fraction, ϕ_p. The two expressions show reasonable agreement even though they are based on two different flow models (Newtonian vs. Power-law).

(2) Updated continuum model with viscosity change

Unfortunately, the current continuum model does not have an ability to deal with non-Newtonian behavior that is predicted for the microfine cement suspension. Therefore, a Newtonian fluid approximation is used (similar to Bouchelaghem and Vulliet, 2001). The linear expression in equation 7.13 is applied, replacing μ in equation 7.6a, previously considered a constant, 3cp. Figure 7.6a presents a revised calculation of the pressure evolution. It shows an overall decrease in pressure, especially at two downstream measuring points (z = 45cm and 65cm). This is because the suspension concentration decreases with filter bed elevation due to successive filtration. As a result, the post-breakthrough pressures for the downstream points match much better the experimental values than for the original condition (Figure 7.3a). However, now the pressures for two upstream points are grossly underestimated.

Filtration is solely responsible for the pressure development after breakthrough, and it is clearly underestimated at points simulation near to the injection point, (i.e. at z = 5cm, 15cm). Thus, it seems clear that the continuum model underestimates upstream filtration. This trend is concurrent to what is observed in continuum approach in Chapter 6. Figures 7.6b, c show the continuum model results for larger trial values of the λ = 3.0×10^{-4} sec^{-1} and 4.5×10^{-4} sec^{-1}. Although higher values of λ increase in final pressure at the top elevation (z = 5cm), it seems clear that no improvement can be expected by simply increasing the constant value of filtration rate. Thus, improvement will be pursued through bubble model simulations in subsequent sections.

7.3 PORE SIZE DISTRIBUTION CALCULATION

In order to construct a network model, geometric features of the Leman sand bed (i.e. pore size distribution, location, orientation and connectivity) should be known.

In principle, a three-dimensional representation is possible through reconstruction of pore space using stochastic simulation techniques from experimental data. This can be done by serial sectioning of a sample with pore casting (e.g., Lymberopoulos and Payatakes, 1992, and Tsakiroglou and Payatakes, 2000) or with nondestructive techniques such as X-ray or magnetic resonance microtomography (e.g. Spanne et al.,1994, Baldwin et al., 1996, and Vogel and Roth, 2001). However, the majority of the existing work for deriving geometric parameters corresponding to construct the pore network are based on fitting the experimentally measured pressure-saturation relations using either mercury intrusion porosimetry (e.g. Tsakiroglou and Payatakes, 1990,1991) or soil water characteristic retention curves (e.g. Chandler et al., 1982, Wilkinson and Willemsen, 1983, Koplik et al., 1988, Le Bray and Prat, 1999, and Carmeliet et al., 1999). When a network model is calibrated with the experimental results, some postulations on the shape and connections of pores and pore throats are inevitably made.

In contrast to the glass-bead filter column used in the colloid transport experiments described in Chapter 6, little is known about the pore structure of the Leman sand column in the tests by Bouchelaghem and Vulliet (2001). Instead, pore sizes must be estimated from the particle size distribution shown in Figure 7.1.

The current interpretation uses a method proposed by Arya and Paris (1981). This method uses a capillary tube model in order to predict moisture characteristic curves for unsaturated soils. Arya and Paris (1981) assume all soil grains are spherical. They first select a number of grain radii, a_{gi}, and corresponding weight fractions, w_i, from the particle size distribution curve. The pore volume formed by the assemblage of spherical grains of radius a_{gi}, is simplified as a single cylinder of radius R_i, and length, h_i. The volume balance between pores and grains gives the following equation:

$$e(4a_{gi}^3 N_i \pi / 3) = R_i^2 \pi h_i$$

$$\Leftrightarrow R_i = \left[4a_{gi}^3 N_i e / 3h_i\right]^{1/2} \tag{7.14}$$

where N_i is the equivalent number of spherical particles of radius, a_{gi}, per unit weight and e denotes the macroscopic void ratio.

The length of the pore, h_i, can be simply assumed equivalent to total pore length when grains are aligned, i.e., $h_i = N_i(2a_{gi})$.

However, Arya and Paris (1981) argued that because particles are not perfectly spherical, the contribution from each particle to the pore length is greater than $2a_{gi}$, and proposed to increase the number of spherical particles in estimating the pore length:

$$h_i = \overline{N}_i^{\delta} 2a_{gi} \tag{7.15a}$$

$$\delta = \log N_i / \overline{N}_i \tag{7.15b}$$

where, $\overline{N}_i$, is the number of real, non-spherical particles considered to have a dimension equivalent to a_{gi} per unit weight of solid, which must be greater than N_i. By substituting equation 7.15 to equation 7.14, the equivalent radius of the pore becomes:

$$R_i = a_{gi}[0.66e\overline{N}_i^{(1-\delta)}]^{1/2} \tag{7.16}$$

In Arya et al. (1999a), several values of δ of various types of soils were obtained empirically by comparing soil moisture characteristic curves.

They also suggested an empirical relationship between $\overline{N}_i$ and the fraction of weight of the i^{th} size range, w_i, from the particle size distribution curve:

$$\log \overline{N}_i = a + b\log(w_i / a_{gi}^3) \tag{7.17}$$

The two empirical constants a and b were reported for various soils in the same publication (see Table 7.2). For example, they proposed values of a = -2.478 and b = 1.490 for typical sands.

Arya et al. (1999b) successfully applied equation 7.8 and 7.9 to predict the hydraulic conductivity of unsaturated soil as a function of the moisture content.

Equations 7.16 and 7.17 have been applied to the grain size distribution of the Leman sand shown in Figure 7.1. Using the same coefficient values (a = -2.478 and b = 1.490) proposed by Arya and Paris (1981), the resulting pore diameter distribution is plotted in Figure 7.7. Unlike grain sizes, the calculated pore size overlaps with the cement particle sizes. This means that filtration by sieving should occur, although not to significant extent (less than 5% of pores overlap with the cement particles), as will be explained later when bubble model simulation results are presented.

It is noticeable that there is a wider spread in pore diameter than grain particle size. The 50% passing diameter for the pores, D_{p50} = 0.025mm is smaller than D_{50} = 0.05mm for the sand grains.

7.4 MODEL PORE PARTICLE FLOW SIMULATION RESULTS

Although Chapter 5 has presented data from simulations of collection in model pores, an independent series of flow simulations have been done for the current case, using material parameters from Bouchelaghem and Vulliet (2001).

Three different types of model tubes were used in these for simulations: 1) small horizontal tube with radius, R = 0.125mm, and length, L = 0.25mm; 2) small inclined tube with same radius and length, but with dip angle, θ = 45°(cf. Figure 5.1); and 3) a larger horizontal tube with radius, R = 0.25mm, and length, L = 0.5mm. All tubes maintain the pore aspect ratio, L/R = 2. It is assumed that the cement particles are uniformly distributed. Considering that the cement particles used in the experiments range in size from 0.001 to 0.012mm in diameter as shown in Figure 7.1, a representative radius, r_p = 0.005mm, is selected for the small pore. A radius of 0.01mm is used for larger particles, scaled with the tube radius. Table 7.3 summarizes the parameters used in the model pore simulations. For each case, a series of random particle injections are performed and the results are presented collectively.

Particles are injected at a rate of 10 particles per second at randomly selected positions (and uniform distribution) over the entrance of the tube (this assumption does not affect the subsequent collection efficiency). The particles move under the influence of hydrodynamic forces and gravity. The hydrodynamic forces on the suspended particles

are not explicitly calculated but are indirectly invoked by assuming the particles move at the same velocity as the suspension fluid. The gravitational force, on the other hand, is introduced by specifying a constant settling velocity, v_s, according to Stokes Law:

$$v_s = \frac{2}{9}\frac{(\rho_s - \rho)}{\mu} g r_p^2 \qquad (4.10\text{bis})$$

i.e. for the small tube simulations (Cases 1, 2), v_s = 0.034mm/sec and the average flow velocity is set to be same as the seepage velocity ($v = V_a/n_0$).

When a particle either encounters the pore wall or makes contacts with previously deposited particles, it is considered 'collected'. Whenever a new collection occurs, the particle-fluid coupling force density is updated by the iteration scheme explained in Section 4.4.3. Collected particles remain under the influence of gravity until they make at least 3 contacts with other collected particles and form stable deposits.

Figure 7.8 shows a snapshot of a simulation for the large pore tube (Case 3) after an injection time of 934 seconds, when the number of collected particles, N_c = 705. The streamline pattern shows clearly the interference effects caused by the collected particles on the flow field.

7.4.1 Collection efficiency

Figure 7.9 summarizes the cumulative number of collected particles, N_c as a function of the total number of injected particles, N_{in} for small tube simulations. The results in Figure 7.9a correspond to 14 simulations for flow in a horizontal pore tube (i.e. gravity affects only the settling velocity), while Figure 7.9b corresponds to 30 simulations (of shorter duration) for upward flow through a tube oriented at θ = 45° to the horizontal (Case 2).

In both cases, the data can be well described by a linear relation, whose slope η is the efficiency of collection for the pore tube.

$$\eta = \frac{N_c}{N_{in}} \tag{7.18}$$

According to the correlation gained through parametric study presented in Chapter 5 (equation 5.7), the collection efficiency of a pore of aspect ratio, L/D = 1 and θ = 0, and v_s / U_{flav} = 0.01m/sec is η_1 = 0.078. Similarly, prior results in Chapter 5 show that the orientation angle of the pore tube, θ, described by equation 5.9. According to this equation with θ = 45°, $F(\theta)$ = 0.069, and hence, $\eta_1(45°)$ = 0.054. In comparison the current simulations generate η = 0.088 and 0.058 for Cases 1 and 2 as shown in Figure 7.7. These results are therefore in reasonable agreement with prior calculations presented in Chapter 5.

7.4.2 Maximum deposit depth, d_{max} and mound height, h_{max}

Figure 7.10 shows the maximum deposit depth, d_{max} and mound height, h_{max} (cf. Figure 5.4) increase with the normalized deposit volume, V_d, for the horizontal pore case. These parameters show the same characteristic pattern of monotonic increase at a decreasing rate as was found in previous simulations in Section 5.3 using the specified settling velocity, v_s / U_{flav} = 0.01, the correlation for mound height h_{max} can be described by a bilinear function using equations 5.13a, 5.16a, and 5.18 as follows for Case 1:

$$h_{max} / D = 0.04 + 87.5\, V_d \quad \text{for } h_{max} / D < 0.45 \tag{7.19a}$$

$$h_{max} / D = 0.426 + 5.06 V_d \quad \text{for } h_{max} / D \geq 0.45 \tag{7.19b}$$

where D = 2R. Figures 7.11a shows good matching between these correlations, and the simulations.

For the inclined pore, Case 2, the correlation for β (i.e. slope of the maximum deposit depth/mound height increase) as a function the dip angle θ in equation 5.22 can be applied, which, gives β / β_0 = 0.854 for θ = 45 ° (β_0 corresponds to horizontal pore tube). The corresponding β = 4.32 and α = 74.7. Figure 7.11b shows the comparison of

simulation data and the values obtained with these α and β values and again shows good agreement with the simulation results.

7.4.3 Rejection efficiency

In Chapter 3, it was explained that the rejected particles (i.e. the particles blocked at the entrance due to deposits in the pore) accumulate linearly with the deposit volume. Accordingly, the rejection efficiency, η_{reject} was defined as a linear increasing function of normalized deposit volume, V_d with slope γ in equation 5.24.

According to the equation 5.27a, the value of γ corresponding to the given settling velocity for the small tube case, v_s / U_{flav} = 0.01, is γ = 8.52. This value is directly applicable to the horizontal small tube case. For inclined tube, equation 5.27a used to get β value can be used, resulting in $\gamma = 8.0$. The actual γ values deduced from the current simulations using the method presented in Section 5.4.1 are γ= 9.0 and 8.2 for Cases 1 and 2, respectively. These are slightly higher than the correlation proposed in Chapter 5.

7.4.4 Pressure build-up

Figure 7.12a compares the normalized pressure difference across the model pore tube, $\Delta p/\Delta p_0$, where Δp_0 corresponds to the reference Poiseuille flow condition for results of simulations with the small horizontal pore, Case 1 with the small inclined pore, Case 2. When plotted against the normalized volume of deposit of collected particles, V_d, these results are conveniently modeled by a quadratic function (cf. Equation 5.12):

$$\frac{\Delta p}{\Delta p_0} = 1 + a_1 V_d + a_2 V_d^2 \tag{7.20}$$

Case	θ	a_1	a_2	R^2
1	0°	227	4.49	0.972
2	45°	220	1.25	0.9332

The correlation line for the horizontal tube (Case 1) is plotted in the same figure. The plots as well as the correlation parameters indicate that pressure build-up is slower in inclined pore compared to the horizontal Case 1.

Figure 7.12b compares pressure results of Case 1 (R = 0.125mm and r_p = 0.005mm) with those of Case 2 (R = 0.25mm, L = 0.5mm and r_p = 0.01mm). The pressure drops from two different tube sizes matches well, proving there is no scale effect on the resulting pressure change.

Figure 7.13a shows pressure change data shown in Figure 7.12a re-plotted against the maximum deposit depth. Now the two data sets show better accordance, supporting the idea of using the deposit depth to parameterize pressure change as in Chapter 5 with equation 5.12, rather than using deposit volume as in equation 7.20. The correlation equation 5.12 is applied to the maximum deposit depth d_{max}/D and the resulting pressure drop values are plotted in Figure 7.13b with those from Case 3 simulation. This figure proves that the correlation can work best for all three cases (Case 3 results match Case 1 results well, as shown in Figure 7.12a, which in turn, match Case 2 well as shown in Figure 7.13a). Thus, correlation equation 5.12 is used in bubble model simulations.

7.5 BUBBLE MODEL SIMULATIONS

The bubble model simulation is based on the pore size distribution shown in Figure 7.4. However, the number distribution of pores must first be extracted from the volume distribution. The numbers of pore tubes are dependent on the square of radius if their lengths are assumed constant. Thus, a large number of pore tubes of the smallest radius are needed to fit the assumed volume distribution. For example, 3 million tubes of 0.01mm radius will be required when one 20mm pore tube is to be used. Due to limitations on available computational power, the pores are divided into 33 size ranges with a single pore tube used to represent each group. In order to satisfy this assumption, the number of particles collected by the pore is multiplied by the actual number of pore tubes, which can be determined using the volume relation:

$$N_{pore}^{i} = \frac{V_{pore} F(R_i)}{\pi R_i^2}, \quad i = 1-33 \tag{7.21}$$

where V_{pore} is the total pore volume, $F(R_i)$ is the volume fraction corresponding to the pore size R_i.

Two different lengths of pores are evaluated, L = 0.25mm (short-bond model), and, L = 0.5mm (long-bond model corresponding to D_{50}), which is chosen the same as the particle diameter of 50% passing. Accordingly, the number of bubbles for short and long bonds becomes B = 1640 and 3280, respectively.

7.5.1 Pressure build-up evaluation procedure

For the bubble model simulation, the current particle size distribution in Figure 7.1 is discretized into 24 size ranges. Then the particle injection rate of particles with radius, r_{pm}, $\dot{N}_m$, can be estimated from volume balance and given particle size distribution. This, in turn, gives the input particle number during the time step, Δt, $\Delta N_{in,m} = \dot{N}_m \Delta t$, with time step $\Delta t = L/v$. The number of particles collected in the first bubble after the first time step, t_1, will be controlled by the corresponding collection efficiency, $\eta(r_{\mathrm{p,m}})$:

$$\Delta N_c^1(t_1) = \sum_{m=1}^{24} \eta(r_{p,m}) \Delta N_{in,m} \tag{7.22}$$

The grout front at the k^{th} time step, $t = t_k$, will be located at $z = vt_k$, at the end of the k^{th} element, while the total number of collected particles at the i^{th} element from the injection point can then be written:

$$N_c^i(t_k) = \sum_{q=i}^{k} \Delta N_c^i(t_q) \tag{7.23}$$

Ahead of the grout front, the pore water pressure is controlled by Darcy's law. The pressure at the grout front is then given by:

$$p_k(t_k) = \frac{\mu_w V_a (H - vt)}{k_0} \tag{7.24}$$

Note that the pore pressure is zero at the top of the sand column, (z = 82cm).

Pore pressures inside the grouted zone are determined from the pressure development equation ($\Delta p/\Delta p_0$). At the end of the i^{th} bubble at $t = t_k$ is given by:

$$p_i(t_k) = \Delta p_0 \sum_{j=1}^{W} N_{pore}^{j} \frac{q_{ij}}{Q} \frac{\Delta p}{\Delta p_0} \left(nV_d^{ij}(t_k)\right) + p_{i+1} \text{ for } i = 1,\ldots,k\text{-}1 \tag{7.25}$$

where W is the number of bonds in each bubble, 33, nV_d^{ij} is the normalized deposit volume in the j^{th} bond of i^{th} bubble, q_{ij} the flow rate thorough the bond while Q is the total flow rate.

The bond radius is updated using as explained in Section 5.3 in equation 5.38 as collected and rejected particles accumulate. The reference pressure drop, Δp_0, can be specified by Darcy's law:

$$\Delta p_0 = \frac{\mu V_a L}{k} \tag{7.26}$$

with parameters listed in Table 7.1.

7.5.2 Related parameters

It is well known that the settlement is hindered by other suspended particles (hindered settling, Probstein, 1994). Consequently, the settling velocity decreases with increasing volumetric fraction of particles. The current particle flow simulator, which was employed to provide key correlations for the bubble model, does not explicitly model interactions between particles. Therefore, an empirical model for settling velocity is

required to simulate the deposition process for a concentrated suspensions. A simple and often applied empirical relationship is given by Richardson and Zaki (1954):

$$v_s = v_{s0}\left(1 - 0.5\frac{\phi_p}{\phi_{pm}}\right)^n \tag{7.27}$$

where v_{s0} is the single particle settling velocity (i.e. Stokes velocity in equation), ϕ_{pm} the maximum possible volumetric fraction (65% for randomly close-packed uniform spheres), n an empirical constant typically between 5.1-5.5.

Struble and Sun (1995) reported values of $\phi_{pm} = 0.64$ through experiment with Type I Portland cement. This value was used in the current bubble model simulation with $n = 5.3$. With the initial volume fraction, $\phi_p = 0.075$, equation 7.27 gives 0.73 v_{s0}. Using this settling velocity as an input, the rejection and collection efficiencies and pressure drop correlations presented in Chapter 5 can be evaluated. Uniform distribution of orientation is assumed and the homogeneous values, η_H and η^H_{reject} (equation 5.11, 5.30) are used.

The attachment probability, A_p, used in Chapter 6 is again applied. Unlike in Chapter 6, it is calibrated by matching the pressure evolution curve for the observation point at z = 5cm, because no breakthrough concentration information was published for these experiments.

7.5.3 Simulation results

When constant viscosity is assumed, A_p = 0.0016 gives the best-fit pressure evolution curves with the long-bond model and the short-bond model respectively, as shown in Figures 7.14a and b, respectively, together with measured values.

The first observation is that bond length has minimal effect on the simulation results. This confirms prior expectations that pore length is addressed in the proposed correlations for collection efficiency and pressure build-up (Sections 5.1 and 5.2). These bubble model results are almost identical with the continuum results, as compared in

Figure 7.15. Thus, the same trend in overestimation of the two far observation points (z = 45cm and 65cm) is also applicable to the bubble model simulations. Therefore, the linear decreasing function of viscosity with volume fraction of solid particles in equation 7.13 is employed as was done previously to update the continuum approach.

At the same time, the detachment process that was modeled in Chapter 6 is added in the model because detachment process amplifies nonlinearity in spatial deposit distribution (i.e. more filtration near injection point and less downstream filtration) as illustrated in Figure 6.12a. The same trend is observed in the current simulation. It is clearly noticeable from the normalized deposit concentration (S/C_0) profiles with varying $\bar{k}_0$ values (a constant at reference pore velocity, $v_0 = 1.38\times10^{-2}$ cm/sec in equation 6.33) presented in Figure 7.16. The profile obtained with the updated continuum model (Figure 7.6) is plotted together. Interestingly, the continuum model simulation result is slightly different from the bubble model result with full detachment condition although the two models give almost identical pressure evolution curves. This is because filtration rate increases as deposits accumulates in the bubble model simulation due to particle rejection, which increases with volume of deposits (see Section 5.4).

Figure 7.17a illustrates the contributions of the deposit concentration for $\bar{k}_0 = 2.1\text{cm}^{-1}$ from the different collection mechanisms: sieving, entrapment, hindrance, and rejection. It shows that the most of the deposit are derived by rejection. More specifically, 74% to 42% of total deposit volume, decreasing with elevation, is collected by rejection as illustrated in Figure 7.17b. This occurs because hindered particles (although temporarily collected) induce rejections as well as entrapment. As expected from the pore and particle size distribution comparison shown in Figure 7.7, there are some sieved particles, but these correspond to less than 0.5% of the total deposit volume throughout the sand column.

The effect of rejection increasing overall filtration (i.e. ripening) is also well presented by the effluent concentration decreasing with time as shown in Figure 7.18, which was not observed in simulations in Chapter 6. That was because the deposit volume was not substantial enough to cause significant amount of rejected particles in the acrylic particle suspension filtration. The same effect of the detachment process in slowing down the initial effluent concentration increase rate can be observed in

breakthrough curves as in Chapter 6. However, the effluent concentration in later stages is also affected and decreasing with the value of $\bar{k}_0$. This is also due to ripening.

Figures 7.18a, b show the pressure evolution curves for $\bar{k}_0$ = 7.7 and 2.1cm^{-1}. As expected from the comparison of deposit concentration profiles in Figure 7.16, decreasing the detachment rate (i.e. longer retention of particles) induces higher pressure build-up. Especially, with $\bar{k}_0$ = 7.7cm^{-1}, there is almost no post breakthrough ($t > t_{br}$) pressure build-up. This is a result of tradeoff between viscosity decrease and deposit volume increase, which are both outcomes of filtration. Pressure evolution curves with $\bar{k}_0 = 2.1\text{cm}^{-1}$ matches the measured values much better than the continuum model at the two tapping points near the injection point ($z = 5$cm and 15cm), as compared in Figure 7.19.

The bubble model underestimates the pre-breakthrough pressure values at z = 45cm while overestimating pressures after breakthrough. In addition, post-breakthrough pressures at $z = 65$cm are also slightly overestimated. Compared to the continuum model results, the initial development of pressure at z = 45cm is much slower. The decrease in detachment rate works to increase the amount of hindered particles near injection point, which are later re-suspended and effectively increase downstream suspension concentrations. Therefore, if the detachment rate is too small, the parameter $\bar{k}_0$ will be responsible for the initial underestimation and subsequent overestimation of pressure build-up at z = 45cm. It is not clear what caused this change in detachment rate for downstream. Physicochemical changes related to hydration and resulting changes in rheological properties, as earlier noted in Section 7.1, may be responsible (although the experiment was completed within the expected induction period). However, further study (both experimental and theoretical) study on suspension behavior seems imperative to elucidate this matter.

It should be noted that $\bar{k}_0$ = 2.1cm^{-1} resulted in best matching with the measurements of Bouchelaghem and Vulliet (2001) values was much higher than $\bar{k}_0$ = 0.28 cm^{-1} used to match tests by Yoon et al. (2004) (Chapter 6). This fact may suggest more unfavorable conditions for particle-particle or particle-grain attachment

with the cement suspension than with the acrylic particle suspension, which is consistent with the decreased attachment probability, from $A_p = 0.09$ (for rough beads) in Chapter 6 to $A_p = 0.0016$ for the current application.

Another difference found comparing the case in Chapter 6 is that limit particle size by introducing r_{limit}, had minimal effect on simulation results for the cement injection. It must be due to the fact that the cement particles are less distributed (diameter 1μm-13μm) than the acrylic particle suspension used in Chapter 6 (diameter 1μm-25μm).

7.6 CONCLUSIONS

This chapter describes the interpretation of one-dimensional injection tests published in the literature using a dense suspension of microfine cementitious grout in sand using continuum models and the proposed bubble model. For the continuum models, the filtration rate, λ is an essential parameter that should be known a priori for prediction with the model. It is not easy to evaluate the filtration rate, and a separate experimental and statistical study was used to predict its initial value. It is even harder, however, to make prediction on evolution of spatial and temporal change in filtration rate during injection, and an assumption of constant filtration rate was assumed. The simulations results applying the constant filtration rate had some success on predicating the measured values, but found characteristically overestimating the post-breakthrough measured pressures further up the column ($z = 45$, 65cm). This overestimation was found partially due to overestimated extent of filtration, but mainly due to decrease in suspension concentration (at least to 50% of initial value) and a related decrease in viscosity. When the continuum model was updated to include the decrease in viscosity due to filtration, most of the overestimation of the measured pressure build-up was addressed. However, it also produced much less filtration near the injection source. This trend was consistent with observations of continuum models in Chapter 6.

A bubble model was constructed, with representative pore radii of the medium calculated using a semi-empirical method proposed by Arya and Paris (1981) based on the given sand particle size distribution. The empirical parameters, attachment probability

A_p and detachment rate, $k_r = \bar{k}_0 v$ were used. As a result, it was learned that the detachment rate does play a crucial role in producing a non-linear trend in the deposit profile. Thus, the pressure evolution curves showed much improved by including particle detachment.

In order to further improve model simulations, more research is needed on suspension behavior. It was noted by other studies (e.g. Mittag, 2000) that microfine cement suspensions exhibit non-Newtonian flow behavior. The chemistry of cement particles and its effect on flow and microscopic collection mechanism are also needed to be studied for more complete analysis of the filtration of the microfine cement suspension.

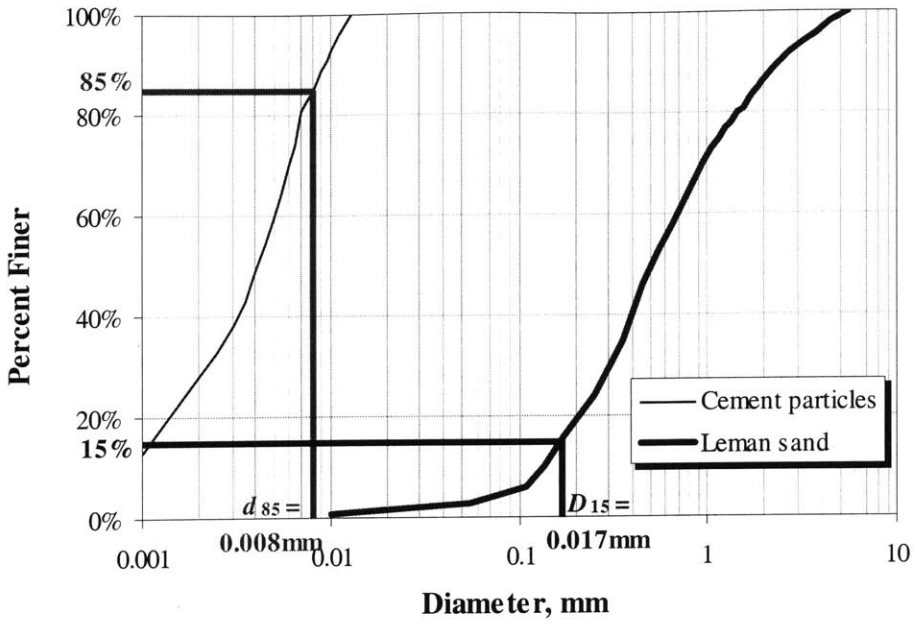

Figure 7.1 Cement particle and sand grain size distribution reported by Bouchelaghem and Vulliet (2001)

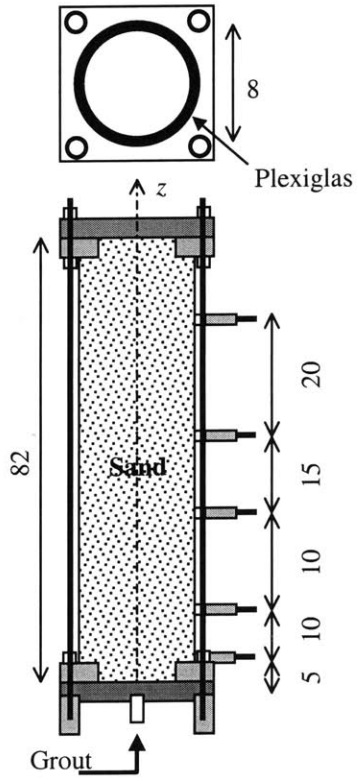

Figure 7.2 One-dimensional injection test configuration after Bouchelaghem and Vulliet (2001) (dimensions are in cm)

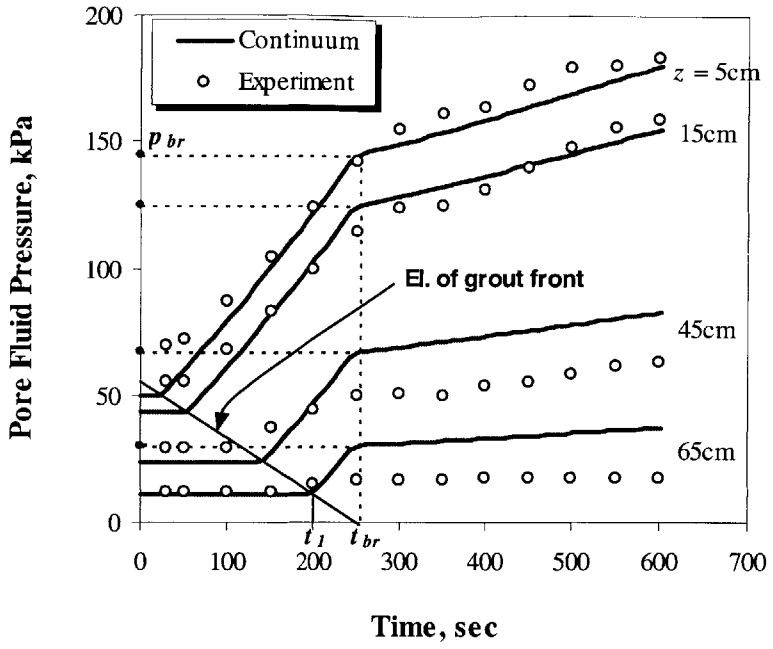

(a) Pressure evolution

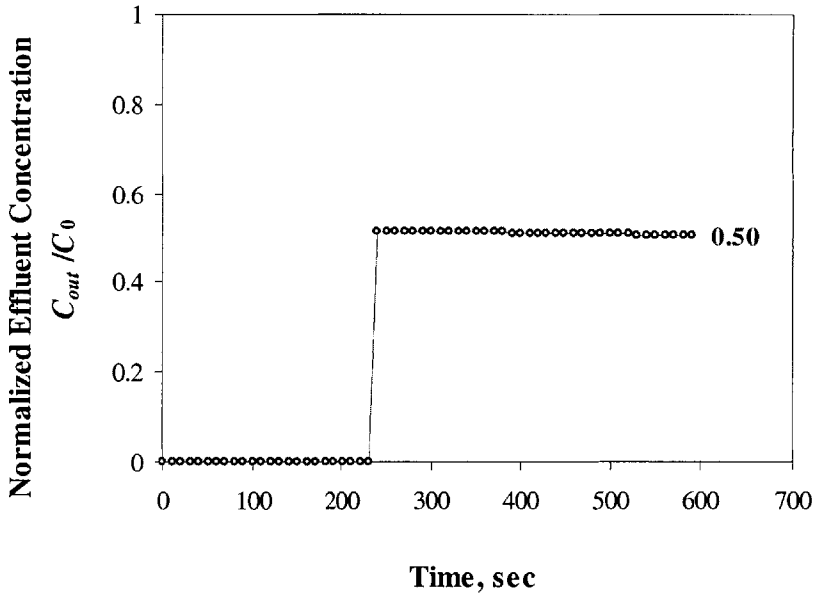

(b) Breakthrough curve

Figure 7.3 Results of continuum model

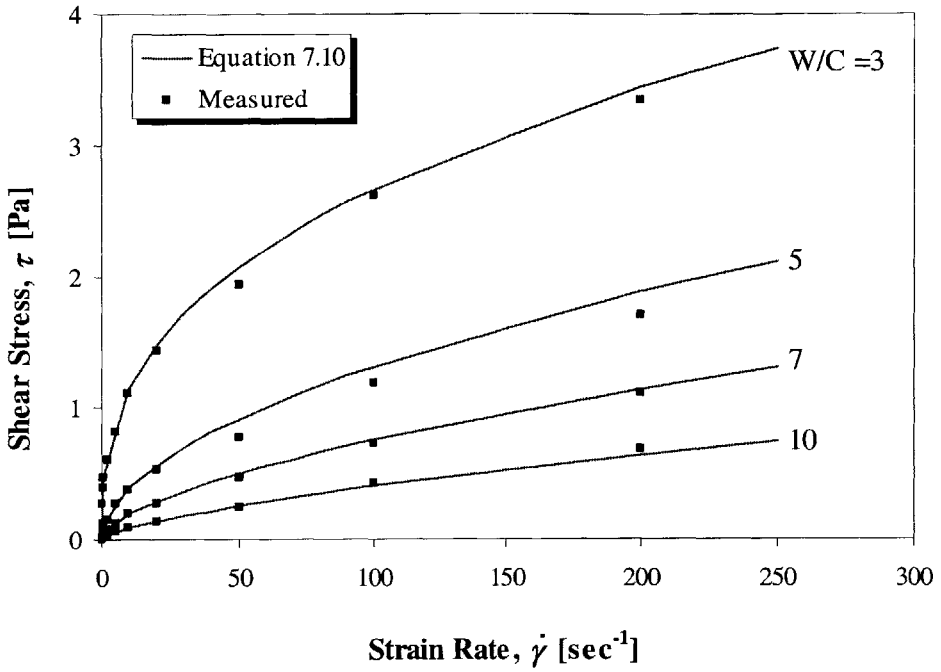

(a) Measured stress-strain relationship compared with a power-law relation

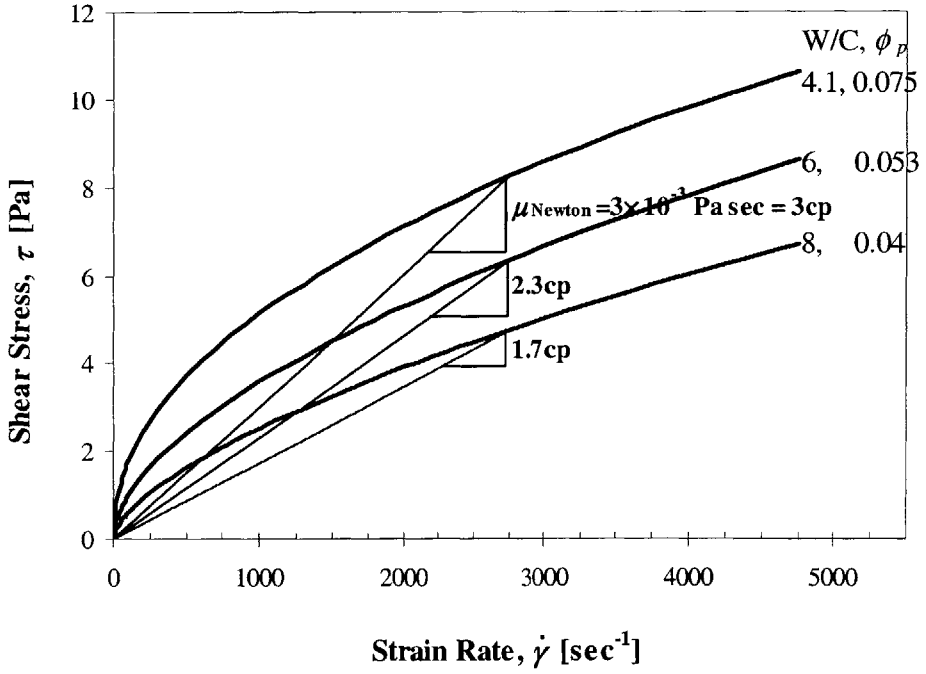

(b) Secant viscosities, μ_{Newton} for W/C=4.1, 6,8

Figure 7.4 Shear stress-strain rate relationship proposed by Mittag (2000)

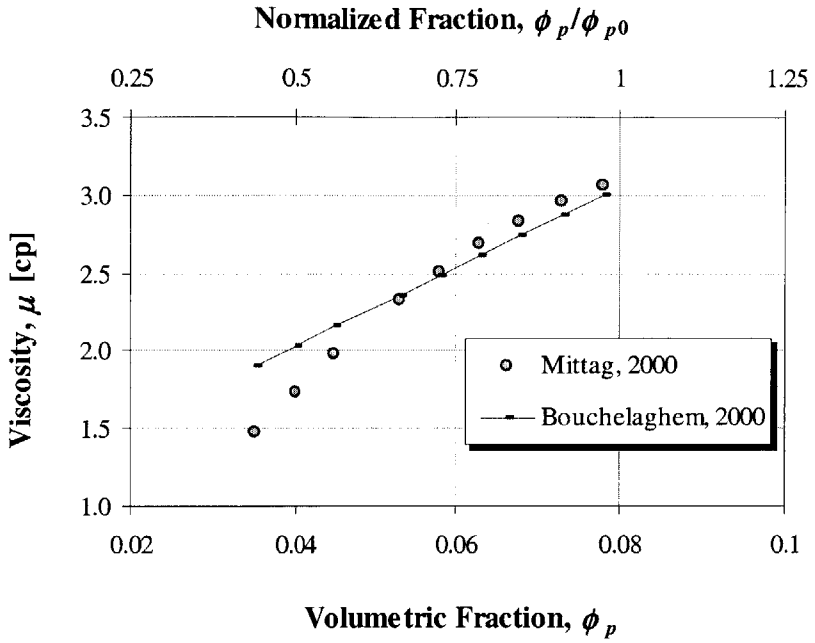

Figure 7.5 Comparison of viscosity for cementitious suspension as functions of volumetric fraction of solid particles

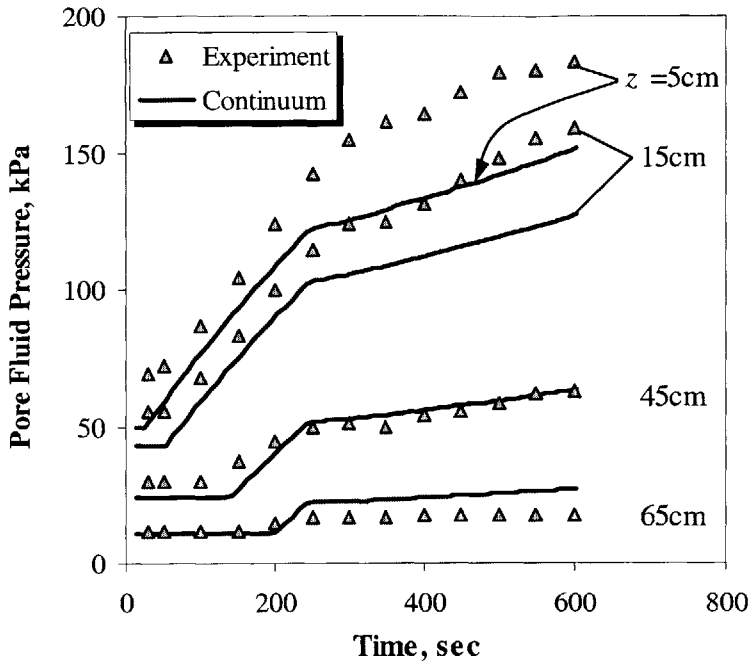

(a) with $\lambda = 1.5\times10^{-4}$ sec $^{-1}$

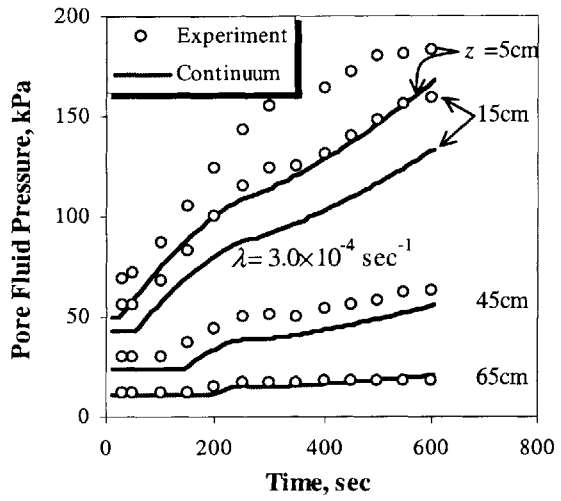

(b) with $\lambda = 3.0\times10^{-4}$ sec $^{-1}$

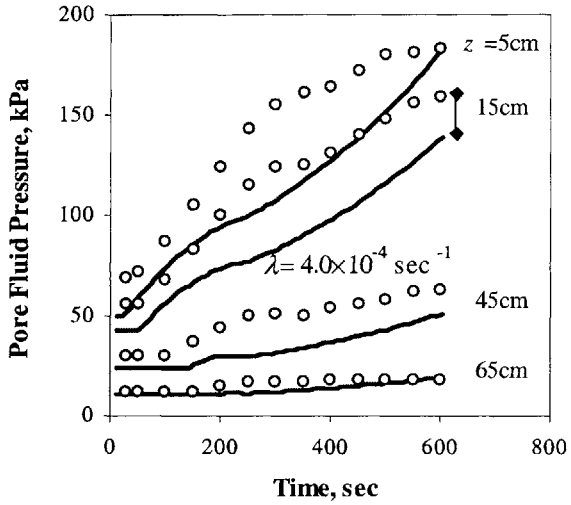

(c) with $\lambda = 4.5\times10^{-4}$ sec $^{-1}$

Figure 7.6 Computed pressures by the updated continuum model with viscosity change

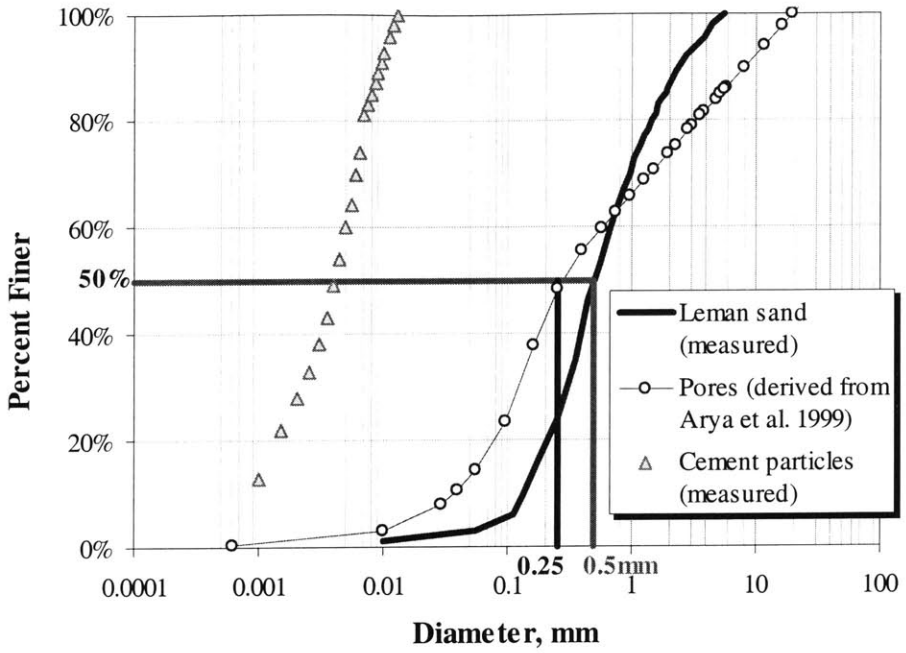

Figure 7.7 Pore size distribution obtained after Arya and Paris (1981)

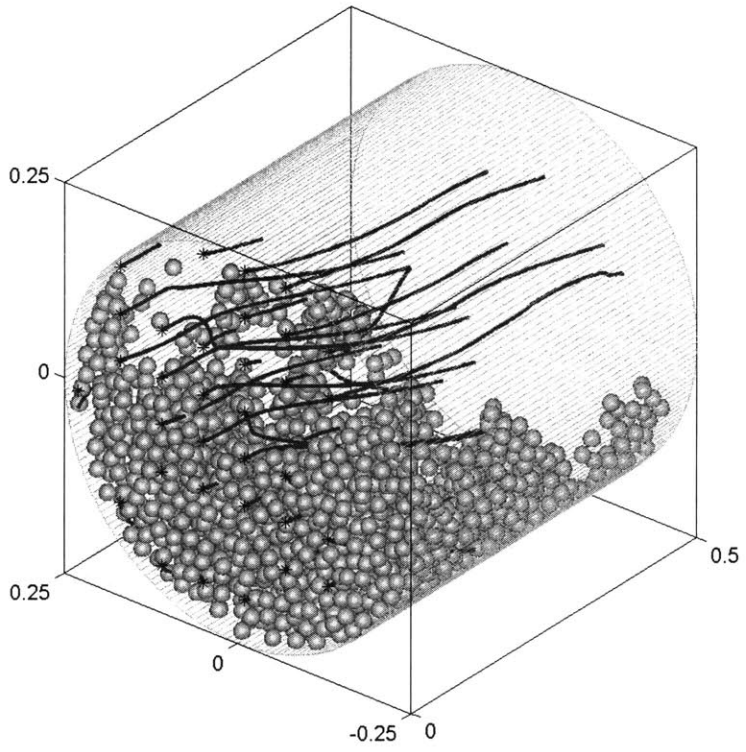

Figure 7.8 Snapshot of model pore tube (Case 3) after 934 seconds with 705 particles collected

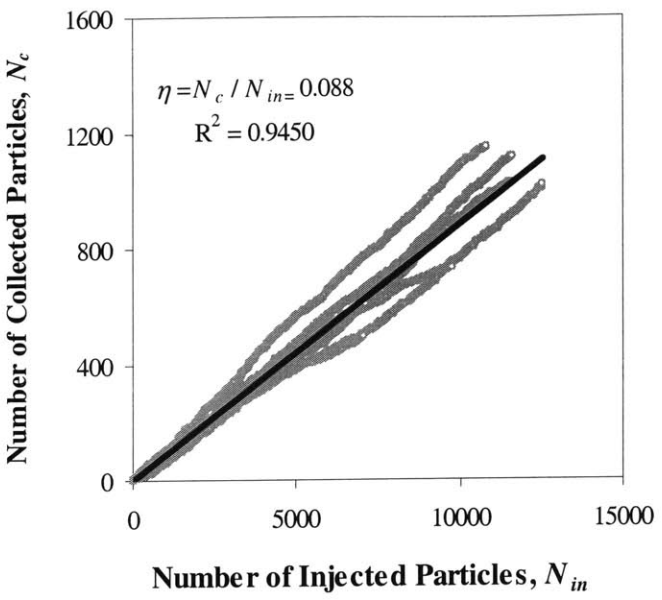

(a) Horizontal pore tube, Case 1

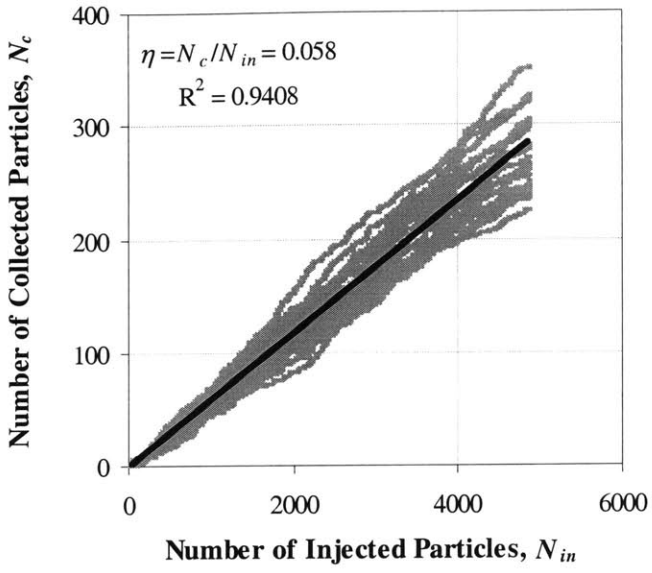

(b) Pore tube inclined at 45°, Case 2

Figure 7.9 Particle collection rate for small pore tube

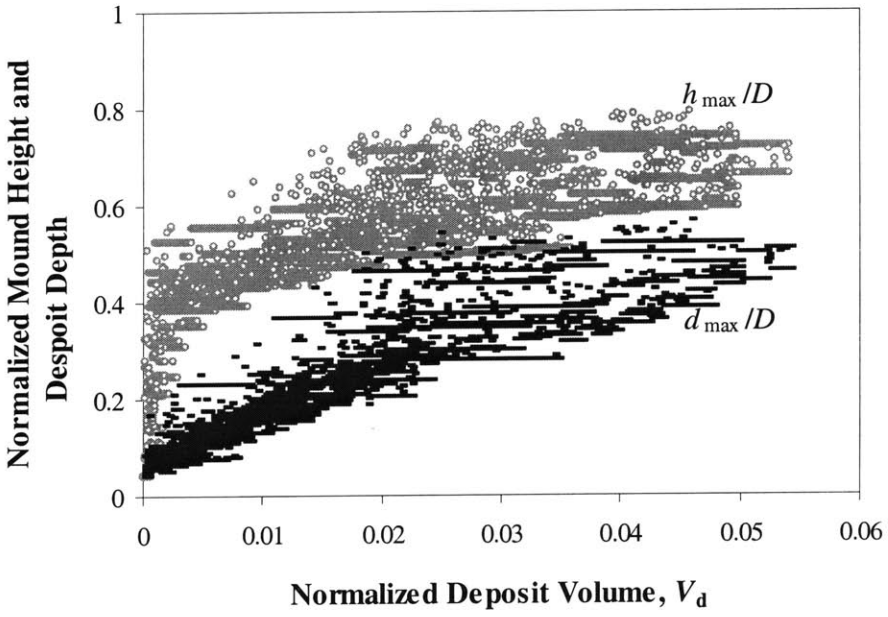

Figure 7.10 Maximum mound height, h_{max} and deposit depth, d_{max} increase from horizontal small pore tube simulations

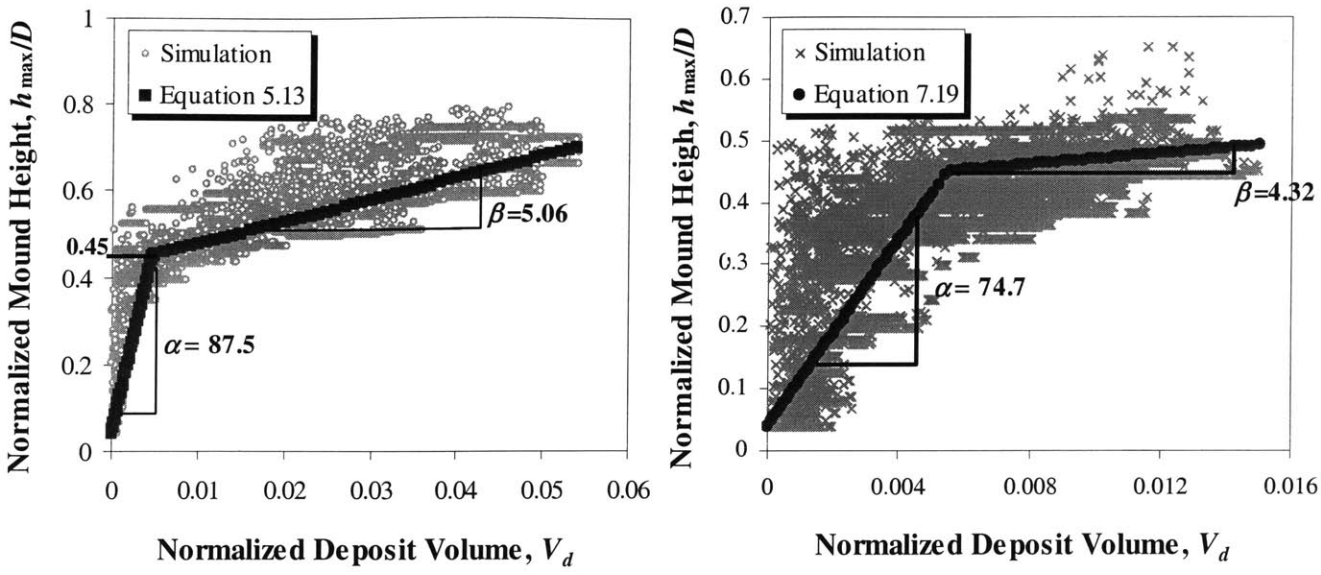

(a) Horizontal pore tube, Case 1 (b) Pore tube inclined at 45°, Case 2

Figure 7.11 Maximum mound height and deposit depth from model pore tube simulations

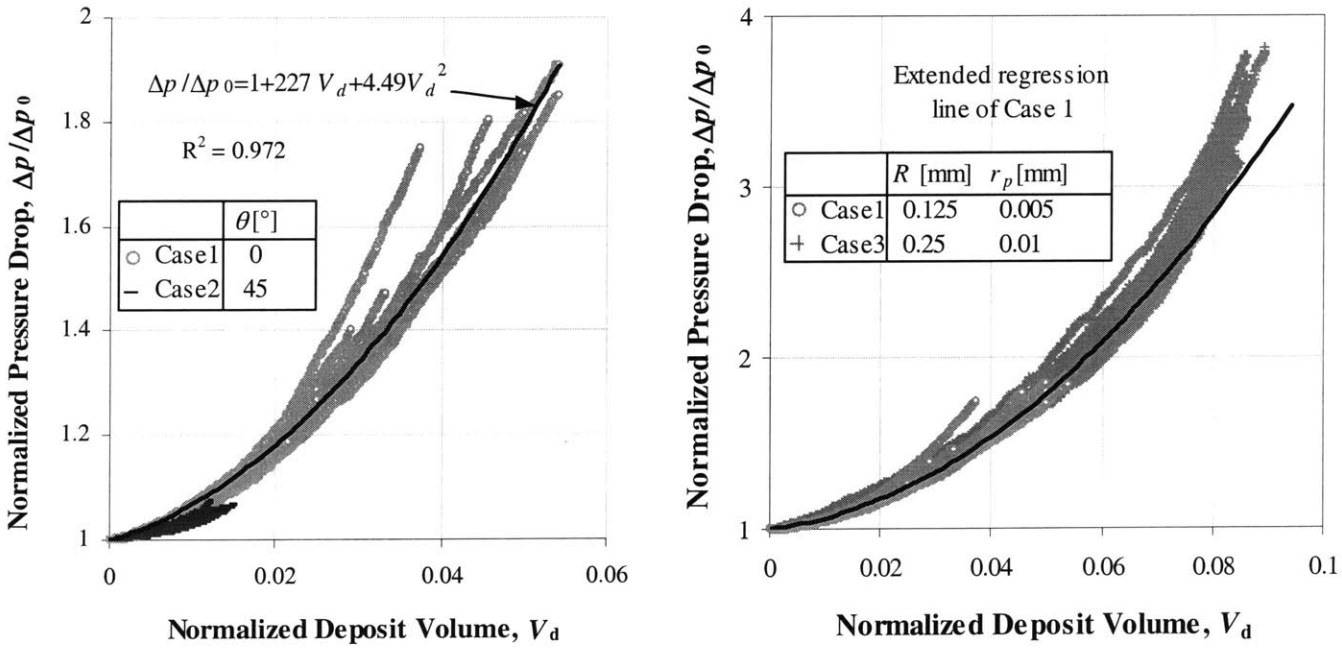

(a) Case 1 vs. Case 2 (b) Case 1 vs. Case 3

Figure 7.12 Evolution of pressure change across model pores

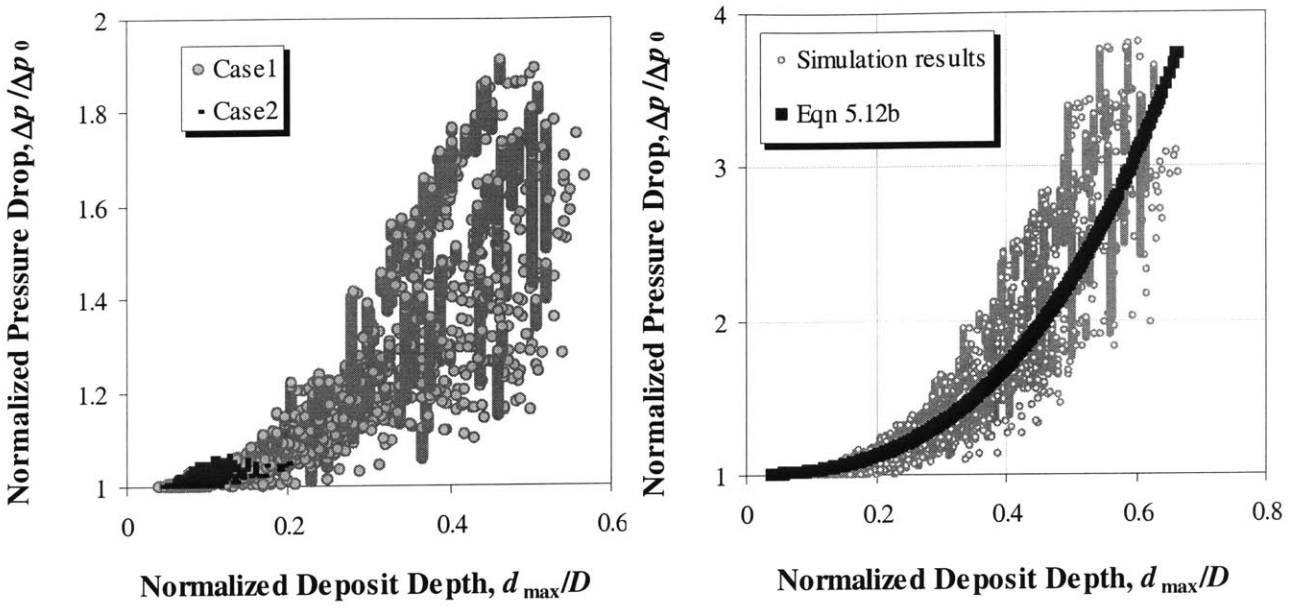

(a) Case 1 vs. Case 2

(b) Case 3 vs. equation 5.12b

Figure 7.13 Pressure change plotted against maximum deposit depth

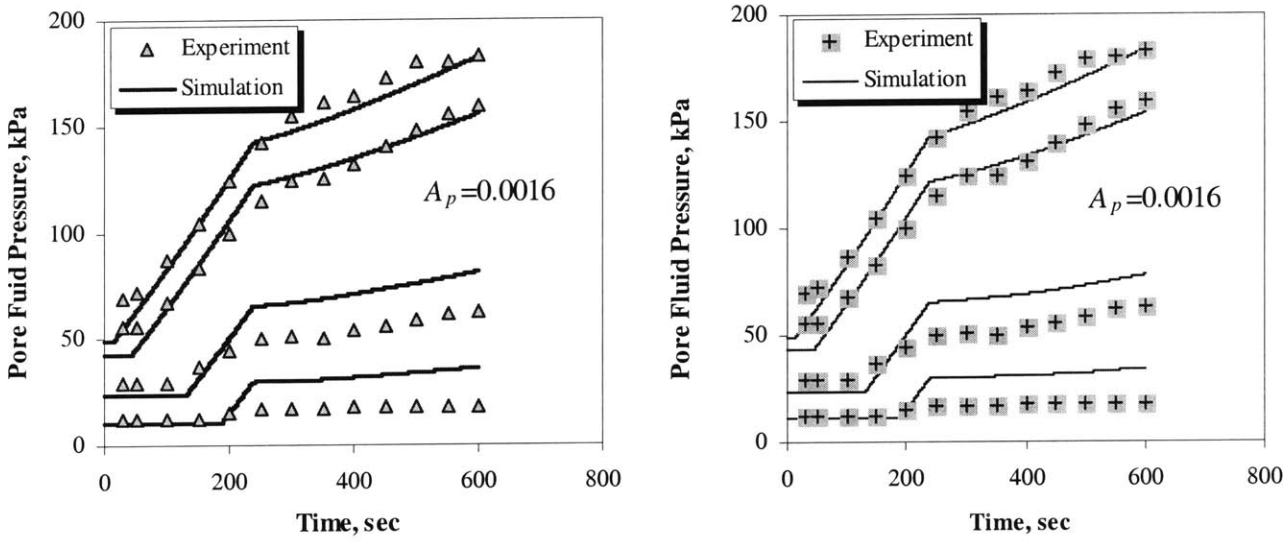

(a) Long bond, L = 0.5mm

(b) Short bond, L = 0.25mm

Figure 7.14 Comparison of measured fluid pressures and bubble model simulation (without considering viscosity change) results

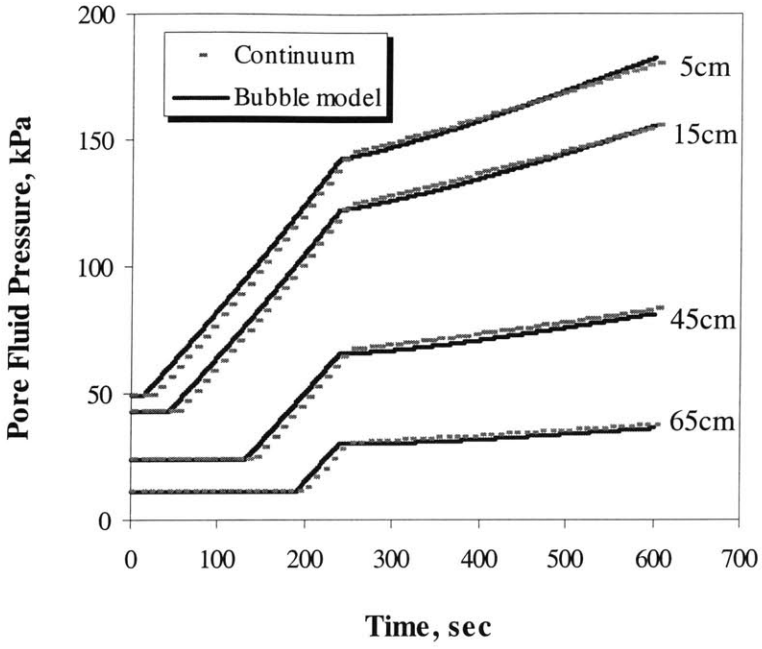

Figure 7.15 Comparison of bubble model results with continuum model results without viscosity model

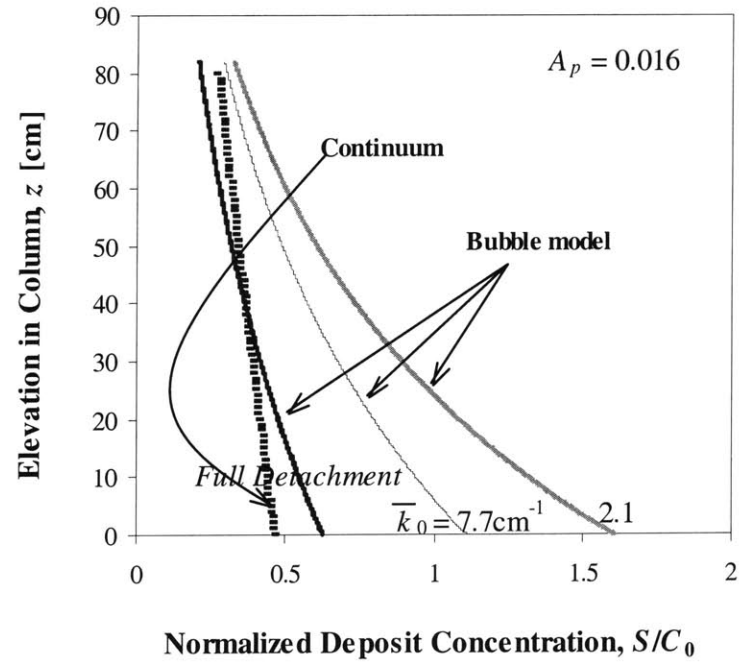

Figure 7.16 Change in deposit concentration profile with varying detachment ratio

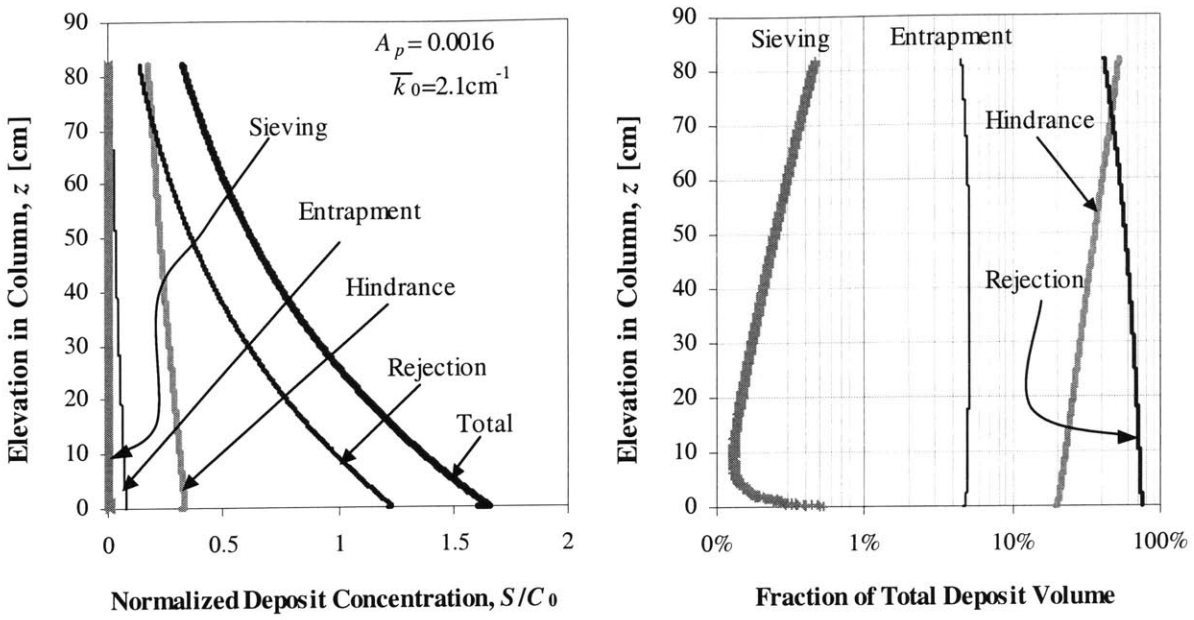

(a) Normalized concentration (b) Fraction

Figure 7.17 Parts from different collection mechanisms of total deposit concentration

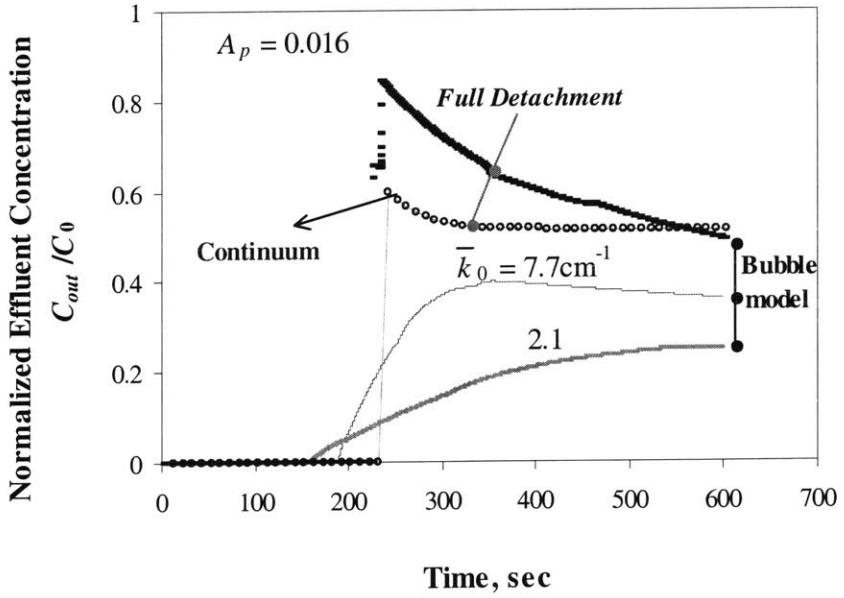

Figure 7.18 Effect of detachment ratio on breakthrough curve

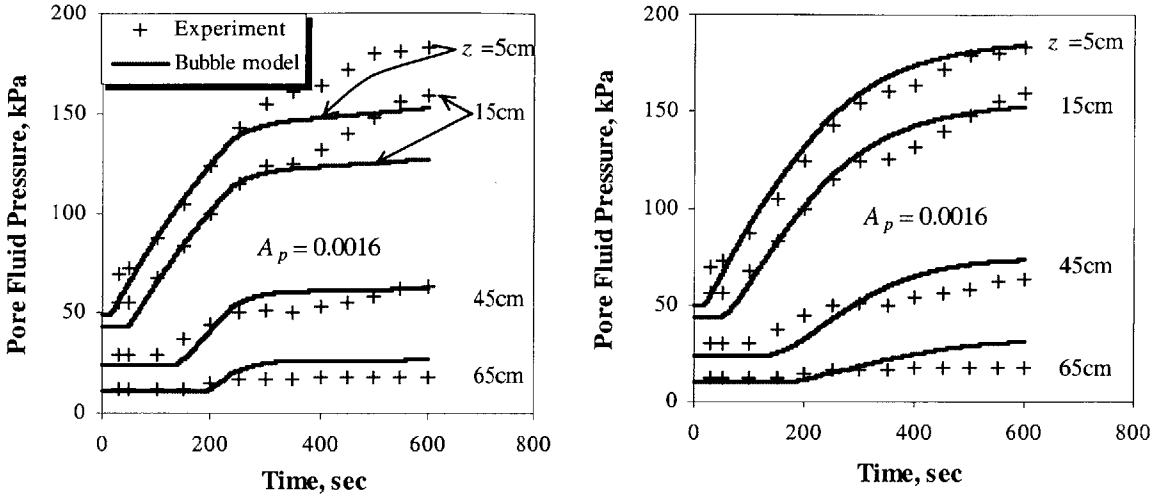

(a) with $\bar{k}_0 = 7.7\ \text{cm}^{-1}$ (b) with $\bar{k}_0 = 2.1\ \text{cm}^{-1}$

Figure 7.19 Effect of particle detachment on bubble model simulation of pressure evolution

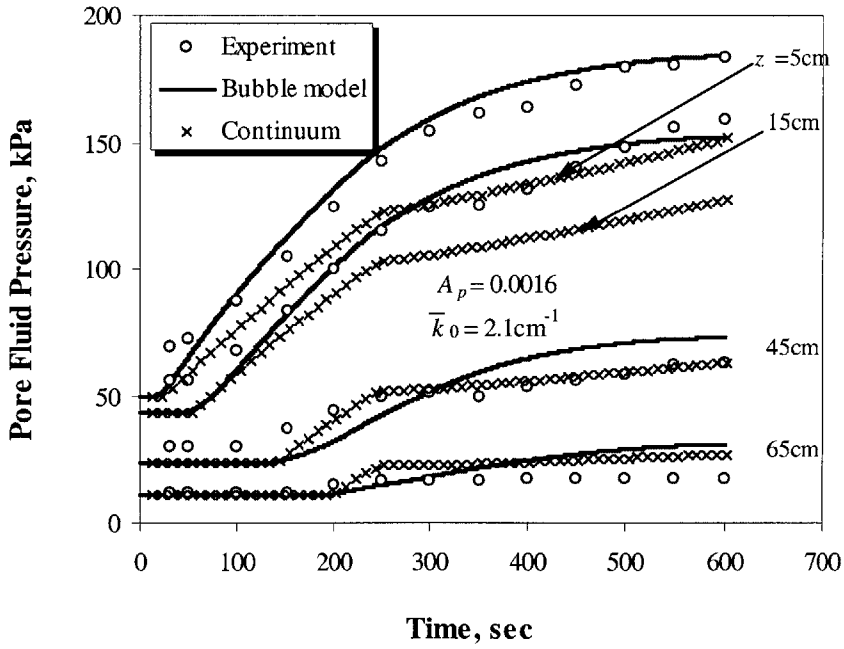

Figure 7.20 Comparison of measured pressure data with bubble model and continuum model results including changes in suspension viscosity

Table 7.1 Material parameters (Bouchelaghem and Vulliet, 2001)

Mean particle diameter	0.005 mm
Sand grain D_{50}	0.5 mm
Initial porosity, n_0	0.34
Initial permeability, k_0	2×10^{-11} m^2
Grout viscosity, μ	0.003 Pa sec (3 centi Poise)
Grout density, ρ	1.15 g/m^3
Grout solid density, ρ_s	3.0 g/m^3
Sand column height, H	82 cm
Apparent flow velocity, V_a	0.117 cm/sec

Table 7.2 Parameters of equation 7.17 for four soil classes by Arya et al. (1999)

Soil class	No. of soils	Data pairs	a	b	R^2
Sand	6	62	-2.478	1.490	0.882
Sandy loam	6	75	-3.398	1.773	0.952
Loam	4	50	-1.681	1.395	0.936
Clay	5	88	-2.600	1.305	0.954

Table 7.3 Parameters used in particle flow simulations

Parameters	Case		
	1	2	3
Particle radius, r_p [mm]	0.005	0.005	0.01
Model pore radius, R [mm]	0.125	0.125	0.25
Model pore length, L[mm]	0.25	0.25	0.5
Model pore dip angle, q [°]	0	45	0
Total particles injected	12,000	5,000	10,000
Particle injection rate [particles/sec]	10		
Average flow velocity, v [mm/sec]	3.4		
Time step [sec]	1×10^{-4}		
Stiffness, K	1		
Number of iterations	50		

CHAPTER 8. SUMMARY, CONCLUSIONS AND RECOMMENDATIONS

8.1 SUMMARY

This thesis has presented a novel method of analyzing the filtration of suspension particles transported through a granular porous medium, and its application in interpreting two sets of 1-D column injection experiments. The contents of the thesis can be summarized as follows:

(1) Chapters 1, 2 describe phenomenological aspects of filtration process commonly observed during suspension transport through a granular filter bed. The chapter reviews continuum models for filtration rate kinetics and the concept of trajectory analysis as an analytical method for predicting filtration rate.

(2) Chapter 3 presents a review of network models as an alternative discrete approach for modeling porous media. A quasi one-dimensional "bubble model" (Datta and Redner, 1998) is discussed in detail and the algorithm of particle transport is presented for the model.

(3) Chapter 4 describes the particle-laden flow simulator. The simulator is designed to realize particle depositions inside a cylindrical model pore. Particles are deposited under the action of hydrodynamic and gravitational forces. They can mound up and ultimately clog the pore. This analysis uses Stokes equations for the flow and tracks particle movements under influence of gravity for constant flow rate boundary condition. The key feature of the simulator is that it considers

coupling forces between deposited particles and the fluid, which are responsible for changing the flow field and hence, the deposition mechanism of suspended particles. After validation for flow around single stationary particles, multiple injections of mono-disperse particles were simulated. The results show that deposited particles increase the pressure difference across pore tube and enhance particle deposition rate.

(4) Chapter 5 presents a parametric study results done by using the particle simulator. The effects of particle size, pore radius, aspect ratio (length to diameter ratio) and orientation, particle settling velocity and attachment probability were studied. The following trends in collection efficiency and pressure change were found:

- Collection efficiency is well represented by a power law function of the particle settling velocity (equation 5.7). It also increases as a power law of pore aspect ratio, and decreases quadratically with the pore dip angle of the pore (equation 5.8, 5.9 respectively).
- Pressure changes across the model pore are larger for filtration of smaller particles than for larger particles with the same volume of deposits (i.e. smaller particles form deposits that mounds higher and block more cross-sectional area).
- The maximum mound height, h_{max} and maximum deposit depth, d_{max} are selected as the parameters that measure both the amount and density of the deposit layer. Two separate third-order polynomial equations have been proposed to correlate d_{max} and h_{max} with the pressure change at initial and advanced stages of filtration, respectively (equation 5.12).
- h_{max} and d_{max} are found to increase linearly with volume of deposits. A bilinear equation for h_{max}, and a linear one for d_{max} are suggested. The parameters are given as linear functions of settling velocity. Both increase as functions of the pore aspect ratio (power-law), and pore dip angle (quadratic).
- The number of particles blocked at the inlet (i.e. "rejected particles"), is found to increase linearly with the deposit volume. The rejection efficiency is parameterized as bilinear function of the settling velocity. The increase in rate of particle rejection is closely related to the deposit depth and mound height.

- The initial collection rate reduces with the attachment probability, A_p ($0 \leq A_p \leq 1$). As particles mound inside the pore, the collection rate increases as a power law function of the surface saturation (equation 5.35) and eventually reaches full efficiency (i.e. effect of $A_p < 1$ is progressively removed during the mounding process).

(5) Chapter 6 presents the first application of the proposed method for 1-D column injection tests, performed by Yoon et al. (2004) at three different injection velocities with a dilute acrylic particle (size ranging 1-25μm) into a glass bead (4mm diameter) bed. In order to do this, the bubble model presented in Chapter 3 was used. An analytical solution for regular packed spheres was used to define the size distribution of the pores. For individual bonds in the model, the particle collection efficiency was based on correlations from the particle flow simulator (Chapter 5). In addition, the capacity change of the bond is directly calculated from the pressure change across the model pore (also given in Chapter 5). It was found that two empirical parameters: i) the attachment probability, A_p and ii) the detachment rate, k_r, were critical in explaining the microscopic observations by Yoon et al. (2004) on two different collection mechanisms: entrapment and hindrance. Through simulations with different injection rates ('slow', 'medium', 'fast') on beads with smooth surface, it was found that k_r was linearly proportional to pore fluid velocity, while A_p remained constant. Since most entrapment on smooth beads were observed having occurred at solid-solid contact points of beads (contact entrapment) by Yoon et al. (2004), a higher A_p value was needed to match measurements for tests on rough beads was attributed to entrapment by surface roughness (surface entrapment).

(6) Through comparisons between the measured inflow and effluent particle distributions, it was found that almost none of particles smaller than 5μm had been collected in a test with 'slow' injection rate on rough beads. It was hypothesized that smaller particles than this limit size, r_{limit} were only subjected to contact entrapment, and accordingly, the attachment probability found in smooth bead cases ($A_p = A_{pc}$) was applied for $r < r_{limit}$. By increasing r_{limit} while keeping A_p and k_r the same with the slow injection rate case for medium and fast injection

rate tests, the simulated results showed reasonable agreement with the measured values.

(7) Chapter 7 considers simulation of 1-D injection test of microfine cement suspensions (size ranges 1-13μm) through a sand column (Leman sand, grain size ranging 0.01-6mm). An empirical relationship by Arya and Paris (1981) was used to obtain the input pore size distribution of the bubble model. Due to the relatively high concentration of this suspension (0.075 volume solid fraction, ϕ_p), extensive filtration was observed and consequently, the evolution in pressures was observed (in contrast to experiments in Chapter 6). The measured pressure data were compared with continuum model results and it was concluded that viscosity of the suspension was decreasing due to filtration. An empirical model was introduced to characterize decrease in viscosity with solid fraction. The updated pressure evolution results generally underestimated filtration near the injection point (consistent with results in Chapter 6).

(8) Particle flow simulations have been done with model pore tubes and particles of sizes more comparable to the current case. The results showed a good agreement with the correlation equations for collection efficiency and pressure changes from the parametric study in Chapter 5.

(9) With these correlations, bubble model simulations were carried out. When viscosity model was not included, the pressure curves obtained were almost identical to the continuum model solutions with assuming an attachment probability value, $A_p = 0.0016$. By including the viscosity model and detachment rate, significant improvements were observed in matching the simulated and measured pressure curves.

8.2 CONCLUSIONS

8.2.1 Microscopic modeling of filtration

Phenomenological filtration laws introduced in Chapter 2 are intrinsically limited in dealing with microscopic features of the filtration process. Trajectory analysis based

on the assumption of an unit filter bed (Unit Bed Element) of a simplified geometry (explained in Chapters 2, 4) are also limited to clean bed conditions and eventually involve empirical relations to account for effects of deposits on subsequent filtration (i.e. in advanced stages of injection tests).

The current particle-laden flow simulator enables full modeling of hydrodynamic interactions between the particles and fluid and hence, provides a basis for rigorous studies of the microscopic filtration process. The parametric study results identify features of the deposition mechanisms and particles accumulation that are not represented by empirical rate laws or trajectory analyses (with UBE):

- Collection efficiency is higher when hydrodynamic coupling between particles and fluid are considered because the flow velocity near the deposit layer decreases.
- Collection efficiency increases as filtration progresses because of blocking by deposits. This was parameterized as 'rejection efficiency'.
- Decrease in hydraulic capacity of a pore, which is represented by the pressure difference increase at a constant flow rate condition, is closely linked to the extent of filtration. More specifically, it was found that at a given volume, a deposit layer comprised of smaller particles tend to cause higher pressure drop across a pore than those with larger particles, because the density of deposit layer increases as the particle size decreases. Therefore, deposit depth or mound height (as opposed to deposit volume) should be used as a measure of clogging on pressure changes.
- Effects of the pore aspect ratio and orientation strongly affect the filtration process. It was found that the collection efficiency and pressure drop generally increase as the pore aspect ratio increases at a given relative volume (normalized by the pore volume) of deposit because the particles usually form higher mounds near the inlet. The collection efficiency decreases as the dip angle increases (i.e. as the pore becomes aligned with the gravitational direction). On the other hand, the pressure drop was found to increases as the tube becomes more aligned with the gravity. This is because the blocking of

inlet is more effective for an inclined model pore compared to a horizontal one.

- The rejection efficiency, which is closely linked to deposit depth, shows the same trend with the aspect ratio and the dip angle.

8.2.2 Bubble model and its application on column tests

Bubble models were found to be effective in scaling up the microscopic filtration mechanisms from the particle-flow simulator to predict macroscopic changes in porous media. The bubble model is able to track movements of particles of different sizes base on correlations found using the particle flow simulator (which are in turn, given as functions of the settling velocities of individual particles). In addition, bubble models incorporate the distribution of pore size and orientation, the two variables that principally affect the deposition mechanism. With size distribution, bubble models also intrinsically replicate the hydrodynamic dispersion in random porous media, enabling more particles to flow through larger bonds (pores). As shown in Chapter 7, pore size distribution is imperative in modeling filtration due to sieving.

For the two applications of the bubble model presented in Chapters 6 and 7, the collection efficiency correlations were obtained from Chapter 5 simulations assuming full attachment of all deposited particles. This resulted in an overestimation of the measured filtration rates suggesting the importance of detachment of deposited particles. This result was supported by microscopic observations made by Yoon et al. (2004). Lack of quantified information on the microscopic attachment and detachment processes has forced the use of empirical parameters within the bubble model simulations. The attachment probability, A_p, partitions the collected particles between those that are fully entrapped and those that are only hindered (i.e. released back into flow at a given detachment rate). Although these parameters are analogous to the filtration and detachment rates used in macroscopic filtration laws of the two-site continuum model, the bubble model produced predictions that are far more successful in Chapter 6. Both the prediction of total depositions by the suggested correlation equation and scaling-up with bubble model must have contributed on the successful prediction.

Filtration of the microfine cement suspension in Chapter 7, compared to that of acrylic particle suspension in Chapter 6, showed different macroscopic characteristics because it involved far significant changes in pore pressure, decrease in viscosity of the suspension, and changes in filtration rate. Among these, the pore-pressure increase was effectively modeled by decreasing the capacities of individual bonds with the bubble model. Considering that there exist few analytical models directly relating changes in flow and filtration, it seems that the current method will provide a valid option. Changes in filtration rate due to deposited particles were also successfully modeled through the concept of 'rejected' particles.

8.3 RECOMMENDATIONS

Future work should include the unresolved issues of detachment and attachment probability in microscopic process and also consider expanding the application to filtration problems.

1. All particle flow simulations done in the current study use uniformly sized particles. Since most suspensions in practical applications have a distribution of particle sizes, these need to be considered in the simulations.
2. Only constant flow rate conditions have been implemented. For comparison, particle flow simulations need to be done at constant pressure conditions and further employed for simulations of tests done at constant pressure condition.
3. The effect of attachment probability on collection efficiency is studied in Chapter 5, but with the limited assumption of it only affecting attachment between particle and the pore wall. More detailed analyses including the effects of particle-particle attachment probability will be useful in applications where partial attachment occurs between particles, as well as particles and surface of the porous filtering medium.
4. It was concluded in simulations presented in Chapters 6, 7, that the detachment mechanism has an important influence on deposit concentration distribution, inducing a nonlinear spatial distribution of filtration deposit accumulation. Currently, an empirical parameter, k_r, is used to represent the detachment process.

More studies (both experimental and theoretical) are needed to understand the mechanisms of detachment (between particles, and between particles and surfaces) in order to assess critical drag forces that can induce detachment. This data can then be applied directly in the particle flow simulator to enable more rigorous modeling of the detachment process.

5. This thesis has not investigated the effects of flow direction on macroscopic filtration although its microscopic effect is well explained by dip angle of model pore. The link between microscopic and macroscopic effects of flow direction with respect to the gravitational field should be examined in more detail.
6. Both application cases presented have minimal straining effects. It will be interesting to see the effect of straining and related changes in pore size distribution in macroscopic filtration.

   An optimization study of 1-D filtration where pore size distribution, injection rate, direction of flow are selected to be controlled to maximize (or minimize) filtration, would excellent tests of the predictive capabilities of the proposed bubble model.
7. Finally, the current bubble model can be expanded to 2-D and 3-D problems with appropriate network models. 3-D injection tests such as Bouchelaghem (2002) can be used to test the feasibility of particle-flow simulator.

APPENDIX A: EFFECT OF HYDRATION ON PENETRATION OF CEMENTITIOUS GROUT SUSPENSION

A.0 INTRODUCTION

Hydration, the solidification process of a cementitious material is usually considered to start at least a few hours after mixing when the cement starts to 'set'. The ACI (American Concrete Institute) definition of set is the condition reached by a cement paste, mortar or concrete when it has lost plasticity to a reference amount, usually measured in terms of resistance to penetration or deformation. The initial set refers to the first stiffening and the final set refers to attainment of significant rigidity. The duration before initial set after mixing is finished is called the induction period (e.g. McKinley and Bolton, 1999). Retarders and accelerators are commonly used to advance or delay the induction period, and can be designed to match the time required for mixing and injection of grout. Retarders can extend induction period up to 30 hours (Gause and Bruce, 1997), which is generally sufficiently longer than time needed for injecting a grout. Thus, hydration has been typically assumed to have no effect on its penetrability. However, if the injection process continues over the induction period, flow of grout suspension can be seriously inferred by cement hydrates that remain inside pores and hence, limit space available for flow. In this case, hydration kinetics have to be incorporated into analysis of grout penetration into soil as they determine the rate of pore volume change.

Although little hydration is expected to occur during the induction period (less than 5%), it has been well reported that rheological properties of cementitious material evolve even with this small amount of hydrates. This provides another reason for hydration kinetics to be considered in modeling permeation grouting.

This Appendix first presents an analytical solution for spherically radial permeation grouting with constant injection pressure. Then two aspects of hydration on penetration of grout, by filling pore space with solidified grout and by change of rheological properties during induction period, are studied.

A.1 EFFECT OF SOLIDIFIED GROUT ON PERMEATION GROUTING

A.1.1 Degree of hydration

Cement hydrates (solid grout) can seriously affect penetrability of a grout by inhibiting flow of grout remained at liquid state (liquid grout) by reducing pore space. This might not happen frequently in practice because hydration is generally suppressed by additives to assure grouting to be carried out within induction period, in which no significant amount of solid grout is produced. Nevertheless, it can be worthwhile incorporating effect of long-term hydration in modeling of permeation grouting as a limit case.

Hydration is a complex set of sequential and simultaneous chemical reactions at microscopic levels (Ulm and Coussy, 1996). More details of these reactions will be discussed later. Kinetics of hydration depends on many physicochemical parameters such as degree of hydration, water-to-cement ratio, curing conditions (Nonat et al., 1997). The degree of hydration, ξ, can be calculated from the evolution of either mechanical properties or physical properties such as strength, heat or concentration:

$$\xi(t) = \frac{X(t)}{X(\infty)} \tag{A1}$$

where $X(t)$ and $X(\infty)$, respectively, represent the value of the physical or mechanical property at the moment and at an infinite time(Kada-Benameur et al., 2000). For present problem, the mass of solid grout, m_{solid}, is used to define the degree of hydration, as the property that determines change in pore volume. Then, equation A1 can be re-written:

$$\xi(t) = \frac{m_{solid}(t)}{m_{solid}(\infty)} \tag{A2}$$

Since hydration kinetics is determined by sequential processes that have different rates of reactions, it must depend on the age of a cementitious grout (relative to the time of mixing). The age of the material can differ from the time of injection, t, in case freshly mixed grout is continuously added and a separate time variable, s, is necessary to describe the age of the grout. Thus, the age, s, is separately defined and accordingly, the degree of hydration becomes a function of s, $\xi(s)$.

A.1.2 Modeling of permeation grouting

If the homogeneity of liquid grout is kept during grouting process, the permeation grouting can be modeled as a well defined problem of pumping a liquid into the ground and replacing pore water, while hydration can be incorporated as a phase change process (based on the kinetics of hydration). Figure A.1 shows the Representative Elementary Volume (REV) for the three-phase system considered. The analysis assumes:

1. There is no displacement in the skeleton (i.e. ϕ_s remains constant).
2. Densities of liquid grout, ρ_{gl} and solid grout, ρ_{gs} remain constant.
3. The whole pore space is occupied either by the water or by liquid grout (i.e. saturation degree of liquid is always 100%).

As the total volume of the REV is conserved according to assumption 1, and is fully saturated, the initial porosity n_0 is the same as the total volume fraction of grout.

$$\phi_{gl} + \phi_{gs} = n_0 \tag{A3}$$

The mass balance equation of the liquid grout phase is as follows.

$$\frac{\partial(\rho_{gl}\phi_{gl})}{\partial t} + \nabla \cdot (\underline{v}_{gl}\phi_{gl}\rho_{gl}) + R = 0 \tag{A4}$$

In this equation, R is the ratio of the liquid grout mass changes to the solid grout mass by the hydration. Therefore, this rate is same as the creation rate of the solid grout mass:

$$R = \frac{\partial(\rho_{gs}\phi_{gs})}{\partial t} \tag{A5}$$

Darcy's law can be used for the liquid grout velocity, $\underline{v}_{gl}\phi_{gl}$. This law defines the apparent velocity of the pore fluid as a function of pressure gradient, ∇p:

$$\underline{v}_{gl}\phi_{gl} = \underline{v} = -\frac{k(\phi_{gl})}{\mu}\nabla p \tag{A6a}$$

where μ is the dynamic viscosity and $k[\mathrm{L}]^2$ is the permeability tensor of the media depending on the porosity, $k = k(\phi_{gl})$. By defining a new parameter, fluidity $\frac{k(\phi_{gl})}{\mu_{gl}} = C(\phi_{gl})$, Darcy's law can be rewritten:

$$\underline{v}_{gl}\phi_{gl} = \underline{v} = -C(\phi_{gl})\nabla p \tag{A6b}$$

By substituting equation A3, A5 and A6b to equation A4 and applying assumption 2 of constant densities, the conservation equation is obtained as follows:

$$\left\{\frac{\rho_{gs}}{\rho_{gl}} - 1\right\}\frac{\partial\phi_{gs}}{\partial t} - \nabla \cdot (C(\phi_{gl})\nabla p) = 0 \tag{A7}$$

The age of the grout depends on the time of mixing. If new material is mixed continuously, a 'perfect mix' is obtained as shown in Figure A.2a. In this case, the solid grout phase in the REV comprises layers of material of different age. The age of liquid grout, s, also varies as a function of time and location. On the other hand, if the material is mixed in one batch, the material at all locations will have a same age, $s = t$ as shown in Figure A.2b. This case is referred to as the 'single batch' case.

The mass of solid grout at a specific time, $m_{solid}(t)$ in equations A2 is $\rho_{gs}\phi_{gs}(t)$, while the total mass of material that will be completely solidified an infinite time, $m_{solid}(\infty)$ is the mass of liquid grout in place, $\rho_{gl}\phi_{gl}(t)$. Therefore, the rate of solid grout increase can be directly related to hydration rate:

$$\frac{d\xi}{dt} = \frac{\partial(\rho_{gs}\phi_{gs}(t))/\partial t}{\rho_{gl}\phi_{gl}(t)} \tag{A8}$$

Substituting this into equation A7 for perfect mix case:

$$\nabla \cdot (C(\phi_{gl})\nabla p) = \frac{(\rho_{gs} - \rho_{gl})}{\rho_{gs}}\phi_{gl}\frac{d\xi(s)}{dt} \tag{A9a}$$

while for the single batch case:

$$\nabla \cdot (C(\phi_{gl})\nabla p) = \frac{(\rho_{gs} - \rho_{gl})}{\rho_{gs}}\phi_{gl}\frac{d\xi(t)}{dt} \tag{A9b}$$

By defining a dimensionless coefficient, $b = \frac{(\rho_{gs} - \rho_{gl})}{\rho_{gs}}\phi_{gl}$, equation A9b can be rewritten in a general form,

$$\nabla \cdot (C(\phi_{gl})\nabla p) = b\frac{d\xi}{dt} \tag{A10}$$

The simplest relevant model of permeation grouting involves injection from a single point source in an infinite medium, a process that assumes radial flow with a spherical geometry. In this case, the radial velocity of the fluid, v_r, is driven by the radial gradient of pressure, $\partial p/\partial r$. Equation A10 becomes

$$\frac{1}{r^2}\frac{\partial}{\partial r}(r^2 C(n)\frac{\partial p}{\partial r}) = b\frac{d\xi}{dt} \tag{A11}$$

where, the symbol n is used to represent the porosity (i.e. $n = \phi_{gl}$).

Figure A.3 illustrates the spherical permeation model assuming no diffusion at the interface ($r = r_w$) between the penetrating grout and in-situ pore water (liquids 1 and 2 in the figure). The pressure boundary conditions when a well pressure p_w is applied to inject grout into the ground where the initial pore pressure is p_e are:

$$p_1 = p_w \quad \text{at} \quad r = r_w \tag{A12}$$

$$p_2 = p_e \quad \text{at} \quad r = r_e \tag{A13}$$

where p_1 and p_2, respectively, indicate the pressure inside fluid 1 (liquid grout) and fluid 2 (pore water). At the interface of these two fluid, at $r = r_0$, pressures and radial velocities ($v_{r,1}$, $v_{r,2}$) have to be identical:

$$p_1\Big|_{r=r_0} = p_2\Big|_{r=r_0} \tag{A14}$$

$$v_{r,1}\Big|_{r=r_0} = v_{r,2}\Big|_{r=r_0} \Leftrightarrow C_1\frac{\partial p_1}{\partial r}\Big|_{r_0} = C_2\frac{\partial p_2}{\partial r}\Big|_{r_0} \tag{A15}$$

where C_1 and C_2 represent fluidity of fluid 1 and 2, respectively.

The rate of advance of this interface coincides with the velocity of the liquid grout:

$$n(r_0)\frac{\partial r_0}{\partial t} + C_1\left(\frac{\partial p_1}{\partial r}\right)_{r_0} = 0 \tag{A16}$$

where $n(r_0)$ is the porosity at the interface and multiplied to the rate of advance, $\partial r_0/\partial t$, because the velocity of the liquid grout, $C_1\left(\frac{\partial p_1}{\partial r}\right)_{r_0}$, is an apparent velocity, not an absolute velocity (true fluid velocity).

Inside the region occupied by pore water ($r \geq r_0$), there is no phase change and flow can be described by the Laplace equation ($\frac{1}{r^2}\frac{\partial}{\partial r}\left(r^2\frac{\partial p_2}{\partial r}\right) = 0$), having a general solution of $p_2 = \frac{A}{r} + B$. By applying the boundary condition equation A13 and assuming no change in water pressure in the far field ($r_e \to \infty$), the pressure in the pore water is given by:

$$p_2 = \frac{A}{r} + p_e \tag{A17}$$

The boundary conditions at the interface, equations A14, A15, and A16 can be applied to give the following relation.

$$\left.\frac{\partial p_1}{\partial r}\right|_{r_0} = -\frac{C_2}{C_1(n)|_{r_0}}\frac{p_1(r_0) - p_e}{r_0} \tag{A18}$$

Assuming that there is no change in the porosity at the grout front, i.e., $C_1(n)|_{r_0} = C_1(n_0)$, a viscosity ratio, $\alpha = \frac{C_w}{C_1(n_0)} = \frac{\mu_1}{\mu_2}$, can be introduced in equation A18. Now the pressure of the pore water, p_2 can be eliminated from the governing equation system and the following equations summarize the remaining governing differential equation and boundary conditions for the grout phase only.

$$\frac{1}{r^2}\frac{\partial}{\partial r}(r^2 C(n)\frac{\partial p}{\partial r}) = b\dot{\xi} \quad \text{for} \quad r_w \le r \le r_0 \tag{A19a}$$

$$p = p_w \quad \text{at} \quad r = r_w \tag{A19b}$$

$$\frac{\partial p}{\partial r} = -\alpha\frac{p - p_e}{r} \quad \text{at} \quad r = r_0 \tag{A19c}$$

$$\phi(r_0)\frac{\partial r_0}{\partial t} - C_w\frac{p(r_0) - p_e}{r_0} = 0 \tag{A19d}$$

where the subscript 2 indicating pore water was replaced with w indicating water and subscript 1 dropped.

Without hydration, the time-dependent term in equation A19a is zero and this differential equation reduces to the Laplace equation. The pressure distribution and grout front progress are found analytically and identical with solutions reported by Raffel and Greenwood, (1961):

$$p = \frac{\alpha(p_e - p_w)}{\frac{(\alpha-1)}{r_0} - \frac{\alpha}{r_w}}\left(\frac{1}{r} - \frac{1}{r_w}\right) + p_w \tag{A20}$$

$$t = \frac{n_0 r_w^2}{C_w(p_w - p_e)}\left[\frac{\alpha}{3}\left(\frac{r_0^3}{r_w^3} - 1\right) - \frac{(\alpha-1)}{2}\left(\frac{r_0^2}{r_w^2} - 1\right)\right] \tag{A21}$$

A.1.3 Dimensional analysis

For a problem involving many physical quantities dimensional analysis can provide a simplification. This section presents a dimensional analysis of the governing equation system composed of equations A19a-A19d.

The rate of hydration, $d\xi/dt$, can be defined to be a constant for the dimensional analysis:

$$\frac{d\xi}{dt} = \frac{1}{\tau_H} \tag{A22}$$

where τ_H is the characteristic time of hydration and considered intrinsic to the cementitious material. The kinetics of hydration are characterized by sequential stages that are distinguished by different major reactions and kinetics laws (refer to Section 3.2). However, in order to identify the effect of hydration, the hydration process can be represented by characteristic time. All variables used in the governing equations, including hydration rate, $\dot{\xi}$, are considered linearly transformed from dimensionless counterparts by corresponding dimensions:

$$\begin{aligned} r &= Rr' \\ r_w &= Rr'_w \\ t &= Tt' \\ p &= Pp' \\ p_w &= Pp'_w \\ p_e &= Pp'_e \\ C &= \Sigma C' \\ C_w &= \alpha C(n_0) = \alpha \Sigma C'(n_0) \\ \tau_H &= T_H \tau'_H \end{aligned} \tag{A23}$$

i.e. $r', r'_w, t', p', p'_w, p'_e, C', C'(n_0), \tau'_H$ are dimensionless variables corresponding to $r, r_w, t, p, p_w, p_e, C, C(n_0), \tau_H$ of dimensions $R, R, T, P, P, P, \Sigma, \Sigma, T_H$ (same letters indicate the same dimensions).

Equations A19a-A19d can be re-written with dimensionless variables in equations in A23:

$$\left(\frac{T_H \Sigma P}{R^2}\right) \frac{1}{r'^2} \frac{\partial}{\partial r'} \left(r'^2 C'(n) \frac{\partial p'}{\partial r'}\right) = b \frac{1}{\tau'_H} \quad \text{for} \quad r'_w \le r' \le r'_0 \tag{A24a}$$

$$p' = p'_w \quad \text{at} \quad r' = r'_w \tag{A24b}$$

$$\frac{\partial p'}{\partial r'} = -\alpha \frac{p' - p'_e}{r'} \quad \text{at} \quad r' = r'_0 \tag{A24c}$$

$$\left(\frac{R^2}{\Sigma T P}\right) n_0 \frac{\partial r'_0}{\partial t'} - \alpha C' \frac{p'(r_0) - p'_e}{r'_0} = 0 \tag{A24d}$$

This system of equations is identical with that of equation A19, except for terms comprised of dimensions shown inside parentheses, $\left(\frac{T_H \Sigma P}{R^2}\right)$ and $\left(\frac{R^2}{\Sigma TP}\right)$. Since a physical equation is dimensionally homogeneous (dimensions on either side of the equal sign are identical), these two terms must be unities.

$$\left(\frac{T_H \Sigma P}{R^2}\right) = \left(\frac{R^2}{\Sigma TP}\right) = 1 \tag{A25a}$$

Equation A25a can be rearranged:

$$T_H = \frac{R^2}{\Sigma P} = T \tag{A25b}$$

where T_H has dimensions of time. Therefore, a new time variable can be defined:

$$\tau_r = \frac{br_0^2}{C(n(r_0))(p(r_0) - p_e)} \tag{A26}$$

where $b = \frac{(\rho_{gs} - \rho_{gl})}{\rho_{gs}} n(t)$ as defined before. This new variable, τ_r, is related to the progress of grout front, as it is comprised of values at the grout front, radius, r_0, fluidity, $C(n(r_0))$, and pressure, $p(r_0)$.

Variables used in the conservation equation for grout, equation A19a, radius, r, pressure, p, and fluidity, C, can be re-scaled by any characteristic values of the problem:

$$r = \mathsf{R}\bar{r}, p = \mathsf{P}\bar{p}, C = \mathsf{C}\,\bar{C} \tag{A27}$$

where $\bar{r}$, $\bar{p}$ and $\bar{C}$ are, respectively, re-scaled radius, pressure and fluidity through linear transformations by characteristic values of radius,R, pressure,P, and fluidity,C. Equation A19a can be rewritten with new variables:

$$\frac{1}{\bar{r}^2}\frac{\partial}{\partial \bar{r}}(\bar{r}^2 \bar{C}\frac{\partial \bar{p}}{\partial \bar{r}}) = \frac{b\mathsf{R}^2/\mathsf{PC}}{\tau_H} \quad \text{for} \quad \bar{r}_w \le \bar{r} \le \bar{r}_0 \tag{A28}$$

where $r_w = \mathsf{R}\bar{r}_w$, and $r_0 = \mathsf{R}\bar{r}_0$. It can be noticed that the numerator in the right hand side, $b\mathsf{R}^2/\mathsf{PC}$, has the same structure with τ_r in equation A26. Actually, if the characteristic radius, pressure, and fluidity are chosen to be the values at grout front, r_0, this value coincides with τ_r. In this case, a non-dimensional number, T, can be defined as a ratio between the time scale of penetration, τ_r, and that of hydration τ_H in order to evaluate the effect of hydration on the penetration of the grout:

$$\mathsf{T} = \frac{\tau_r}{\tau_H} \tag{A29}$$

A.1.4 Example application

The governing equation system in equation A19 can be solved numerically (using a forward time integration scheme) for cases involving hydration. This section considers one simple example application of permeation grouting in a medium-grained sand, using a water-to-cement ratio, W/C = 3. Table A.1 summarizes the input parameters for this case. The calculations assume that hydration starts 10 hours after mixing, after which time there is a constant rate of hydration, $d\xi/dt = 1/\tau_H$ as shown in Figure A.4.

Figure A.5a shows the radial variations in relative porosity, n/n_0 at selected injection times for the case where there is perfect mixing of the grout. As fresh grout is continuously pumped, there is no change in porosity at the injection point. The results show that the minimum porosity (i.e. maximum formation of solid grout) occurs at a radius, $r \cong 0.5r_0$. Figure A.5b shows the location of the grout front versus time and compares the results for cases with and without hydration. The results show that

hydration retards the movement of the grout front. The non-dimensional number, T, defined in equation A29 are plotted in this figure together. In this problem, T number only depends on the time scale of grout front progress, τ_r, because that of hydration, τ_H, is fixed. As the grout front advances, the pressure at the front decreases and the time scale τ_r increases to reaches the value of time scale of hydration. At this point (18hrs), the T number becomes 1. This defines approximately the time when the hydration starts affecting grout progress noticeably. After this time, the time scale or grout front progress, τ_r, is always larger than that of hydration, τ_H. The T number reaches 150 when time reaches 260 hrs and hydration prevents further movement of the front almost completely.

The solutions for the case where there is single-batch mixing of the grout are shown in Figures A.6a and A.6b. In this case, the largest decreases in porosity occur close to the injection point (Figure A.6a). The effects of hydration become noticeable after 20hours due to the rapid draw-down of the pressure at the front caused by clogging at the well. The trend of the T number change shown in Figure A.6b is similar to the perfect mixing case in Figure A.5b.

A.2 EFFECT OF HYDRATION DURING INDUCTION PERIOD ON GROUT PENETRATION

A.2.1 Cement hydration and increase in yield stress

Although advanced stage hydration can seriously affect the permeation of cement suspension as discussed in the previous section, it is unlikely that extensive amounts of solid grout will form during the injection period, especially as the induction period is often extended in practice using retarders. However, it is well known that rheological properties of cement suspensions change during the induction period. Even if the cement used in permeation grout is designed to maintain enough fluidity, some chemical and physical changes during the period required for preparation and injection of the grout seem unavoidable. As discussed in Chapter 7, the Bingham model is often applied to represent non-linear shear stress behavior of fresh mixed cement suspension (equation 7.9), characterized by two rheological properties, the yield stress, τ_f , and viscosity, μ.

This section discusses a Bingham model for cement grout behavior in order to describe the evolution of rheological properties during the induction period.

The chemical processes occurring during the induction period are usually considered associated with the autocatalytic nucleation-growth of hydrates (Taylor 1997, Gartner 1997). Hydrates of cement have various chemical compositions because cement itself is a mixture of many kinds of cementitious material. Most hydrates, especially early products are amorphous compounds of calcium and silicate hydrates, often referred to as calcium silicate hydrates (C-S-H) because of their undefined stoichiometry. The most abundant cementitious material in commercial cement is tri-calcium silicate, or alite (C3A). Alite provides most of the C-S-H in the early stage of hydration. Therefore, much of the research on cement chemistry, especially on the early hydration process, has been actually carried out with pure alite. In fact, there exists a faster reacting compound in most cement products: calcium aluminate (C3A) hydrates almost instantaneously producing a set that is undesirable for most situations in practice. In order to prevent hydration of C3A, gypsum is added producing ettringite (Aft) as the first reactant (replacing C-S-H). The amount of hydrates generated during the induction period is known to be very small, less than 5% (Berliner et al. 1998). Hence, the degree of hydration during the induction period is almost undetectable. Several authors have questioned that hydration is responsible for changes in rheological properties, (i.e. yield stress and viscosity). Many researchers have reported the evolution of rheological properties with time during the induction period (Toumbakari et al. ,1999; Shroff et al.,1996; Perret et al., 2000; Zebovitz et al., 1989; Schwarz and Krizek, 1994; De Paoli et al., 1992). Figures A.7 and A.8 show the values of viscosity and yield stress reported during the induction time of typical cementitious grouts. As each study applied a different test method and a different grout, the values vary with a wide range. It is generally agreed that C-S-H gel coats the cement particles and increases viscosity. Ettringite is also known to coat the cement particles to prevent further hydration of them. Therefore, either ettringite gel or C-S-H gel increases viscosity of the suspension by coating the cement particles almost instantaneously. Besides hydration, mechanical agglomeration of cement particles is often considered as a cause of rheological changes. Viscosity is well known to increase by agglomeration (Struble and Sun, 1995), while the effects on yield stress are

less well defined. However, agglomeration occurs within a certain range of calcium concentration, (i.e. when there are sufficient ions to increase attraction between particles but less than the amount necessary to start nucleation of hydrates; Nonat et al., 1997). For the practical range of water-to-cement ratio of grouts (W/C $\leq$ 5), this level of concentration is rapidly gained after mixing. Therefore, agglomeration would not be able to explain evolution of rheological properties occurring throughout the induction period. Superplasticizers (sometimes referred dispersant) are used to enhance the fluidity of the suspension as commonly as retarders and accelerators. Although superplasticizers reduce the viscosity of the suspension as low as water ($\alpha \cong 1$) without losing stability and durability, they do not prevent the yield stress build up.

Lei and Struble (1997) supported the idea that a small amount of hydration during the induction period increases yield stress by connecting cement particles, based on creep-recovery tests measuring yield stresses of cement suspensions. These results have been re-plotted in Figure A.9. It should be noted that the water-to-cement ratio used for these tests were much lower (W/C = 0.45) than for those in Figures A.8 and values of yield stress are much higher. The data can be divided into two phases: the first corresponding to the induction period, and the second (for t >100 mins) corresponding to a much more rapid strength gain in the post induction phases. The earlier values increasing linearly indicate existence of induction period. An Arrhenius-type relation was used as a kinetics law for induction period:

$$\frac{d\xi}{dt} \propto \exp\left(-\frac{E_a}{RT}\right) \tag{A30}$$

where E_a is the activation energy, R is the gas constant, and T is temperature in Kelvin. Creep-recovery test results with different temperatures were calibrated with this equation giving E_a = 22 kJ/mol as a result.

Barret and Bertrandie (1997) suggested a different kinetics equation while providing the test results to determine the effect of the water-to-solid ratio of alite (C3S) on hydration:

$$\frac{d\xi}{dt} = k_T \xi \tag{A31}$$

k_T is the reaction kinetic depending on temperature. The degree of hydration and time relation is plotted using this equation in Figure A.10. The value of k_T in this example is chosen arbitrarily because the purpose of it is to examine only the trend of relation, not exact values of the degree of hydration. In this figure, the degree of hydration increases almost linearly with time similar to the yield stress reported in Figure A.9 during the induction period. Therefore, Lei and Struble (1997)'s suggestion that yield stress increases due to hydration during the induction period is supported by the kinetics equation of Barret and Bertrandie (1997). Therefore, if the value of yield stress at initial set is known, a linearly increasing function of time can be defined for yield stress during induction period.

While the characteristics of 'very' early hydration during induction period adversely affect the injectibility, the continuing hydration process determines the long-term properties of the grouted soils (increased strength and decreased permeability) to serve the objectives of the grouting operation. The 'accelerated' and 'diffusion-controlled' stages of hydration follow the induction stage and represent the dominant chemical processes. As mentioned earlier, autocatalytic growth of hydrates (the rate of growth depends on the amount of hydrates) is the dominant process during accelerated period hydration. The Avrami relation is commonly used to define the rate of the hydration process during this period (Krstulović and Dabić, 2000):

$$[-\ln(1-\xi)]^{1/3} = K_{NG} t \tag{A32}$$

where K_{NG} is the parameter deciding the kinetics during the nucleation and growth (NG) period. During the subsequent diffusion-controlled stage, hydration is slowed as the movement of water is blocked by hydrate products. Therefore, this stage is controlled by diffusion of water and affected largely by the water cement ratio (Berliner et al., 1998):

$$(1-\xi)^{1/3} = -2(K_D)^{1/2}(t-t_0)^{1/2}/R + (1-\xi_0)^{1/3} \tag{A33}$$

where K_D $[L^2/T]$ is the diffusion coefficient, R is the original radius of the cement grain and ξ_0 is the degree of hydration at time t_0.

The rate of hydration, $d\xi/dt$ is summarized in Figure A.11 is gained by applying the different kinetics laws in equations A30, A32 and A33 for three different periods of hydration. While the last two periods are clearly depicts the well-known trend of hydration rate often observed by hydration heat evolution (for example, Ulm and Coussy, 1996), the first part of it during induction period is still not as clear as others.

A.2.2 Flow of Bingham fluid in porous media

An incompressible Bingham fluid flowing steadily in a circular pipe of radius, R, with a rough (no-slip) boundary has a shear stress profile shown in Figure A.12. Near the center of the pipe, there is a region of plug where the shear stress is less than the yield stress and there is no radial gradient in the axial fluid velocity. This central part of the tube has a constant velocity forming a plug flow inside the pipe. In Figure A.12, this plug is characterized by a radius, r_p. For a Bingham fluid the volumetric flow rate in the pipe can be obtained from the Buckingham-Reiner equation:

$$Q = -\frac{\pi R^4}{8\mu}\left(\frac{\partial p}{\partial x}\right)\left(1 - \frac{4}{3}\left(\frac{r_p}{R}\right) + \frac{1}{3}\left(\frac{r_p}{R}\right)^4\right) \tag{A34a}$$

$$r_p = -\frac{2\tau_f}{(\partial p/\partial x)} \tag{A34b}$$

The first term in equation A34a is identical to the Poiseuille equation for laminar flow of an incompressible Newtonian fluid[13], while terms involving r_p represents the effects of

---

[13] The flow rate of a fully developed laminar flow of an incompressible Newtonian fluid in a pipe is described by the Poiseuille equation:

$$Q = -\frac{\pi R^4}{8\mu}\left(\frac{\partial p}{\partial x}\right)$$

the yield stress. If the absolute value of the pressure gradient $\left(\frac{\partial p}{\partial x}\right)$ becomes too small and the boundary of the plug flow region r_p reaches the pipe radius R, the flow will stop. In other words, a minimum absolute value has to be exceeded in order for the Bingham fluid to flow in a pipe of radius, R. This minimum absolute value of pressure gradient is defined as the critical pressure gradient (CP):

$$\text{CP} = \left(-\frac{\partial p}{\partial x}\right)_{r_p=R} = \frac{2\tau_f}{R} \tag{A35}$$

The similarity between the Buckingham-Reiner equation and the Poiseuille equation suggests that a law defining the apparent flow velocity, v, for a Bingham fluid such as Darcy's law for a Newtonian fluid can be established with a permeability, $k_{Bingham}$:

$$v = -\frac{k_{Bingham}}{\mu}\left(\frac{\partial p}{\partial x}\right)$$

$$k_{Bingham} = k\left(1 - \frac{4}{3}\left(\frac{r_p}{R}\right) + \frac{1}{3}\left(\frac{r_p}{R}\right)^4\right) \tag{A36}$$

In comparison, Darcy's equation defines the apparent flow velocity, v, in a porous medium in terms of pressure gradient.

$$v = -\frac{k}{\mu}\left(\frac{\partial p}{\partial x}\right)$$

where k[L^2] is the permeability intrinsic of the porous medium and μ is the dynamic viscosity of the fluid. Similarity between above two equations seems to be encouraging use of capillary model. In fact, Darcy's equation, which was originally developed empirically, can be derived by applying homogenization techniques to the Poiseuille equation applied for capillary tubes of different radii (for example, see Sanchez-Palencid, 1980).

where k is the permeability of the porous medium and μ is the viscosity of the Bingham fluid.

A.2.3 Permeation limit and critical pressure gradient, CP

Raffel and Greenwood (1961) were the first to point out that permeation of a cementitious grout could be limited in progress when the pressure gradient was not enough to overcome the yield stress. They used an equation for estimating the radius, R, in calculations of CP, based on known values of the permeability, k, and porosity, n_0, of the porous medium:

$$R = \sqrt{\frac{8k}{n_0}} \tag{A37}$$

This equation can be derived by assuming all pores as circular tubes with radius R in which flow is described by the Poiseuille equation. The flow velocity in a tube is then:

$$V = \frac{Q}{\pi R^2} = -\frac{R^2}{8\mu}\left(\frac{\partial p}{\partial x}\right) \tag{A38}$$

The superficial velocity of this flow in a porous medium with porosity n_0 is $n_0 V$. Equation A37 is directly obtained by equating this with the apparent flow velocity, v, by Darcy's law. The fact that Raffel and Greenwood (1961) did not consider that a Bingham fluid is not controlled by the Poiseuille equation and that they did not apply a homogenization technique implies equation A37 cannot be reliable. In order to verify this, a case of spherically radial permeation grouting without hydration effect was considered. The complete analytic solution for this case of a grout with a viscosity of α times larger than that of water injected into a soil with permeability k and porosity n_0 can be obtained from equations A20 and A21[14].

The pressure gradient can be calculated by differentiating equation A20.

[14] x_0, x_w replace r_0, r_w in the original equation.

$$\frac{\partial p}{\partial x} = \frac{\alpha(p_e - p_w)}{\frac{(\alpha-1)}{x_0} - \frac{\alpha}{x_w}}\left(-\frac{1}{x^2}\right) \tag{A39}$$

The absolute value of gradient will be always the smallest at the boundary between pore water and the grout, $x = x_0$. By equating this smallest value, $\left(-\frac{\partial p}{\partial x}\right)_{x=x_0}$ with CP in equation A35 and assuming the environmental pressure p_e is zero, the limit of grout front can be found by identifying the value of x_0 where CP is reached:

$$\left.\frac{x_0}{x_w}\right|_{\text{limit}} = \frac{(\alpha-1) + \sqrt{(\alpha-1)^2 + (2\alpha^2 p_w/\tau_f)(R/x_w)}}{2\alpha} \tag{A40}$$

Figure A.13 summarizes the limit of the grout front as a function of the pore radius, R , for a given well radius, x_w, calculated by applying equation A40. The calculations assume a viscosity ratio, α = 10, and yield stress, τ_f =1Pa permeating a medium with porosity, n_0 = 0.35 and permeability, $k = 5 \times 10^{-11}$ m^2 by the well pressure p_w = 100kPa.

Equation A37 suggested by Raffel and Greenwood (1961) estimates that a pore radius, R, of this porous medium will be 0.0034cm. The ratio of this pore radius to the assumed well radius, x_w=10 cm is $R/x_w = 3.4 \times 10^{-4}$. In this case, the permeation limit was calculated as x_0/x_w = 4.6 implying that the grout extends to a radius of 0.46m in 2.6 minutes of pumping. This represents a very ineffective permeation especially considering that the selected viscosity and yield stress values are relatively low. In fact, a single pore radius estimate is not appropriate at all for a Bingham fluid, as the grout will continue to flow through larger pores while the pressure gradient is too small initiate flow in smaller pores. Therefore, the distribution of pore sizes, rather than a single characteristic representative pore radius must be considered for permeation of a Bingham fluid.

A.2.4 Partial hydraulic conductivity by Arya et al. (1999)

As presented in Section 7.3, Arya and Paris (1981) proposed an analytical method to predict pore size distribution from known particle size distribution using moisture characteristic curves for unsaturated soils. Arya et al. (1999) applied resulting equation for pore radius (equations 7.16) to approximate the hydraulic conductivity corresponding with water content θ_i of a sample up to i^{th} sized pores, saturated with water. They used an empirical relationship for flow rate inside a pore cylinder of radius R_i:

$$q_i = cR_i^x \tag{A41}$$

where q_i is the volumetric flow rate per unit hydraulic gradient , i.e., $q_i = Q/(-\nabla p/\gamma_w)$ with the total flow rate, Q corresponding the pressure gradient, ∇p and the unit weight of water, γ_w. Parameters were log c = 2.570, x = 4.471 (with q_i in cm^3/sec) [cf] for a medium-grained sand in Arya et al. (1999). The partial hydraulic conductivity when the i^{th} and smaller pores were saturated was found as:

$$K(\theta_i) = n_0 \sum_{j=1}^{j=i} (cr_j^x) w_j / \pi r_j^2 \tag{A42}$$

while the value when all pores up to the largest size were saturated is the 'saturate' hydraulic conductivity that is applied in Darcy's law:

$$K_{saturate} = n_0 \sum_{j=1}^{j=n} (cr_j^x) w_j / \pi r_j^2 \tag{A43}$$

when r_n is the largest pore size. Equation A42 was originated in the purpose of estimating unsaturated hydraulic conductivity increasing as water fills pores starting from smaller

---

[cf] From Hagen-Poiseuille equation, $q = \frac{\pi \gamma_w}{8\mu} R^4$ with $\log\left(\frac{\pi \gamma_w}{8\mu}\right) = 4.5856$

ones moving to larger ones. Therefore, with the complete range of particle sizes, this equation will give the saturated hydraulic conductivity.

A.2.5 Application of Arya et al. (1999)'s equations for a Bingham fluid

Since equation A42 is based on experiments with water (a Newtonian fluid), the conductivity is Newtonian. As noted earlier, the yield stress in a Bingham fluid flowing in a pipe induces a plug flow region developed when the shear stress does not exceed the yield stress. Therefore, volumetric flow rate of a Bingham fluid is less than that of a Newtonian fluid and this effect can be quantified by deducing an apparent permeability, $k_{Bingham}$ defined in equation A36. Equation A36 can be directly applied for conductivities because hydraulic conductivity is proportional to permeability (i.e. $K = k\gamma_w / \mu_w$). This equation is developed for flow through a single pipe with radius, R, while in present pore model, there exist multiple capillary tubes of different radii. Therefore, the conversion term in equation A36, $\left(1-\frac{4}{3}\left(\frac{r_p}{R}\right)+\frac{1}{3}\left(\frac{r_p}{R}\right)^4\right)$, should change for each capillary tube radius. As for the plug flow radius, r_p, it is equivalent to the largest pore radius the fluid can penetrate, which is r_i when i^{th} and smaller pores were saturated resulting in the water content of θ_i. Therefore, equation A42 can be converted for a Bingham fluid:

$$K_{Bingham}(\theta_i) = n_0 \sum_{j=1}^{j=i} (cr_j^x) w_j / \pi r_j^2 \left(1 - \tfrac{4}{3}\frac{r_i}{r_j} + \tfrac{1}{3}\left(\frac{r_i}{r_j}\right)^4\right) \qquad \text{(A44)}$$

However, equation A43 is not affected by yield stress in a Bingham fluid because all pores are saturated and limit pore size for penetration, $r_i \rightarrow 0$.

The critical pressure gradient of cement grout is inversely proportional to the radius of the pore (equation A35). When a distribution of pore radii is considered, there exist multiple values of the critical blocking pressure gradient (CP). The largest CP value (corresponding to the smallest current pore radius) will be reached first as the pressure gradient drops. This will decrease the hydraulic conductivity, the grout will continue to

progress through larger pores. The new value of hydraulic conductivity can then be obtained by eliminating contributions from the blocked pores. For example, if the largest blocked pore radius is r_i, the equivalent hydraulic conductivity of the porous medium with pores only larger than r_i is:

$$K_{Bingham}(r_i) = K_{saturate} - n_0 \sum_{j=1}^{j=i} (cr_j^x) w_j / \pi r_j^2 \left(1 - \frac{4}{3} \frac{r_i}{r_j} + \frac{1}{3} \left(\frac{r_i}{r_j} \right)^4 \right) \tag{A45}$$

with corresponding CP:

$$\mathrm{CP}(r_i) = \frac{2\tau_f}{r_i} \tag{A46}$$

Equation A45 is obtained by subtracting the partial conductivity for Bingham fluid, $K_{Bingham}(\theta_i)$ when the i^{th} and smaller pores were saturated in equation A44 from saturated conductivity, $K_{saturate}$ in equation A43 in order to remove contributions by blocked pores.

In order to estimate the effect of the conductivity change to injection of cement grout, example calculations were carried out using the particle-size-distribution curve shown in Figure A.14, presenting a soil mainly comprised of medium-sized sand. Values of pore radius calculated following Arya and Paris (1981)'s method were plotted next to the PSD curve in Figure A.15. As shown in this figure, pore sizes are reduced to those of fine sand and coarse silt, while two largest sizes of pores become bigger than those of soil particles do. For each of these pore sizes, equation A44 gives an apparent hydraulic conductivity for a Bingham fluid when it is the largest blocked radius. This hydraulic conductivity was plotted in Figure A.16. As shown in this figure, the saturated hydraulic conductivity calculated when no pore was blocked is 0.04814 cm/sec, which is close to that used in previous example in Section A.1, K = 0.049 cm/sec (corresponding to permeability $k = 5 \times 10^{-11}$ m^2). The Bingham hydraulic conductivity values from Figure A.16 were plotted in Figure A.17 with CP values by equation A46 with yield stress

values of 1, 10, 30 Pa respectively. In this figure, it is noticeable that there exists a finite value of CP for each yield stress below which the conductivity becomes zero. Therefore, if this threshold CP= CP_{min} is reached at the grout front, there will be no further permeation possible (i.e. the permeation limit was reached).

A.2.6 Effect of changes in yield stress change and permeation limit

As the pressure gradient decreases, pores that have corresponding CPs larger than the absolute value of this gradient will be blocked and the (effective) conductivity of the medium will decrease. Once the absolute value of pressure gradient becomes less than the CP_{min}, permeation will stop. Therefore, hydraulic conductivity decrease with CP shown in Figure A.16 should act to shorten the limit of permeation. If the yield stress also increases due to hydration, CPs for pores of various sizes will increase and conductivity will drop more rapidly. Changes in the permeation limit when the conductivity decreases and the yield stress increases with time were investigated with the conditions used for constructing Figures A.13. As the conductivity now depends on the pressure gradient, the continuity equation is nonlinear. Figure A.18 shows the movement of grout front with time gained by numerical integration of this nonlinear equation. The case when conductivity does not change until CP_{min} is leached is presented as the reference. Because the governing equation for this case is linear, the analytical solution equation A20 was directly applied. As shown in this figure, the time at the permeation limit is 15.7 hours. This reduces to 12.5 hours when gradual decrease of conductivity is considered.

Furthermore, the effect of increasing yield stress was added in the analysis, assuming that it increases linearly with time following Lei and Struble (1997)' s suggestion explained in Section A.2.1. The permeation limit was reached at 2.2 hours after injection started when a rate, 1Pa/hour was used as shown in Figure A.18. This substantial change is remarkable considering that this rate is less than any reported yield stress increase rate summarized in Figure A.7. Figure A.19 presents all the simulated results for duration for permeation limit reached (limit duration), which was found rapidly decreasing with the yield stress increase rate.

A.3 CONCLUSIONS

A non-steady conservation equation of a permeated cementitious grout has been established using the kinetics law of the hydration reaction for the spherically radial case. Through the dimensional analysis on this equation and boundary conditions, a dimensionless time, T number, the ratio of time scale of penetration to that of hydration, was selected as the measure of the effect of hydration on permeation grouting. It was found that the hydration reaction and resultant porosity change affects the grout progress more as this number grows (i.e. the penetration time becomes comparable with the hydration time). The spatial distribution and penetration extent of reduced porosity depends on the age of grout mix pumped in at the source. Two limit cases: the perfect mixing (grout freshly mixed right before injection) and the single batch mixing (all grout from a single batch) were considered and the perfect mixing case showed much higher penetration extent (T number 150 for perfect mixing vs. 84 for single batch mixing). In addition, the perfect mixing batch showed minimum porosity in the middle of the grouted area, while the single batch mixing case caused most changes in porosity next to the injection point.

The effect of rheological properties during induction period is estimated by using Bingham fluid model. Yield stress in a Bingham fluid and resulting critical pressure gradient (CP) stops flow in small pores where pressure gradient is less than CP at a constant-flow rate condition. This pore-scale effect of CP on total permeability of soil was modeled by using a semi-empirical approach by Arya et al. (1999a). It was found with this model that the yield stress increase could greatly affect the extent of permeation grouting even at slow rates found typically during induction period.

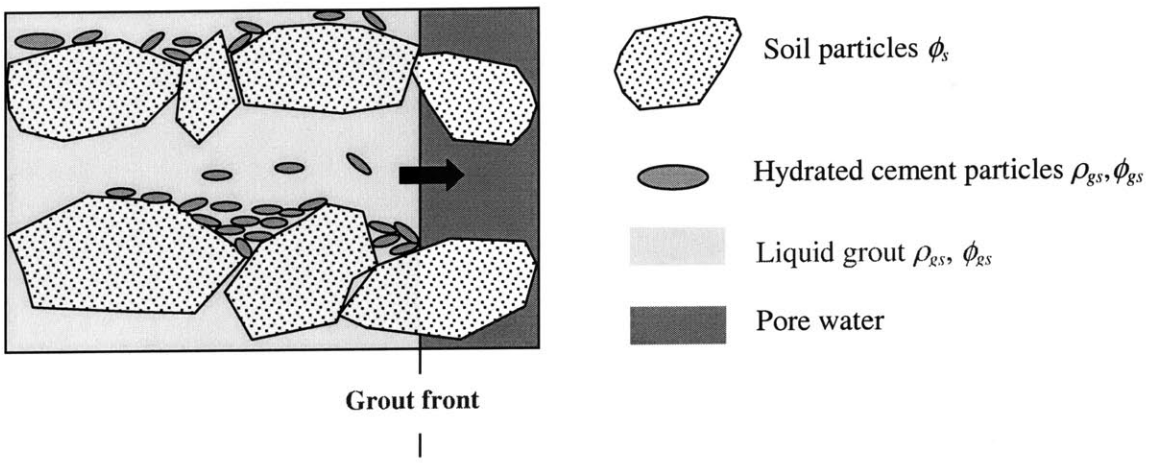

Figure A.1 A representative elementary volume (REV)

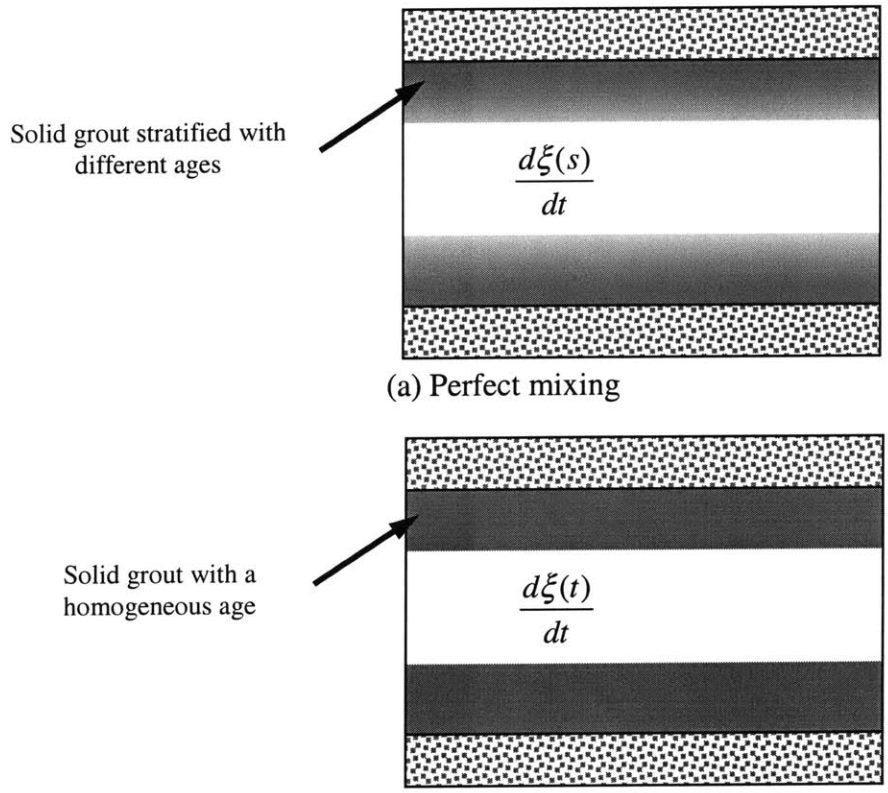

Figure A.2 REVs of perfect mixing case and single-batch mixing case

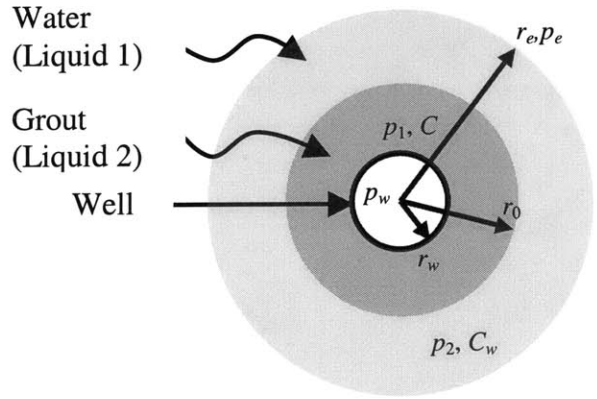

Boundary Conditions

$$At \quad r = r_w : \; p_1 = p_w$$

$$At \quad r = r_e : \; p_2 = p_e$$

$$At \quad r = r_0 :: \; C_1 \left.\frac{\partial p_1}{\partial r}\right|_{r_0} = C_2 \left.\frac{\partial p_2}{\partial r}\right|_{r_0} \; ; \; p_1\big|_{r=r_0} = p_2\big|_{r=r_0} \; \phi(r_0)\frac{\partial r_0}{\partial t} + C\left(\frac{\partial p}{\partial r}\right)_{r_0} = 0$$

Figure A.3 Boundaries of spherically radial permeation

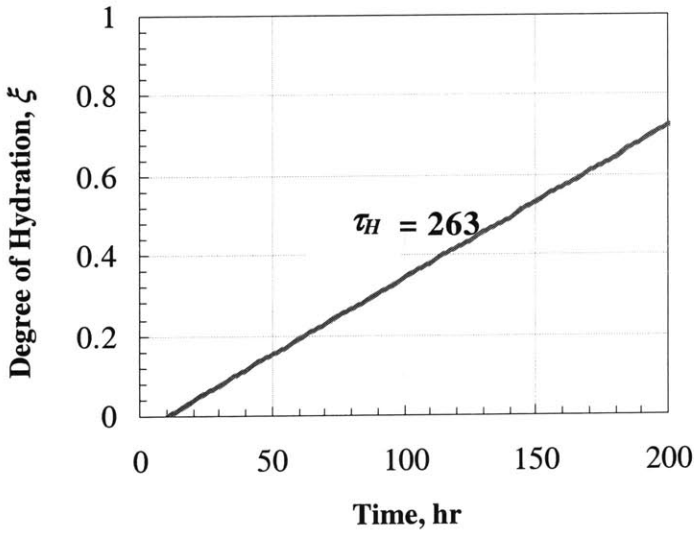

Figure A.4 Hydration degree and the time scale of hydration degree, τ_H

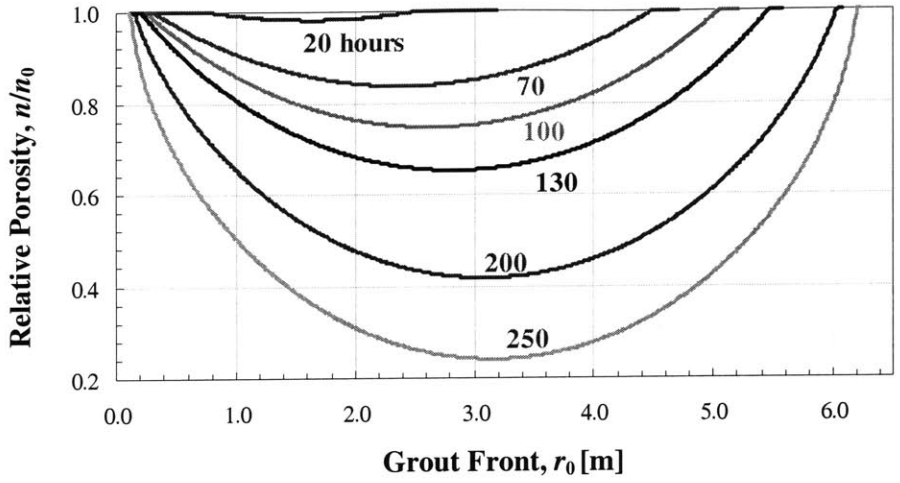

(a) Porosity distribution

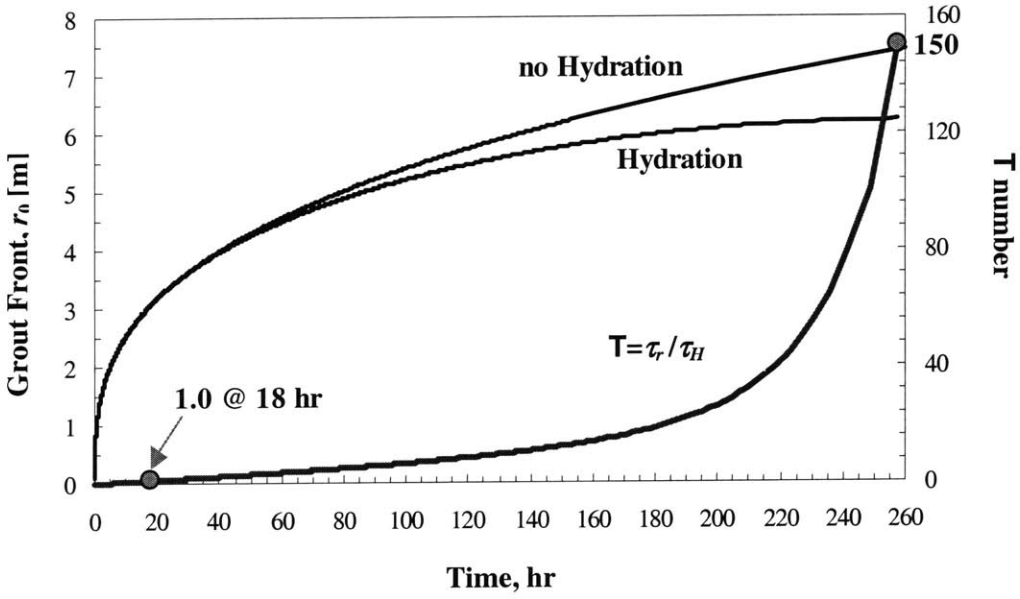

(b) Grout front progress

Figure A.5 Grout penetration of perfect mixing case

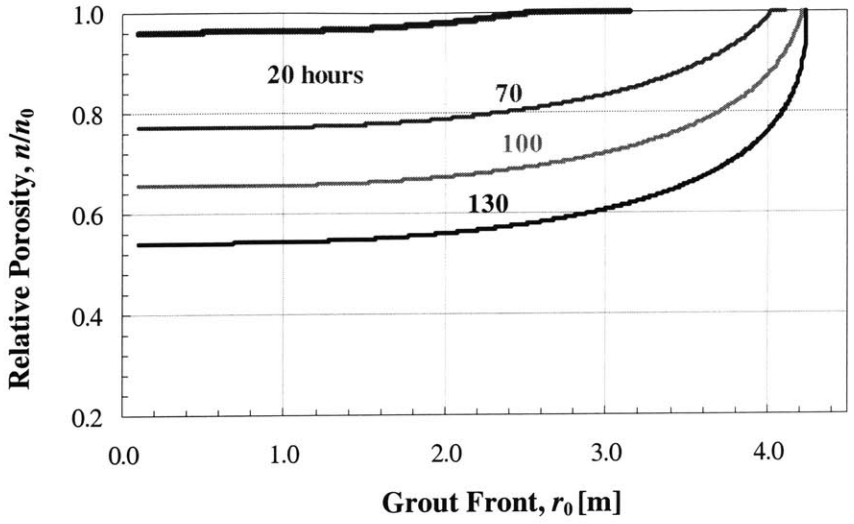

(a) Porosity distribution

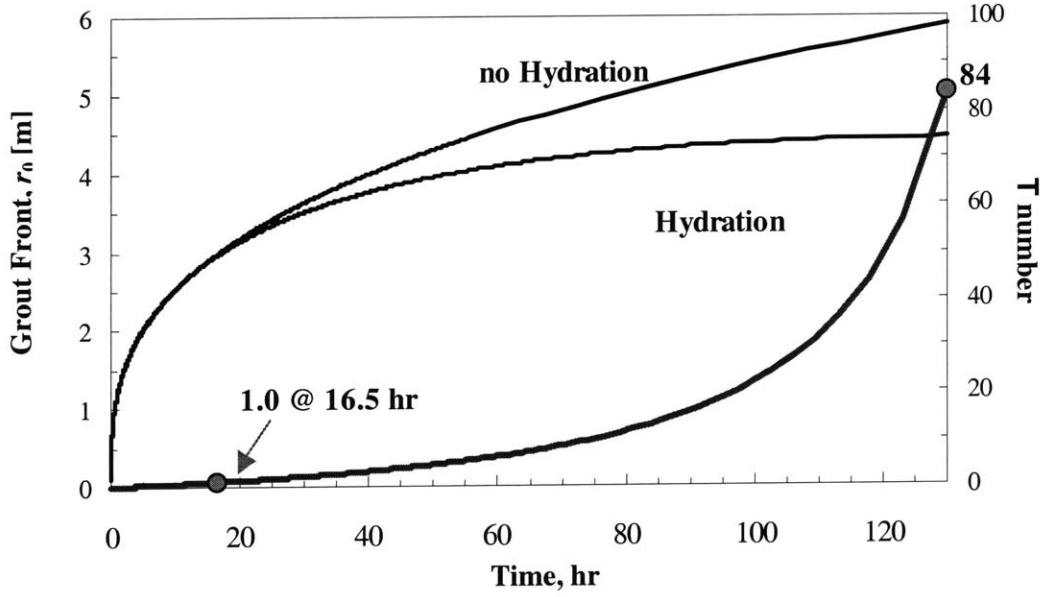

(b) Grout front progress

Figure A.6 Grout penetration of single batch mixing case

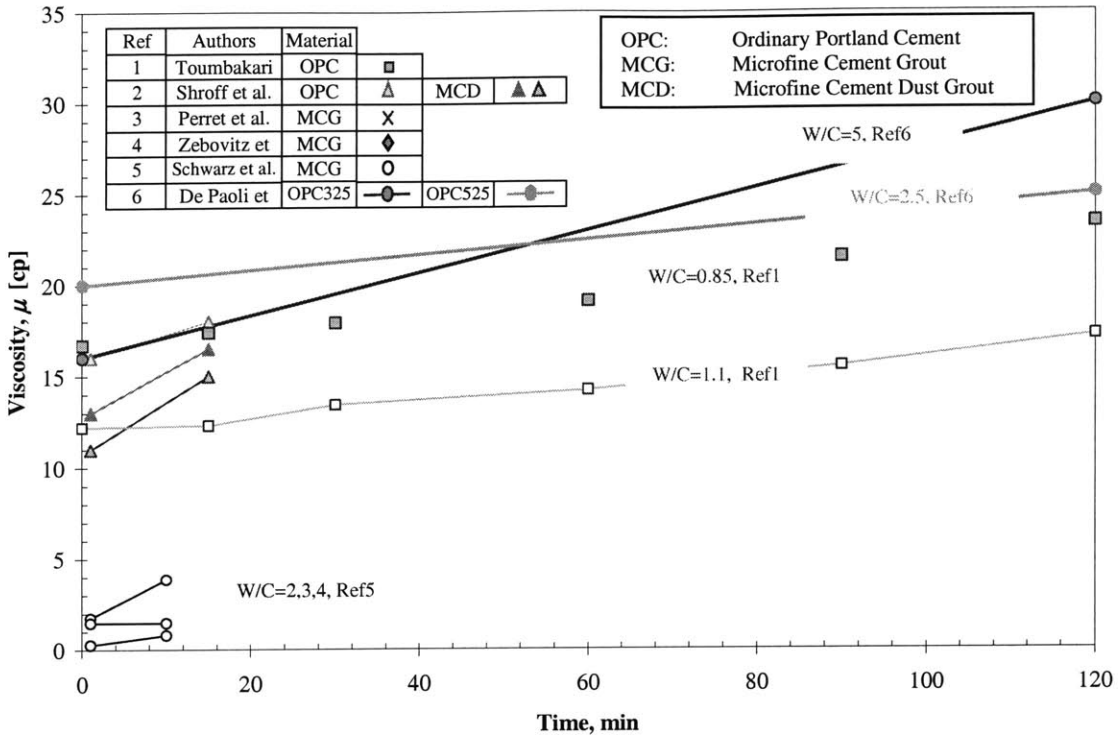

Figure A.7 Reported viscosity increase with time during induction period

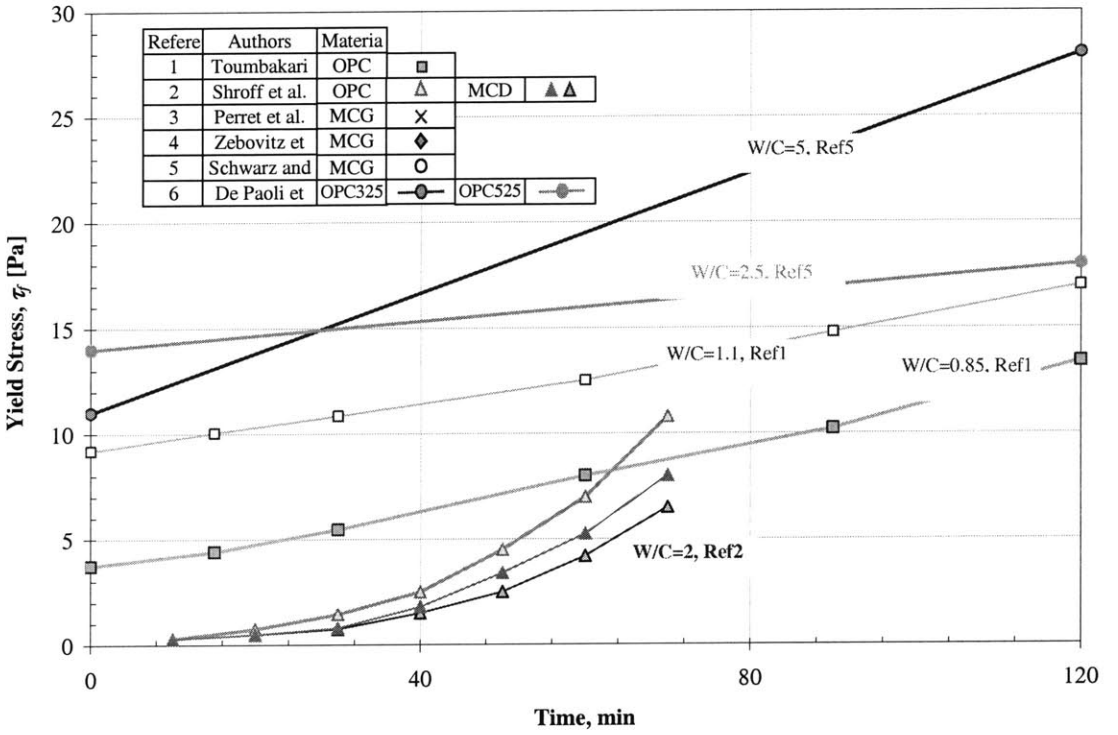

Figure A.8 Reported yield stress increase with time during induction period

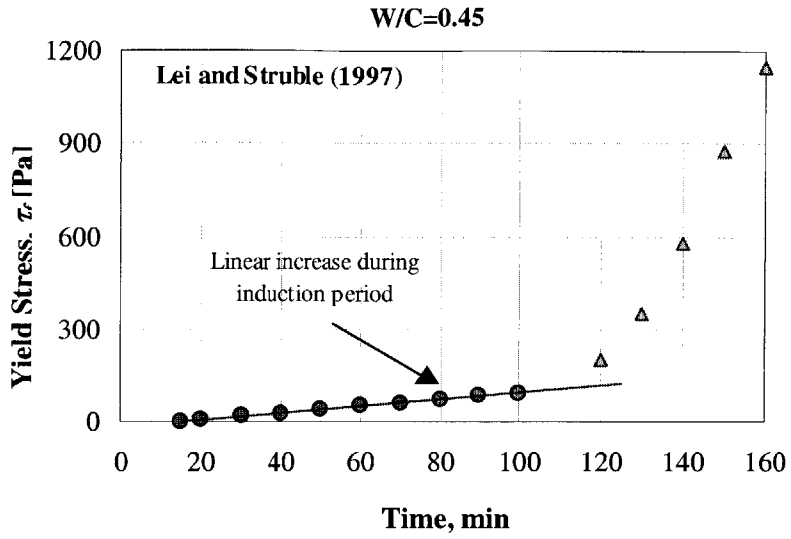

Figure A.9 Yield stress measured by Lei and Struble (1997)

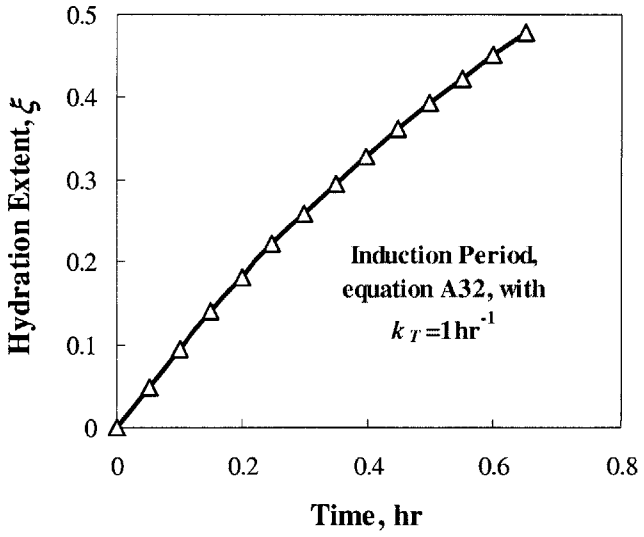

Figure A.10 Hydration extent increasing with time according to equation A32 by Barret and Bertrandie (1997)

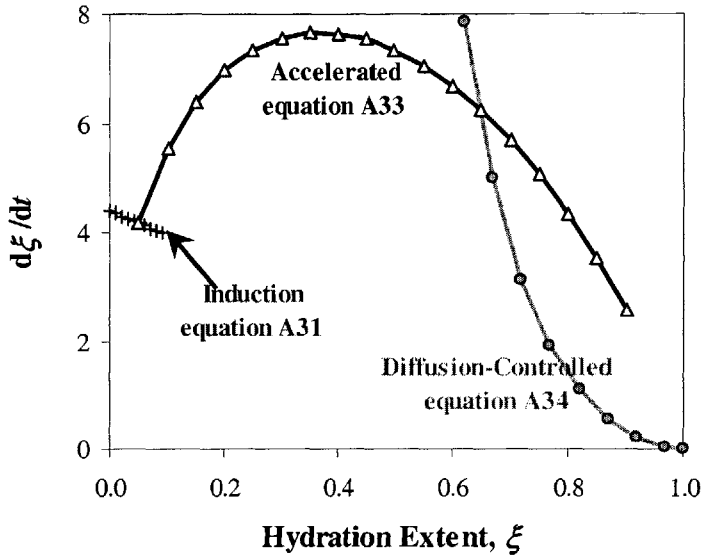

Figure A.11 Rates of hydration based on kinetics theories

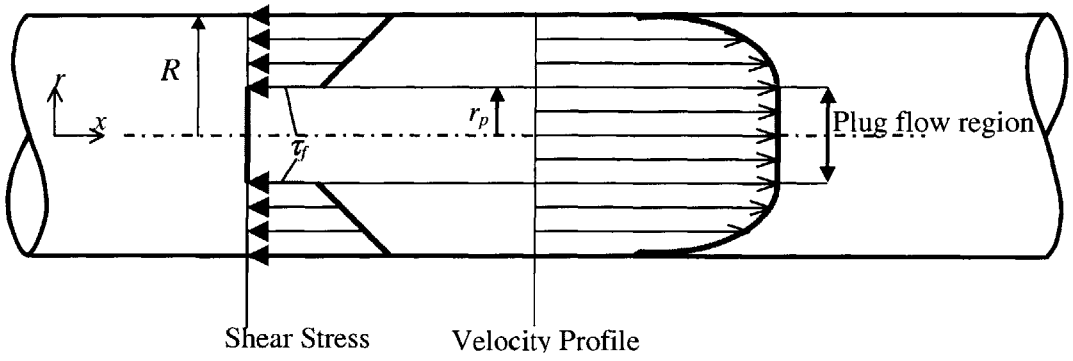

Figure A.12 Incompressible steady flow in a circular pipe of a Bingham fluid

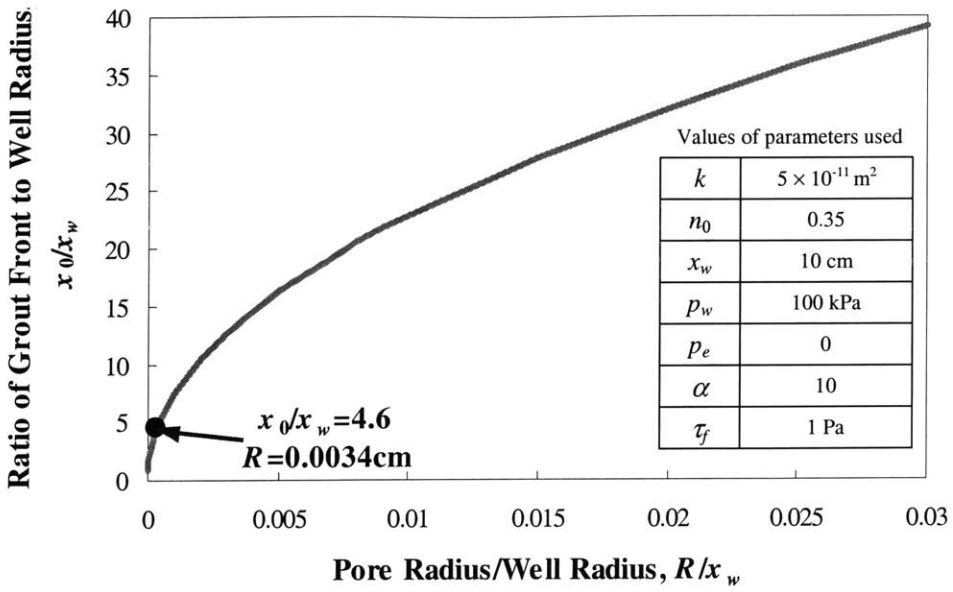

Figure A.13 Grout front movement versus pore radius calculated by equation A40 (based on Raffel and Greenwood, 1961)

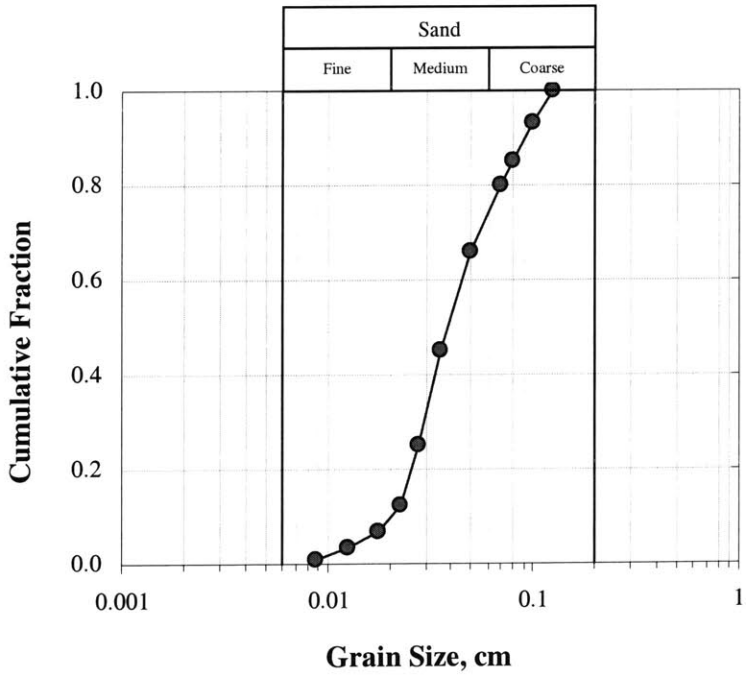

Figure A.14 Particle-size-distribution used for the example problem

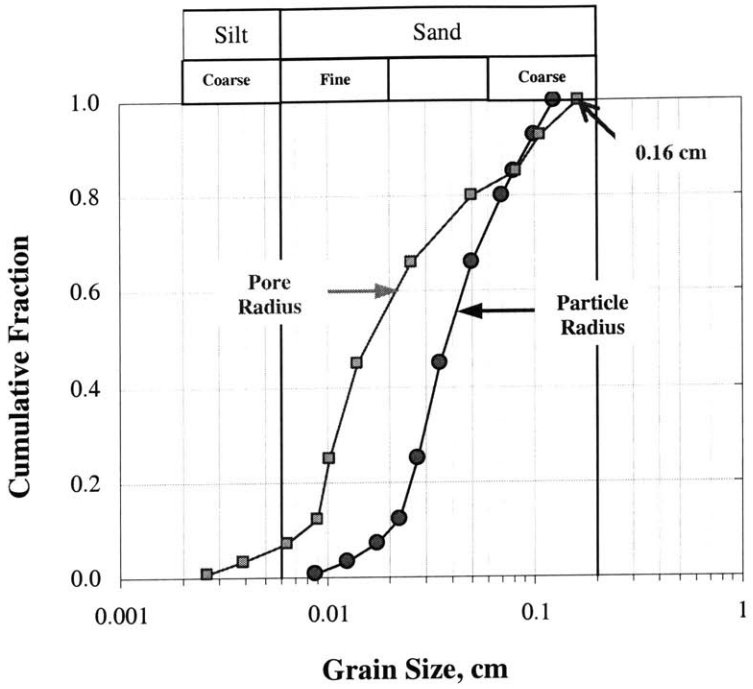

Figure A.15 Pore radius and particle radius distribution

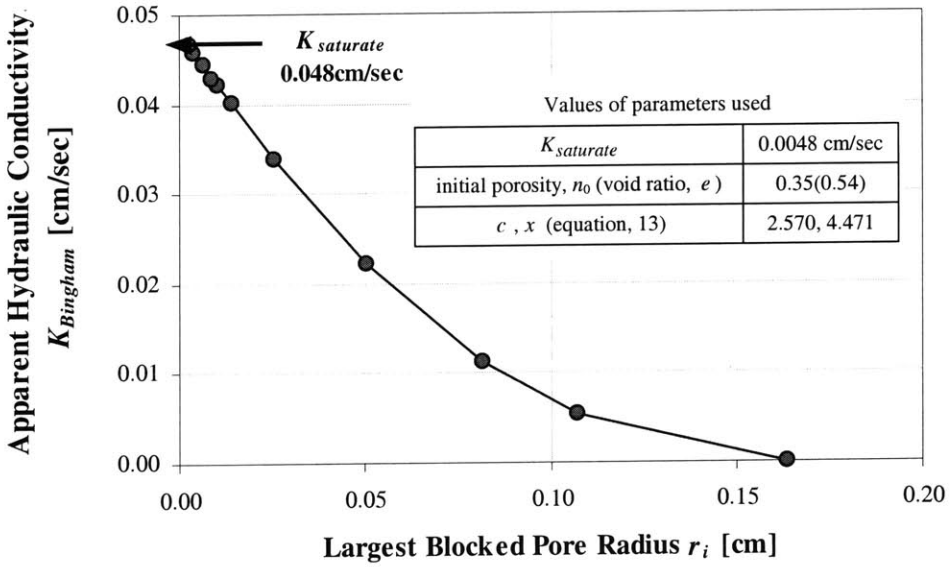

Figure A.16 Apparent hydraulic conductivity for a Bingham fluid, by equation A45

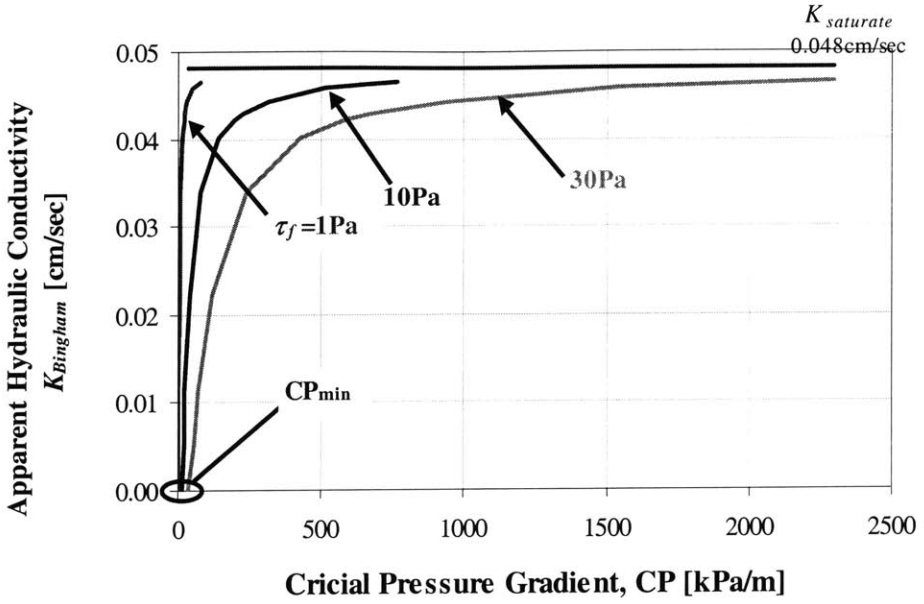

Figure A.17 Bingham hydraulic conductivity versus critical pressure gradient

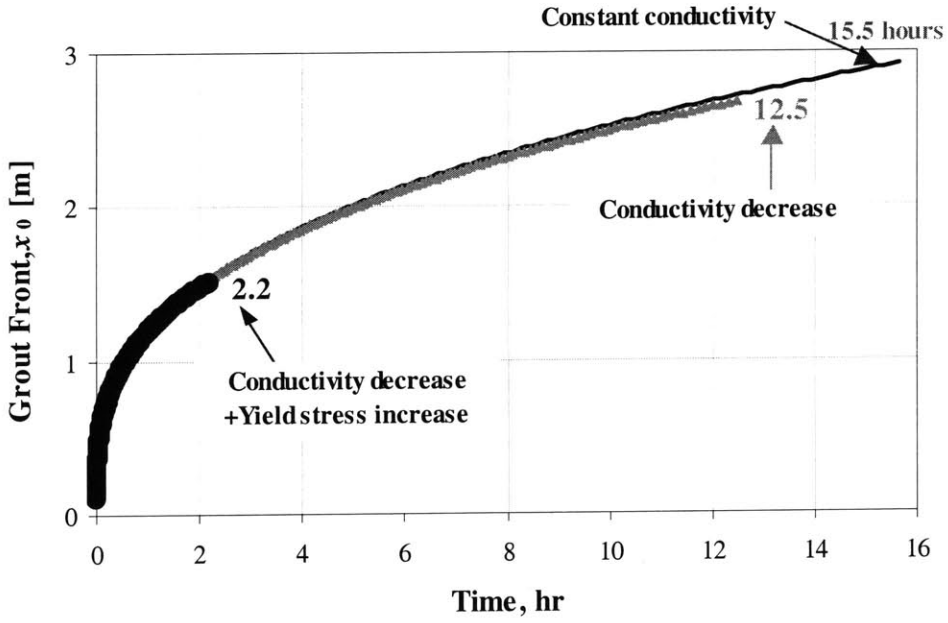

Figure A.18 Grout front movement with time when yield stress changes

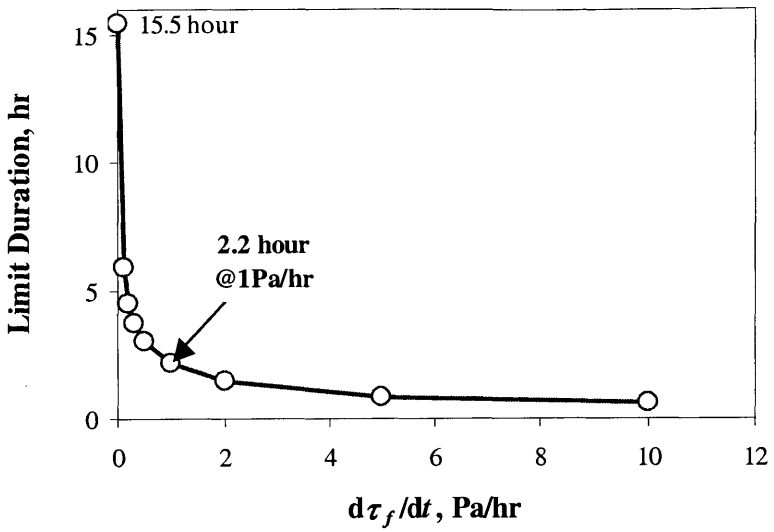

Figure A.19 Numerical analysis results of time at the permeation limit with various rate of increase of yield stress

Table A.1 Physical values used in the sample problem

r_w	0.1 m	k	5×10^{-11} m^2
p_w	100 kPa	μ_w	1 cp
p_e	0 kPa	μ_g	10 cp
n_0	0.35	C_w	0.18 m^2/hr/kPa
ρ_{gl}	1200 kg/m^3	$C(n_0)$	0.018 m^2/hr/kPa
ρ_{gs}	2300 kg/m^3	$C(n) = C(n_0)\frac{n^3(1-n_0)^2}{n_0^3(1-n)^2}$ (Kozeny-Carman)	
Set time	10 hours	α	10

REFERENCES

Adams, J. C. (1989), "MUDPACK: multigrid Fortran software for the efficient solution of linear elliptic partial differential equations," *Applied Mathematics and Computations*, **34**: 113-146

Adams, J. C. (1990), *MUDPACK: Multigrid Software for Linear Elliptic Partial Differential Equations*, SCD UserDoc, Version 2.0, National Center for Atmospheric Research

Arenzana, L., Krizek, R. J., and Pepper, S. F. (1989) "Injection of dilute microfine cement suspensions into fine sands," *Proceeding of 12th ICSMFE, Rio de Janeiro*: 1331-1334

Arya, L. M., Leij, F. J., van Genuchten, M. Th., and Shouse, P. J. (1999a), "Scaling parameter to predict the soil water characteristic from particle-size distribution data," *Soil Science Society of America Journal* **63**: 510-519

Arya, L. M., Leij, F. J., Shouse, P. J. and van Genuchten, M. Th. (1999b), "Relationship between the hydraulic conductivity function and the particle-size distribution," *Soil Science Society of America Journal* **63**: 1063-1070

Arya, L. M., and Paris, J. F. (1981), "A physicoempirical model to predict soil moisture characteristics from particle-size distribution and bulk density data," *Soil Science Society of America Journal* **45**: 1023-1030

Bai, R. B., and Tien, C. (1997), "Particle detachment in deep bed filtration," *Journal of Colloid and Interface Science* **186**(2): 307-317

Baldwin, C. A., Sederman, A. J., Mantle, M. D., Alexander, P., and Gladden, L. F. (1996), "Determination and characterization of the structure of a pore space from 3D volume images," *Journal of Colloid and Interface Science* **181**: 79-92

Barret, P., and Bertrandie, D. (1997), "Importance of the liquid to solid weight ration in the powdered solid-liquid reactions: example drawn from cement constituent hydration," *Solid State Ionics* **101-103**: 359-365

Bear, J., and Bachmat, Y. (1991), *Introduction to Modeling of Transport Phenomena in Porous Media*, Kluwer Academic Publishers, Dordrecht

Berkowitz, B, and Ewing, R. P. (1998), " Percolation theory and network modeling: applications in soil physics," *Surveys in Geophysics* **19**: 23-72

Berliner, R., Popovici, M., Herwig, K. W., Berliner, M., Jennings, H. M., and Thomas, J. J. (1998), "Quasielastic neutron scattering study of the effect of water-to-cement ratio on the hydration kinetics of tricalcium Silicate," *Cement and Concrete Research* **28**(2): 231-243

Biggs, M. J., Humby, S. J., Buts, A., and Tüzün, B. U. (2003), "Explicit numerical simulation of suspension flow with deposition in porous media: influence of local flow field variation on deposition processes predicted by trajectory methods," *Chemical Engineering Science* **58**: 1271-1288

Bird, R. B., Steward, W. E., and Lightfoot, E. N. (1960), *Transport Phenomena*, Wiley, New York

Boller, M. A., and Kavanaugh, M. C. (1995), "Particle Characteristics and Headloss Increase in Granular Media Filtration," *Water Research* **29**(4): 1139-1149

Bolster, C. H., Mills, A. L., Hornberger, G. M., and Herman, J. S. (1999), "Spatial distribution of deposited bacteria following miscible displacement experiments in intact cores," *Water Resources Research* **35**(6): 1797-1807

Bouchelaghem, F., and Vulliet, L (2001), "Mathematical and numerical filtration-advection-dispersion model of miscible grout propagation in saturated porous media," *International Journal for Numerical and Analytical Methods in Geomechanics* **25**: 1195-1227

Bouchelaghem, F., Vulliet, L., Leroy, D., Laloui, L., and Descoeudres, F. (2001), "Real-scale miscible grout injection experiment and performance of advection-dispersion-filtration model," *International Journal for Numerical and Analytical Methods in Geomechanics* **25**: 1149-1173

Bouchelaghem, F. (2002), "Two large-scale injection experiments, and assessment of the advection-dispersion-filtration model," *Géotechnique* **52**(9): 667-682

Bradford, S. A., Yates, S. R., Bettahar, M., and Simunek, J. (2002), "Physical factors affecting the transport and fate of colloids in saturated porous media," *Water Resources Research* **38**: 1327–1338

Brady, J. F., and Bossis, G. (1988), "Stokesian dynamics," *Annual Review of Fluid Mechanics* **20**: 111-157

Bremond, R., Jeulin, D., Abouaf, M., and His, C. (1995), "Simulation of the filtration of cast-iron," *La Vevue de Métallurgie-Cahiers D Informations Techniques* **92**(5): 593-606

Briggs, W. L., Henson, Van E., and McCormick, S. F. (2000), *A Multigrid Tutorial*, 2nd Edition, SIAM, Philadelphia

Bruce, D. A., Littlejohn, G. S., and Naudts, A. M. C. (1997), "Grouting materials for ground treatment: a practitioner's guide," *Grouting: Compaction, Remediation and Testing*, Geotechnical Special Publication **66**, ASCE: 306-334

Bryant, S., and Blunt, M. (1992), "Prediction of relative permeability in simple porous media," *Physical Review A* **46**(4): 2004-2011

Burganos, V. N., Skouras, E. D., Paraskeva, C. A., and Payatakes, A. C. (2001) "Simulation of the dynamics of depth filtration of non-Brownian particles," *AIChE Journal* **47**(4): 880-894

Carmeliet, J., Descamps, F., and Houvenaghel, G. (1999), "A multiscale network model for simulating moisture transfer properties of porous media," *Transport in Porous Media* **35**(1): 67-88

Chandler, R., Koplik, J., Lerman, K., Willemsen, J. F. (1982), "Capillary displacement and percolation in porous-media," *Journal of Fluid Mechanics* **119**: 249-267

Chatzis, I., and Dullien, F. A. L.(1977), "Modeling pore structures by 2-D and 3-D networks with application to sandstones," *Canadian Journal of Petroleum Technology* Jan.-Mar.: 97-108 (referred by Berkowitz and Ewing, 1998)

Chiang, H. W., and Tien, C. (1985) "Dynamics of deep bed filtration: 1. Analysis of two limiting situations," *AIChE Journal* **31**: 1349-1359

Choo, C.-U., and Tien, C. (1995), "Analysis of the transient behavior of deep-bed filtration," *Journal of Colloid and Interface Science*, **169**: 13-33

Coelho, D., Thovert, J.-F., and Adler, P. M. (1997), "Geometrical and transport properties of random packings of spheres and aspherical particles," *Physical Review E* **55**(2): 1959-1977

Corapcioglu, M. Y., and Choi, H. (1986), "Modeling colloid transport in unsaturated porous media and validation with laboratory column data", *Water Resources Research* **32**(12): 3437-3449

Datta, S., and Redner, S. (1998a), "Gradient clogging in depth filtration," *Physical Review E* **58**(2): R1203-R1206

Datta, S., and Redner, S. (1998b), "Gradient and percolative clogging in depth filtration," *International Journal of Modern Physics C* **9**(8): 1535-1543

De Paoli, B., Bosco, B., Granata, R., and Bruce, D. A. (1992), "Fundamental observations on cement based grouts," *Soil Improvement and Geosynthetics*, Geotechnical Special Publication **30**, ASCE: 474-485

Duxbury, P. M., and Leath, P. L. (1994), "Exactly solvable models of material breakdown," *Physical Review Letter* **49**(18): 12676-12687

Einstein, A. (1956), *Investigations on the Theory of the Brownian Movement* (ed. R. Furth), Dover, New York (referenced by Probstein, 1994)

Elimelech, M., and O'Melia, C. R. (1990), "Effect of particle-size on collision efficiency in the deposition of Brownian particles with electrostatic energy barriers," *Langmuir* **6**(6): 1153-1163

Fatt, I. (1956), "The network model of porous media," *Petroleum Transactions AIME* **207**: 144-159 (referred by Berkowitz and Ewing, 1998)

Feder, J., and Giaever, I. (1980), "Adsorption of ferritin," *Journal of Colloid and Interface Science* **78**(1): 144-154

Fedkiw, P., and Newman, J. (1979), "Entrance region mass-transfer coefficients in packed-bed reactors," *AIChE Journal*, **25**(6): 1077-1080

Filippova, O., and Hänel, D. (1997), "Lattice-Boltzmann simulation of gas-particle flow in filters," *Computers and Fluids* **26**(7): 697-712

Finney, J. (1968), *Random Packings and the Structure of the Liquid State*, Ph.D. dissertation, London University (referred by Bryant and Blunt, 1992)

Gartner, E. M. (1997), "A proposed mechanism for the growth of C-S-H during the hydration of tricalcium silicate," *Cement and Concrete Research*, **27**(5): 665-672

Gause, C., and Bruce, D. A. (1997), "Control of fluid properties of particulate grouts: Part 1-General concepts, Part 2-Case histories," *Grouting: Compaction, Remediation and Testing*, Geotechnical Special Publication **66**, ASCE: 306-334

Goldman, A. J., Cox, R. G., and Brenner, H. (1967a), "Slow viscous motion of a sphere parallel to a plane wall: 1. Motion through a quiescent fluid," *Chemical Engineering Science* **22**: 637-650 (referred by Imdakm and Sahimi, 1991)

Goldman, A. J., Cox, R. G., and Brenner, H. (1967b), "Slow viscous motion of a sphere parallel to a plane wall: 2. Couette flow," *Chemical Engineering Science* **22**: 637-650 (referred by Imdakm and Sahimi, 1991)

Graton, L. C., and Fraser, H. J. (1935), "Systematic packing of spheres with particular relation to porosity and permeability," *Journal of Geology* **43**: 785-909 (referred by Johnson and Elimelech, 1995)

Gruesbeck, C., and Collins, R. E. (1982), "Entrainment and deposition of fine particles in porous media," *Society of Petroleum Engineering Journal*: 847-856

Haberman, W. L., and Sayre, R. M. (1958), *David Taylor Model Basin Report* **1143**, Washington, D.C., U.S. Navy Department

Happel, J. (1958), "Viscous flow in multiparticles systems: Slow motion of fluids relative to beds of spherical particles," *AIChE Journal* **4**: 197 (referred by Tien, C., 1989)

Happel, J., and Brenner, H. (1965), *Low Reynolds Number Hydrodynamics*, Prentice-Hall

Harvey, R. W., and Garabedian, S. P. (1991), "Use of colloid filtration theory in modeling movement of bacteria through a contaminated sandy aquifer," *Environmental Science and Technology*, **25**(1): 178-185

Hendry, M. J., Lawrence, J. R., and Maloszewski, P. (1997), "The role of sorption in the transport of *Klebsiella oxytoca* through saturated silica sand," *Ground Water* **35**: 575-584.

Herzig, J. P., Leclerc, D. M., and LeGolf, P. (1970), "Flow of suspension through porous media – application to deep filtration," *Industrial and Engineering Chemistry Research* **62**: 8-35

Higdon, J. J. L., and Muldowney, G. P. (1995), "Resistance functions for spherical particles, droplets and bubbles in cylindrical tubes," *Journal of Fluid Mechanics* **298**: 193-210

Hilpert, M., Glantz, R., and Miller, C. T. (2003), "Calibration of a pore-network model by a pore-morphological analysis," *Transport in Porous Media*, **51**: 267-285

Höfler K., and Schwarzer, S. (2000), "Navier-Stokes simulation with constraint forces: Finite-difference method for particle-laden flows and complex geometries," *Physical Review E* **61**(6): 7146-7160

Hwang, W., and Redner, S. (2001), "Infiltration through porous media," *Physical Review E*, **63**(2): 021508-1-13

Hunt, J. R., Hwang, B. C., and McDowellboyer, L. M., (1993), "Solids accumulation during deep bed filtration," *Environmental Science and Technology* **27**(6): 1099-1107

Imdakm, A. O., and Sahimi, M. (1987), "Transport of large particles in flow through porous-media," *Physical Review A* **36**(11): 5304-5309

Imdakm, A. O., and Sahimi, M. (1991), "Computer simulation of particle transport processes in flow through porous media," *Chemical Engineering Science* **46**(8): 1977-1993

Ives, K. J. (1960), "Filtration through a porous septum: a theoretical consideration of Boucher's Law," *Proceeding of Institution of Civil Engineers, London* **17**: 333-338

Ives, K. J. (1961)," Filtration using reduction algae," *Proceeding of ASCE Journal of Sanitary Engineering Division* **87,** SA3, 23

Ives, K. J. (1969), "Theory of Filtration," *Special subject* **7**, International Water Supply Congress and Exhibition, Vienna

Iwasaki, T., "Some notes on sand filtration," *Journal of American Water Works Association* **29**: 1951 (referred by Rege and Fogler, 1988)

Jerauld, G. R., and Salter, S. J. (1990), " The effect of pore-structure on hysteresis in relative permeability and capillary pressure: Pore-level modeling," *Transport in Porous Media* **14**: 33-72

Johnson, P. R., and Elimelech, M. (1995), "Dynamics of colloid deposition in porous-media-blocking based on random sequential adsorption," *Langmuir* **11**(3): 801-812

Jung, Y., and Tien, C. (1965), "Increase in collector efficiency due to deposition in polydispersed granular filtration-an experimental study," *Journal of Aerosol Science* **23**(5): 525-537

Kaada-Benameur, H., Wirquin, E., and Duthoit, B. (2000), "Determination of apparent activation energy of concrete by isothermal calorimetry," *Cement and Concrete Research* **30**: 301-305

Ko, C. H., and Elimelech, M. (2000), "The "shadow effect" in colloid transport and deposition dynamics in granular porous media: Measurements and mechanisms," *Environmental Science and Technology* **34**(17): 3681-3689

Koplik, J. (1982), "Creeping flow in two-dimensional networks," *Journal of Fluid Mechanics* **119**: 219-247

Krstulović, R, and Dabić, P. (2000), "A conceptual model of the cement hydration process," *Cement and Concrete Research* **30**(5): 693-698

Kruyer, S. (1958), "The penetration of mercury and capillary condensation in packed spheres," *Transaction of Faraday Society* **54**: 1758-1767 (referred by Yanuka et al., 1986)

Ladd, A. J. C. (1994), "Numerical simulations of particulate suspensions via a discretized Boltzmann-equation: 1. Theoretical foundation," *Journal of Fluid Mechanics* **271**: 285-309

Lamb, H. (1895), *Hydrodynamics*, 2nd Edition Cambridge University Press

Landry, E., Lees, D., and Naudts, A. (2000), "New developments in permeation grouting: design and evaluation," *Concrete International* **22**: 47-52

Langmuir, I. (1918), "The adsorption of gases on plane surfaces of glass, mica, and platinum," *Journal of the American Chemical Society* **40**: 1361-1403 (referred by Johnson and Elimelech, 1995)

Lawrence, J. R., and Hendry, M. J. (1995), "Mesocosms for subsurface research," *Water Quality Research Journal Canada*, **30**(3): 493-512

Le Bray, Y., and Prat, M. (1999), "Three-dimensional pore network simulation of drying in capillary porous media," *International Journal of Heat and Mass Transfer* **42**(22): 4207-4224

Lee, J., and Koplik, J. (2001), "Network model for deep bed filtration," *Physics of Fluids* **13**(5): 1076-1086

Lei, W.-G., and Struble, L. J. (1997), "Microstructure and flow behavior of fresh cement paste," *Journal of American Ceramic Society* **80**(8): 2021-2028

Levich, V. G. (1962), *Physicochemical Hydrodynamics*, Prentice Hall, Englewood Cliffs, NJ

Lymberopoulos, D. P., and Payatakes, A. C. (1992), "Derivation of topological, geometrical, and correlational properties of porous media from pore-chart analysis of serial section data," *Journal of Colloid and Interface Science* **150**(1): 61-80

Mackie, R. I., and Bai, R. (1992), "Suspended particle-size distribution-size distribution and the performance of deep bed filters," *Water Research* **26**(12): 1571-1575

Mackie, R. I., Horner, R. M. W., and Jarvis, R. J. (1987), "Dynamic modeling of deep-bed filtration," *AIChE Journal* **33**(11): 1761-1775

Mackie, R. I. and Zhao, Q. (1999), "A framework for modeling removal in the filtration of polydispersed suspensions," *Water Resources* **33**(3): 794-806

Mackrle, V., Draka, O., and Svec, J. (1965), *Hydrodynamics of the Disposal of Low Level Liquid Radioactive Wastes in Soil*, International Atomic Energy Agency, Contract Report **98**, Vienna

McKinley, J. D., and Bolton, M. D. (1999), "A Geotechnical description of fresh cement grout-filtration and consolidation behavior," *Magazine of Concrete Research* **51**(5): 295-307

Meinders J. M., and Busscher, H. J. (1995), "Influence of interparticle interactions on blocked areas and desorption during particle deposition to glass in a parallel-plate flow chamber," *Langmuir* **11**(1): 327-333

Mints, D. M. (1966), "Modern Theory of Filtration," *Special Report* **10**, International Water Supply Congress, Barcelona

Mitchell, J. K. "Soil Improvement – state-of-the-art report," *Proceedings of the 10th International Conference on Soil Mechanics and Foundations, Stockholm, Sweden, June 15-19*

Mittag, J. (2000), *Investigations on the Filtration Behavior of Microfine Cement Suspensions during Injection into Sands*, Ph.D. Thesis, Technical University of Berlin

Mohanka, S. S. (1969), "Theory of multistage filtration," Proceedings of the ASCE, *Journal of Sanitary Engineering Division* **95**(SA6): 1079 (referred by Bouchelaghem and Vulliet, 2001)

Neira, M.A., and Payatakes, A.C. (1978), "Collocation solution of creeping Newtonian flow through periodically constricted tubes with piecewise continuous wall profile," *AIChE Journal* **24**(1): 43-54

Nonat, A., Mutin, J. C., Leoq, X., and Jiang, S. P. (1997), "Physico-chemical parameters determining hydration and particle interactions during the setting of silicate cements," *Solid State Ionics* **101-103**: 923-930

Ornatski, N. V., Sergeev, E. V., and Shekhtman, Y. M. (1955), *Investigations of the Process of Clogging of Sands*, University of Moscow

Paraskeva, C. A., Burganos, V. N., and Payatakes, A. C. (1991), "3-dimensional trajectory analysis of particle deposition in constricted tubes," *Chemical engineering communications* **108**: 23-48

Pascal, H. (1986), "Rheological effects of non-Newtonian behavior of displacing fluids on stability of a moving interface in radial oil displacement mechanism in porous-media," *International Journal of Engineering Science* **24**(9): 1465-1476

Payatakes, A. C. (1973), *A New Model for Granular Porous Media: Application to Filtration through Packed Beds*, Ph.D. dissertation, Syracuse University (referred by Tien and Payatakes, 1979)

Payatakes, A. C., Ng, K. M., and Flumerfelt, R. W. (1980), "Oil ganglion dynamics during immiscible displacement: Model Formulation," *AIChE Journal* **26**(3): 430-443

Payatakes, A. C., Park, H. Y., and Petrie, J. (1981), "A visual study of particle deposition and reentrainment during depth filtration of hydrosols with a poly-electrolyte," *Chemical Engineering Science* **36**(8): 1319-1335

Payatakes, A. C., Tien, C., and Turian, R. M. (1973a), "A new model for granular porous media: part 1. Model formulation," *AIChE Journal* **19**(1): 58-67

Payatakes, A. C., Tien, C., and Turian, R. M. (1973b), "A new model for granular porous media: part 2. Numerical solution of steady state incompressible Newtonian flow through periodically constricted tubes," *AIChE Journal* **19**(1): 67-76

Payatakes, A. C., Tien, C., and Turian, R. M. (1974), "Trajectory calculation of particle deposition in deep bed filtration," *AIChE Journal* **20**(5): 889-900

Perret, S., Khayat, K. H., and Ballivy, G. (2000), "The effect of degree of saturation of sand on groutability-experimental simulation," *Ground Improvement* **4**: 13-22

Pilotti, M. (1998), "Generation of realistic porous media by grains sedimentation," *Transport in Porous Media* **33:** 257-278

Pomeau, Y. (1980), "Some asymptotic estimates in the random packing problem," *Journal of Physics A* **13**: L193-L196

Probstein, R. F. (1994), *Physicochemical Hydrodynamics-An Introduction*, 2nd Edition, John Wiley and Sons

Putnam, D. D., and Burns, M. A. (1997), "Predicting the filtration of noncoagulating particles in depth filters," *Chemical Engineering Science* **52**(1): 93-105

Raiskinmäki, P., Shakib-Manesh, A., Koponen, A., Jäsberg, A., Kataja, M., and Timonen, J. (2000), "Simulations of non-spherical particles suspended in a shear flow," *Computer Physics Communications* **129**: 185-195

Raffel, J. F., and Greenwood, D. A. (1961), "The relation between the rheological characteristics of grouts and their capacity to permeate soil," Proceeding of 5th ICSMFE, 789-793

Rajagopalan, R., and Tien, C. (1976), "Trajectory analysis of deep-bed filtration with sphere-in-cell porous-media model," *AIChE Journal* **22**(3): 523-533

Reddi, L. N., and Bonala, M. V. S. (1997), "Analytical solution for fine particle accumulation in soil filters," *ASCE Journal of Geotechnical and Geoenvironmental Engineering*, **123**(12): 1143-1152

Reddi, L. N., Ming, X., Hajra, M. G., and Lee, I. M. (2000), "Permeability reduction of soil filters due to physical clogging," *Journal of Geotechnical and Geoenvironmental Engineering*, **126**(3): 236-246

Redner, S., and Datta, S. (2000), "Clogging time of a filter," *Physical Review Letters* **84**(26): 6018-6021

Rege, S. D., and Fogler, H. S. (1987), "Network model for straining dominated particle entrapment in porous-media," *Chemical Engineering Science* **42**(7): 1553-1564

Rege, S. D., and Fogler, H. S. (1988), "A network model for deep bed filtration of solid particles and emulsion drops," *AIChE Journal* **34**(11): 1761-1772

Richardson, J. F. and Zaki, W. N. (1954), "Sedimentation and fluidisation, Part 1," *Transaction of the Institution of Chemical Engineers* **32**: 35-53

Russell, W. B., Saville, D. A., and Schowalter, W. R. (1989), *Colloidal Dispersions*, Cambridge University Press, Cambridge

Ryan, J. N., and Elimelech, M. (1996), "Colloid mobilization and transport in groundwater," *Colloids and Surfaces A* **107**: 1-56

Sahimi, M. (1998), "Non-linear and non-local transport processes in heterogeneous media: from long-range correlated percolation to fracture and materials breakdown," *Physics Reports* **306**: 213-395

Sahimi, M., and Imdakm, A. O. (1991), "Hydrodynamics of particulate motion in porous-media," *Physical Review Letters* **66**(9): 1169-1172

Sahimi, M., and Goddard, J. D. (1986), "Elastic percolation models for cohesive mechanical failure in heterogeneous systems," *Physical Review B* **33**(11): 7848-7851

Saiers, J. E., Hornberger, G. M., and Liang, L. Y. (1994), "First-order and second-order kinetics approaches for modeling the transport of colloidal particles in porous-media," *Water Resources Research* **30**(9): 2499-2506

Santagata, M. C., and Collepardi, M. (1998), " Selection of cement-based grouts for soil treatment," *Grouts and Grouting: A Potpourri of Projects,* Geotechnical Special Publication **80** ASCE: 177-195

Sanchez-Palencia, E. (1980), "Non-homogeneous media and vibration theory," *Lecture Notes in Physics* **127**, Springer Verlag

Schijven, J. F., and Hassanizadeh, S. M. (2000), "Removal of viruses by soil passage: Overview of modeling, processes, and parameters," *Critical Reviews in Environmental Science and Technology* **30**(1): 49-127

Schwarz, L. G., and Krizek, R. J. (1994), "Effect of preparation technique on permeability and strength of cement-grouted sand," *Geotechnical Testing Journal* **17**(4): 434-443

Schaaf, P., and Talbot, J. (1989), "Kinetics of random sequential adsorption," *Physical Review Letters* **62**(2): 175-178

Sharma, M. M., and Yortsos, Y. C. (1987a), "Transport of particulate suspensions in porous-media: Model formulation," *AIChE Journal* **33**(10): 1636-1643

Sharma, M. M., and Yortsos, Y. C. (1987b), "A network model for deep bed filtration processes," *AIChE Journal* **33**(10): 1644-1653

Shroff, A.V., Joshi, N. H., and Shah, D. L. (1996), "Rheological properties of microfine cement dust grouts," *Grouting and Deep Mixing*, Balkema, Rotterdam

Soo, H., and Radke, C. J. (1986), "A filtration model for the flow of dilute, stable emulsions in porous-media: 1. Theory," *Chemical Engineering Science* **41**(2): 263-272

Sorensen, E. N., Burgreen, G. W., Wagner, W. R., and Antaki, J. F. (1999a), "Computational simulation of platelet deposition and activation: I. Model development and properties," *Annals of Biomedical Engineering* **27**(4): 436-448

Sorensen, E. N., Burgreen, G. W., Wagner, W. R., and Antaki, J. F. (1999b), "Computational simulation of platelet deposition and activation: II. Results for Poiseuille flow over collagen," *Annals of Biomedical Engineering* **27**(4): 449-458

Spanne, P., Thovert, J. F., Jacquin, C. J., Lindquist, W. B., Jones, K. W., and Adler, P. M. (1994), "Synchrotron computed microtomography of porous media: topology and transports," *Physical Review Letters* **73**(14): 2001-2004

Stein, P. C. (1940), *A Study of the Theory of Rapid Filtration of Water through Sand*, D.Sc. dissertation, Massachusetts Institute of Technology, Cambridge, Mass

Stepanek, F., Marek, M., and Adler, P. (1999), "Modeling capillary condensation hysteresis cycles in reconstructed porous media," *AIChE Journal* **45**(9): 1901-1912

Stephan, E. A., and Chase, G. G. (2000), "Development of volume-average theory for deep-bed filtration," *AIChE Journal* **46**(10): 1918-1926

Struble, L. J., and Sun, G.-K. (1995), "Viscosity of Portland cement paste as a function of concentration," *Advance Cement Based Material* **2**: 62-69

Suchomel, B. J., Chen, B. M., and Allen, M. B. (1998a), "Network model of flow, transport and biofilm effects in porous media," Transport in Porous Media 30(1): 1-23

Suchomel, B. J., Chen, B. M., and Allen, M. B. (1998b), "Macroscale properties of porous media from a network model of biofilm processes," Transport in Porous Media 31(1): 39-66

Tattersall, G. H., and Banfill, P. F. G. (1983), *The Rheology of Fresh Concrete*, Pitman Publishing, Boston

Taylor, H. F. W. (1997), "*Cement Chemistry*," 2nd edition, Thomas Telford

Thompson, K. E., and Fogler, H. S. (1997), "Modeling flow in disordered packed beds from pore-scale fluid mechanics," *AIChE Journal* **43**(6): 1377-1389

Thompson, K. E., and Fogler, H. S. (1998), "Pore-scale model for fluid injection and in situ gelation in porous media," *Physical Review E* **57**(5): 5825-5832

Tien, C. (1989), *Granular Filtration of Aerosols and Hydrosols*, Butterworths

Tien, C., and Payatakes, A. C. (1979), "Advances in deep bed filtration," *AIChE Journal* **25**(5): 737-759

Toumbakari, E. E., Van Gemert, D., Tassio, T. P., and Tenoutasse, N. (1999), "Effect of mixing procedure on injectability of cementitious grouts," *Cement and Concrete Research*, **29**(6): 867-872

Tsai, S. C., Botts, D., and Plouff, J. (1992), "Effects of Particle Properties on the Rheology of Concentrated Noncolloidal Suspensions," *Journal of Rheology* **36**(7): 1291-1305

Tsakiroglou, C. D., and Payatakes, A. C. (1990), "A new simulator of mercury porosimetry for the characterization of porous materials," *Journal of Colloid and Interface Science* **137**(2): 315-339

Tsakiroglou, C. D., and Payatakes, A. C. (1991), "Effects of pore-size correlations on mercury porosimetry curves," *Journal of Colloid and Interface Science* **146**(2): 479-494

Tsakiroglou, C. D., and Payatakes, A. C. (2000), "Characterization of the pore structure of reservoir rocks with the aid of serial sectioning analysis, mercury porosimetry and network simulation," *Advances in Water Resources* **23**: 773-789

Tufenkji, N., and Elimelech, M. (2004), "Correlation equation for predicting single-collector efficiency in physicochemical filtration in saturated porous media," *Environmental Science and Technology* **38**: 529–536

Ulm, F.-J., and Coussy, O. (1996), "Strength growth as chemo-plastic hardening in early age concrete," *ASCE Journal of Engineering Mechanics* **122**(12): 1123-1132

Vaidyanathan, R., and Tien, C. (1988), "Hydrosol deposition in granular beds, " *Chemical Engineering Science* **43**: 289-302

Venkatesan, M., and Rajagopalan, R. (1980), "A hyperboloidal constricted tube model of porous-media," *AIChE Journal* **26**(4): 694-698

Wang, W., and Parker, K. H. (1998), "Movement of spherical particles in capillaries using a boundary singularity method," *Journal of Biomechanics* **31**: 347-354

Widom, B. (1966), "Random sequential addition of hard spheres to a volume," *Journal of Chemical Physics* **44**: 3888-3894

Wilkinson, D., and Willemsen, J. F. (1983), "Invasion percolation-a new form of percolation theory," *Journal of Physics A* **16**(14): 3365-3376

Wu, B. Q., and Leath, P. L. (1999), "Failure probabilities and tough-brittle crossover of heterogeneous materials with continuous disorder," *Physical Review B* **59**(6): 4002-4010

Yanuka, M. (1989), "Percolation processes and porous media: 3. Prediction of the capillary hysteresis loop from geometrical and topological information of pore space," *Journal of Colloid and Interface Science* **127**: 48-57

Yanuka, M., Dullien, F. A. L., and Elrick, D. E. (1986), "Percolation processes and porous media, 1. Geometrical and Topological model of porous media using a three-dimensional joint pore size distribution," *Journal of Colloid and Interface Science* **112**(1): 24-41

Yao, K.M., Habibian, M.T., and O'Melia, C.R. (1971) Water and waste water filtration: Concepts and applications. *Envonmental Science and Technology* **5** , 1105-1112

Yates, M. V., and Yates, S. R. (1988), "Modeling microbial fate in the subsurface environment," *CRC Critical Review of Environmental Control* **17**: 307-344

Yoon, J. S., Culligan, P. J., and Germaine, J. T. (2004), "Direct observations of discrete particle behavior in a porous medium: evidence of particle entrapment and hindrance," submitted to *Water Resources Research*

Zebovitz, S., Krizek, R. J., and Atmatzidis, D. K. (1989), "Injection of fine sands with very fine cement grout," *ASCE Journal of Geotechnical Engineering* **115**(12): 1717-1733

Zhou, D., and Stenby, E. H. (1993), "Interpretation of capillary pressure curves using invasion percolation theory," *Transport in Porous Media* **11**: 17-33